Photocataly
Engineering

Hugo de Lasa
Benito Serrano
Miguel Salaices

CuuDuongThanCong.com https://fb.com/tailieudientu

Photocatalytic Reaction Engineering

Hugo de Lasa
Benito Serrano
Miguel Salaices

cuu duong than cong . com

CuuDuongThanCong.com https://fb.com/tailieudientucntt

Library of Congress Cataloging-in-Publication Data

De Lasa, Hugo I.
Photocatalytic reaction engineering / Hugo deLasa [sic], Benito Serrano, and Miguel Salaices.
p. cm.
Includes bibliographical references and index.
ISBN 978-1-4419-3627-1 ISBN 978-0-387-27591-8 (eBook)
DOI 10.1007/978-0-387-27591-8

1. Photocatalysis. 2. Reaction mechanisms (Chemistry) 3. Chemical engineering. I. Serrano, Benito. II. Salaices, Miguel, III. Title
QD716.P45.D4 2005
541′.395–dc22 2004065093

A C.I.P. Catalogue record for this book is available
from the Library of Congress.

ISBN 978-1-4419-3627-1

© 2005 Springer Science+Business Media New York
Originally published by Springer Science+Business Media,Inc. in 2005
Softcover reprint of the hardcover 1st edition 2005
All rights reserved. This work may not be translated or copied in whole or in part without the written permission of the publisher Springer Science+Business Media, LLC,
except for brief excerpts in connection with reviews or scholarly analysis. Use in
connection with any form of information storage and retrieval, electronic adaptation, computer software, or by similar or dissimilar methodology now know or hereafter developed is forbidden.

The use in this publication of trade names, trademarks, service marks and similar terms, even if they are not identified as such, is not to be taken as an expression of opinion as to whether or not they are subject to proprietary rights.

9 8 7 6 5 4 3 2 1

springeronline.com

CuuDuongThanCong.com https://fb.com/tailieudientucntt

Photocatalytic Reaction Engineering

cuu duong than cong . com

CuuDuongThanCong.com https://fb.com/tailieudientucntt

About the Authors

Hugo de Lasa is a Professor at the Faculty of Engineering of the University of Western Ontario in Canada. He is the Director of the Chemical Reactor Engineering Centre (CREC), the author of many peer reviewed publications, several books, and patents, and co-founding editor of the International Journal of Chemical Reactor Engineering. As a teacher, Dr. de Lasa has been actively involved in the training of numerous graduate students. His activities have contributed to furthering the understanding of the science and the technology of chemical reactors. Dr. de Lasa is the recipient of several awards and distinctions which include the Research Excellence Award from the University of Western Ontario (1998), the Fellowship of the Chemical Institute of Canada (2000), the Medal of Research and Development from the Professional Engineers of Ontario (2000), the Award in Industrial Practice (2001) and the R.S. Jane Lecture Award (2004) both from the Canadian Society for Chemical Engineering.

Benito Serrano-Rosales is a Professor at the Department of Chemical Engineering, of the Universidad Autónoma de Zacatecas in Mexico. Dr. Serrano is a tenured member of the Mexican Sistema Nacional de Investigadores (S.N.I.) holding a significant record of referred publications and conference proceedings. His research focuses on environmental remediation, with emphasis on water decontamination using photocatalysis. Dr.Serrano is actively involved in university research and in the supervision of graduate students. He is a member of the AMIDIQ (Academia Mexicana de Investigación y Docencia en Ingeniería Química) and has collaborated in this capacity in the organization of several Mexican and international conferences. Dr. Serrano has established valuable working relationships with several universities in Canada, USA, Mexico and Latin America.

Miguel Salaices-Arredondo is a PhD graduate from the University of Western Ontario in Canada. Since 1990, Dr. Salaices has worked as a research engineer in the Nuclear Energy Department of the Instituto de Investigaciones Eléctricas in Mexico. His research interests include the development of reactors for water treatment with a focus on the optimization and the modeling of radiation distribution in photocatalyst suspended media. Dr. Salaices is also involved in the development of computational systems for the

CuuDuongThanCong.com https://fb.com/tailieudientucntt

improvement of reactor safety in nuclear power plants. He has contributed to a considerable number of refereed papers, technical reports, design specifications, and refereed proceedings. Dr. Salaices is a member of the Mexican Nuclear Society and a tenured member of the Mexican Sistema Nacional de Investigadores (S.N.I.).

cuu duong than cong . com

CuuDuongThanCong.com https://fb.com/tailieudientucntt

Preface

The pursuit of knowledge and discovery ebbs and flows. Peaks of innovation and discovery are often followed by periods of calm that invite reflection and reassessment, which in turn motivate renewed efforts towards further advancement. It is our view that the study of photocatalytic reaction engineering is in a phase of reassessment. The very principles of reaction engineering are under review at this time when environmental pressures and social concerns are changing the way we perceive and use technology. The application of photocatalytic reaction technology holds great promise in these changing times.

It is our aspiration to offer with this book a coherent and comprehensive treatment of the subject with thoroughly integrated contributions of the three co-authors.

Chapter I examines the basic principles involved in modeling photocatalytic reaction rates. Clarification in this area is needed as it is often lacking and is required for proceeding with the design, the simulation and the scale-up of the photocatalytic reactor units. Once these concepts are established, Chapter II describes various novel photocatalytic reactors designed by research groups around the world including the Photo-CREC reactors, developed in the context of the authors' research activities at the Chemical Reactor Engineering Centre (CREC), the University of Western Ontario in London, Canada and at the Universidad Autónoma de Zacatecas, Mexico. This chapter provides insight on the opportunities to extend the application of this technology through innovation in chemical reactor engineering.

Chapter III addresses the need of reviewing various types of photocatalysts, power sources and auxiliary equipment available for photocatalytic studies. Description of these matters is of essential importance for establishing radiation source power spectra, their lifetime and their power decay, for describing the available tools for macroscopic radiation balances and for effective kinetic and reaction rate modeling.

Chapter IV elucidates the methodology to develop a macroscopic radiation balance. This methodology allows the effective assessment of absorbed irradiation and irradiation transmission involving apparent extinction coefficients. The focus is put on demonstrating the applicability of these relatively simple functions to make the prediction of photon transfer and photon absorption a tractable mathematical problem. Thus, this chapter provides valuable tools from the perspective of the photocatalytic reactor designer.

Chapter V addresses the important task of accounting for the complex network of photochemical reactions, establishing viable kinetic modeling. This modeling is essentially based on a series-parallel model of the photocatalytic reaction network.

CuuDuongThanCong.com https://fb.com/tailieudientucntt

Examples are given to demonstrate the extent of applicability of this approach to the photoconversion of phenol.

Furthermore, the extensive applicability of photocatalysis has essentially become a problem of energy efficiency. As a result, the quantification of these energy efficiency factors is a major issue. Thus, Chapter VI considers these factors from two perspectives: quantum efficiencies and Photochemical Thermodynamic Efficiency Factor (PTEF), the latter being a new efficiency factor introduced by the authors.

Chapter VII addresses the need to account for both physical and chemical phenomena, reaction and adsorption. In fact, consideration of these combined phenomena is, in the view of the authors, essential to provide effective kinetic and rate modeling for the photo conversion of organic and inorganic pollutants. Cases with several organic species are presented including methylene blue, phenol, chloro-phenol, di-chloro-phenol, catechol, and pyrogallol.

Air decontamination is another potential innovative application of photocatalysis. Chapter VIII focuses on air decontamination using Photo-CREC reactors. Several examples are provided by examining the photoconversion of acetone, iso-propanol, and acetaldehyde. Special attention is paid to the quantum efficiencies for air decontamination, exceeding 100% in many cases, which demonstrates the distinctive chain mechanism character of the photoconversion of organic pollutants in air.

Finally, Chapter IX, discusses recent research on the concurrent oxidation-reduction of organic and inorganic compounds and on the inactivation of model microorganisms. These two applications of photocatalysis have the potential of significantly improving the prospects for this novel technology.

In summary, our book contains an up-to-date discussion of photocatalytic reaction engineering and the application of these principles. Altogether it is an invitation to reflect on the possibilities of photocatalysis as a new and unique technique with great potential for air and water treatment. We offer our book as a contribution to the development of reaction engineering in photocatalysis as well as to the extensive potential for application of this technology.

We would like to express our appreciation to the University of Western Ontario, Canada, the Universidad Autónoma de Zacatecas, México and the Instituto de Investigaciones Eléctricas, México for their onthusiastic support of this project.

The authors wish to acknowledge the contributions of Dr. H. Ibrahim, Mr. J. Stuart, Mr. Jesus Moreira del Rio and Salvador Escobedo Salas whose research enriched some of the sections of this book. We are thankful to Ms. Naomi Pavan and Mrs. Graciela Lamana de Lasa who helped with the proofreading and technical editing of the manuscript. We would also like to express our appreciation to Mr. Martin de Lasa who designed the book cover and to Ms. Cristina de Lasa who offered valuable advice for the preparation of this cover. Finally, we are indebted to Mr. Kenneth Howell Senior Editor for Chemistry, Springer who provided guidance from a publisher's perspective.

London, Canada, August 2004

Hugo de Lasa
University of Western Ontario, Canada
Benito Serrano
Universidad Autónoma de Zacatecas, México
Miguel Salaices
Instituto de Investigaciones Eléctricas, México

CuuDuongThanCong.com https://fb.com/tailieudientucntt

Contents

CuuDuongThanCong.com https://fb.com/tailieudientucntt

CuuDuongThanCong.com https://fb.com/tailieudientucntt

CuuDuongThanCong.com https://fb.com/tailieudientucntt

cuu duong than cong . com

CuuDuongThanCong.com https://fb.com/tailieudientucntt

1

Establishing Photocatalytic Kinetic Rate Equations: Basic Principles and Parameters

1.1. INTRODUCTION

Heterogeneous photocatalysis is a promising new alternative method for the removal of organic pollutants in water (Carey, 1976). The degradation of organic pollutants in water, using irradiated dispersions of titanium dioxide, is a growing area of both fundamental and applied research.

This chapter reviews the basic principles involved in modeling the rates of photocatalytic reactions. These matters require clarification in order to proceed with the successful design, simulation and scale-up of photo catalytic reactor units.

1.2. THE PHOTOCATALYTIC REACTION AND THE INITIATION STEP

Three components must be present in order for the heterogeneous photocatalytic reaction to take place: an emitted photon (in the appropriate wavelength), a catalyst surface (usually a semi-conductor material) and a strong oxidizing agent (in most cases oxygen). Pasquali *et al.*, (1996) indicated that absorbed photons should be considered to be a nonmaterial reactant, which, like other reacting species, must be present for the reaction to occur.

The heterogeneous photocatalytic process is initiated when a photon with energy equal to or greater than the band gap energy (E_{bg}) of the photocatalyst reaches the photocatalyst surface, resulting in molecular excitation. E_{bg} is defined as the difference between the filled valence band and the empty conduction band of the photocatalyst, in the order of a few electron volts.

This molecular excitation results in the generation of mobile electrons in the higher energy conduction band (E_{cb}) and positive holes in the lower energy valence band (E_{vb}) of the catalyst, according to equation 1-1 and the reaction illustrated in Figure 1.1.

$$photocatalyst \xrightarrow{E_{ph} \geq E_{bg}} e^- + h^+ \qquad (1\text{-}1)$$

CuuDuongThanCong.com https://fb.com/tailieudientucntt

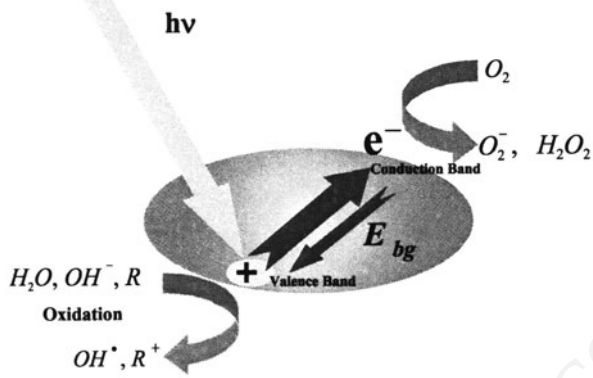

FIGURE 1.1. Schematics of the electron-hole generation in a photocatalyst particle and some of the mechanisms involved: a) Ray promotes the formation of the electron-hole and electron, b) electron-hole is used in the formation of the $OH^\bullet$ groups promoting oxidation processes, c) the electron is utilized in a number of reduction processes, d) electron and electron-hole can recombine contributing to process inefficiency.

The photocatalytic reaction proceeds via a series of chemical events, following the initiation step of pair electron-hole formation. This leads to the utilization of both the electron-hole h^+ for oxidation processes and eventually to the capture of the e^- electron for reduction processes, as well as the potential formation of super oxides anions and hydrogen peroxide from oxygen.

Unfortunately, there is a competing electron and electron-hole recombination step (the reverse of equation (1-1)), and this result in process inefficiencies and the waste of the energy supplied by the photon. The electron-hole recombination can be considered as one of the major factors limiting the efficiency of the photocatalytic processes.

Every effort to prevent electron and electron-hole recombination will improve the efficiency of heterogeneous photocatalytic processes and will considerably help to achieve the application of this technique for water and air purification.

1.3. THE PHOTOCATALYTIC REACTION

The heterogeneous photocatalytic reaction can be represented as a number of mechanistic steps (Legrini *et. al.*, 1993; Hoffman *et. al.*, 1995; Turchi and Ollis, 1990).

A photo-excited TiO_2 generates an electron and an electron-hole.

$$TiO_2 \xrightarrow{h\nu} e^- + h^+ \tag{1-2}$$

Electron transfer from the adsorbed substrate (RX_{ad}), adsorbed water or the OH_{ad} ion, to the electron-hole.

$$h^+ + RX_{ad} \rightarrow RX_{ad}^+ \tag{1-3}$$

$$h^+ + H_2O_{ads} \rightarrow OH_{ads}^\bullet + H^+ \tag{1-4}$$

$$h^+ + OH_{ad}^- \rightarrow OH_{ad}^\bullet \tag{1-5}$$

CuuDuongThanCong.com https://fb.com/tailieudientucntt

The third step is of great importance, mostly because of the high concentrations of OH^-, given water dissociation into ions.

$$H_2O \rightarrow OH^-_{ad} + H^+ \tag{1-6}$$

Molecular oxygen acts as an acceptor species in the electron-transfer reaction.

$$e^- + O_2 \rightarrow O_2^- \tag{1-7}$$

Super-oxide anions, (equation 1-7), can subsequently be involved in the following reactions.

$$O_2^- + H^+ \rightarrow HO_2^\bullet \tag{1-8}$$

$$H^+ + O_2^- + HO_2^\bullet \rightarrow H_2O_2 + O_2 \tag{1-9}$$

Photoconversion of hydrogen peroxide gives more $OH^\bullet$ free radical groups.

$$H_2O_2 + h_\upsilon \rightarrow 2OH^\bullet \tag{1-10}$$

Finally, $OH^\bullet$ radicals oxidize organic adsorbed pollutants (RX_{ad}) onto the surface of the titanium dioxide particles.

$$OH^\bullet_{ad} + RX_{ad} \rightarrow Intermediate \tag{1-11}$$

The $OH^\bullet$ radicals, as described by equation (1-11), are very reactive and attack the pollutant molecule to degrade it into mineral acids including carbon dioxide and water (Al-Ekabi *et al.*, 1993).

There are two possible explanations of photocatalytic reactions. While some authors suggest an indirect oxidation via a surface-bound hydroxyl radical (refer to equations (1-5) and (1-11)) (Mills and Hoffmann, 1993; Terzian *et al.*, 1991; Turchi and Ollis, 1990), another group argues in favor of a direct oxidation via the valence-band hole (equation (1-3) (Draper and Fox, 1990).

In support of the argument for the surface-bound hydroxyl radical mechanism, there is an intermediate presence of hydroxylated structures during the photocatalytic degradation of halogenated aromatics. These hydroxylated intermediates are also found when similar aromatics react with a known source of hydroxyl radicals. Furthermore, ESR studies confirm the existence of hydroxyl and hydro-peroxy radicals in aqueous solutions of illuminated TiO_2 (Hoffman *et al.*, 1995; Linsebigler *et al.*, 1995).

1.4. MODELING PHOTOCATALYTIC REACTION RATES

The modeling of photocatalytic reaction rates is essentially based on a number of mathematical statements, which can be expressed by a set of ordinary differential

CuuDuongThanCong.com https://fb.com/tailieudientucntt

equations. Each of these equations is established for the key chemical species and therefore species' balances in photocatalytic reactors can be typically described as follows:

$$V\frac{dC_i}{dt} = \left[\sum_k \nu_{i,k}\ R_k\right]\ W_{irr} \tag{1-12}$$

with V being the total reactor volume in L, C_i being the concentration of the i chemical species in g L^{-1}, t being the time in s, $\nu_{i,k}$ being a dimensionless stochiometric coefficient for i species involved in reaction step k and R_k being the rate of photoconversion of step k based on the unit weight of irradiated catalyst, W_{irr}, in mole $(g_{cat}\ s)^{-1}$.

This equation involves a number of important assumptions satisfied by most photocatalytic reactor units, either in the case of reactors with suspended TiO_2 or in reactors with immobilized TiO_2.

(a) The photocatalytic reactor unit is operated in the batch mode. This condition is typically required because of the relatively low photocatalytic reaction rates.
(b) W_{irr}, the weight of irradiated catalyst is known.
(c) Mixing and fluid recirculation are high enough so that a *quasi* constant reaction rate can be defined in the irradiated reactor section.

Equation (1-12) can be rearranged and simplified in some situations; such as in the case of model pollutant consumption. The rate of photoconversion can then be expressed in terms of measurable parameters and variables

$$r_1 = \frac{V}{W_{irr}}\frac{dC_1}{dt} = \sum_k \nu_{1,k} R_k \tag{1-13}$$

with $i = 1$ and "1" representing the model compound.

The consideration of equations (1-12) and/or (1-13) leads to the advancement of photocatalytic conversion rate models, such as the series-parallel model proposed by Salaices *et al.* (2004) where the derived kinetic parameters are based on the irradiated weight of catalyst. As such, these can be considered as *intrinsic parameters* with phenomenological meaning pertinent to the photocatalytic reaction.

$$\frac{dC_i}{dt} = \frac{-k_i''' C_i}{1 + \sum_{j=1}^{n} K_j C_j} \tag{1-14}$$

with k_i representing the kinetic constants for the i species in s^{-1} and K_j is the adsorption constant for the species j (any of the species present) in L $mole^{-1}$.

A similar approach to that used in equation (1-13) can be adopted by referring the rate of model pollutant photoconversion to A_{irr}, the external area of irradiated catalyst,

$$r_1' = \frac{V}{A_{irr}}\frac{dC_1}{dt} = \sum_k \nu_{1,k} R_k' \tag{1-15}$$

CuuDuongThanCong.com https://fb.com/tailieudientucntt

Another possible approach is the use of less meaningful "apparent" rates of photoconversion employing a different basis, such as in the case of V_{irr}, the irradiated reactor volume. Thus, the basic balance, as described in equation (1-12), becomes

$$V\frac{dC_i}{dt} = \left[\sum_k \nu_{i,k}\ R_k''\right]\ V_{irr} \tag{1-16}$$

with V being the total reactor volume in L, C_i being the concentration of the i chemical species in g L^{-1}, t being the time in s, $\nu_{i,k}$ being a dimensionless stochiometric coefficient for i species involved in reaction step k and R_k'' being the rate of photoconversion of k step, based in the unit irradiated reactor volume, V_{irr}, in mole $(L\ s)^{-1}$.

Thus, for the case of a model pollutant photoconversion equation (1-16) can be expressed as follows.

$$r_1'' = \frac{V}{V_{irr}}\frac{dC_1}{dt} \tag{1-17}$$

with $i = 1$ and 1 being the model compound.

The definition of the rate of photoconversion then becomes:

$$r_1'' = \frac{V}{V_{irr}}\frac{dC_1}{dt} = \frac{(V_{irr} + V_d)}{V_{irr}}\frac{dC_1}{dt} \tag{1-18}$$

with V, the system reactor volume, being the combined irradiated volume V_{irr} and non-irradiated volume (dark reactor volume section) V_d.

During the process of calculating the rates of photoconversion, frequently researchers make no distinction between the total reactor volume, V, and the irradiated reactor volume. It should be stressed that only under very special conditions and designs one can adopt the $V = V_{irr}$ assumption and consider an apparent rate of photoconversion directly obtained from the change in concentration of an i chemical pollutant species.

$$\frac{dC_1}{dt} = \sum_k \nu_{1,k}\ R_k''' \tag{1-19}$$

or

$$r_1''' = \frac{dC_1}{dt} \tag{1-20}$$

with $i = 1$ for the model pollutant.

In summary, one can establish for a model pollutant the following,

$$r_1''' = r_1''\frac{V_{irr}}{V} = r_1'\frac{A_{irr}}{V} = r_1\frac{W_{irr}}{V} \tag{1-21}$$

Thus, when relating the observed changes in concentration of chemical species in a given reactor geometry with the rate of photodegradation, the irradiated catalyst weight

CuuDuongThanCong.com https://fb.com/tailieudientucntt

(W_{irr}) or the irradiated reactor volume (V_{irr}) should be carefully considered as two key parameters. This makes photocatalytic rate definition and kinetic parameter calculations phenomenologically sound and meaningful.

The kinetic parameters obtained should otherwise be subjected to corrections using factors suggested by Salaices et al. (2002). For a first order decomposition, apparent reaction parameters should be corrected as follows:

$$k_1''' = k_1'' \frac{V_{irr}}{V} = k_1' \frac{A_{irr}}{V} = k_1 \frac{W_{irr}}{V} \tag{1-22}$$

1.5. EFFECT OF THE LAMP IRRADIATION AND CATALYST LOADING ON THE PHOTOCATALYTIC RATE

Both lamp irradiation and catalyst concentration play very important roles in photocatalytic processes. The effect of the irradiation parameter on the overall (apparent) rate of photoconversion can be represented by a power varying between 0.5 and 1. The influence of the photocatalyst weight can also be considered using a generic function of the irradiated catalyst.

The overall (apparent) initial reaction rate can be represented as the product of several functionalities, which include a function dependent on the i chemical species concentration defined at the initial condition $f_1(C_{i,in})$, a function dependent on the catalyst concentration $f_2(C_C)$ or the catalyst weight, and a function dependant on the rate of absorbed photons $f_3(P_a)$.

$$r_{i,in}''' = f_1(C_{i,in}) f_2(C_C) f_3(P_a) \tag{1-23}$$

In order to clarify the dependence of the initial photoconversion rate with $f_3(P_a)$, Salaices *et al.* (2001) developed experiments with phenol with a changing incident absorbed radiation. As suggested by a number of authors (Okamoto et al., 1985; Ollis, 1991; Pelizzetti et al., 1993; Trillas et al., 1996, 1992; Wei et al., 1994), it is proven that at low levels of absorbed incident radiation there is a linear relationship between the initial photoconversion rate of phenol and the incident absorbed radiation, $r_{1,in}''' = m_3 f_3(P_a) = m_3 P_a^{\delta}$, with $\delta = 1$ and $m_3 = f_1(C_{1,in}) f_2(C_C)$ as the proportionality factor in μ mole L^{-1} einstein^{-1} (refer to Figure 1.2).

This dependence of the photoconversion rate with the incident radiation is established in a Photo-CREC-Water II unit using removable glass tubes and meshes having different openings (for additional details refer to Chapter IV).

The effect of catalyst loading over Degussa P25, $f_2(C_C)$, on the overall initial photoconversion rate is illustrated in Figure 1.3. The catalyst concentration changes from zero to 0.35 g L^{-1}, corresponding to 100 and 0.005 % radiation transmission, respectively. It is observed that a minimum amount of catalyst is required to start the photodegradation, C_{wf}. It is also noticed that the overall reaction rate increases with catalyst loading until it reaches a $r_{1,in}'''$ maximum value of approximately 7.0 μ mole-C (L min)$^{-1}$, at catalyst concentrations higher than 0.14 g L^{-1}.

CuuDuongThanCong.com https://fb.com/tailieudientucntt

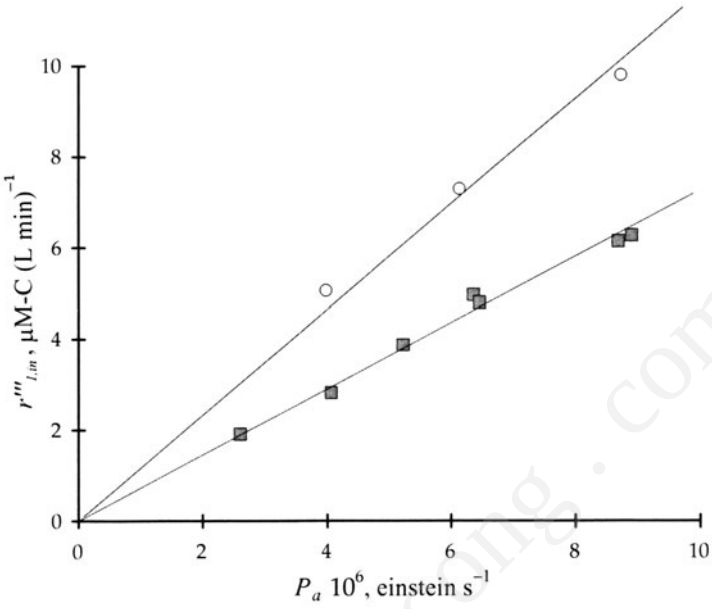

FIGURE 1.2. Initial phenol photoconversion rate ($r'''_{1,in}$) versus incident radiation intensity. (■) Removable 3.2-cm diameter glass inner tube, (○) Removable 5.6-cm diameter glass inner tube. (Reprinted with permission from *Ind. Eng. Chem. Res.*, **40**(23), M. Salaices, B. Serrano and H.I. de Lasa, Photocatalytic conversion of organic pollutants: Extinction coefficients and quantum efficiencies, 5455–5464. Copyright 2001 American Chemical Society).

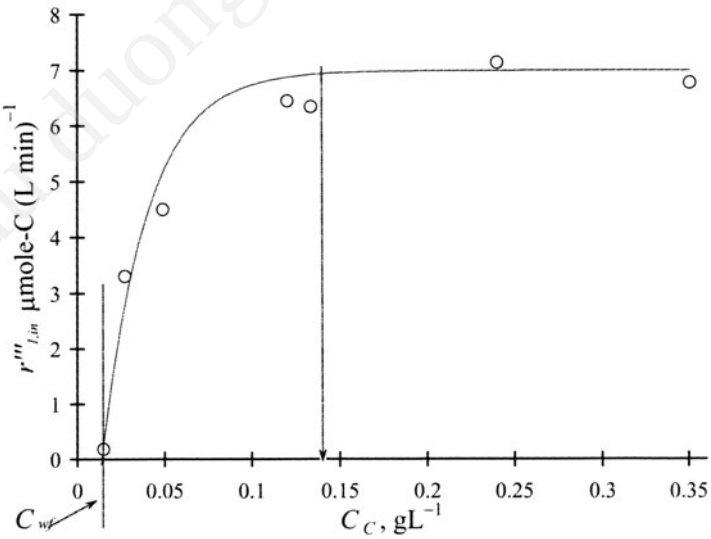

FIGURE 1.3. Initial reaction rate as a function of the catalyst loading. Catalyst: Degussa P25 (Reprinted with permission from *Ind. Eng. Chem. Res.*, **40**(23), M. Salaices, B. Serrano and H.I. de Lasa, Photocatalytic conversion of organic pollutants: Extinction coefficients and quantum efficiencies, 5455–5464. Copyright 2001 American Chemical Society).

CuuDuongThanCong.com https://fb.com/tailieudientucntt

These results can be explained as follows:

$$r'''_{1,in} = m_2 f_2(C_C) = m_2 P_i \big|_{C_C \to 0} [1 - \exp(-\alpha C_C)] \tag{1-24}$$

Given $P_i \big|_{C_c \to 0} = P_i - P_{bs}$ (refer to Chapter IV), then,

$$r'''_{1,in} = m_2 P_i [1 - \exp(-\alpha C_C)] - m_2 P_{bs} [1 - \exp(-\alpha C_C)] \tag{1-25}$$

where C_C is the catalyst concentration in g L^{-1}; $m_2 = f_1(C_{1,in}) f_3(P_a)$ is the proportionality constant, μ mole L^{-1} einstein^{-1}; P_i is the rate of photons reaching the inner reactor surface, einstein s^{-1}; P_{bs} is the rate of backscattered photons exiting the system, einstein s^{-1} and α is the effective extinction coefficient of the TiO_2 suspension, L g^{-1}.

It is postulated that the backscattering (refer to Chapter IV) is completed at very low catalyst concentrations, therefore the term $m_2 P_{bs}[1 - \exp(-\alpha C_C)]$ can be approximated to a constant value, $m_2 P_{bs}$, and equation (1-25) is reduced.

$$r'''_{1,in} = a_C [1 - \exp(-\alpha\ C_C)] - b_C \tag{1-26}$$

with $a_C = m_2 P_i$ and $b_C = m_2 P_{bs}$ in μ mole-C (L s)$^{-1}$, α the apparent extinction coefficient in L g^{-1}, C_C the Degussa P25 catalyst concentration in g L^{-1}.

Salaices *et al.* (2001) fitted the a_C, α and b_C parameters to the experimental data reported in Figure 1.3 using a non-linear, least squares method. These parameters can also be calculated independently by using the values for P_i, P_{bs}, α, and m_2 (refer to Chapter IV). These results are summarized in Table 1.1. As noted, the calculated and regressed values are statistically similar, validating the applicability of the proposed model for the prediction of the $f_2(C_C)$ functionality.

Concerning the physical interpretation of C_{wf} in Figure 1.3, this represents the wall fouling catalyst concentration, or the minimum catalyst concentration necessary to start the reaction. It is postulated that, at very low concentrations, the catalyst particles tend to adhere to the system walls, including to some non-illuminated sections. Additionally, a fraction of the irradiated catalyst found close to the reactor walls does not produce any significant photodegradation due to its poor contact with the fluid. It is not until a minimum catalyst loading value is reached that the irradiated catalyst becomes available for the photoconversion reaction. The calculated value of C_{wf} was 0.014 g L^{-1}.

Results of Figures 1.3 and 1.4 show that for $W_{irr} < W_{irr,\,\max}$ all the catalyst available contribute to the photocatalytic conversion. Beyond this $W_{irr,\max}$ value, additional catalyst does not influence the rate of photoconversion. Thus, one should consider, as suggested in equation (1-12) and shown in Figures 1.4 and 1.5, a photocatalytic reaction rate

TABLE 1.1. Parameter values for the $r'''_{1,in}$ as a function of C_c (equation. (1-26))

Parameter	Value	+/-σ	Calculated	+/-σ
a_c	11.988	2.2032	9.388	1.18
α	38.450	9.012	41.1	3.451
b_c	4.992	2.2488	1.77816	0.7776

CuuDuongThanCong.com https://fb.com/tailieudientucntt

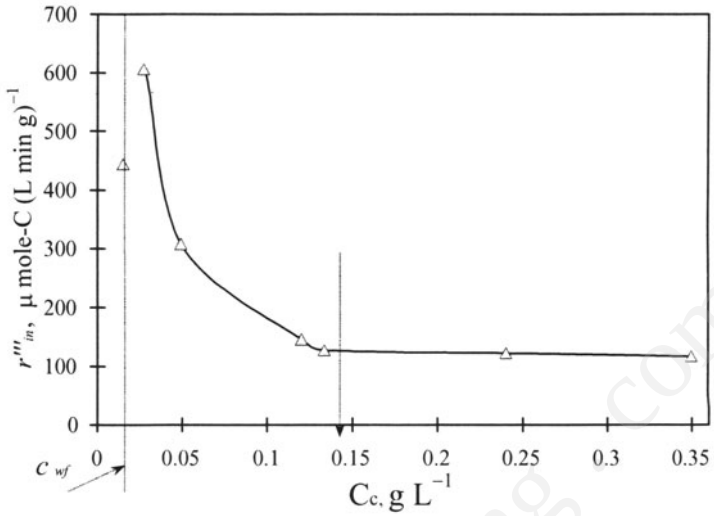

FIGURE 1.4. Change of $r_{1,in}$, the initial reaction rate per unit weight of irradiated catalyst with catalyst loading.

based on the irradiated weight of catalyst for properly expressing the photoconversion using a phenomenologically based rate parameter.

These results highlight: a) Photodegradation reaction rates should be defined on the basis of phenomenologically meaningful parameters, case of W_{irr}, b) Reaction rate evaluation is a task that should be developed carefully, accounting for possible non-idealities in the photocatalytic reactor such as particle wall fouling.

1.6. MODELING PHOTOCONVERSION OF POLLUTANTS: THE PARALLEL-SERIES REACTION MODEL

The functionality of the initial reaction rate on the i chemical species concentration defined at the initial condition $f_1(C_{1,in})$ is illustrated in Figures 1.5 and 1.6.

The ordinates show the phenol concentration (Figure 1.5) and Total Organic Carbon (TOC) (Figure 1.6) changes with reaction time. These results were obtained for different initial phenol concentrations, under the conditions reported by Salaices et al. (2001).

The examination of these experimental data, expanded details are reported in Chapter V, illustrates the basic parallel-series mechanism for photocatalytic reactions including the possible influence of the distribution of photocatalytic site activity.

The model pollutant, phenol, is photo-converted via a first order or pseudo-first order reaction consistent with equation(1-14) considering in this manner all possible sources of phenol consumption.

TOC changes, describing the overall degradation of organic species, follow a near-zero order reaction rate. This shows that some fractions of phenol are fully photo-converted and mineralized into CO_2 at the very early stages of the photocatalytic conversion.

CuuDuongThanCong.com https://fb.com/tailieudientucntt

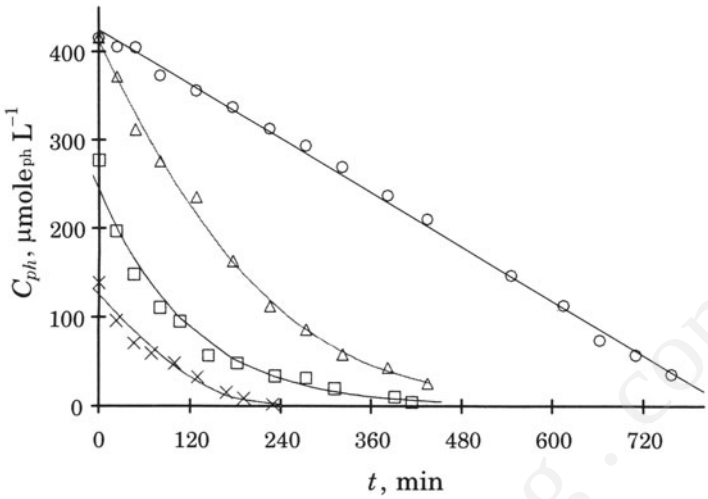

FIGURE 1.5. Phenol photodegradation at several initial concentrations. (○) TOC 412.5 μ- mole L^{-1} (30 ppm), Phenol concentrations: (△) 412.5 μ- mole L^{-1} (30 ppm) , (□) 242.0 μ- mole L^{-1} (20 ppm), (x) 124.8 μ- mole L^{-1} (10 ppm). (Reprinted with permission from *Ind. Eng. Chem. Res.*, **40**(23), M. Salaices, B. Serrano and H.I. de Lasa, Photocatalytic conversion of organic pollutants: Extinction coefficients and quantum efficiencies, 5455–5464. Copyright 2001 American Chemical Society).

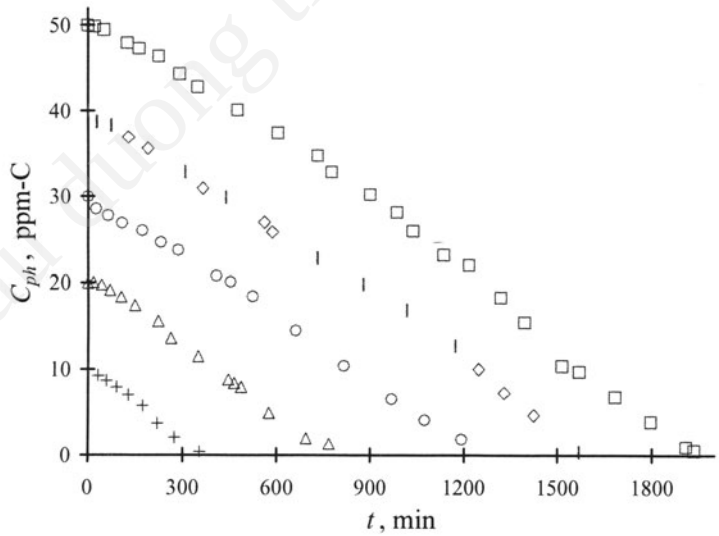

FIGURE 1.6. TOC profiles for the photodegradation of several initial concentration of phenol. (□) 50 ppm, (◇) 40 ppm, (○) 30 ppm, (△) 20 ppm, (+) 10 ppm. (Reprinted with permission from *Ind. Eng. Chem. Res.*, **40**(23), M. Salaices, B. Serrano and H.I. de Lasa, Photocatalytic conversion of organic pollutants: Extinction coefficients and quantum efficiencies, 5455–5464. Copyright 2001 American Chemical Society).

CuuDuongThanCong.com https://fb.com/tailieudientucntt

1.7. ADSORPTION AND PHOTOCATALYTIC REACTION RATES

In photocatalytic reactors, the depletion of model pollutant in the fluid phase is the combined result of adsorption and photoconversion processes.

To describe this, a mole balance applied to the model pollutant can be represented as,

$$N_{1T} = N_1 + N_{1s} \tag{1-27}$$

where N_{1T} is the total number of moles; N_1 is the number of moles in the fluid phase, and N_{1s} is the number of moles adsorbed on the solid.

When equation (1-27) is divided by V the total system volume the result is

$$C_{1T} = C_1 + N_{1s}/V \tag{1-28}$$

where C_{1T} is the total concentration, mole L^{-1}; C_1 is the number of moles in the fluid phase, mole L^{-1}; and V is the total system volume, L.

Assuming that adsorption equilibrium is reached at all times during the photocatalytic conversion, the amount of model pollutant on the solid phase can be estimated given that,

$$N_{1s} = q_1 W = \theta W q_{1.m}, \quad \text{with} \quad \theta = q_1/q_{1.m} \tag{1-29}$$

where q_1 is the specific amount of model pollutant adsorption on the solid, mole g^{-1}; q_{1m} is the maximum amount of model pollutant adsorption in the solid, mole g^{-1}; and W is the total weight of the adsorbent substrate, g.

The θ can be related to the model pollutant concentration in the fluid phase through a pseudo equilibrium constant (K^*) evaluated at one point of the adsorption equilibrium isotherm,

$$\theta = K^* C_1 \tag{1-30}$$

and equation (1-28) can be written as,

$$C_{1T} = C_1(1 + K'), \quad \text{with} \quad K' = K^* W q_{1.m}/V \tag{1-31}$$

Taking the derivative of equation (1-31) with respect to time, it yields,

$$r'''_T = r'''_1(1 + K') \tag{1-32}$$

Thus, equation (1-32) relates the total reaction rate (r'''_T) with a reaction rate involving the observed chemical species concentration changes in the fluid phase (r'''_1). This equation describing the total rate of pollutant depletion is valuable for efficiency estimations in photocatalytic reactor units.

CuuDuongThanCong.com https://fb.com/tailieudientucntt

1.8. CONCLUSIONS

The main conclusions of the present chapter are:

(a) The definitions of photocatalytic reaction rates have to be developed using meaningful parameters, as it is the case of the irradiated reactor volume, the irradiated catalyst weight or the irradiated catalyst area.
(b) The definitions of photocatalytic reaction rates have to take into account the irradiation absorbed in the reactor media as well as the effect of the catalyst concentration. These are important variables that may be modified and carefully selected in the design of a reactor.
(c) The photoconversion rate has to take into account the change of chemical species both in the fluid phase and in the solid phase using a total rate of photoconversion.
(d) The photocatalytic reaction rate evaluations have to be developed, considering the unit's non-idealities such as the anomalies observed at very low catalyst concentrations with particle fouling on the reactor walls.
(e) The intrinsic character of the parallel-series reaction mechanism must be considered when a reaction rate model is established.

NOTATION

Symbols

a_C	regression parameter in equation (1-26) $= m_2 P_a$	μ mole $(L\ s)^{-1}$
b_C	regression parameter in equation (1.26) $= m_2 P_{bs}$	μ mole $(L\ s)^{-1}$
A_{irr}	external area of irradiated catalyst	m^2
C_C	catalyst concentration	$g\ L^{-1}$
C_i	Concentration of the i chemical species	$g\ L^{-1}$, μ mole L^{-1}
C_j	concentration of the j chemical species	$g\ L^{-1}$, μ mole L^{-1}
C_{wf}	minimum concentration of catalyst required to start the photodegradation	$g\ L^{-1}$
C_1	concentration of model pollutant	$g\ L^{-1}$
C_{1T}	total concentration of model pollutant	$g\ L^{-1}$, μ mole L^{-1}
$C_{1,in}$	initial concentration of model pollutant	$g\ L^{-1}$, μ mole L^{-1}
E_{bg}	band gap energy	Joules
E_{cb}	energy conduction band	Joules
E_{ph}	energy of the photon	Joules
E_{vb}	energy valence band	Joules
$f_1(C_{i,in})$	$C_{i,in}$ concentration function	-
$f_2(C_c)$	C_c concentration function	-
$f_3(P_a)$	P_a concentration function	-
$h\nu$	energy of photon	Joules
k_i	kinetic reaction constant for i species	$L(g_{cat,irr}s)^{-1}$

CuuDuongThanCong.com https://fb.com/tailieudientucntt

k_i'	kinetic reaction constant for i species	$L(m_{irr}^2 s)^{-1}$
k_i''	kinetic reaction constant for i species	$L(L_{irr} s)^{-1}$
k_i'''	kinetic reaction constant for i species	s^{-1}
k_1	kinetic reaction constant for i species	$L(g_{cat,irr} s)^{-1}$
k_1'	kinetic reaction constant	$L(m_{irr}^2 s)^{-1}$
k_1''	kinetic reaction constant	$L(L_{irr} s)^{-1}$
k_1'''	kinetic reaction constant	s^{-1}
K_j	adsorption constants for j species	L mole^{-1}
K'	dimensionless adsorption constant (equation 1-31)	
K^*	slope of the adsorption constant at $C_{1,eq}$	L mole^{-1}
N_1	number of moles of "1" chemical species in the fluid phase	moles
N_{1s}	number of moles of "1" chemical species adsorbed in the solid phase	moles
N_{1T}	total number of moles of "1" species in fluid and solid phases	moles
m_2	proportionality constant in equation (1-24)	
m_3	proportionality constant in equation (1-23)	
P_a	rate of photons absorbed	moles of photons s^{-1}, Einstein s^{-1}
P_{bs}	rate of backscattered photons leaving the system	moles of photons s^{-1} Einstein s^{-1}
$P_i\|_{C_c \to 0^+}$	rate of photons transmitted when catalyst concentration approaches to zero from the right hand side of the dP_t/dC discontinuity	moles of photons s^{-1} Einstein s^{-1}
q_1	solid phase pollutant concentration	g g_{ads}^{-1}, μ mole g_{ads}^{-1}
$q_{1,m}$	maximum solid phase pollutant concentration	g g_{ads}^{-1}, μ mole g_{ads}^{-1}
r_i	reaction rate for chemical species i with units consistent with R_k	
r_i'	reaction rate for chemical species i with units consistent with R_k'	
r_i''	reaction rate for chemical species i with units consistent with R_k''	
r_i'''	reaction rate for chemical species i with units consistent with R_k'''	
r_1	reaction rate for model pollutants 1 with units consistent with R_k	μ moles $(g_{cat,irr} s)^{-1}$
r_1'	reaction rate for model pollutant with units consistent with R_k'	μ mole $(m_{irr}^2\ s)^{-1}$
r_1''	reaction rate for model pollutant with units consistent with R_k''	μ mole $(L_{irr}\ s)^{-1}$
$r_{1,in}'''$	initial reaction rate for model pollutants 1 with units consistent with $R_{k,in}'''$	

CuuDuongThanCong.com https://fb.com/tailieudientucntt

R_k	reaction rate for reaction step k based on irradiated weight of catalyst	μ moles $(g_{cat,irr}s)^{-1}$
R'_k	reaction rate for reaction step k based on irradiated reactor area	μ mole $(m^2_{irr}\ s)^{-1}$
R''_k	Reaction rate for reaction step k based on total reactor volume	μ mole $(L_{irr}\ s)^{-1}$
R'''_k	reaction rate for reaction step k based on total reactor volume	μ mole $(L\ s)^{-1}$
$R'''_{k,in}$	initial reaction rate for reaction step k based on total reactor volume	μ mole $(L\ s)^{-1}$
t	time	s
V	reactor volume	L
V_d	non-irradiated reactor volume	L
V_{irr}	irradiated reactor volume	L
W	weight of adsorbent material	g_{ads}
W_{irr}	weight of irradiated catalyst	g_{cat}
$W_{irr,\ max}$	maximum amount of irradiated catalyst	g_{cat}

Greek letters

α	effective extinction of the suspension	$L\ g^{-1}$
δ	equation (1-23) parameter	
$\nu_{i,k}$	stoichiometric coefficient for chemical species i involved in reaction step k	
θ	dimensionless solid phase model pollutant concentration	

Subscript

i	chemical species used as a key species for mass balances
j	chemical species other than i involved in equation (1-14)
k	reaction step
in	initial
irr	irradiated
max	maximum
ph	photon
1	model pollutant

REFERENCES

Al-Ekabi, H., and Serpone, N., 1993, TiO_2 advanced photo-oxidation technology: effect of electron acceptors, in: *Photocatalytic purification and treatment of water and air*, Ollis, D., and Al-Ekabi, H., eds., Elsevier, New York, pp. 321–335.

Carey, J. H., Lawrence, J., and Tosine, H. M., 1976, Photodechlorination of PCB's in the presence of titanium dioxide in aqueous suspensions, *Bull. Environ. Contam. Toxicol*, **16:**697–701.

Draper, R. B., and Fox, M. A., 1990, Titanium dioxide photosensitized reactions studied by diffuse reflectance flash photolysis in: Aqueous suspensions of TiO_2 powder, Langmuir, **6:**1396–1402.

CuuDuongThanCong.com https://fb.com/tailieudientucntt

Hoffmann, M. R., Martin, S. T., and Choi, W., 1995, Environmental applications of semiconductor photocatalysis, *Chem. Rev.*, **95:**69–96.

Legrini, O., Oliveros, E., and Braun, A. M., 1993, Photocatalytic processes for water treatment, *Chem. Rev.*, **93:**671–698.

Linsebigler, A., Lu, G., and Yates, J. T. Jr., 1995, Photocatalysis on TiO_2 surfaces: principles, mechanisms and selected results, *Chem. Rev.*, **95:**735–758.

Mills, G., and Hoffmann, M. R., 1993, Photocatalytic degradation of pentachlorophenol on TiO_2 particles: Identification of intermediates and mechanism of reaction, *Environ. Sci. Tech.*, **27:**1681–1689.

Okamoto, K., Yamamoto, Y., Tanaka, H., and Itaya, A., 1985, Kinetics of heterogeneous photocatalytic decomposition of phenol over anatase TiO_2 powder. *Bull. Chem. Soc. Japan*, **58:**2023–2028.

Ollis, D. F., 1991, Solar assisted photocatalysis for water purification, issues, data, questions, in: *Photochemical conversion and storage of solar energy*, Pelizzetti, E., Schiavello, M., eds., Kluwer Academic, Dordrecht, The Netherlands, pp. 593–622.

Pasqualli, M., Santarelli, F., Porter, J. F., and Yue, P. L., 1996, Radiative transfer in photocatalytic systems, *AIChE J.*, **42:**532–537.

Pelizzetti, E., Minero, C., and Pramauro, E., 1993, photocatalytic processes for destruction of organic water contaminants, in: *Chemical reactor technology for environmentally safe reactors and products*. de Lasa, H. I., Doğu, G., and Ravella, A., eds., Kluwer Academic Publishers, Netherlands, pp. 577–608.

Salaices, M., Serrano, B., and de Lasa, H., 2001, Photocatalytic conversion of organic pollutants. Extinction coefficients and quantum efficiencies, *Ind. Eng. Chem.* Res., **40:**5455–5464.

Salaices, M., Serrano, B., and de Lasa H., 2002, Experimental evaluation of photon absorption in an aqueous TiO_2 slurry reactor, *Chem. Eng. J.*, **90:**219–229.

Salaices, M., Serrano, B., and de Lasa H., 2004, Photocatalytic Conversion of phenolic compound in slurry reactors, *Chem. Eng. Sci.*, **59:**3–15.

Terzian, R., Serpone, N., and Minero, C., 1991, Photocatalyzed mineralization of cresols in aqueous with irradiated titania, *J. Catal.*, **128:**352–365.

Trillas, M., Pujol, M. and Domenech, X., 1992, Phenol photodegradation over titanium dioxide. *J. Chem. Tech. Biotech.*, **55**(1):85–90.

Trillas, M., Pujol, M. and Domenech, X., 1996, Photocatalyzed degradation of phenol, 2,4-dichlorophenol, phenoxyacetic acid and 2,4-dichlorophenoxyacetic acid over supported TiO_2 in a flow system. *J. Chem. Tech. Biotech.*, **67**(3):237–242.

Turchi, C. S., Ollis, D. F. 1990, Photocatalytic degradation of organic water contaminants: Mechanisms involving hydroxyl radical attack, *J. Catal.*, **122:**178–192.

Wei, Chang., Lin, W. Y., and Zainal, Z., 1994, Bactericidal activity of TiO_2 photocatalyst in aqueous media: Toward a solar-assisted water disinfections system. *Environ. Sci. Techn.*, **28:**934–938.

CuuDuongThanCong.com https://fb.com/tailieudientucntt

2

Novel Photocatalytic Reactors for Water and Air Treatment

2.1. PHOTOCATALYTIC REACTORS: OVERVIEW AND ADVANCES

The development of water and air treatment systems based on heterogeneous photocatalysis is an area of major technical importance (Blanco and Malato, 1993; Matthews, 1993; Ollis et al., 1989; Pelizzetti et al., 1992). Harada et al., (1999) have stated, "... the design of highly efficient photocatalytic systems is of vital interest and one of the most desirable yet challenging goals in the research of environmentally friendly catalysts". There is general agreement that an important obstacle in the development of highly efficient photocatalytic reactors is the establishment of effective reactor designs for intermediate and large-scale use, as demanded by industrial and commercial applications. To achieve a successful commercial implementation, several reactor design parameters must be optimized, such as the photoreactor geometry, the type of photocatalyst and the utilization of radiated energy. A fundamental issue regarding the successful implementation of photocatalytic reactors is the transmission of irradiation in a highly scattering and absorbing medium composed of water and fine TiO_2 particles.

The evaluation of irradiation and its distribution inside photocatalytic reactors is essential for the extrapolation of laboratory scale results to large-scale operations and the comparison of the efficiencies of different installations (Curco et al., 1996). The successful scaling-up of photocatalytic reactors involves increasing the number of photons absorbed per unit time and per unit volume as well as efficiently using the electron holes created during the photocatalytic transformations.

While some of the physico-chemical principles of photocatalysis are relatively well understood, reactor design and reactor engineering of photocatalytic units still require consideration (Bahnemann et al., 1991; Fox and Dulay, 1993; Gerischer, 1993; Gerischer and Heller, 1991; Linsebigler et al., 1995; Turchi and Ollis, 1990). This is particularly true in the context of scaled reactors processing large volumes of water and using high levels of irradiation. Cassano et al. (1995) stressed that several aspects of design,

CuuDuongThanCong.com https://fb.com/tailieudientucntt

optimization and operation of photochemical reactors that are not usually considered in the design of conventional chemical reactors, should be taken into account. Some of these aspects are

- The selection of radiation sources including output power, source efficiency, spectral distribution, shape, dimensions, maintenance and operating requirements (warm up and cooling periods)
- The design of reactor geometry with respect to the irradiation source
- The design of reactor irradiation devices including mirrors, reflectors and windows, their construction materials, shape, dimensions and cleaning procedures

Lamps with emission spectra similar to those used at the laboratory scale, but with higher electrical power, may be needed in the future. This will require longer-lasting, more powerful lamps and the adaptation of the photo reactor geometry to accommodate increased power requirements.

The selection of a photocatalyst offers special challenges. Aside from the more conventional TiO_2, there are other available photocatalyst choices: TiO_2/Pt or ZnO. This is particularly relevant as the overall rate of oxidative degradation appears to be limited by the electron transfer from the valence band to the semiconductor conduction band (Linsebigler et al., 1995; Choi et al., 1994).

In addition to the reactor design strategies and the catalyst selection, a number of important operating variables exists, affecting both the rate and the extent of chemical species transformation. These include semiconductor concentration, reactive surface area, particle aggregate size, concentration of electron donors and acceptors, incident light intensity, pH, presence of competitive sorbates and temperature (Augugliaro et al., 1995).

Photocatalytic reactors can also be powered by solar light as 4-5% of the wavelengths of the solar spectrum can excite TiO_2. For low intensities, there is a first order relation between the rate of photoreaction and the irradiation intensity. At higher levels of irradiation, the relation between the photoconversion rate and the irradiation intensity becomes of fractional order. Increased inefficiencies with increasing irradiation are a significantly limiting factor in solar photoreactor applications.

With the need to develop new photocatalytic reactors, there is also the issue of establishing performance indicators to enable the comparison of photoreactor performance on the basis of photochemical and thermodynamic principles (Serrano and de Lasa, 1997; Yue, 1985).

In the case of water treatment, it can be stated that current technologies concerning photocatalyzed oxidative degradation processes can be considered as practical alternatives to existing wastewater treatments. Photocatalysis has already found applications in small to medium sized units in the treatment of contaminated ground waters and in the production of ultrapure water for pharmaceutical and micro electronic industries (Crittenden et al., 1997; Nogueira and Jardim, 1996; Parent et al., 1996). Relevant application examples to be cited are the solar-powered 300-liter/hour capacity solar unit in Almeria, Spain (Blanco et al., 1996a; Minero et al., 1996) and the 60-6000 liter/hour units commercialized by Purifics (Butters and Powell, 1995).

CuuDuongThanCong.com https://fb.com/tailieudientucntt

2.2. REACTORS FOR WATER TREATMENT

Photocatalytic reactors for water treatment can be classified according to their design characteristics.

a) State of the photocatalyst: The photocatalyst can be either suspended or attached to a support:
   - Photocatalytic slurry reactors
   - Photocatalytic reactors with immobilized photocatalyst.

   In slurry reactors, the catalyst particles are freely dispersed in the fluid phase (water) and consequently, the photocatalyst is fully integrated in the liquid mobile phase. The immobilized catalyst reactor design features a catalyst anchored to a fixed support, dispersed on the stationary phase (the catalyst-support system).

b) Type of illumination: The type of irradiation is a major design issue for photocatalytic reactors. Reactors can be irradiated using
   - UV polychromatic lamps
   - Solar light

   Two subcategories branch off from solar illuminated reactors: non-concentrating reactors and concentrating reactors. Non-concentrating solar irradiated reactors employ intensities equal or lesser than natural solar irradiation while concentrating solar reactors use irradiation intensities that surpass irradiations equivalent to one sun.

c) Position of the irradiation source: The position of the lamp or source of irradiation is a distinguishing feature of a photocatalytic reactor. The lamp position determines different configurations:
   - Reactors with an immersed light source
   - Reactors with an external light source
   - Reactors with distributed light sources (Mukherjee and Ray, 1999).

   In immersed source reactors, the lamp is placed inside the unit. External source photocatalytic reactors have lamps located outside the reactor vessel. In distributed reactors, irradiation is transported from the source to the reactor by optical means such as reflectors or light guides.

2.3. TiO_2 SLURRY REACTORS

The majority of the photocatalytic reactors currently in use for water treatments are of the well–mixed slurry variety (Augugliaro et al., 1990; Pichat, 1988). Slurry systems have shown the largest photocatalytic activity when compared to photocatalytic reactors with immobilized photocatalyst (Matthews and McEvoy, 1992; Parent et al., 1996; Pozzo et al., 1999; Wyness et al., 1994b).

In a comparative study of the photodegradation of aqueous phenol using natural sunlight and a reactor geometry simulating shallow ponds, the free photocatalyst suspensions display degradation rates about 3 times greater than those observed for immobilized

CuuDuongThanCong.com https://fb.com/tailieudientucntt

photocatalysts (Matthews and McEvoy, 1992). When Wyness et al. (1994b) investigated the performance of solar photocatalytic reactors, they also found that the reaction rate constant for suspended photocatalyst operation was 2 to 5 times larger than that of an immobilized catalyst. In spite of these encouraging results, such comparisons should be cautiously considered, given that other parameters such as absorbed radiation may not be the same in each of the reactors.

In addition, slurry systems require separation of the fine sub–micron particles TiO_2 (0.1-micron size) from the treated milk-like water suspension. Separation steps complicate the treatment process and decrease the economical viability of the slurry reactor approach. Several techniques have been proposed including high-cost ultra centrifugation and inexpensive overnight particle settling. Two additional techniques with associated intermediate costs have also been considered: ultra filtration using a hollow fiber membrane (Sopajaree et al., 1999a, 1999b), and coagulation with ferrous sulfate or basic aluminum chloride (Kagaya et al., 1999; Watts et al., 1995).

2.4. IMMOBILIZED TiO_2 PHOTOCATALYTIC REACTORS

Photocatalytic reactors with immobilized TiO_2 have suitable configurations for both water and air treatment. These include reactors in which the catalyst is fixed (anchored) on a support via physical surface forces or chemical bonds.

Typical TiO_2 supports are

- Activated carbon (Torimoto et al., 1996; Uchida et al., 1993)
- Fiber optic cables (Hofstadler et al., 1994; Peill and Hoffmann, 1997)
- Fiberglass (Al–Ekabi and Serpone, 1993; Matthews, 1987b; Serrano and de Lasa, 1997; Wyness et al., 1994a; Zhang et al., 1994)
- Glass (Aguado and Anderson, 1993; Al–Ekabi and Serpone 1988; Fernandez et al., 1995; Matthews, 1987b; Mukharjee and Ray, 1999; Zhang et al., 1994)
- Glass beads (Al–Ekabi and Serpone 1988; Reeves et al., 1992; Serpone et al., 1986)
- Glass wool (Zhang et al., 1994)
- Membranes (Aguado and Anderson, 1993; Barni et al., 1995; Bellobono et al., 1994; Gianturco et al., 1996)
- Quartz sand (Pozzo et al., 2000)
- Zeolites (Domenech and Peral, 1989 ; Torimoto et al., 1996)
- Silica gel (Crittenden et al., 1996; Matthews and McEvoy, 1992; Matthews, 1988; Zhang et al., 1996, 1994)
- Stainless steel (Byrne et al., 1998; Fernandez et al., 1995; Ha and Anderson, 1996)
- Teflon (Low and Matthews, 1990).

In typical fixed photocatalytic reactors, the photocatalyst can be coated or anchored on the reactor walls around the light source casing or attached to a solid matrix. Since TiO_2 is not present in the water or air streams at any time, these reactors have the intrinsic advantage of not requiring a catalyst recovery operation. Relevant examples of this type of reactor are the coated fiber optic cable reactor and the multiple tube reactor (Peill and Hoffmann, 1995, 1996, 1997, 1998, Ray and Beenackers, 1998a).

CuuDuongThanCong.com https://fb.com/tailieudientucntt

Other options for the fixed photocatalyst design are to entrap the TiO_2 particles on glass beads, to immobilize them on fiberglass or woven fibers and to hold particles in ceramic membranes by compression.

Immobilized catalyst photoreactor systems permit the continuous use of the photocatalyst, eliminating the need for post-process filtration coupled with particle recovery and catalyst regeneration. Such reactors may display a number of drawbacks

- Low surface area to volume ratios
- Inherent inefficiencies introduced by light absorption and light scattering in the particle suspension medium
- Significant pressure drop
- Catalyst fouling or catalyst wash out
- Difficult "in situ" catalyst regeneration (Parent et al., 1996).

Critical reviews of the designs described above emphasize the need for suitable irradiation, appropriate for given geometrical configurations (Borello et al., 1989; Cabrera et al., 1994; Robertson and Henderson, 1990). In addition, adequate mixing patterns and high water-photocatalyst interaction are identified as essential factors to achieve an optimized operation of these reactor units.

2.5. COMPARING TiO_2 SLURRY PHOTO REACTORS AND TiO_2 IMMOBILIZED PHOTOREACTORS

Table 2.1 summarizes the advantages and disadvantages of slurry and immobilized photocatalytic reactors as reported by Alfano et al. (2000), Parent et al. (1996), and Ollis

TABLE 2.1. Suspended versus immobilized photocatalytic systems

Slurry reactors	Immobilized reactors
Advantages	*Advantages*
• Fairly uniform catalyst distribution	• Continuous operation
• High photocatalytic surface area to reactor volume ratio	• Improved removal of organic material from water phase while using a support with adsorption properties
• Limited mass transfer	• No need for an additional catalyst separation operation
• Minimum catalyst fouling effects due to the possible continuous removal and catalyst replacement	
• Well mixed particle suspension	
• Low pressure drop through the reactor	
Disadvantages	*Disadvantages*
• Requires post – process filtration	• Low light utilization efficiencies due to light scattering by immobilized photo catalyst
• Important light scattering and adsorption in the particle suspended medium (Ollis, 1991)	• Restricted processing capacities due to possible mass transfer limitations (Matthews, 1991; Matthews and McEvoy, 1992; Turchi and Ollis, 1988)
	• Possible catalyst deactivation and catalyst wash out (Serrano and de Lasa, 1997)

CuuDuongThanCong.com https://fb.com/tailieudientucntt

(1991). Some of these characteristics may be specific to one type of reactor and can be totally or partially overcome in other designs.

2.6. ARTIFICIALLY ILLUMINATED REACTORS

Several configurations have been proposed for artificially illuminated photocatalytic reactors. These can be grouped into two main categories, as described in Table 2.2, with respect to the state of the TiO_2 catalyst as either immobilized or in suspension (slurry).

2.6.1. Slurry Reactors

a) *Slurry Annular Reactor* (SAR): Two concentric tubes, the inner being transparent to radiation, make-up the SAR unit. The TiO_2 suspension flows through an annular channel created by the two tubes. The lamp is placed inside the inner transparent tube. This geometry has the advantage of providing a symmetric irradiation field. SAR reactors have been used extensively in bench scale experiments, are easy to operate and altogether appear as an attractive alternative for industrial applications (Andreozzi et al., 2000; Cassano et al., 1995; Davydov et al., 1999, 2000; Hoffman et al., 1995; Salaices et al., 2001; Sopajaree et al., 1999a, 1999b).

TABLE 2.2. Artificially Illuminated Reactor Configurations

Configuration	Catalyst	Reference
Slurry Annular Reactor (SAR)	Suspended	Andreozzi et al 2000; Cassano et al., 1995; Chester et al., 1993; Davydov et al., 2000, 1999; Sopajaree et al., 1999a, 1999b.
Open Upflow Reactor (OUR)	Suspended	Alberici and Jardim, 1994.
Integrated Flow Reactor – Membrane Filtration (IFR–MF)	Suspended	Sopajaree et al., 1999a, 1999b.
Swirl Flow Reactor (SFR)	Suspended	Chen and Ray, 1999, 1998; Ray and Beenackers, 1997.
Taylor Vortex Reactor (TVR)	Suspended	Karpel et al., 1997; Sczechowski et al., 1995a.
Turbulent Slurry Reactor (TSR)	Suspended	Butters and Powell, 1995; Say et al., 1990.
Photo CREC Water II	Suspended	Salaices et al., 2001.
Falling Film Reactor (FFR)	Immobilized	Puma and Yue, 1999a, 1999b, 1998.
Fiber Optic Cable Reactor (FOCR)	Immobilized	Hofstadler et al., 1994; Peill and Hoffmann, 1998, 1997, 1996, 1995.
Multiple Tube Reactor (MTR)	Immobilized	Mukherjee and Ray, 1999; Ray, 1998.
Packed Bed Reactor (PBR)	Immobilized	Al–Ekabi et al., 1989; Raupp et al., 1997.
Rotating Disk Reactor with Controlled Periodic Illumination (RDR–CPI)	Immobilized	Buechler et al., 1999.
Spiral Glass Tube Reactor (SGTR)	Immobilized	Al-Ekabi and Serpone, 1988; Matthews, 1987b.
Tube Light Reactor (TLR)	Immobilized	Ray and Beenackers, 1998a.
Photo CREC Water I	Immobilized	de Lasa and Valladares, 1997; Serrano and de Lasa, 1997; Valladares, 1995.

CuuDuongThanCong.com https://fb.com/tailieudientucntt

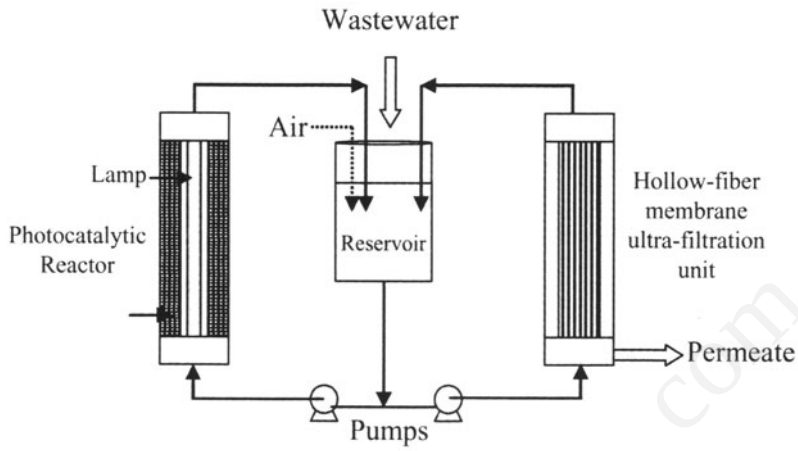

FIGURE 2.1. Schematic diagram of the integrated photoreactor-membrane UF system (Reprinted with permission from *J. App. Electrochem.* **29**(5):533–539. Copyright 1999 Kluwer Academic Publishers).

b) *Open Upflow Reactor* (OUR): The OUR has immersed lamps placed perpendicularly to the dominant direction of the water flow (Alberici and Jardim, 1994). This configuration with a non-symmetric irradiation field entails a more complex reactor model and requires a larger reactor volume than that of the SAR to achieve the same performance.

c) *Integrated Flow Reactor Membrane with Filtration System* (IFR-MF): The IFR-MF involves an annular, well-mixed, slurry batch including a hollow–fiber membrane with ultra–filtration capabilities. The IFR–MF allows the TiO_2 particle separation from the treated water as well as the recycle of TiO_2 to the reactor (Sopajaree et al., 1999a, 1999b). Figure 2.1 describes the IFR-MF unit.

d) *Swirl Flow Reactor* (SFR): Two circular glass plates constitute the SFR reactor. The TiO_2 water suspension is injected tangentially in the outer reactor section creating a swirl and promoting high mixing of the TiO_2 suspension. The TiO_2 suspension leaves the unit from the center of a top plate (Chen and Ray, 1999, 1998; Ray and Beenackers, 1997). This unit provides a well–mixed slurry with potentially non-uniform irradiation, which results in an associated complex reactor model.

e) *Taylor Vortex Reactor* (TVR): The TVR (Figure 2.2) consists of two coaxial cylinders and free-flowing particle slurry circulating in the annular channel. Light bulbs are mounted in the inner cylinder. A vortex-induced fluid instability is generated via inner cylinder rotation (Karpel et al., 1997). The catalyst is irradiated periodically as vortices move catalyst particles closer to the irradiated reactor section. Optimum operating conditions of 300-rpm inner cylinder rotation and a catalyst loading of 10 g/L provide an efficiency that is three times larger than that of a conventional slurry reactor (Karpel et al., 1997; Sczechowski et al., 1995a, 1995b, 1993). A disadvantage of the TVR configuration is the added complexity of its moving parts.

f) *Turbulent Slurry Reactor* (TSR): The TSR is a finned, turbulent slurry system with a ceramic membrane for the separation and the recycling of the catalyst.

CuuDuongThanCong.com https://fb.com/tailieudientucntt

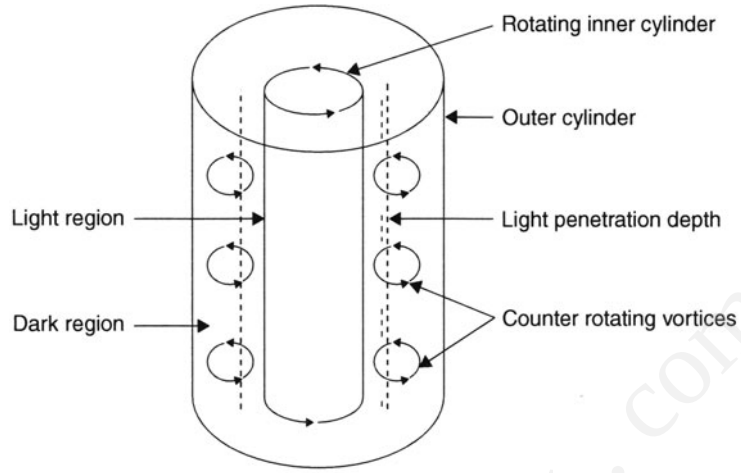

FIGURE 2.2. Taylor vortex reactor in operation (Reprinted from *Chem. Eng. Sci.*, **50**(20), J.G. Sczechowski, C.A. Koval and R.D. Noble, A taylor vortex reactor for heterogeneous photocatalysis, pp. 3163–3173, Copyright 1995, with permission from Elsevier)

The membrane is periodically cleaned with an air back-flow. According to their developers, the TSR's main advantages are its compact design and its expected high efficiency (Butters and Powell, 1995; Say et al., 1990).

g) *Photo-CREC-Water-II:* Photo-CREC-Water II is an annular vessel with a lamp placed in the center of the reactor. In the upper section, there is a slurry distribution system ensuring intense mixing of the slurry suspension at the reactor entry. The unit is equipped with quartz windows and accessory collimator tubes. As described in Chapters III and IV, this configuration allows the measurement of photon absorption and the quantification of back and forward reflection, and it is of particular value to establish energy and quantum efficiencies in photocatalytic reactor units.

h) *Photo-CREC-Water-III:* Photo-CREC-Water III is an annular vessel with external illumination. This unit is designed to simulate a solar irradiated reactor. This unit shares a number of features with Photo-CREC-Water II, case of the TiO_2 suspension forming a particle slurry. A schematic representation of this reactor is included later in this chapter.

2.6.2. *Immobilized TiO_2 reactors*

a) *Falling Film Reactor* (FFR): The FFR is recognizable by the following components (Figure 2.3):
- The immobilized TiO_2 coating the internal column wall
- A descending film of water
- A lamp placed in the central section of the column (Puma and Yue, 1999a, 1999b, 1998).

This reactor configuration may only provide a limited active catalyst surface per unit reactor volume.

CuuDuongThanCong.com https://fb.com/tailieudientucntt

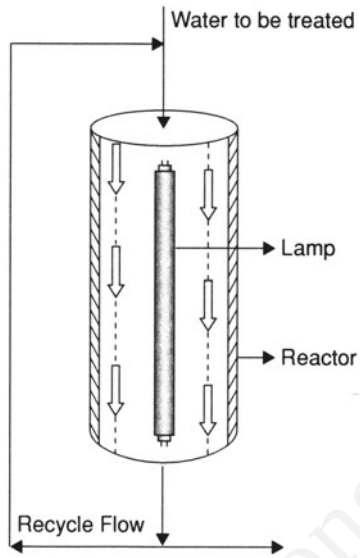

FIGURE 2.3. Schematic representation of the Falling Film Reactor (Reprinted from *Chem. Eng. Sci*, **53**(16), G.L. Puma and P.L. Yue, Laminar falling film slurry photocatalytic reactor: Part I: model development, 2993–3006, Copyright 1998, with permission from Elsevier)

b) *Fiber Optic Cable Reactor* (FOCR): The FOCR is designed with fiber optic cables bringing irradiation to the supported TiO_2 (Figure 2.4). This system can allow the irradiation of a remotely located photocatalyst with minimum scattering and uniform irradiation. The cost of optic fibers and the energy losses during beam focusing and photon transfer are two disadvantages that can lessen the appeal of the FOCR design. A typical FOCR includes Degussa P25 immobilized on quartz optical fibers and a Xe arc UV–radiation lamp (310–375 nm) (Hofstadler et al., 1994; Peill and Hoffman, 1998, 1996, 1995).

c) *Multiple Tube Reactor* (MTR): The MTR is designed with a cylindrical vessel (5-6 cm of diameter) containing 54 hollow quartz glass tubes (diameter 0.6 cm) externally coated with photocatalyst (Figure 2.5). The MTR resembles a shell and tube heat exchanger with the water to be treated flowing in the shell side of the MTR. The irradiation is distributed in hollow tubes via an aluminum reflector (Mukherjee and Ray, 1999; Ray, 1998). The MTR provides a large activated photocatalyst area per unit reactor volume.

d) *Packed Bed Reactor* (PBR): The PBR is an annular packed unit irradiated by a central lamp (Figure 2.6). Several variations of the PBR are reported:
   - TiO_2 coated glass mesh (Robertson and Henderson, 1990)
   - TiO_2 coated glass wool (Al-Ekabi et al., 1989)
   - TiO_2 coated glass beads (Al-Ekabi et al., 1989; Raupp et al., 1997).

   A possible drawback of the PBR results from the uneven or partial photocatalyst irradiation. Uneven flow distribution may also limit the amount of water contacting the irradiated TiO_2 and negatively influencing the overall PBR unit's performance.

CuuDuongThanCong.com https://fb.com/tailieudientucntt

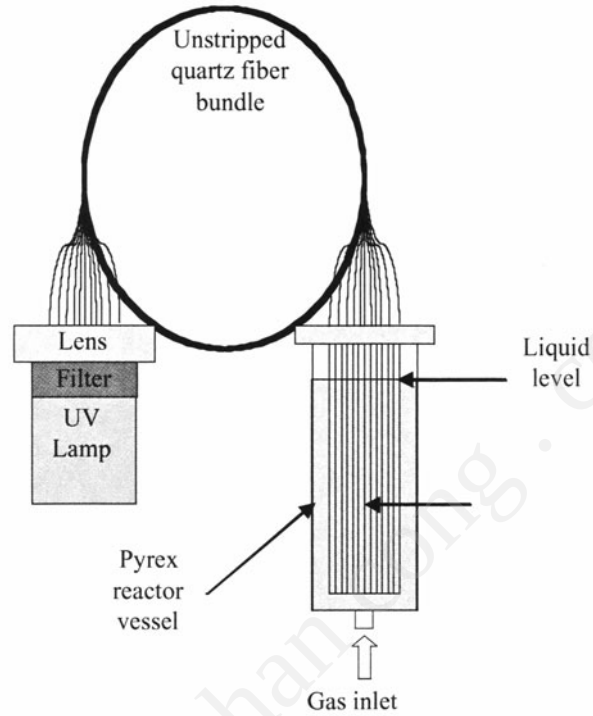

FIGURE 2.4. Schematic representation of the optical-fiber bundled array photocatalytic reactor system (Reprinted with permission from *Environ. Sci. & Tech.*, **32**(3), N.J. Peill and M.R. Hoffmann, Mathematical model of a phtoocatlaytic piber-optic cable reactor for heterogeneous photocatalysis, 398–404. Copyright 1998 American Chemical Society).

e) *Rotating Disk Reactor with Controlled Periodic Illumination* (RDR-CPI): The RDR-CPI contains immobilized TiO_2 films placed on the surface of a rotating disk (Figure 2.7). The disk is attached to a power-driven shaft that rotates at a rate of 20–100 rpm. An arrangement of lamps are used to irradiate the disk surface. The rotating hydrodynamics provides good reagent access to the catalyst surface (Buechler et al., 1999; Sczechowski et al., 1995b). The moving parts of the RDR-CPI add complexity to the photoconversion system.

f) *Spiral Glass Tube Reactor* (SGTR): The SGTR consists of a TiO_2-coated spiral tube wrapped around a lamp. While this configuration may provide a relatively

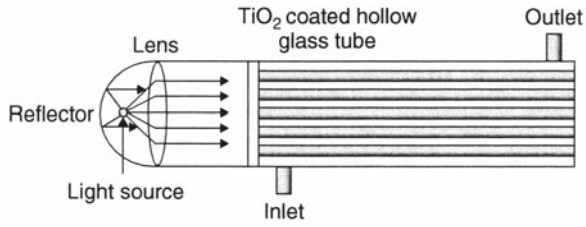

FIGURE 2.5. Schematic representation of a multiple tube reactor (Reprinted from *Catal. Today*, **40**(1), A.K. Ray and A. Beenackers, Development of a New Photocatalytic Reactor for water purification, 73–83, Copyright 1998, with permission from Elsevier).

CuuDuongThanCong.com https://fb.com/tailieudientucntt

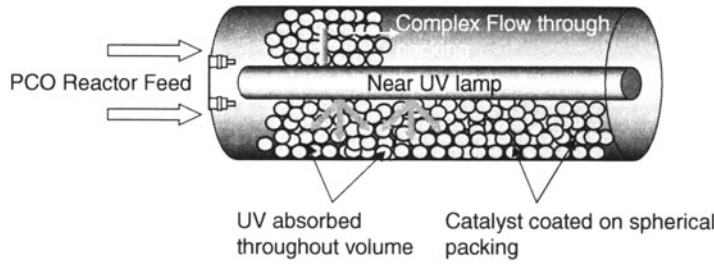

FIGURE 2.6. Annular packed-bed reactor (*AIChE Jour.*, **43**(3), G.B. Raupp, J.A. Nico and S. Annangi, Two-flux radiation-field model for an annular packed photocatalytic oxidation reactor, 792–801. Reproduced with permission. Copyright © 1997 AIChE)

large area of irradiated catalyst per unit of reactor volume (Al-Ekabi and Serpone, 1988; Matthews, 1987b), it may involve a complex hydrodynamic fluid pattern with limited contact between the water and the irradiated catalyst.

g) *Tube Light Reactor* (TLR): A stainless steel flat top plate and an inner welded plate characterize the TLR (Figure 2.8). Several U-shaped TiO_2-coated lamps are placed around the welded plate. The assembly is enclosed in a rectangular stainless steel vessel. Possible advantages of the TLR are a high catalyst surface area per unit volume and favorable scaling-up possibilities (Mukherjee and Ray, 1999; Ray and Beenackers, 1998a). One of this unit's shortcomings is a non–uniform irradiation and a complex water contacting hydrodynamics.

h) *Photo-CREC Water I*: The Photo-CREC Water I reactor is an annular reactor with a lamp placed at the reactor centerline. This configuration allows high TiO_2 loading of the glass mesh, good catalyst irradiation and uniform contact of the TiO_2 with the circulating water. Additional details about this unit are provided later in this chapter.

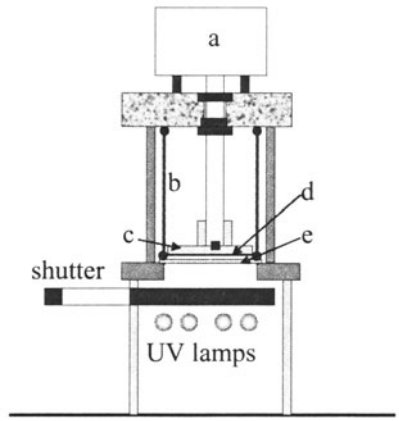

FIGURE 2.7. Rotating disk reactor. (a) variable speed motor, (b) Pyrex reactor wall, (c) support disk, (d) TiO_2 catalyst coating, and (e) quartz base plate (Reprinted with permission from *Ind. Eng. Chem. Res.*, **38**(4), K.J. Buechler, C.H. Nam, T.M. Zawistowski, R.D. Noble and C.A. Koval, Design and Evaluation of a Novel-Controlled Periodic Illumination Reactor to Study Photocatalysis, 1258-1263. Copyright 1999 American Chemical Society.)

CuuDuongThanCong.com https://fb.com/tailieudientucntt

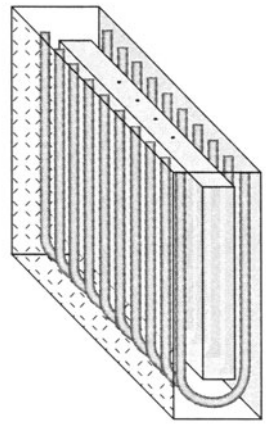

FIGURE 2.8. Tube light Reactor (TLR) (*AIChE. Jour.*, **44**(2), A.K. Ray and A, Beenackers, Novel Photocatalytic Reactor for Water Purification, 477-483, reproduced with permission. Copyright © 1998 AIChE).

2.7. SOLAR PHOTOCATALYTIC REACTOR DESIGNS

Most of the reactor designs tested for the photooxidation of organic pollutants by solar radiation are TiO_2 slurry reactors. The implementation of solar photocatalytic reactors has occurred concurrently with advances in the design of solar thermal collectors, given the important characteristics shared by these units. There are, however, specific constraints for the design of solar photocatalytic reactors.

- The need of UV transparent materials
- Reduced insulation requirements, given that the reactor temperature has a small effect on the aqueous phase photoreactions (Fox and Dulay, 1993).

According to the received irradiation, solar reactors can be divided into concentrating or non–concentrating (or one sun) reactors depending on the irradiation received. For the same harvesting area, concentrating reactors require smaller volumes than non-concentrating reactors. When land cost is a concern, the use of more expensive components can be justified without unreasonably increasing the overall unit cost (Alfano et al., 2000).

The main advantages and drawbacks of concentrating and non-concentrating solar photocatalytic are summarized in Table 2.3.

Non-concentrating reactors involve negligible optical losses due to the reflective surfaces; therefore, these reactors can benefit from both direct and diffuse sun irradiation. In fact, non-concentrating reactors can continue their operation under cloudy conditions when only diffuse solar light is available. Furthermore, under clear sky conditions, they can take advantage of the diffuse sun irradiation component, close to 50% of the total available UV light (Alfano et al., 2000).

Finally, non-concentrating reactors tend to be more efficient than concentrating units given that at high–energy flux densities the reaction rate depends on a fraction of

CuuDuongThanCong.com https://fb.com/tailieudientucntt

TABLE 2.3. Main advantages and drawbacks of concentrating and non–concentrating solar photocatalytic reactors

Non - concentrating reactors	*Concentrating reactors*
Advantages 1. Negligible optical losses 2. Direct and diffuse light utilization 3. Simple designs and low investment cost 4. Linear dependence between efficiency and radiation intensity	Advantages 1. Smaller reactor volume 2. Smaller harvesting area
Disadvantages 1. High frictional pressure losses 2. Larger reactor	Disadvantages 1. High investment cost 2. Direct light is utilized only 3. Square-root dependence between efficiency and radiation intensity

the power irradiation intensity (Herrmann, 1999; Hoffmann et al., 1995; Ollis, 1991; Pelizzetti et al., 1993).

Solar photocatalytic reactors can be operated in either continuous single pass mode or discontinuous batch mode. In the continuous single pass mode, complete oxidation of the contaminant is achieved in a single pass with the water flow rate being adjusted for fixed solar flux densities. On the other hand, batch mode operation requires a set volume of water to be treated with varying solar flux densities (Alfano et al., 2000). Table 2.4 reports the main types of solar reactors reported in the technical literature.

Regarding solar photocatalytic reactors the following characteristics and performance indicators can be mentioned

TABLE 2.4. Main types of solar reactors

Reactor type	Suspended photocatalyst	Immobilized photocatalyst
Concentrating reactors	- Parabolic trough reactor, (PTR) (Bockelmann et al., 1995 and 1993; Malato et al., 1997; Malato et al., 1996; Mehos and Turchi, 1993; Pacheco et al., 1993).	
Non-concentrating reactors with reflector	- Parabolic collecting reactor (Malato et al., 1996).	- Tubular reactor (Zhang et al., 1996 and 1994) - Fiber optic cable reactor (Peill and Hoffmann, 1997)
Non-concentrating reactors	- Double skin sheet reactor (van Well et al., 1997). - Tubular reactor (Turchi et al., 1993) - Solar pond (Wyness et al., 1994b)	- Thin film fixed bed reactor (Bockelmann et al., 1993; Krysova et al., 1998; Muradov, 1994; Nogueira and Jardim, 1996). - Flat plate reactor (Wyness et al., 1994a;)

CuuDuongThanCong.com https://fb.com/tailieudientucntt

a) *Parabolic Trough Reactors* (PTR) are concentrating-type units configured with a tubular reactor section and a parabolic reflecting trough. The reflector concentrates the sunlight to an aperture on the reactor tube. A one or two-axis sun tracking system is recommended for adequate operation (Alfano et al., 2000; Bockelmann et al., 1993, 1995; Malato et al., 1996, 1997; Mehos and Turchi, 1993; Pacheco et al., 1993).

b) *Parabolic collecting reactors* are trough reactors without light concentrating devices. Reflectors in these reactors consist of two half-cylinders of parabolic profile enabling the light to enter from virtually any direction and to be reflected into the tubular reactor (Malato et al., 1997, 1996). The principal advantages of these units are a very limited mass transfer limitation due to turbulent conditions and a nearly close-system configuration, which minimizes the vaporization of volatile contaminants. This configuration presents, however, the following potential drawbacks:
   - It solely uses direct UV irradiation
   - It displays low optical efficiency
   - It requires an oxygen injection
   - It involves high investment cost
   - It requires a post-separation step of TiO_2

c) The *non-concentrating double skin reactor* is a slurry type flat plate unit, which is designed using a modified double skin Plexiglas sheet (van Well et al., 1997). Water flows through a thin slit formed in between two Plexiglas sheets. Their principal advantages are
   - Possible use of the complete UV irradiation spectrum
   - Operation of the unit under turbulent flow conditions
   - Nearly sealed reactor with no vaporization of contaminants
   - Simple construction
   - Low investment cost.

   Their main disadvantages could be
   - Low optical efficiency
   - Large irradiation area for the purification of large volumes of water
   - Need of separation of TiO_2 particles
   - Bubble entrapment resulting from aeration.

d) The *non-concentrating thin film fixed bed configuration* consists of an inclined glass plate coated with photocatalyst (Degussa P25 of Hombikat UV-100). The polluted water flows along the inclined glass panel forming a thin film (100 microns) (Bahnemann et al., 1994, 1993). Their main advantages are
   - Possible use of the complete UV irradiation spectrum
   - High optical efficiency
   - Simple construction
   - No need of TiO_2 particles' separation.

   The main drawbacks of this configuration are:
   - Laminar flow conditions
   - Vaporization of volatile contaminants
   - Catalyst film exposed to pollution agents
   - Large area required for treating large water volumes (van Well et al., 1997).

CuuDuongThanCong.com https://fb.com/tailieudientucntt

e) The *non-concentrating flat plate configuration* consists of a rectangular flat plate with a thin glass cover. The photocatalyst is suspended in the water phase forming a slurry. This design prevents the contact between the wastewater and the ambient air. A spray bar located near the top of the reactor evenly distributes the wastewater (Wyness et al., 1994a).

In summary, there are a number of available photocatalytic reactor configurations for the photoconversion of water pollutants. These reactors are based on either suspended or immobilized TiO_2. It is expected that enhanced energy efficiencies could be achieved by improving the engineering of the above-described designs. This could considerably expand the prospects of the use of photocatalysis for water purification.

2.8. PHOTOCATALYTIC REACTORS FOR AIR TREATMENT

The removal of airborne contaminants is an area of promising applications for photocatalysis. The challenges to be faced involve the treatment of relatively large gas flows in devices with low pressure-drops, good photocatalyst irradiation and efficient reactant species-photocatalyst contacting (Dibble and Raupp, 1992). In the near future photocatalytic reactors, incorporating the use of solar energy, are also anticipated to be developed.

It is also expected that these novel designs, as in the case of water treatment, could be engineered to efficiently achieve total pollutant mineralization (Serrano and de Lasa, 1997).

To achieve these goals, photocatalytic reactors for air treatment require careful design and the selection of a number of reactor parameters such as

- UV source
- Reactor configuration
- Lamp location
- Catalyst type, distribution and impregnation
- Interaction between the light, catalyst and reacting fluid

Several laboratory photocatalytic reactor configurations have been described in recent years:

- Fluidized Photo Catalyst Bed (Dibble and Raupp, 1992; Yue et al., 1983);
- Annular Packed Bed (Raupp et al., 1997);
- Photocatalytic Coated Honeycomb Monoliths (Sauer and Ollis, 1994; Suzuki, 1993);
- Fixed Powder Layer (Formenti et al., 1971; Peral and Ollis, 1992);
- Fiber Optic Based Reactor (Peill and Hoffmann, 1995)
- Photo-CREC Air Unit with Venturi (Ibrahim and de Lasa, 2003)

These designs were tested considering as performance qualifiers the levels of photoconversion of various classes of pollutants at different concentrations, temperatures, relative humidity, pressures, space-times and irradiation times.

CuuDuongThanCong.com https://fb.com/tailieudientucntt

A common characteristic of these units is the state of the photocatalyst: TiO_2 supported on a solid surface, either stationary or mobile. Typical examples are

- A thin TiO_2 film coated on the inner surface of the reactor wall (Jacoby et al., 1996)
- Supported TiO_2 on porous fibrous meshes (Ibrahim and de Lasa, 2002; Peral and Ollis, 1992), on monoliths (Blanco et al., 1996b), on honeycombs (Suzuki, 1993)
- TiO_2 entrapped in supporting particles (Anderson and Bard, 1997; Yamazaki–Nishida et al., 1994)
- TiO_2 coated on an optical fiber bundle. Optical fibers could provide direct photocatalyst radiation transfer and high activated surface area to reactor volume. Care has to be taken, however, because of the possibility of catalyst deactivation due to heat build up in the fiber optic bundle array (Peill and Hoffmann, 1996, 1995)

Supported TiO_2 photocatalysts can be implemented in fluidized beds, fixed powder layer reactors, annular reactors and monolith reactors. Examples of these reactors are described in the following section:

a) *Flat Plate Fluidized Bed* (Dibble and Raupp, 1992). The photocatalytic conversion of tri-chloro-ethylene is achieved through the air stripping of contaminated ground water. TiO_2 is supported on fluidized 250–450 micron silica gel beads inside a 10 mm wide, 60 mm high and 4 mm thick reactor column. TiO_2 is irradiated using a 4-W lamp with maximum irradiation intensity at 390 nm. The fluidized bed design is adequate for processing large gas flows and for isothermal operation, ensuring high heat transfer and reduced mass transport limitations. Catalyst regeneration is also relatively easy to implement. Remaining issues are gas bypass, photocatalyst attrition and non-uniform residence times for the solids (Ollis, 1993).

b) *Fluidized Bed Photocatalytic Reactor* (Yue et al., 1983). This unit provides good mixing of TiO_2 with the polluted air stream. TiO_2 can be supported on other particles, such as silica gel. This is a convenient alternative given the poor fluidization properties of TiO_2. Fluidized beds in the bubbling regime should be operated with caution since they favour bubble formation, gas bypass and low pollutant conversions (Ollis, 1993). Fluidized beds may also offer other challenges such as low irradiation utilization efficiency, non-uniform solid mixing and catalyst attrition.

c) *Fixed Layer Photocatalytic Reactor* as proposed by Peral and Ollis (1992). TiO_2 is held on a metallic support or on a fritted glass plate. Fixed layer reactors could be suitable for compact treatment systems with little gas back mixing. These reactors could also offer challenges given the limited light distribution and the relatively small air flow treatment capacity (Ollis, 1993).

d) *Annular Photocatalytic Reactor* (Jacoby et al., 1996). These reactors can be used for controlling VOC emissions in indoor air. A UV lamp is placed in the center of the unit with the outer surface of the inner central tube coated with a thin layer of TiO_2. This design provides a low area of photocatalyst per unit reactor volume.

CuuDuongThanCong.com https://fb.com/tailieudientucntt

e) *Packed Bed Photocatalytic Reactor.* The fluid stream to be treated flows through the packed bed, coming into contact with the irradiated particles holding the TiO_2. This configuration may suffer from a low surface area to reactor volume ratio and low use of irradiation and this considering both light absorption and scattering (Al-Ekabi *et al.*, 1989; Raupp *et al.*, 1997).

f) *TiO_2 Coated Monolith Photocatalytic Reactor.* TiO_2 is coated on the inner surface of honeycomb-shaped cells. Honeycombs are designed to operate much like car exhaust systems, processing high flows with low-pressure drops, allowing for short gas residence times and providing high surface area to reactor volume ratios (Ollis, 1993; Sauer and Ollis, 1994). Blanco et al., (1996b) used irradiated monoliths for toluene oxidation in an air stream at 150–450°C. These monoliths suffer from poor irradiation distribution (Obee and Brown, 1995; Ollis, 1993).

g) *Photocatalytic Reactors with Fiber Optic Bundles.* These reactors can be employed as a mean of light transmission to supported TiO_2, located at a distance from the light source (Peill and Hoffmann, 1995). While fiber optic bundles enhance the uniformity and the irradiation distribution within a given reactor volume, they can negatively be affected by catalyst deactivation due to heat buildup in the fiber bundle and low beam focusing efficiencies (Peill and Hoffmann, 1996).

h) *Photo-CREC Air with Venturi.* This photocatalytic reactor (full characteristics to be provided later on in this chapter) features external, near-UV lamps placed in parabolic reflectors, a basket supporting the irradiated glass mesh with TiO_2, and a fluid flow pattern ensuring high gas velocities close to the mesh region. This design optimizes mesh irradiation as well as the contacting of the air stream with the supported TiO_2.

Photoconversion of air contaminants in photocatalytic reactors has been considered through a diversity of reactor configurations and designs. The high quantum yields observed, surpassing the value of 1, suggest that this approach will become a major area for future applications of photocatalysis.

2.9. PHOTOCATALYTIC REACTORS: SPECIAL APPLICATIONS

Several unique photocatalytic reactor applications are emerging in the scientific literature. These areas of special interest consider the need for extending photocatalysis to the inactivation of microorganisms, the removal of inorganic contaminants and the improvement of energy efficiencies. Shama et al., (1996) described a novel thin-film UV sterilization photo reactor for bacterial inactivation. This unit has a specially designed nozzle that generates a thin liquid film containing the catalyst. Another interesting approach for optimizing energy savings is the periodically illuminated reactor that could allow a reduction of process energy input, maintaining the photocatalytic effect (Buechler et al., 1999).

CuuDuongThanCong.com https://fb.com/tailieudientucntt

2.10. NOVEL CREC PHOTOCATALYTIC REACTORS

Since 1990, the authors of this book have been dedicating their efforts towards the design of novel photocatalytic reactors at the Chemical Reactor Engineering Centre (CREC) of the University of Western Ontario. Their aim has been the development of photocatalytic reactors that optimize efficiency through an enhanced contact between the photocatalyst and the fluid stream (either gas or fluid) and an improved irradiation of the photocatalyst.

Three photocatalytic reactors for water treatment and one for air treatment have been conceptualized:

a) The Photo-CREC-Water I with immobilized TiO_2
b) The Photo-CREC-Water II, with suspended TiO_2 and artificial irradiation.
c) The Photo-CREC-Water III, with suspended TiO_2 and simulated solar irradiation.
d) The Photo-CREC-Air unit with a Venturi design and TiO_2 anchored on an irradiated mesh.

2.10.1. Photo CREC Water-I Reactor

The Photo-CREC-Water I reactor was originally proposed by de Lasa and Valladares (1997), and Valladares (1995). Modifications were introduced to the original design as reported in Table 2.5 by Serrano and de Lasa (1997).

An annular channel with 16 baskets positioned at 45° angles characterizes the Photo-CREC-Water I (Figure 2.9). The Photo-CREC reactor is configured with stainless steel spacers placed between the baskets. These spacers secure the basket in position

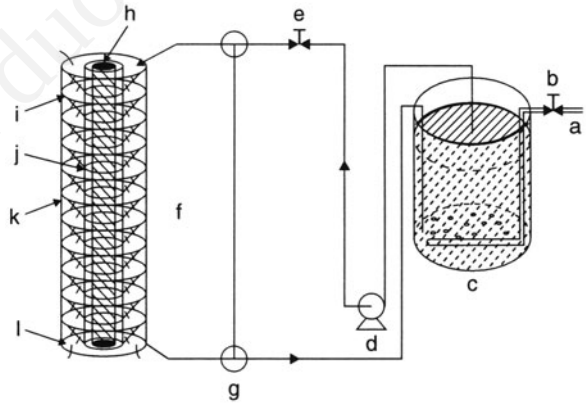

FIGURE 2.9. Schematic representation of the photocatalytic reactor. (a) Compressed air, (b) air gas regulator, (c) oxygenator with air pipe distributor, (d) Gilson water pump, (e) valve for controlling water circulation, (f) concentric Photo-CREC unit with lamp placed in the center and 16 conical baskets spaced throughout the unit, (g) three-way valve, (h) lamp, (i) basket, (j) Pyrexglas tube, (k) external Plexiglas tube, (l) annular channel. (Reprinted with permission from *Ind. Eng. Chem. Res.*, **36**(11), B. Serrano and H.I. de Lasa, Photocatalytic degradation of water organic pollutantws. Kinetic modeling and energy efficiency, 4705–4711, Copyright 1997 American Chemical Society).

CuuDuongThanCong.com https://fb.com/tailieudientucntt

TABLE 2.5. Characteristics of Photo-CREC-Water I.

Component	Parameter	Value
Basket reactor	Internal radius, external radius, height, reactor volume	1.9, 4.05, 42.0 cm 2.5 L
Stirred tank	Tank volume	0.5 L
Lamp	Lamp radius, Lamp length	1.27, 40 cm
	Nominal power	15 W
	Lamp efficiency	15-20 %
	Characteristic emission	Isotropic and superficial
	Emission range	300–405 nm
	Emission rate	1.03×10^{-5} einstein s^{-}

and ensure minimum loss of light. The near-UV lamp is located in the central channel, providing 15 W of monochromatic light (365 nm). Water is circulated in a downward flow, with the only exception being the startup of the run when an upward flow evacuates the air pockets. Water exiting the reactor is discharged into an oxygenator. This unit is equipped with a perforated pipe air distributor and a magnetic stirrer securing water saturation with oxygen. A variable-flow Gilson pump completes the experimental system. This pump is used to return the water to the upper section of the photoreactor unit, closing in this way the cycle of water oxygenation and recirculation.

2.10.1.1. "In Situ" Impregnation of the Meshes A unique feature of the Photo-CREC-Water I is the method of preparation of the TiO_2-mesh. The fiberglass mesh organic matter coating, which could hinder the TiO_2 attachment, is removed using a nitric acid solution (70 wt %). After the acid treatment, the mesh is calcined, at 550°C for an extended period (e.g. 5.5 h), and weighted to confirm that the organic matter is fully removed.

The mesh is then ready to be mounted on the inner face of each of the conical baskets and to proceed to its "in situ" impregnation. A TiO_2 particle slurry (5 wt % TiO_2 in a 30% methanol-water solution) is circulated at a 1720 mL min^{-1} flow rate for a 10-hour period. Typically, 15 g of TiO_2 are used in 3 L to impregnate 73.5 g of mesh available in the 16 baskets of the Photo-CREC-unit. This impregnation technique provides substantial catalyst loading (16.5 wt %) on the impregnated fiberglass mesh.

EDX microanalysis can be used to collect information, from a depth of 1-μm, depending on the TiO_2 coverage on the mesh surface. According to the EDX, the mesh is covered with an average Ti / (Ti+Si) surface ratio of 57.9%. After 2250 hours of operation, the EDX surface ratio lowers to 25 %. This suggests that there is a mild catalyst wash off taking place during operation.

Serrano and de Lasa (1997) established strong TiO_2 particle attachment on the fiberglass mesh, when translucid water was obtained after the first washing and in all subsequent experiments. This confirms that the Photo-CREC-Water I reactors, using immobilized TiO_2 anchored on fiberglass mesh, do not require particle recovery.

2.10.1.2. Minimization of Mass Transfer Controls To study the eventual effect of mass transfer on the performance of the Photo-CREC-Water I, several experiments were conducted wherein the water flow circulation rate varied from 150 to 1700 mL min^{-1} and

CuuDuongThanCong.com https://fb.com/tailieudientucntt

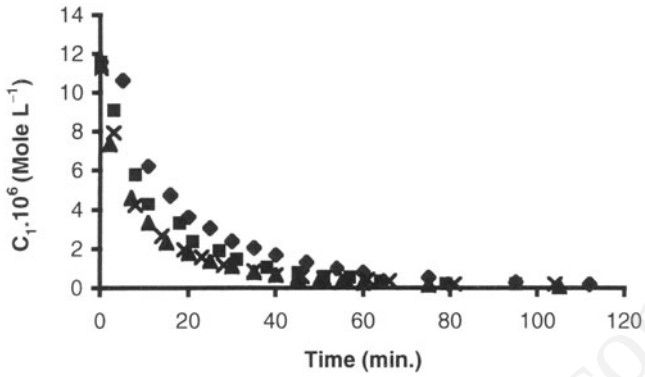

FIGURE 2.10. Concentration change of methylene blue in the liquid phase with irradiation time at various water recirculation rates. Initial concentration of MeB: 12.10^{-6} mol L^{-1}. (▲) 1700 mL/min, (×) 1200 mL/min, (■) 800 mL/min (♦) 500 mL/min. Photoreactor unit: Photo-CREC Water-I (Reprinted with permission from *Ind. Eng. Chem. Res.*, **36**(11), B. Serrano and H.I. de Lasa, Photocatalytic degradation of water organic pollutantws. Kinetic modeling and energy efficiency, 4705–4711, Copyright 1997 American Chemical Society).

the initial pollutant concentration was of 12 10^{-6} moles L^{-1} (Figure 2.10). It is observed that the methylene blue concentration profiles for 500, 800 and 1200 mL min^{-1} water flows display an increasing rate of decay, or the equivalent increase of the overall rate of photoconversion. This effect, however, becomes negligible for the 1200 and 1700 mL min^{-1} water flow rates. It can be concluded that at flow rates equal or higher than 1700 mL min^{-1}, there is no mass-transfer limitation. As a result, recommended experiments are to be carried out at 1700 mL min^{-1}.

2.10.1.3. Residence Time Distribution: Photo CREC Water-I Flow patterns in photocatalytic reactors are of critical importance since they can affect the applicability of the proposed Photo-CREC-Water I model. In order to assess the deviation of the flow regime from the ideal plug flow, several experiments were developed under the following conditions:

a) Baskets with the mesh-TiO_2 system
b) Phenol as a non-reactive tracer.

Both, a phenol step perturbation and phenol pulse perturbation were applied.

During this residence time distribution testing, the Photo-CREC-Water I was operated in the single pass mode with no water recycling and samples taken every 10 seconds. The Peclet number assessed with this method was 30 and the number of ideal CSTR tanks was estimated as 15. Since the number of baskets in Photo-CREC-Water I is 16, this demonstrates that each basket can be viewed as a close equivalent to an ideal single mixing stage.

2.10.2. Photo-CREC Water-II Reactor

Figure 2.11 illustrates the components of Photo-CREC Water-II reactor. It consists of two concentric tubes (or containers) with a UV lamp inside the transparent inner

CuuDuongThanCong.com https://fb.com/tailieudientucntt

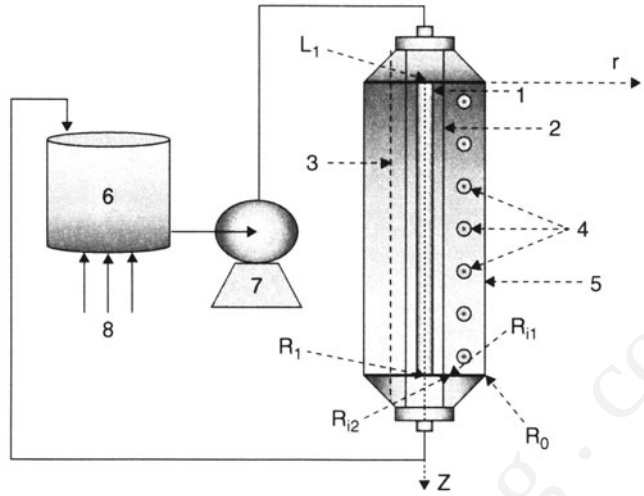

FIGURE 2.11. Schematic representation of the Photo-CREC Water-II Reactor: (1) *MR* or *BL* lamp, (2) replaceable 3.2-cm-diameter glass inner tube, (3) replaceable 5.6-cm-diameter glass inner tube, (4) fused-silica windows, (5) UV-opaque polyethylene outer cylinder, (6) stirred tank, (7) centrifugal pump, and (8) air injector. (Reprinted with permission from *Ind. Eng. Chem. Res.*, **40**(23), M. Salaices, B. Serrano and H.I. de Lasa, Photocatalytic conversion of organic pollutants: Extinction coefficients and quantum efficiencies, 5455–5464. Copyright 2001 American Chemical Society).

container and a free-flowing TiO_2 suspension in the concentric channel. Table 2.5 summarizes the main geometrical characteristics of the reactor.

An interchangeable inner Pyrex glass tube varying in thickness and diameter enables the Photo-CREC-Water II to modify the dimension of the annular cross-section and adjust the flow conditions in the annular reactor space. Pyrex glass combines good UV light transmission properties (in excess of 90% of the UV radiation greater than 315 nm in wavelength) and low cost.

A 3.5-L stirred tank is connected in series with a tubular photocatalytic reactor (Figure 2.11). The tank is used for

TABLE 2.5. Photo CREC Water-II Most Important Geometrical Characteristics

Component	Symbol	Value
Annular reactor	Internal radius 1, internal radius 2, external radius, height	1.74, 2.82, 4.45, 44.0 cm
	V_{pfr} for 3.2-cm-d.	2.5 L
	V_{pfr} for 5.6-cm-d.	1.4 L
Stirred tank	V_{st}	3.5 L
Reactor inner tube		
3.2-cm-diameter	Thickness	0.23 cm
5.6-cm-diameter	Thickness	0.32 cm
Lamps		
	Lamp radius Lamp length	1.27, 40 cm
Windows (fused silica)		
	Window radius,	0.5 cm

CuuDuongThanCong.com https://fb.com/tailieudientucntt

- Aliquot sampling
- Pollutant and catalyst addition
- pH monitoring
- Temperature monitoring
- Air injection.

A centrifugal pump circulates the fluid throughout the system and is used to modify the flow rate.

To facilitate radiometric and spectro-radiometric measurements, the unit is equipped with seven circular windows equally spaced (6.4 cm) along the outer tube wall. Since radiation measurements are considered, the outer reactor tube is made of UV-opaque polyethylene to minimize radiation reflection.

The reactor is also equipped with a four-point flow distributor injector at the reactor entrance. These ensure uniform injection and intense mixing. The injection points are located in the top section of the reactor at 90°-radial and 45°-azimuthal positions.

2.10.3. Reactor Hydrodynamics and Mixing

Water/catalyst/light-contacting has an important influence on the reactor's performance. Flow patterns determine the extent of the segregation and the non-ideal mixing.

To establish the mixing conditions in Photo-CREC-Water II, step and impulse phenol concentration perturbations were applied at the reactor entry. Data are analyzed using an axial dispersion model and a series-of-tanks model.

In the case of the axial diffusivity model with step perturbation, the following equation was used (Levenspiel, 1999; Smith, 1986):

$$C^*_{Z=L} = \left(\frac{C}{C_0}\right)_{step} = \frac{1}{2}\left[1 - erf\left(\frac{1}{2}\sqrt{Pe}\frac{1-\theta}{\sqrt{\theta}}\right)\right] \tag{2-1}$$

where C is the tracer concentration in mole L^{-1}, Pe is the dimensionless Peclet number ($Pe = \frac{uL}{D_L}$), θ is the dimensionless time ($\theta = \frac{t}{L/u}$), u is the volumetric flow rate L min^{-1}, L is the reactor length in m, D_L is the axial diffusivity coefficient in m^2 s^{-1}, and z is the axial coordinate in m.

Alternatively, for the agitated tanks in series model, the following relationship was used:

$$(C/C_0)_{step} = 1 - e^{-n\theta}\left[1 + n\theta + \frac{1}{2!}(n\theta)^2 + \cdots + \frac{1}{(n-1)!}(n\theta)^{n-1}\right] \tag{2-2}$$

where C is the tracer concentration in mole L^{-1}, n is the number of tanks and θ is the dimensionless time.

Figure 2.12 reports the system's response to a step function using phenol as the tracer. Given a 4.47 L min^{-1} volumetric flow and 2.78 L reactor volume, the average residence time can be assessed at 37.3 s. The Reynolds number in the annulus was in the 3200–range, suggesting a potentially turbulent flow. Using the tank-in-series model, nearly 40 ideal tanks were estimated. Considering the axial dispersion model, a Peclet number of 80 was calculated. These results are consistent with a close-to-plug flow

CuuDuongThanCong.com https://fb.com/tailieudientucntt

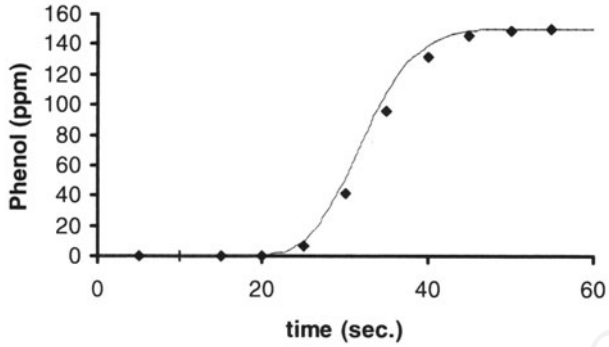

FIGURE 2.12. Experimental results displaying a step perturbation as measured at the outlet of Photo-CREC-Water II. (■) Experimental data, (–) In-series tank model estimation, (- -) Diffusion model estimation.

pattern in the Photo-CREC-Water II annulus with many tanks in series ideal stages and an axial dispersion coefficient that approaches zero.

2.10.4. Photo-CREC Water-III Reactor

Figure 2.13 shows the Photo-CREC Water-III reactor. This design incorporates to the Photo-CREC Water II the following main features:

- External illumination to simulate solar irradiation
- Larger irradiation area
- Incorporation of a mobile internal sensor to measure the radiation transmission inside the inner reactor tube
- Possibility of incorporate internal irradiation to smooth the radiation field radial distribution.

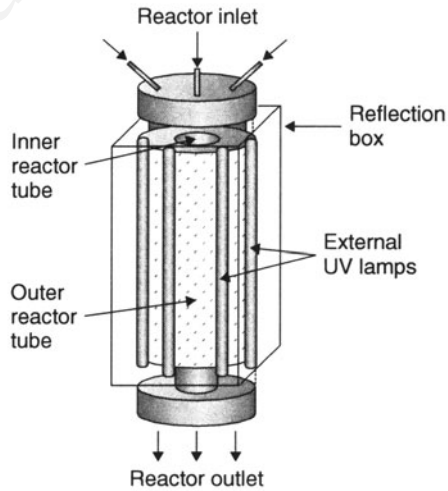

FIGURE 2.13. Schematics representation of Photo-CREC Water-III reactor: Solar photocatalytic reactor simulator.

CuuDuongThanCong.com https://fb.com/tailieudientucntt

The reactor is irradiated externally by a set of 8 UV-lamps each of them supplying 15 watts nominal power. The radiation field distribution can be measured using a fiber optic sensor placed inside a concentric inner tube with this sensor device connected to a spectrophotoradiometer. The external illumination permits the simulation of solar irradiation whereas the combination of internal and external illumination allows the smoothing of the radiation field radial distribution and the increase of irradiation efficiency.

2.10.5. Photo-CREC Air Reactor

The main body of the 14.7 L-capacity closed-loop system is made of zinc-plated pipes connected with aluminized-steel 90° elbows and a stainless steel Venturi section. External lamps irradiate the reaction section. Radiation penetrates through windows cut out of acrylic sheets (UL Light Technology, Birminghan UK) placed in the divergent section of the Venturi. Eight Pen-Ray 1-watt lamps are symmetrically placed around the reaction section and housed in reflectors for the uniform irradiation distribution (Ibrahim, 2001). The reaction section is formed by a basket supporting a fiberglass mesh impregnated with TiO_2. The lamp intensity spectrum is measured using the SolaScope 2000 spectro-radiometer over the 300-390 nm range.

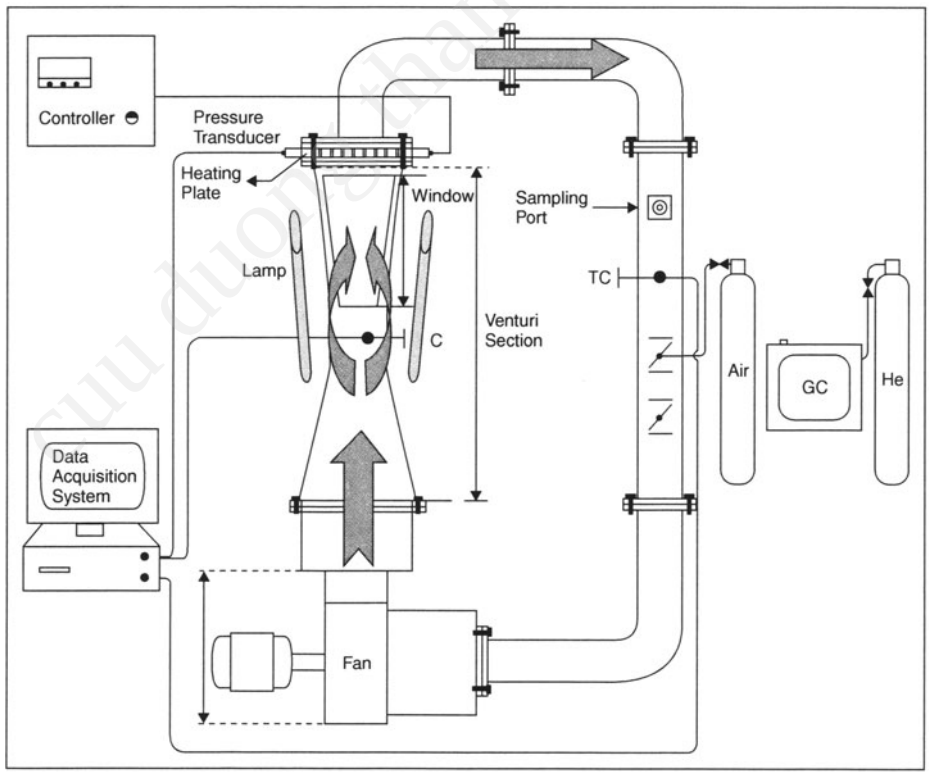

FIGURE 2.14. Schematic diagram of the Photo-CREC-Air unit set-up (AIChE Journal Copyright 2004, Vol. 50, Issue. 5,Wiley InterScience, p. 1017–1027).

CuuDuongThanCong.com https://fb.com/tailieudientucntt

Measurements performed at different locations using the SolaScope 2000 probe confirm the uniform distribution of photons provided via external lamps and reaching the 510 cm^2 glass fiber mesh area holding the TiO_2: 8.0-8.8wt% for Degussa P25 and 3.6-4.8% for Hombikat UV100 (Ibrahim and de Lasa, 2002). Radiation exiting the Pen-Ray lamps was estimated at 0.068 watts while radiation reaching the mesh was determined to be 0.02 watts providing an overall irradiation efficiency of 29.4%.

The Photo-CREC-Air unit operates in a batch mode with a given amount of model pollutant injected in a set volume of air. Model pollutants are vaporized almost instantaneously and mixed intimately with the air stream.

Development of the Photo-CREC-Air reactor also involved the characterization of fluid flow patterns in the unit and the assessment of the UV radiation reaching the impregnated mesh. The fluid flow pattern calculation and the fluid flow visualization can be developed using CFX-4.3 software for fluid flow simulation. A plane of symmetry in both the x and y directions can be assumed by simulating the flow patterns in the Venturi section. This enables the sub-division of the reactor's physical volume into 4 quarters. This makes possible the use of smaller cell sizes and an improved convergence (Ibrahim, 2001).

Results from the simulated flow indicate that the proposed design provides the highest gas velocity in the near-window region, ensuring a high degree of window sweeping and preventing the TiO_2 particle deposition on the acrylic windows. The proposed design also ensures a uniform velocity distribution (10-15 m s^{-1}) in the near-mesh region, guaranteeing good contact between the polluted fluid and the TiO_2 particles held on the mesh.

2.11. CONCLUSIONS

This chapter highlights the characteristics of current photocatalytic reactor designs, the gaps in the current understanding of the technology and the research community's interest in designs based on fundamental principles to achieve increased photoconversion performance and the pollutant mineralization.

The bench-scale Photo-CREC reactors are also described focusing on their important prospects for their scale-up because of their mixing, the catalyst-fluid contact and efficient light and TiO_2 interaction. The Photo-CREC reactors are specially designed and equipped with auxiliary components to facilitate the study of important reaction engineering parameters such as the adsorption and the reaction rates of model compounds, the photo degradation mechanisms and the photocatalyst efficiency.

NOTATION

Symbols

C	Concentration	mole L^{-1}
C^*	Dimensionless concentration	$\frac{C}{C_{in}}$
C_{in}	Step tracer concentration at the reactor entry	mole L^{-1}
D_L	Axial diffusivity coefficient	m^2 s^{-1}

CuuDuongThanCong.com https://fb.com/tailieudientucntt

H	Reactor height	cm
L	Reactor or lamp length	m
n	Number of tanks	
Pe	Dimensionless Peclet number	uL/D_L
r	Radial coordinate	
u	Fluid superficial velocity	m s^{-1}
V	Volume	L
z	Axial coordinate	m

Greek letters

θ	Dimensionless time	$\frac{t}{(L/u)}$

Subscripts

0	Evaluated at the inner surface of the outer tube
i	Evaluated at the inner reactor surface, incident
l	Lamp
pfr	Plug flow reactor
st	Stirred tank
w	Window

REFERENCES

Aguado, M. A. and Anderson, M. A., 1993, Degradation of formic acid over semiconducting membranes supported on glass. Effects of structure and electronic doping. *Solar Energy Mat. & Solar Cells.* **28**(4):345–361.

Alberici, R. M. and Jardim, W. F., 1994, Photocatalytic degradation of phenol and chlorinated phenols using Ag-TiO_2 in a slurry reactor. *Wat. Research.* **28**(8): 1845–1849.

Al-Ekabi, H., and Serpone, N., 1988, Kinetic studies in heterogeneous photocatalysis. 1. Photocatalytic degradation of chlorinated phenols in aerated aqueous solutions over TiO_2 suported on a glass matrix, *J. Phys. Chem.,* **92**:5726–5731

Al-Ekabi, H., and Serpone, N., 1993, TiO_2 Advanced photo-oxidation technology: Effect of electron acceptors, in *Photocatalytic purification and treatment of water and air*, Ollis, D. and Al–Ekabi, H., eds., Elsevier, New York, pp. 321–335.

Al-Ekabi, H., Serpone, N., Pelizzeti, E., Minero, C., Fox, M. A. and Draper, B, R., 1989, Kinetic Studies in Heterogeneous Photocatalysis. 2. *TiO_2* Mediated Degradation of 4-Chlorophenol Alone and in a three Component Mixture of 4-Chlorophenol, 2-4 dichlorophenol and 2-4-5Trichlorophenol in Air Equilibrated Aqueous Media, *Langmuir*, 5, pp. 250–255.

Alfano, O., Bahnemann, D., Cassano, A., Dillert, R., and Goslich, R., 2000, Photocatalysis in water environments using artificial and solar light, *Catal. Today*, **58**:199–230.

Anderson, C., and Bard, J., 1997, Improved photocatalytic activity and characterization of mixed TiO_2/SiO_2 and TiO_2/Al_2O_3 materials, *J. Phys. Chem. B*, **101**:2611–2616.

Andreozzi, R., Caprio, V., and Insola, A., 2000, Photocatalytic oxidation of 4-nitrophenol in aqueous *TiO_2* slurries: An experimental validation of literature kinetic models, *J. Chem. Tech. Biotech.,* **75**(2):131–136.

Augugliaro, V., Davi, E., Palmisano, L., Schiavello, M., and Scalfani, A., 1990, Influence of hydrogen peroxide on the kinetics of phenol photodegradation in aqueous titanium dioxide dispersion, *Appl. Catal.,* **65**:101–116.

CuuDuongThanCong.com https://fb.com/tailieudientucntt

Augugliaro, V., Loddo, V., Palmisano, L., and Schiavello M., 1995, Performance of heterogeneous photocatalytic systems: Influence of operational variables on photoactivity of aqueous suspensions of TiO_2, *J. Catal.*, **153**:32–40.

Bahnemann, D., Bockelman, D., Goslich, R., Hilgendorff, M., and Weichegrebe, D., 1993, Photocatalytic detoxification: Novel catalyst, mechanisms and solar applications. In: *Photocatalytic purification and treatment of water and air*, Ollis, D., and Al-Ekabi, H., eds., Elsevier, New York, pp. 301–319.

Bahnemann, D., Bokelman, D., Goslich, R., and Weichgrebe, M., 1994, Photocatalytic detoxification of polluted aquifiers: Novel catalysts, mechanism and solar applications, in: *Aquatic and surface photochemistry*, Hels, G., Zeep, R., Crosby, D., eds., Lewis Publications, Boca Raton, FL., pp. 349–367.

Bahnemann, D., Dockelmann, D., and Goslich, R., 1991, Mechanistic studies of water detoxification in illuminated TiO_2 suspensions, *Solar Energy Mater.*, **24**:564–583.

Barni, B., Cavicchioli, A., Riva, E., Zanoni, L., Bignoli, F., Bellobono, R., Gianturco, F., De Giorgi, A., Muntau, H., Montanarella, L., Facchetti, S., and Castellano, L., 1995, Laboratory-scale photodegradation of chloroaliphatics in aqueous solutions by photocatalytic membranes immobilizing TiO_2, *Chemosphere*, **30**(10):1847–1860.

Bekbolet, M., Lindner, M., Weichgrebe, D., and Bahnemann, D.W., 1995, Photocatalytic detoxification with the thin–film fixed bed reactor (TFFBR): Clean–up of highly polluted landfill effluents using a novel TiO_2–photocatalyst, *Solar Energy*, **56**(5):455–469.

Bellobono, I. R., Carrara, A., Barni B., and Gazzotti, A., 1994, Laboratory-and pilot-plant-scale photodegradation of chloroaliphatics in aqueous solution by photocatalytic membranes immobilizing TiO_2. *J. Photochem. Photob. A: Chem.*, **84**:83–90.

Blanco, J., and Malato, S., 1993, Influence of solar irradiation over phentachlorophenol solar photocatalytic decomposition, in *Photocatalytic purification and treatment of water*, Ollis, D., and Al-Ekabi, H., eds., Elsevier, New York, pp. 639–644.

Blanco, J., Avila, P., Bahamonde, A., Alvarez, E., Sanchez, B., and Romero, M., 1996b, Photocatalytic destruction of toluene and xylene at gas phase on a titania based monolithic catalyst, *Catal. Today.*, **29**:437–442.

Blanco, M. M., Lopez Rueda, A.J., and Milow, B., 1996a, Plataforma solar de Almeria, *Annual technical report 1996*, pp. 61–76.

Bockelmann, D., Goslich, R., Weichgreb, D., and Bahnemann, D., 1993, Solar detoxification of polluted water: Comparing the efficiencies of a parabolic reactor and a novel thin-film fixed-bed reactor. in: *Photocatalytic purification and treatment of water*, Ollis, D., and Al-Ekabi, H., eds., Elsevier, New York, pp. 639–644.

Bockelmann, D., Weichgreb, D., Goslich, R., and Bahnemann, D., 1995, Concentrating versus nonconcentrating reactors for solar water detoxification. *Solar Energy Materials & Solar Cells.* **38**: 441–451.

Borello, R., Minero, C., Pramauro, E., Pelizzetti, E., Serpone, N., and Hidaka, H., 1989, Photocatalytic degradation of DDT mediated in aqueous semiconductor slurries by simulated sunlight, *Environ. Toxicol. Chem.*, **8**:997–002.

Buechler, K. J., Nam, C. H., Zawistowski, T. M., Noble, R. D., and Koval, C. A., 1999, Design and Evaluation of a Novel-Controlled Periodic Illumination Reactor to Study Phtocatalysis, *Ind. Eng. Chem. Res.*, **38**:1258–1263.

Buechler, K. J., Noble, R. D., and Koval, C. A., 1999, Investigation of the effects of controlled periodic illumination on the oxidation of gaseous trichloroethylene using a thin film of TiO_2. *Ind. Eng. Chem. Res.* **38**(3):892–896.

Butters, B.E., and Powell, A. L., 1995, Method and system for photocatalytic decontamination, *US Patent* No. 5,462,674.

Byrne, J. A., Eggins, B. R., Brown, N. M. D., McKinney, B., and Rouse, M., 1998, Immobilisation of TiO_2 powder for the treatment of polluted water. *Appl. Catalysis B. Environ.* **17**:25–36.

Cabrera, M., Alfano, O., and Cassano, A., 1994, Novel reactor for photocatalytic kinetic studies, *Ind. Eng. Chem. Res.*, **33**:3031–3042.

Cassano, A., Martin, C., Brandi, R., and Alfano, O., 1995, Photoreactor analysis and design: Fundamentals and applications, *Ind. and Eng. Chem. Res.*, **34**:2155–2201.

Chen, D. and Ray, A. K., 1998, Photodegradation kinetics of 4-nitrophenol in TiO_2 suspension. *Wat. Res.* **32**(11):3223–3234.

Chen, D., and Ray, A. K., 1999, Photocatalytic kinetics of phenol and its derivatives over UV irradiated TiO_2. *App. Cat. B: Environ.* **23**:143–157.

CuuDuongThanCong.com https://fb.com/tailieudientucntt

Chester, G., Anderson, M., Read, H., and Espulgas, S. A., 1993, Jacketed Annular membrane photocatalytic reactor for wastewater treatment: degradation of formic acid and atrazine. *J. Photochem. Photob. A: Chem.* **71**(3):291–297.

Choi, W., Termin, A., and Hoffman, M. R., 1994, The role of metal dopants in quantum–sized TiO_2: correlation between photo reactivity and charge carrier recombination dynamics, *J. Phys. Chem.*, **98**:13669–13679.

Crittenden, J. C., Liu, J., Hand, D. W., and Perram, D. L., 1997, Photocatalytic oxidation of chlorinated hydrocarbons in water, *Wat. Res.*, **31**(3):429–438.

Crittenden, J. C., Zhang, Y., Hand, D. W., 1996, Solar detoxification of fuel-contaminated groundwater using fixed-bed photocatalysts. *Wat. Environ. Res.* **68**(3):270–278.

Curco, D., Malato, S., Blanco, J., and Gimenez, J., 1996, Photocatalysis and radiation absorption in a solar plant, *Solar Energy Materials and Solar Cells*, **44**:1999–217.

Davydov, L., Pratsinis, S. E., and Smirniotis, P. G., 2000, The intrinsic catalytic activity in photoreactors. *Environ. Sci. Tech.*, **34**(16):3435–3442.

Davydov, L., Smirniotis, P. G., and Pratsinis, S. E., 1999, Novel differential reactor for the measurement of overall quantum yields. *Ind. Eng. Chem. Res.* **38**(4):1376–1383.

de Lasa, H. I., and Valladares, J., 1997, Photocatalytic reactor, *US Patent* No. 5,683,589.

Dibble, L., and Raupp, G., 1992, Fluidized-bed photocatalytic oxidation of trichloroethylene on contaminated air streams, *Environ. Sci. & Technol.*, **26**(3), 492–495.

Domenech, X. and Peral, J., 1989 Cyanide photo-oxidation using a TiO_2-coated zeolite. *Chemistry and Industry.* **18**:606.

Fernandez, A., Lassaletta , G., Jimenez, V. M., Jasto, A., Gonzales-Elipe, A. R., Herrmann, J. M., Tahiri, H., and Ait-Ichou, Y., 1995, Preparation and characterization of TiO_2 photocatalysis supported of various rigid supports (glass, quarts and stainless steel). comparative studies of photocatalytic activity in water purification. *Appl. Catal. B: Environm.* **7**:49–63.

Formenti, M., Juillet, F., Meriaude, P., and Teichner, S., 1971, Heterogeneous photocatalysis for partial oxidation of paraffin, *Chem. Technol.*, **1**:680–681

Fox, M. A., and Dulay, M. T., 1993, Heterogeneous photocatalysis, *Chem. Rev.*, **93**:341–357.

Gerischer, H., 1993, Photo electrochemical catalysis of the oxidation of organic molecules by oxygen on small semiconductor particles with TiO_2 as an example, *Electrochimica Acta*, **38**(1):3–9.

Gerischer, H., and Heller , A., 1991, The Role of oxygen in photooxidation of organic molecules on somiconductor particles, *J.f Phys. Chem*, **95**(13): 5261–5267.

Giaturco, F., Vianelly, L., Tatti, L., Rota, F., Bruzzi, P., Rivas, L., Bellobono, L. R., Bianchi, M., and Muntau, H., 1996, Pilot-plat photomineralization of dichloromethane and tetrachloroethane in aqueous solution, by photocatalytic membranes immobilizing TiO_2 and photopromoters. *Chemosphere.*, **33**(8):1531–1542.

Ha, H. Y., and Anderson, M. A., 1996, Photocatalytic degradation of formic acid via metal-supported titania. *J. Environ. Eng.*, **122**:217–221.

Harada, M., Honda, M., Yamashita, H., and Anpo, M., 1999, Preparation of titanium oxide photocatalysis loaded on activated carbon and their photocatalytic reactivity for the degradation of 2-propanol diluted in water, *Research on Chemical Intermediates*, **25**(8):757–768.

Herrmann J. M., 1999, Heterogeneous photocatalysis: fundamentals and applications to the removal of various types of organic pollutants. *Catal. Today.* **53**:115–129.

Hoffmann, M. R., Martin, S. T., and Choi, W., 1995, Environmental applications of semiconductor photocatalysis. *Chem. Rev.* **95**:69–96.

Hofstadler, K., Bauner, R., Novallc, S., and Heisler, K., 1994, New reactor design for photocatalytic wastewater treatment with TiO_2 immobilized on fused silica glass fibers: photo-mineralization of 4-chlorophenol. *Environ. Sci. & Tech.*, **28**:670–674.

Ibrahim H., 2001, Photocatalytic reactor for the degradation of airborne pollutants. photoconversion efficiency and kinetic modeling, *Ph.D. Dissertation, University of Western Ontario.*

Ibrahim, H., and de Lasa, H., 2002, Photo-catalytic conversion of air borne pollutants. Effect of catalyst type and catalyst loading in a novel photo-CREC-air unit, App. Catal. B: Environ., **38** (3):201–213.

Ibrahim, H., and de Lasa, H., 2003, Photo-catalytic degradation of air borne pollutants apparent quantum efficiencies in a novel photo-CREC-air reactor, *Chem. Eng. Sci.*, **58**(3-6):943–949.

Ibrahim, H., and de Lasa, H., 2004, Kinetic modeling of the photocatalytic degradation of air-borne pollutants, *AIChE J.*, **50**(5):1017–1027

CuuDuongThanCong.com https://fb.com/tailieudientucntt

Jacoby, W., Black, D., Fennell, D., Boulter, J., Vargo, L., George, M., and Dolberg, S., 1996, Heterogeneous photocatalysis for the control of volatile organic compounds in indoor air, *J. of Air & Waste Management Association,* **46**:691–698.

Kagaya, S., Shimizu, K., and Arai, R., 1999, Separation of titanium dioxide photocatalyst in its aqueous suspensions by coagulation with basic aluminium chloride, *Wat. Res.* **33**:1753–1755.

Karpel, N., Leitner, V., Le Bras, E., Foucault, E., and Bousgarbies, J. L., 1997, A new photochemical reactor design for the treatment of absorbing solutions. *Wat. Sci. Tech.,* **35**(4):215–222.

Krysova, H.; Krysa, J., and Macounova, K., 1998, Photocatalytic degradation of diuron [3-(3,4-dichlorophenyl)-1,1-dimethylurea] on the layer of TiO_2 particles in the batch mode plate film reactor. *J. Chem. Tech. Biotech.,* **72**(2):169–175.

Levenspiel, O., 1999, Chemical reaction engineering, 3rd Edition, john Wiley & Sons, New York, pp. 293–320.

Linsebigler, A. L., Guangquan, L., and Yates (Jr.), T. J., 1995, Photocatalysis on TiO_2 surfaces: Principles, mechanisms and selected results, *Chem. Rev.*, **95**:735–758.

Low, G., and Matthews, R. W., 1990, Flow-injection determination of organic contaminants in water using and ultraviolet mediated titanium dioxide film reactor. *Analytica Chimica Acta,* **231**(1):13–20.

Malato, R. S., Richter, C., and Blanco, G. J., 1996, Photocatalytic degradation of industrial residual waters. *Solar Energy,* **56**:401–410.

Malato, S., Blanco, J., Richter, C., Curco, D., and Gimenez, J., 1997, Low-concentrating CPC collectors for photocatalytic water detoxification: comparison with a medium concentrating solar collector. *Wat. Sci. Tech.*, **35**(4):157–164.

Matthews, R. W., 1988, An adsorption water purifier with *in situ* photocatalytic regeneration. *J. Cat.* **113**:549–555.

Matthews, R. W., 1987a, Photooxidation of organic impurities in water using films of titanium dioxide, *J. Phys. Chem.* **91**(12):3328–3334.

Matthews, R. W., 1987b, Solar–electric water purification using photocatalytic oxidation with TiO_2 as a stationary phase, *Solar Energy*, **38**(6):405–413.

Matthews, R. W., 1991, Photooxidative degradation of colored organics in water using supported catalysts: TiO_2 on sand, *Wat. Res.*, **25:**1169–1176.

Matthews, R. W., 1993, Photocatalysis in water purification: possibilities, problems and prospects, in *Photocatalytic purification and treatment of water and air*, Ollis, D., and Al-Ekabi, H., eds., Elsevier, New York, pp. 121–133.

Matthews, R. W., and McEvoy, S. R., 1992, Destruction of phenol in water with sun sand, photocatalysis, *Solar Energy*, **49**(6):507–513.

Mehos, M. S., and Turchi, C. S., 1993, Field testing solar photocatalytic detoxification on TCE-contaminated groundwater. *Environ. Prog.* **12**:194–199.

Minero, C., Pelizzetti, E., Malato, S., and Blanco, J., 1996, Large solar plant photocatalytic water decontamination: effect of operational parameters, *Solar Energy*, **56**(5):421–428.

Mukherjee, P. S., and Ray, A. K., 1999, Major Challenges in the design of a large scale photocatalytic reactor for water treatment, *Chem. Eng. Tech.*, **22**(3):253–260.

Muradov, N. Z., 1994, Solar detoxification of nitroglycerine-contaminated water using immobilized titania. *Solar Energy,* **52**:283–288.

Nogueira, R. F. P., and Jardim, W. F., 1996, TiO_2–fixed–bed reactors for water decontamination using solar light, *Solar Energy*, **56**(5):471–477.

Obee, T., and Brown, R., 1995, TiO_2 photocatalysis indoor air applications: Effects of humidity, trace contaminant levels on the oxidation rates of formaldehyde, toluene, and 1,3-butadiene, *Environ. Sci. & Technol.,* **29**(5):1223–1231.

Ollis, D. F., Pelizzetti, E., and Serpone, N., 1989, Heterogeneous photocatalysis in the environment: Application to water purification, in *Photocatalysis: fundamentals and applications*, Serpone, N., and Pelizzetti, E., eds., Wiley Interscience, p. 603.

Ollis, D. F., 1991, Solar assisted photocatalysis for water purification, issues, data, questions, in *Photochemical conversion and storage of solar energy*, Pelizzetti, E., and Schiavello, M., eds., Kluwer Academic, Dordrecht, The Netherlands, pp. 593–622.

Ollis, D.F., 1993, Photoreactors for purification and decontamination of air. in *Photocatalytic purification and treatment for water and air,* Ollis D. and Al-Ekabi H., eds, Elsevier Science Ltd., pp 481–494.

CuuDuongThanCong.com https://fb.com/tailieudientucntt

Pacheco, J. E., Prairie, M. R., and Yellowhorse, L., 1993, Photocatalytic destruction of chlorinated solvents in water with solar energy. *J. Solar Energy Eng.*, **115**(3):123–129.

Parent, Y., Blake, D., Magrini–Bair, K., Lyons, C., Turchi, C., Watt, A., Wolfrum, E., and Prairie, M., 1996, Solar photocatalytic processes for the purification of water: State of development and barriers to commercialization, *Solar Energy*, **56**(5):429–437.

Peill, N. J., and Hoffmann, M. R., 1996, Chemical and physical characterization of a TiO_2 coated fiber optic cable reactor. *Environ. Sci. Tech.*, **30**:2806–2812.

Peill, N. J., and Hoffmann, M. R., 1997, Solar powered photocatalytic fiber optic cable reactor for waste stream remediation, *J. Solar Energy Eng.*, **119**:229–236.

Peill, N. J., and Hoffmann, M. R., 1998, Mathematical model of a photocatalytic fiber-optic cable reactor for heterogeneous photocatalysis. *Environ. Sci.& Tech.*, **32**:398–404.

Peill, N. J., and Hoffmann, M. R., 1995, Development and optimization of a TiO_2 coated fiber – optic cable reactor: Photocatalytic degradation of 4–chlorophenol, *Env. Sci. Tech.*, **29:**2974–2981.

Pelizzetti, E., Minero, C., and Carlin, V., 1993, Photoinduced degradation of atrazine over different metal oxides, *New J. Chem.*, **17**:315–319.

Pelizzetti, E., Minero, C., and Pramauro E., 1992, Photocatalytic process for destruction of organic chemicals, in *Chemical reactor technologies for environmentally safe reactors and products*, de Lasa, H., Dogu, G., and Ravella, A., eds., Kluwer Academic Publishers, Dordrecht, The Netherlands pp. 557–608.

Peral, J., Ollis, D., 1992, Heterogenous photocatalytic oxidation of gas phase organics for air purification: acetone, 1-butanol, butyraldehyde, formaldehyde, m-xylene oxidation, *J. of Catalysis*, **136**: 554–565

Pichat, P., 1988, Powder photocatalysts: Characterization by isotopic exchanges and photoconductivity, potentialities for metal recovery, catalyst preparation and water pollutant removal, in *Photocatalysis and the environment*, Schiavello, M., ed., Kluwer Academic Publishers, Dordrecht, The Netherlands, p. 399.

Pozzo, R. L., Giombi, J. L., Baltanas, M. A., and Cassano, A. E., 2000, Performance in a fluidized bed reactor of photocatalysts immobilized onto inert supports. *Catalysis Today*, **62**:175–187.

Pozzo, R., Baltanas, M. A., and Cassano, A. E., 1999, Towards a precise assessment of the performance of supported photocatalyst for water detoxification processes, *Catal. Today*, **54**:143–157.

Puma, G. L., and Yue, P. L., 1998, Laminar falling film slurry photocatalytic reactor. Part I-Model development. *Chem. Eng. Sci.*, **53**(16):2993–3006.

Puma, G. L., and Yue, P. L., 1999a, Enhanced photocatalysis in a pilot laminar falling film slurry reactor. *Ind. Eng. Chem. Res.*, 38(9):3246–3254.

Puma, G. L., and Yue, P. L., 1999b, Comparison of the effectiveness of photon-based oxidation processes in a pilot falling film photoreactor. *Environ. Sci. Tech.*, **33**(18):3210–3216.

Raupp, G. B., Nico, J. A., and Annangi, S., 1997, Two-flux radiation-field model for an annular packed photocatalytic oxidation reactor *AIChE J.* **43**:792–801.

Ray, A. K., 1998, Development of a new photocatalytic reactor for water purification. *Catal. Today*, **40**(1):73–83.

Ray, A. K., and Beenackers, A., 1997, Novel swirl-flow reactor for kinetic studies of semiconductor photocatalysis. *AIChE J.*, **43**(10):2571–2578.

Ray, A. K., and Beenackers, A., 1998a, Novel photocatalytic reactor for water purification. *AIChE J.*, **44**(2):477–483.

Ray, A. K., and Beenackers, A., 1998b, Development of a New Photocatalytic Reactor for water purification. *Catakysis Today*, **40**(1):73–83.

Reeves, P., Ohlhausen, R., and Sloan, D., 1992, Photocatalytic destruction of organic dyes in aqueous TiO_2 suspensions using concentrated simulated and natural solar energy. *Solar Energy*, **48**(6):413–420.

Robertson, M., and Henderson, R. B., 1990, Fluid Purification, USA Patent # 4892712.

Salaices, M., Serrano, B., and de Lasa, H., 2001, Photocatalytic conversion of organic pollutants. Extinction coefficients and quantum efficiencies. *Ind. & Eng. Chem. Res.*, **40**:5455–5464.

Sauer, M., and Ollis, D., 1994, Catalyst deactivation in gas-solid photocatalysis, *J. of Catal.*, **163**:215–217.

Say, J., Bonnecaze, R., Heller, A., Sitkiewitz, S., Heller, E., and Haugsja, P., 1990, Apparatus for photocatalytic fluid purification, *US Patent* No. 5,790,934.

Sczechowski, J G., Koval, C. A., and Noble, R. D., 1995b, Use of controlled periodic illumination for and improved method of photocatalysis and an improved reactor design *US Patent No.* 5,439,652.

Sczechowski, J. G., Koval, C. A., and Noble, R. D., 1993, Improved photoefficiencies for TiO_2 photocatalytic reactors through the use of controlled periodic illumination in: *Photocatalytic purification and treatment of water and air,* Ollis, D., Al-Ekabi, H., eds., Elsevier, New York, pp. 645–649.

CuuDuongThanCong.com https://fb.com/tailieudientucntt

Sczechowski, J. G., Koval, C. A., and Noble, R. D., 1995a, A taylor vortex reactor for heterogeneous photocatalysis, *Chem. Eng. Sci.*, **50**(20):3163–3173.

Serpone, N., Borgarello, E., Harris, R., Cahill, P., Borgarello, M., and Pelizzetti, E., 1986, Photocatalysis over TiO_2 supported on a glass substrate. *Solar Energy Materials*. 14(2):121–127.

Serrano, B., and de Lasa, H., 1997, Photocatalytic degradation of water organic pollutants. Kinetic modeling and energy efficiency. *Ind. Eng. Chem. Res.* **36**:4705–4711.

Shama, G., Peppiatt, C., and Biguzzi, M., 1996, A novel thin film photoreactor, *J. of Chem. Technol. and Biotechnol.*, **65**:56–64.

Smith, J. M., 1981, Chemical engineering kinetics, 3rd Ed. McGraw-Hill, New York, pp. 268–297.

Sopajaree, K., Qasim, S. A., Basak, S., and Rajeshwar, K., 1999a, Integrated flow–reactor membrane filtration system for heterogeneous photocatalysis. Part I. Experiments and modeling of a batch – recirculated photoreactor, *J. App. Electrochem.*, **29**(5):533–539.

Sopajaree, K., Qasim, S. A., Basak, S., and Rajeshwar, K., 1999b, Integrated flow–reactor membrane filtration system for heterogeneous photocatalysis. Part II. Experiments on the ultrafiltration unit and combined operation, *J. App. Electrochem.*, **29**(9):1111–1118.

Suzuki, K., 1993, Photocatalytic air purification on TiO_2 honeycomb support, in: *Photocatalytic purification and treatment of water and air*, Ollis, D. and Al–Ekabi, H., eds., Elsevier, New York, pp. 421–434.

Torimoto, T., Ito, S., and Kuwabata, S., 1996, Effects of adsorbents used as supports for titanium dioxide loading on photocatalytic degradation of propyzamide, *Environ. Sci. Tech.*, **30**(4):1275–1281.

Tunesi, S., and Anderson, M., 1991, Influence of chemisorption on the photodecomposition of salicylic acid and related compounds using suspended TiO_2 ceramic membranes, *J. Phys. Chem.*, **95**:3399–3405.

Turchi, C., Mehos, M., and Pacheco, J., 1993, Design issues for solar driven photocatalytic systems, in: *Photocatalytic purification and treatment of water and air*, Ollis, D. and Al–Ekabi, H., eds., Elsevier, New York, pp. 789–795.

Turchi, C. S., and Ollis, D., 1990, Photocatalytic degradation of organic water contaminants: mechanism involving hydroxil radical attack, *J. Catal.*, **122**:178–192.

Turchi, C. S., and Ollis, D. F., 1988, Photocatalytic reactor design: An example of mass transfer limitations with an immobilized catalyst, *J. Phys. Chem.*, **92**:6852–6853.

Uchida, H., Itoh, S., and Yoneyama, H., 1993, Photocatalytic degradation of propyzamide using TiO_2 supported on activated carbon. *Chem. Lett.*, **12**:1995–1998.

Valladares J., 1995, A new photocatalytic reactor for the photodegradation of organic pollutants in water. *Ph.D. Dissertation*, University of Western Ontario, London, Ontario, Ca.

vanWell, M, Dillert, R. H. G., and Bahnemann, D. W., 1997, A novel nonconcentrating reactor for solar water detoxification. *J. Solar Energy Eng.*, **119**:114–119.

Watts, R. J., Kong, S., and Lee, W., 1995, Sedimentation and reuse of titanium dioxide: applications to suspended photocatalyst reactors, *J. Environ. Eng.*, **121**:730–735.

Winterbottom, J. M., Kan, Z., Boyes, A. P., and Raymahasay, S., 1997, photocatalyzed oxidation of phenol in water using a cocurrent downflow contactor reactor (CDCR), *Environ. Prog.*, **16**(2):125–131.

Wyness, P., Klausner, J. F., and Goswami, D. Y., 1994a, Performance of non-concentrating solar photocatalytic oxidation reactors. Shallow pond configuration, *J. Solar Energy Eng.*, **116**:8–13.

Wyness, P., Klausner, J. F., and Goswami, D. Y., 1994b, Performance of non-concentrating solar pPhotocatalytic oxidation reactors. Part II: shallow ponds configuration, *J. Solar Energy Eng.*, **116**:2–7.

Yamazaki-Nishida, S., Read, H., Nagano, J., Jarosh, T., Eddy, C., Cervera-March, S., and Anderson, M., 1994, Gas phase photocatalytic degradation on TiO_2 pellets of volatile chlorinated compounds from a soil vapor extraction well, *J. of Soil Contam.*, **3**(4):363–378.

Yue, P., Khan, F., and Rizzuti, L., 1983, Photocatalytic ammonia synthesis in a fluidized bed reactor, *Chem. Eng. Sci.*, **38**:1893–1900.

Yue, P. L., 1985, Introduction to the modeling and design of photoreactors, in: *Photoelectrochemistry, photocatalysis and photoreactors*, Schiavello, M., ed., Reideal, p. 527.

Zhang, Y., Crittenden, J. C., and Hand, D. W., 1994, Fixed-bed photocatalysts for solar decontamination of water. *Environ. Sci. Tech.*, **28**:435–442.

Zhang, Y., Crittenden, J. C., and Hand, D. W., 1996, Destruction of organic compounds in water using supported photocatalysts. *J. Solar Energy Eng.* **118**:123–129.

CuuDuongThanCong.com https://fb.com/tailieudientucntt

3

Photocatalysts, Radiation Sources and Auxiliary Equipment for Photocatalysis

3.1. INTRODUCTION

A successful implementation of photocatalysis requires very efficient catalysts, illumination sources and reactors. In addition, auxiliary equipment for photocatalytic reactors is of major importance to assess the effectiveness of the reactor and of the kinetic reactor modeling. This requires proper characterization of the near-UV lamps used, in the case of artificially powered photocatalytic reactors, and the characterization of the photons absorbed in the photocatalytic reactor unit.

Potential photocatalysts, radiation sources and auxiliary equipment pertinent to the photocatalytic studies developed at the Chemical Reactor Engineering Centre (CREC) using Photo-CREC reactors, are reported in this chapter. The discussion about the auxiliary equipment can be relevant, however, to photocatalytic studies in general when other reactor configurations are used.

3.2. PHOTOCATALYSTS

A photocatalyst is defined as a substance that is activated by the absorption of a photon and helps accelerate a reaction, without being consumed (Fox, 1988). Factors that influence the photocatalyst activity include: structure, particle size, surface properties, preparation, spectral activation, resistance to mechanical stresses. Many of these factors were investigated by Peill and Hoffmann (1995).

Suri *et al.*, (1993) argue that photoconversion activity is a function of the catalyst properties, the organic species to be degraded and the experimental conditions. They showed that a catalyst having the highest activity with one compound might not necessarily be the best catalyst for the destruction of other organic species.

Metal oxide semiconductors have been found to be the most suitable photocatalysts given their photocorrosion resistance and their wide band gap energies (Fox and

CuuDuongThanCong.com https://fb.com/tailieudientucntt

TABLE 3.1. Band Gap Energies and Corresponding Radiation Wavelength Required for the Excitation of Various Semiconductors (Rajeshwar and Ibanez, 1997)

Semi conductor	Band gap energy (eV)	Wavelength (nm)
TiO_2 (rutile)	3.0	413
TiO_2 (anatase)	3.2	388
ZnO	3.2	388
ZnS	3.6	335
CdS	2.4	516
Fe_2O_3	2.3	539
WO_3	2.8	443

Dulay, 1993). Table 3.1 summarizes the band gap energies and the corresponding radiation wavelength required for the excitation of various semiconductors as reported by Rajeshwar and Ibanez (1997) and Hoffmann et al., (1995).

TiO_2 is the most active photocatalyst, followed by ZnO (Barbeni *et al*, 1985; Gautron *et al.*, 1983; Ibusuki and Takeuchi, 1986). Some of these materials are excited with visible light and this opens important prospects to photocatalysis.

TiO_2 is used extensively in both laboratory and pilot plant studies. Other oxides, such as ZrO_2, SnO_2, WO_2, and MoO_3 are much less active and, as a result, do not have the same application prospects as TiO_2 (Formenti and Teichner, 1979). Davydov *et al.*, (1999) indicate that proper ranking of photo catalysts requires careful uncoupling of the intrinsic catalyst properties from the reactor configuration and the radiation field.

Titanium dioxide is also called titanic anhydride, titanic acid anhydride, titanic oxide, titanium white, or titania. TiO_2 is a powder that varies in colour depending on its purity (passing from white to gray and black). It is prepared from ilmenite and rutile in two crystalline forms: anatase and rutile. When ilmenite is treated with sulfuric acid and the titanium sulfate is further processed, the resulting product is primarily in the anatase form. Raw rutile can be chlorinated and the titanium tetrachloride converted into the rutile form via vapor phase oxidation (Hawley, 1971). TiO_2 purity includes, among other factors, crystal size and porosity, both having a major influence on the catalytic activity (Ibusuki *et al.*, 1993).

TiO_2 is used as a white pigment in paints, paper, rubber, plastics and cosmetics. Titanium dioxide is widely used as a photocatalyst since it is not very expensive, has good thermal stability, is chemically and biologically inert, is non-toxic and is able to promote oxidation of organic compounds, including the inactivation of microorganisms (Mandelbaum *et al.*, 1999).

Anatase is the most popular TiO_2 crystalline form used in photocatalytic processes given its superior activity when compared to rutile, (Augugliaro *et al.*, 1988; Sclafani and Herrmann, 1996). Photons with wavelengths equal to or lesser than 380–388 nm are reported exciting the TiO_2. Anatase has wider band gap energy than rutile at similar conditions, 3.2 eV versus 3.0 eV (Bolton *et al.*, 1995; Sczechowski *et al.*, 1995; Suri *et al.*, 1993), also yielding reduced electron-hole recombination.

Recent studies on TiO_2 focus on its various forms (Yu *et al.*, 1998). TiO_2 particles can be loaded with metals and metal oxides such as vanadium oxide (Blanco *et al.*, 1996; Sanati *et al.*, 1991), platinum (Ait-Ichou *et al.*, 1985; Falconer and Magrini-Bair, 1998; Vorontsov *et al.*, 2000), manganese oxide (Gallardo-Amores *et al.*, 1999),

CuuDuongThanCong.com https://fb.com/tailieudientucntt

palladium (Ikeda *et al.*, 1997) and ruthenium (Beziat *et al.*, 1999). Metals on TiO_2 ease the separation of charges with electrons collected in metal particles (Ikeda *et al.*, 1997; Vorontsov *et al.*, 2000). Vanadia catalyst supported on rutile and anatase has been used for toluene photooxidation (Sanati et al., 1991) and toluene and xylene photoconversion (Blanco *et al.*, 1996).

Ibusuki *et al.*, (1993) showed that TiO_2 and activated carbon composites can have excellent activity for NO_x conversion due to the strong TiO_2 photocatalytic activity and activated carbon adsorption. These authors also claim that the addition of metal oxides such as Fe_2O_3, Co_3O_4 and NiO to the TiO_2-activated carbon composite catalyst noticeably increases the activity. As an option, Harada *et al.*, (1999) considered the impregnation of TiO_2 on activated carbon particles for isopropanol degradation in water. It was shown that there is no serious reduction of activated carbon adsorption due to the loading of titanium oxide particles.

In summary, TiO_2 or modified forms of TiO_2 are currently the materials with the highest prospects for photocatalytic reactors. It is expected that new photocatalysts in the near future may considerably help increase the utilization of visible light.

3.3. RADIATION SOURCES

The radiation source, ultraviolet (UV) radiation or more specifically near-ultraviolet radiation, is a very important ingredient of the photocatalytic process. Ultraviolet radiation refers to electromagnetic radiation in the 200–400 nm wavelength range. UVA covers from 315 to 400 nm, UVB from 280 to 315 nm and UVC from 200 to 280 nm.

Artificial UV lamps can power photocatalytic processes. The band gap of TiO_2 anatase is 3.2 eV and the irradiation portion that can participate in the photocatalytic reaction is the one below 388 nm.

Artificial UV sources are made of different metals including mercury, sodium, zinc/cadmium and rare gases (neon, argon). The mercury emission lines are usually in the desired range of energy for driving the photochemical reactions. Artificial UV lamps, as classified by Bolton *et al.*, (1995) (Table 3.2), can be grouped in low pressure mercury lamp, medium pressure mercury lamp and high pressure mercury lamp categories.

Solar light can also activate TiO_2 given that the TiO_2 activation spectrum overlaps with the solar spectrum (Nimlos *et al.*, 1993). Roughly 4%–5% of the sunlight reaching the earth's surface is in the 300–400 nm near-ultraviolet range and this portion of the solar spectrum can be used to power photocatalytic reactors (Bolton *et al.*, 1995;

TABLE 3.2. Artificial UV Light Sources as reported in Bolton *et al.* (1995)

Parameter	Low Pressure Mercury Lamp	Medium Pressure Mercury Lamp	High Pressure Mercury Lamp
Life time (h)	>5000	>2000	>3000
Output range	80% in a narrow range around 254 nm	Broad but not much below 250 nm	Strong below 250 nm
Energy Density	Low (~1 W/cm)	Moderate (~125 W/cm)	High (~250 W/cm)
Electrical energy to photon energy	High (~30%)	Moderate (~15% for 200–300 nm)	High (~30% for 200–300 nm)

CuuDuongThanCong.com https://fb.com/tailieudientucntt

Matthews, 1993; Wilkins and Blake, 1994). A drawback of solar energy, however, is its intermittency and variability with both factors being geographically dependant (Wilkins and Blake, 1994).

Solar energy cannot be used effectively for homogeneous photochemical processes since typical reagents such as H_2O_2 and O_3 do not significantly absorb radiation above 300 nm and none of the radiation received at the earth surface is below 300 nm (Bolton *et al.*, 1995). Therefore, the application of solar light is clearly favored in photocatalytic heterogeneous processes versus its application in homogenous photoreactors.

3.4. AUXILIARY EQUIPMENT

The evaluation of photocatalytic reactor performance is closely related to the continuous evaluation and reassessment of lamp operation since lamps experience decay with time of utilization. It is recommended that lamps be calibrated and re-recalibrated frequently to estimate their decay. In addition, it is advised to use some auxiliary equipment in performing this task: (a) a UVX digital radiometer, (b) a 4D Controls Ltd spectroradiometer, (c) the *Lamp Testing Unit* (LTU) developed by Serrano and de Lasa (1997), and (d) a set of tubular collimators for radiation transmission measurements.

3.4.1. UVX digital radiometer

The UVX digital radiometer measures the *total radiation flux,* reaching a circular 0.9-cm-diameter sensor cell (UVX-36) built in a rectangular encasement (8.2 × 5.0 × 2.3 cm). This instrument can detect UV intensities in the 1.0 10^{-7} to 2.0 10^{-2} W cm^{-2} range with an accuracy of ±5%. The UVX-36 sensor gives a response that is a function of the wavelength, as reported in Figure 3.1. This response is designed and calibrated to

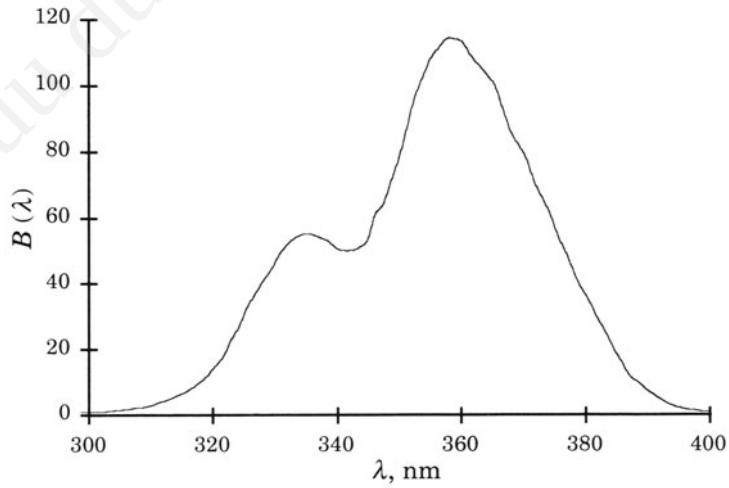

FIGURE 3.1. Spectral Response of the *UVX*-36 Sensor Cell. (Reprinted with permission of M. Salaices, PhD Dissertation, University of Western Ontario© 2002).

CuuDuongThanCong.com https://fb.com/tailieudientucntt

give a value of 1.00 at 365 nm in a line-type mercury arc source. In order to consider the decrease in sensor output with time of exposure, an extra *UVX*-36 sensor can be kept as a reference, using it briefly and only for sensor recalibration.

When measuring intensities for a phosphor-coated lamp, a correction factor is needed to obtain the true absolute reading. A correction factor can be calculated using the following relationship.

$$CF = \frac{\int_{\lambda_1}^{\lambda_2} A(\lambda)d\lambda}{\int_{\lambda_1}^{\lambda_2} A(\lambda)B(\lambda)d\lambda} \tag{3-1}$$

where CF is the correction factor, $A(\lambda)$ is the lamp emission spectrum, $B(\lambda)$ is the UVX spectral response normalized to 365 nm and λ is the radiation wavelength, nm.

Figure 3.2 reports typical radiative flux axial distributions in mW cm^{-2} for a black-light lamp (BL). The values were obtained using a UVX digital radiometer at 3.1 cm from the reactor axis.

3.4.2. 4D Controls Ltd Spectroradiometer

Alternatively, a 4D Controls Ltd spectroradiometer can be used for the measurement of both spectrometric fluxes and total radiation fluxes in the range of 10^{-8} to 50 W cm^{-2} nm^{-1}. This instrument covers a spectrum from low UVC (235 nm) up to the beginning of the visible blue light (470 nm), with a 0.5-nm-width spectral sampling.

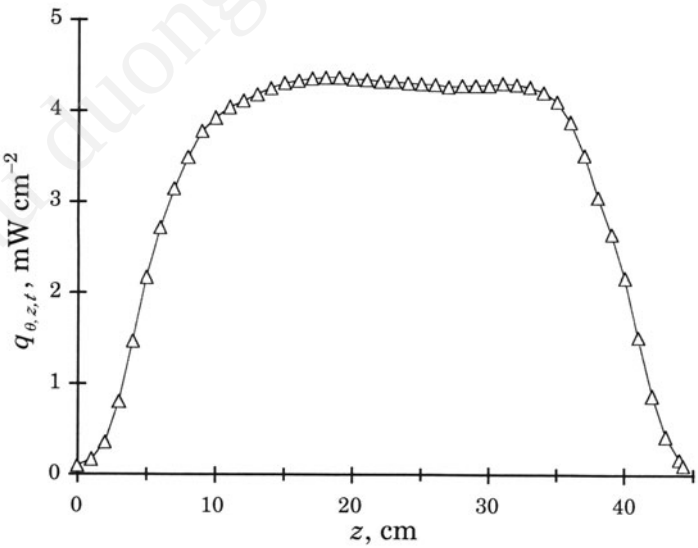

FIGURE 3.2. Typical BL lamp radiative flux axial distribution at 3.1 cm from the reactor axis. (Reprinted with permission from *Ind. Eng. Chem. Res.*, **40**(23), M. Salaices, B. Serrano and H.I. de Lasa, Photocatalytic conversion of organic pollutants: Extinction coefficients and quantum efficiencies, 5455–5464. Copyright 2001 American Chemical Society).

CuuDuongThanCong.com https://fb.com/tailieudientucntt

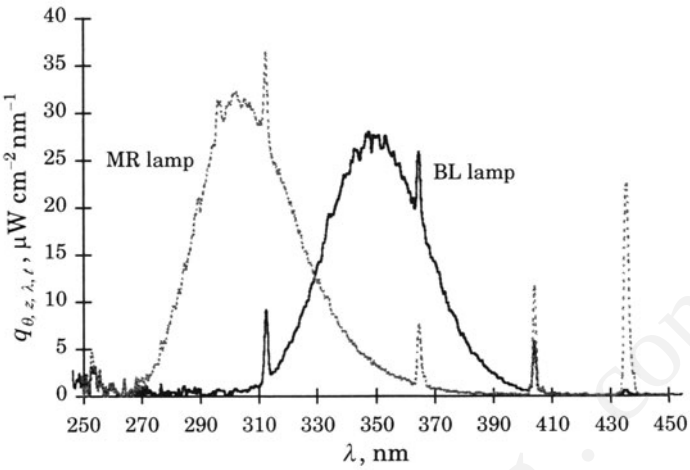

FIGURE 3.3. Typical radiative flux spectra of a medium range lamp (- -) and a BL lamp (_) (Reprinted with permission from *Ind. Eng. Chem. Res.*, **40**(23), M. Salaices, B. Serrano and H.I. de Lasa, Photocatalytic conversion of organic pollutants: Extinction coefficients and quantum efficiencies, 5455–5464. Copyright 2001 American Chemical Society).

The spectroradiometer is equipped with a rectangular sensor (11.8 × 6.9 × 3.2 cm) furnished with a circular (0.4-cm-diameter) UV-transparent sapphire entrance window. A 30-cm-length probe with a 0.25 cm-diameter fused-silica light guide was attached to the sensor. The sensor can be used with or without the probe.

Results can be displayed graphically in the spectroradiometric mode as a line or bar spectrum, or if the radiometric mode is chosen, as total radiation flux over the whole wavelength. Figure 3.3 illustrates the typical radiative flux spectra for two lamps. The spectra were obtained using the spectroradiometer in the line spectrum mode.

3.4.3. Lamp Calibration and the Lamp Testing Unit (LTU)

The LTU consists of a UV-opaque chamber, a lamp holder and a sensor holder rail. A schematic representation of the LTU with one digital *UVX* radiometer is presented in Figure 3.4. The near-UV lamp (365 nm peak) is placed in the lamp holder at a set distance from the detector. The LTU is designed to be flexible in accommodating different detectors.

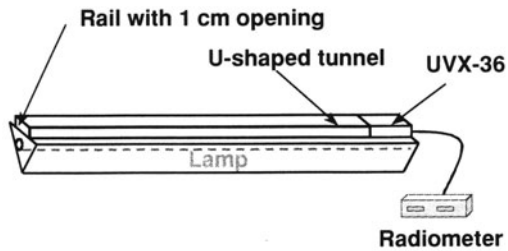

FIGURE 3.4. Schematic Representation of the Lamp-Testing Unit (LTU). (Reprinted with permission from *Ind. Eng. Chem. Res.*, **40**(23), M. Salaices, B. Serrano and H.I. de Lasa, Photocatalytic conversion of organic pollutants: Extinction coefficients and quantum efficiencies, 5455–5464. Copyright 2001 American Chemical Society).

CuuDuongThanCong.com https://fb.com/tailieudientucntt

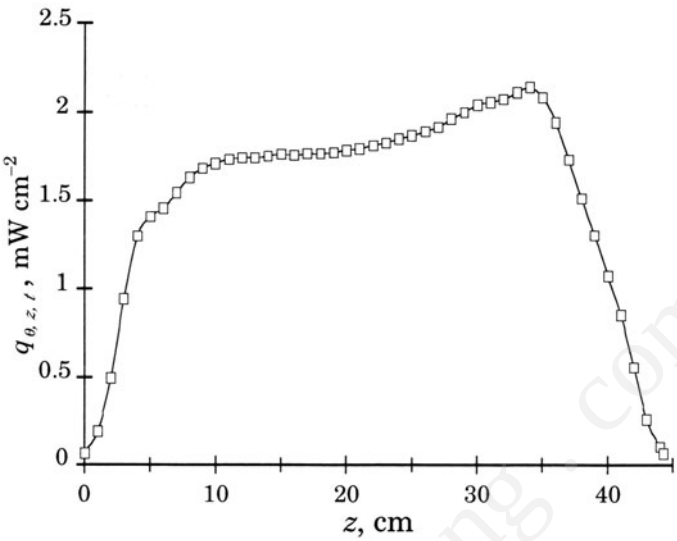

FIGURE 3.5. Typical asymmetrical radiative flux axial distribution of a BL lamp. (Reprinted with permission of M. Salaices, PhD Dissertation, University of Western Ontario©2002).

Radiometric measurements can be performed with the sensor cell facing the lamp through a 1-cm opening. The sensor is displaced along a rail placed at a set distance from the lamp axis. Radiometric measurements can also be performed rotating the lamp at several contour angles for fixed radial distances. Before each measurement, it is recommended that the lamps be warmed up for a period of 5 min to stabilize the lamp's emission.

Most of the characterized BL lamps show quite symmetrical radiation distributions like that showed in Figure 3.2. However, a few types of lamps can present asymmetric radiation distributions along the axial coordinate after more than 1000 hours of operation. Figure 3.5 illustrates a typical asymmetrical axial distribution of a BL lamp used for 1200 hours.

Thus, special care must be taken in order to use lamps that display symmetrical radiation distribution in the experiments.

The integration of the measured light using an imaginary cylindrical surface reveals the total light emitted by the lamp. Using this method, it can be observed that the intensity emitted by the lamp changes as much as 50% in 1000 h of operation. It has been found that frequent lamp recalibrations are required for a better assessment of light energy emitted by the lamp, a quite significant factor when calculating energy efficiency.

This method of measuring the irradiation reaching the reactor is a physical technique and avoids the use of indirect methods, as the case of actinometry. Actinometry only permits the evaluation of photons reaching the slurry, but does not give more detailed information about the irradiation distribution in the reactor.

3.4.4. Tubular Collimator for Radiation Transmission Measurements

When measuring the radiation transmission in slurry-type photocatalytic reactors, the use of collimators made of different materials is highly recommended. UV-opaque and inner-polished aluminum collimators can be attached to the reactor windows to limit

CuuDuongThanCong.com https://fb.com/tailieudientucntt

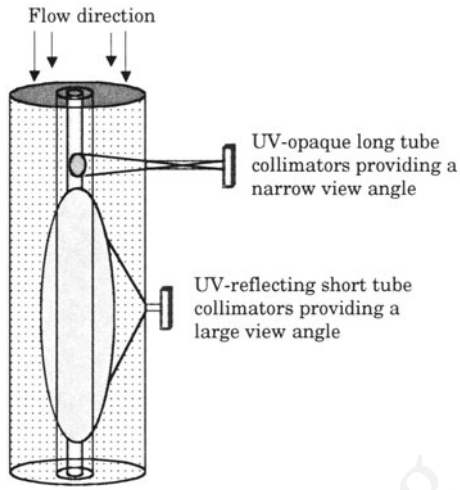

FIGURE 3.6. Virtual detection cones representing the angle of included rays for UV-opaque long tube and UV-reflecting short tube collimators.

the amount and the angle of the radiation being measured. The collimators also fix the position between the sensor and the reactor.

UV-opaque collimators were employed by Salaices el al., (2002) to determine the extinction coefficients since their non-reflective surface minimizes the forward-scattering radiation reaching the detector. Figure 3.6 represents the virtual detection cones of included rays for two kinds of tubular collimators.

Several collimator sizes discriminate between radiations reaching the sensor at different incident angles. Inner-polished aluminum collimators of several sizes can be used to determine the effective extinction coefficients and to assess the total radiation transmission through the slurry at the outer reactor wall (Figure 3.7).

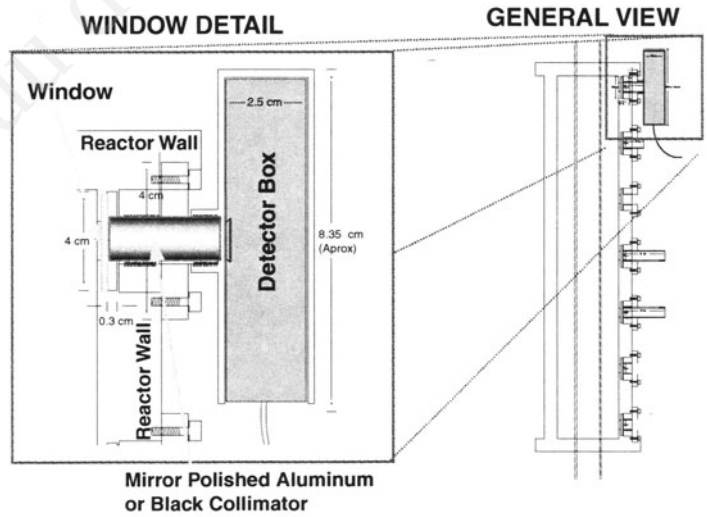

FIGURE 3.7. Detailed view of the sensor collimator arrangement. (Reprinted with permission of M. Salaices, PhD Dissertation, University of Western Ontario© 2002).

CuuDuongThanCong.com https://fb.com/tailieudientucntt

TABLE 3.3. Dimensions of Collimators and Resultant Sensor Radial Positions

Collimator	Dimensions (cm)	Sensor distance to lamp (cm)	View angle (deg)
UV-opaque 1	2.3 × 1.0	7.6	44.4
UV-opaque 2	4.6 × 1.0	12.2	23.8
UV-opaque 3	9.2 × 1.0	16.8	12.2
Polished aluminum 1	2.3 × 1.0	7.6	160
Polished aluminum 2	4.6 × 1.0	12.2	160
Polished aluminum 3	9.2 × 1.0	16.8	160

Table 3.3 reports the dimensions, the resultant radial positions of the sensor and the view angles for each of the collimators. The length of the collimators has to be chosen according to a number of considerations: the outer reactor wall thickness, the window thickness, and the sensor encasement. On these bases, a 2.3 cm-long collimator was adopted (Salaices, 2002). Other collimators were chosen having lengths two and four times greater than 2.3 cm. Lengths in excess of these were not used since radiation readings are too small over distances longer than 20 cm.

3.5. PARTICLE AGGLOMERATION MEASUREMENTS

Particle agglomeration is a matter of concern when using TiO_2 particles in the nano-scale range. TiO_2 tends to form agglomerates, which determine the conditions of light scattering in the slurry medium. A typical example of agglomeration is provided in Figure 3.8.

Particle agglomerate sizes can be determined using a laser diffraction particle size analyzer, such as a Brinkmann PSA-2010. With this instrument, the principle of particle size measurement is based on various light scattering angles generated by particles of

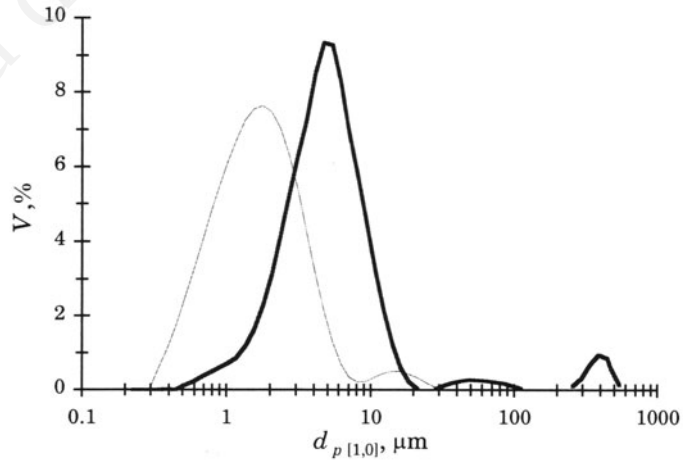

FIGURE 3.8. Particle size distribution change for a Hombikat UV-100: After sonication (—) and after one hour mixing in the reactor (—). (Reprinted with permission of M. Salices, PhD Dissertation, University of Western Ontario© 2002).

CuuDuongThanCong.com https://fb.com/tailieudientucntt

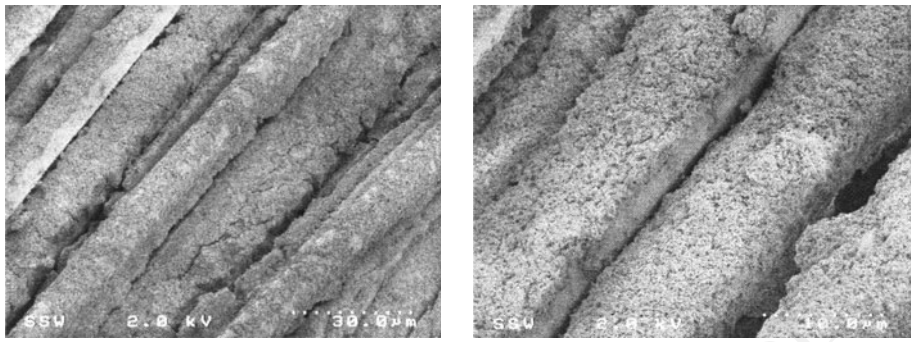

FIGURE 3.9. SEM micrographs showing the distribution of Degussa P25 particles for the 4.8–5.6-wt% loading (Reprinted from *Appl. Catal. B: Environ.*, **1011**, H. Ibrahim and H.I. de Lasa, Photocatalytic conversion of air borne pollutants: Effect of catalyst type and catalyst loading on a novel Photo-CREC-Air unit, 1–13, Copyright 2002, with permission from Elsevier).

different sizes. When this technique is applied, samples from the reactor are obtained during the radiation transmission measurements. This procedure ensures that representative agglomerate dimensions are considered for both the reaction and the light transmission modeling. Suspension samples are taken at catalyst concentrations allowing 50% radiation transmission in order to analyze the samples without diluting them in the particle size analyzer. Moderate stirring is also used to keep the catalyst in suspension during the particle size analyses.

Particle agglomeration and particle layering have also been identified as significant phenomena in the photocatalytic conversion of air pollutants. SEM micrographs provides very useful information when observing these occurrences. In the Photo-CREC-Air unit, SEM micrographs revealed particle layering and non-uniform distribution of catalyst particles with catalyst particles forming agglomerates.

For Hombikat UV-100, increasing the number of particles leads to a reduced number of larger-particle agglomerates (Ibrahim and de Lasa, 2002). The overall effect, as confirmed using SEM, shows that the "total irradiated catalyst" remains close to constant when the catalyst loading is increased. This phenomenon explains the close to constant photo degradation rate.

For Degussa P25, SEMs (Figure 3.9) show particle distribution on the mesh fibers forming a near-uniform layer, with a thickness that increases with the catalyst loading (Ibrahim and de Lasa, 2002). The increase in TiO_2 loading produces more rapid rates of UV photon absorption and consequently, higher photoconversion rates up to a limit called "critical thickness". Once the formed layers reach a critical thickness, there is no further enhancement of photons absorbed and the photo conversion rate becomes independent of the catalyst loading.

3.6. PHOTOCONVERSION EXPERIMENTS

There are a number of recommended model pollutants for photoconversion experiments in water, as shown using Photo-CREC-Water I and II reactors (refer to sections 2.10.1 and 2.10.2). Phenol dissolves well in water and is not stripped significantly by the airflow, as proven experimentally by Salaices et al (2002). Methylene blue has strong

CuuDuongThanCong.com https://fb.com/tailieudientucntt

adsorption on many surfaces, good resistance to light degradation and is a commonly used dye. Although phenol has been studied extensively on a laboratory scale, there remain several issues that need special attention, such as the detection and quantification of intermediates. Alternatively, the abundance of experimental data makes the use of this model contaminant very valuable for comparison purposes. Air used as the oxygen source and the airflow rate is such that it provides oxygen well in excess of the amount required to fully oxidize the model pollutant. In the case of slurry reactors, the airflow is typically fed using air spargers to provide adequate re-suspension of the TiO_2 particles. An airflow that is too high may negatively affect the pump performance, due to gas bubble entrainment and pump cavitation.

It is recommended to monitor a number of parameters such as temperature, reaction time, pH, and radiation transmission conditions during the progress of the photocatalytic reaction.

The concentration change of unreacted phenol can be followed via gas chromatography (e.g. HP 5890A), a Waters Breeze high performance liquid chromatograph (HPLC) and a Carry 50-UV-Vis spectrophotometer. Regarding the overall photoconversion for phenol and methylene blue, it can be measured using a Shimadzu TOC-5050 total organic carbon analyzer (TOC).

Typical HPLC analysis of phenol photoconversion involves a 1 mL sample. This sample is injected into the HPLC unit. A volume of 50 μL is carried through the C_{18} column by a 1.0 mL min^{-1} flow of a 33 % methanol, 77 % water (v/v) mobile phase solution. Species are separated in the column on the basis of their affinity to the non-polar stationary and mobile phases. The detection of the separated components can be performed in a dual λ absorbance detector at 255, 270, 275, and 290 nm wavelengths. These radiation wavelengths are selected according to the absorbance spectra of each of the possible phenol photodegradation intermediates. Following this, the detector output is processed and displayed as a chromatograph on a personal computer. The nature and quantification of each of the separated compounds in the sample is achieved by the use of standards. Using these standards (e.g. phenol) a linear relationship between the phenol concentration in ppm-C and the peak area (V-s) is established.

Additionally, a Carry 50 spectrophotometer can be used for the quantification of the concentration of unreacted phenol. This is particularly true in cases where it can be ensured that the amounts of intermediate chemical species are negligible. The Carry 50 instrument allows the measurement of the relative absorbance of the sample. The Carry 50 incorporates a Xenon flashing tube with a maximum scan wavelength range of 190–1100 nm and a minimum irradiation effect on photosensitive samples. A 4 mL far-UV optical cell is used to place the sample in the spectrophotometer. The sample is scanned for absorbance in the wavelength range of 250–500 nm. Before each measurement, the instrument is zeroed at a wavelength of 500 nm with de-ionized water. A linear relationship is established for the phenol concentrations range used in the 250–290 nm absorbance spectral area. A similar linear relationship is established for the methylene blue concentration range employed in the 500–700 nm spectral area.

The overall reaction rate can also be followed using a Total Organic Carbon Analyzer (e.g. Shimadzu 5050) with an autosampler ASI 5000. The TOC analysis is based on the oxidation of the sample in a combustion chamber heated at 680° using platinum as a catalyst. In this instrument, the total sample carbon (TC) and the total inorganic carbon (IC) content are measured using different analytical methods. Vials with

CuuDuongThanCong.com https://fb.com/tailieudientucntt

4 mL-volumes were used to place the samples in the autosampler. From that amount, a volume between 13 to 50 μL, is injected automatically to the TOC analyzer depending on the calibration curve selected. The organic compounds in the sample are oxidized in the combustion chamber to CO_2, whereas the inorganic carbon is converted to CO_2 using a 25% (v/v) phosphoric acid solution. The CO_2 is then detected in a non-dispersive infrared gas analyzer. The TOC and IC contents are determined using calibration curves obtained prior to the analysis using reagent grade potassium hydrogen phthalate and sodium hydrogen carbonate standards. Finally, the TOC concentration is calculated as the difference between the TC and the IC concentrations.

For photocatalytic conversion of model pollutants in air (refer to section 2.10.5), model pollutants such as iso-propanol, acetone, and acetaldehyde are recommended to be used. Acetone and iso-propanol injections of 40, 50, and 60μl of the liquid pollutant can be employed in the 14.7 L Photo-CREC-Air reactor. For acetaldehyde 30, 40, and 50 μl liquid injections can be used to get the desired initial pollutant concentrations. A gas chromatograph (HP 5890) equipped with a HP-3393A integrator, a TCD and a Poropak Q packed column are adequate to identify and quantify chemical species, including product intermediates and carbon dioxide. Examples of this type of photocatalytic experiments for the photoconversion of model pollutants in air are provided in Chapter VIII.

3.7. CONCLUSIONS

Significant topics covered in the present chapter are:

a) TiO_2 is currently the most popular material for photocatalytic processes.
b) Radiations sources, including near-UV lamps and solar light are the typical radiation sources used to excite the TiO_2.
c) An LTU is recommended for the characterization of the lamp irradiation and for the assessment of the lamp irradiation decay during its utilization.
d) Several equipment components, which involve aluminum and UV-opaque tube collimators operating in conjunction with two types of radiometers can be used in the assessment of photon absorption and photon scattering in photocatalytic reactor units.
e) Particle size analyzers and SEM micrographs can be employed to establish TiO_2 particle agglomeration.
f) Analytical equipments (GC, HPLC, TOC.) are necessary tools to quantify various chemical species, reactants and intermediates involved in the photocatalytic reaction network.

NOTATION

Symbols

CF	Correction factor, equation (3–1)	
$A(\lambda)$	Lamp emission spectrum	W cm^{-2}
$B(\lambda)$	UVX spectral response normalized to 365 nm	

CuuDuongThanCong.com https://fb.com/tailieudientucntt

Greek Letters

λ	Radiation wavelength	nm

REFERENCES

Ait-Ichou, I., Formenti, M., Pommier, B., and Teichner, S., 1985, Photocatalytic dehydrogenation of isopropanol on Pt/TiO_2 Catalysts, *J. Catal.*, **91**:293–307.

Augugliaro, V., Palmisano, L., Sclafani, A., Minero, C., and Pelizzetti, E., 1988, Photocatalytic degradation of phenol in aqueous titanium dioxide dispersions, *Toxicol. Environ. Chem.*, **16**(2):89–109.

Barbeni, M., Pramauro, E., Pelizzetti, E., Borgarello, E., and Serpone, N., 1985, Photodegradation of pentachlorophenol catalyzed by semiconductor particles. *Chemosphere*, **14(2)**:195–208.

Beziat, J., Brsson, M., Gallezot, P., and Durecu, S., 1999, Catalytic wet air oxidation of carboxylic acids on TiO_2-supported ruthenium catalysts, J. Catal., **18**:129–135.

Blanco, J., Avila, P., Bahamonde, A., Alvarez, E., Sanchez, B., and Romero, M., 1996, Photocatalytic destruction of toluene and xylene at gas phase on a titanium based monolithic catalyst, *Catal. Today*, **29**: 437–442.

Bolton, J. R., Safarzadeh-Amiri, A., Cater, S. R., 1995, The detoxification of waste water streams using solar and artificial *UV* light sources, in: *Alternative Fuels and the Environment,* F. S. Sterret, *ed., Lewish Publishers, Boca Raton, FL,* pp. 187–192.

Davydov, L., Smirniotis, G., and Pratsinis, E., 1999, Novel differential reactor for the measurement of overall quantum yields, *Ind.Eng. Chem. Res.*, **38**(4):1376–1383.

Falconer, J., and K. Magrini-Bair, 1998, Photocatalytic and thermal oxidation of acetaldehydeon Pt/TiO_2, *J. Catal.*, **179**:171–178.

Formenti, M., and Teichner, S., 1979, Heterogeneous photocatalysis, *J. Catal.*, **87**:87–106.

Fox, M.A., and Dulay, M.T., 1993, Heterogeneous photocatalysis, *Chem. Rev.*, **93**:341–357.

Fox, M., 1988, Photocatalytic oxidation of organic substances, in: *Photocatalysis and Environment: Trends and Applications*, M. Schiavello, ed., Kluwer Academic Publishers, New York, pp. 445–467.

Gallardo-Amores J., Armaroli, T., Ramis, G., Finocchio, E., and Busca, G., 1999, A study of anatase-supported Mn oxide as catalyst for 2-propanol oxidation, *Appl. Catal. B: Environ.*, **22**:249–259.

Gautron, J., Lemasson, P., Poumellec, B., and Marucco, J., 1983, Photoelectrochemical study of (Ti,V)O_2 and (Ti, Nb)O_2 alloys, *Solar Ener. Mat.*, **9**:101–111.

Harada, M., Honda, M., Yamashita, H., and Anpo, M., 1999, Preparation of titanium oxide photocatalysis loaded on activated carbon and their photocatalytic reactivity for the degradation of 2-propanol diluted in water, *Res. on Chem. Interm.*, **25**(8):757–768.

Hawley, G., 1971, The condensed chemical dictionary (8^{th} edition), revised, Litton Educational Publishing Inc.,Toronto.

Hoffmann, M., Martin, S., Choi, W., and Bahnemann, D., 1995, Environmental applications of semiconductor photocatalysis, *Chem. Rev.* **95**(1):69–96.

Ibrahim H. and de Lasa H., 2002, Photo-catalytic conversion of air borne pollutants. Effect of catalyst type and ctalyst loading a a novel Phot-CREC-air unit. *Applied Catalysis B: Environmental* **1011**: 1–13

Ibusuki, T., and Takeuchi, K., 1986, Toluene oxidation on UV irradiated titanium dioxide with and without O_2, N_2 or H_2O at ambient temperature, *Atmos. Environ.,* **20**(9):1711–1715.

Ibusuki, T., Kutsuna, S., and Takeuchi, K., 1993, Removal of low concentration air pollutants through photoassisted heterogeneous catalysis, in: Photocatalytic *purification and treatment of water and air,* Ollis, D., and Al-ekabi, H., eds., Elsevier, pp:375–386.

Ikeda, K., Sakai, H., Baba, R., Hashimoto, K., and Fujishima, A., 1997, Photocatalytic reactions involving radical chain reactions using microelectrodes, *J. Phys. Chem. B,* **101**:2617–2620.

Mandelbaum, P., Regazzoni, A., Belsa, M., and Bilmes, S., 1999, Photo-electro-oxidation of alcohol on titanium dioxide thin film electrodes, *J. Phys. Chem. B,* **103**(26):5505–5511.

Matthews, R.W., 1993, Photocatalysis in water purification: Possibilities, problems and prospects, in Photocatalytic *purification and treatment of water and air*, Ollis, D., and Al–Ekabi, H., eds., Elsevier, pp. 121–133.

CuuDuongThanCong.com https://fb.com/tailieudientucntt

Nimlos, M., Jacoby, W., Blake, D., and Milne, T., 1993, Direct mass spectrometric studies of the destruction of hazardous wastes. 2-Gas phase photo-catalytic oxidation of trichloroethylene over TiO_2: Products and mechanisms, *Environ. Sci. & Technol.*, **27**(4):732–740.

Peill, N., and Hoffmann, M., 1995, Development and optimization of a TiO_2 coated fiber optic cable reactor: Photocatalytic degradation of 4-chlorophenol, *Environ. Sci. & Technol.*, **29**:2974–2981.

Rajeshwar, K., and Ibanez, J., 1997, Environmental electrochemistry, fundamentals and fundaments in pollution abatement, Academic Press Inc., San Diego.

Salaices, M., Serrano, B., de Lasa, H., 2001, Photocatalytic conversion of organic pollutants. Extinction coefficients and quantum efficiencies, *Ind. Eng. Chem. Res.*, **40**:5455–5464.

Salaices M., 2002, Photocatalysis in Slurry Reactors: Radiation, Transmission and Kinetic Modeling. PhD Dissertation, University of Western Ontario.

Salaices, M., Serrano, B., de Lasa H., 2002, Experimental evaluation of photon absorption in an aqueous TiO_2 slurry reactor, *Chem. Eng. J.*, **90**:219–229.

Sanati, M., Wallenberg, R., Andersson, A., Jasen, S., and Tu, Y., 1991, Vanadia catalyst on anatase, rutile and TiO_2(B) for the ammoxidation of toluene: An ESR and high resolution electro microscopy characterization, *J. Catal.*,**132**:128–144.

Sclafani, A., and Herrmann, J., 1996, Comparison of photoelectronic and photocatalitic activities of various anatase and rutile forms of titania in pure liquid organic phases in aqueous solutions, *The J. of Phys. Chem.,* **100**:13655–13661.

Sczechowski, J., Koval. C., and Noble, R., 1995, A Taylor vortex reactor for heterogeneous photocatalysis, *Chem. Eng. Sci.,* **50**(20):3163–3173.

Serrano, B., and de Lasa, H., 1997, Photocatalytic degradation of organic pollutants. Kinetic modelling and energy efficiency. *Ind. Eng. Chem. Res.* **36**:4705–4711.

Suri R., Liu, J., Hand, D., Crittenden, J., Perram, D., and Mullims, M., 1993, Heterogeneous photocatalytic oxidation of hazardous organic contaminants in water, *Water Environ. Res.,* **65**(5):665–673.

Vorontsov, A. V., Stoyanova, I. V., and Kozlov, D. V., 2000, Kinetics of the photocatalytic oxidation of gaseous acetone over platinized titanium dioxide. *J. Catal.,* **189**(2):360–369.

Wilkins, F., and Blake, D., 1994, Use solar energy to drive chemical processes, *Chem. Eng. Prog.*, **90**:41–49.

Yu, J., Lin, J., and Kwok, R., 1998, $Ti_{1-x}Zr_xO_2$ solid solutions for the photocatalytic degradation of acetone in air, *The J. of Phys. Chem. B,* **102:**5094–5098.

cuu duong than cong . com

CuuDuongThanCong.com https://fb.com/tailieudientucntt

4

The Irradiation Field in Photocatalytic Reactors

4.1. MACROSCOPIC ENERGY BALANCES AND EXTINCTION COEFFICIENTS

The evaluation of absorption photon rates in slurry reactors is a rather challenging task since light can experience a combination of reflection, scattering and absorption in the TiO_2 particle suspension.

4.1.1. Determination of Absorption of Radiation

Several approaches with different degrees of complexity are reported in the technical literature to estimate the radiation distribution and consequently the light absorption in slurry reactors.

a) *Measurements at the Inlet Boundary*. This approach relies on radiative flux radiometric or actinometric measurements performed in the near reactor wall region. This method assumes that all the radiation entering the reactor is fully absorbed inside the heterogeneous medium. This approach does not consider heterogeneous medium light scattering and therefore it only provides an estimation of the upper limit of the absorption of radiation (Matthews and McEvoy, 1992; Pruden and Ollis, 1983; Turchi and Ollis, 1989).

b) *Homogeneous Actinometry*. This method makes use of homogeneous photochemistry to evaluate the radiation absorbed in the entire reactor volume. Using this approach, the photocatalyst is removed and irradiation is evaluated via homogeneous actinometry using a liquid phase free of TiO_2 particles. This is equivalent to neglecting the particle radiation scattering in the evaluation of light absorption (Bahnemann et al., 1991; Mills and Hoffmann, 1993).

c) *Partial Application of the Radiation Transfer Equation (RTE)*. This is a more complex method that employs the Beer-Lambert equation with true absorption and scattering coefficients and a radiation model for the source to estimate the amount of light absorbed in the heterogeneous medium. True extinction

CuuDuongThanCong.com https://fb.com/tailieudientucntt

coefficients are determined from special spectrophotometric measurements. This approach tends to underestimate the light absorption since the radiation scattering by the semiconductor particles is included as radiation losses (Brucato and Rizzuti, 1997a and 1997b; Martín et al., 1996a and 1996b).

d) *Radiation Balance and Measurements at the Outlet Reactor Boundaries*. Using this approach, the light absorption is determined via the Beer-Lambert equation for the media with apparent or effective extinction coefficients obtained via spectroscopic measurements. A combination of homogeneous actinometry and photodetectors, placed at the reactor walls, is used to measure exiting radiation at the system boundaries (Brandi et al., 2000). On this basis, a radiation balance is performed considering the outer scattered radiation, the incoming radiation and the radiation source. This procedure considers averaged values of radiation absorption and of radiation transmission losses (Augugliaro et al., 1991, 1995; Palmisano et al., 1993; Salaices et al., 2001, 2002; Schiavello et al., 1991).

e) *Complete Application of the RTE*. This is the most complex methodology. It relies on the use of the RTE and on assumptions for the modeling of radiation scattering (Brandi et al., 2000; Cassano et al., 1995). One of these assumptions is the phase function for suspended media. This phase function contains information about light scattering, with respect to the radiation reaching the particles. In this respect, several authors have adopted a diffuse reflection phase function for TiO_2 irregular non-transparent particles (Alfano et al., 1994; Brandi et al., 1996 and 1999; Cabrera et al., 1994 and 1996; Cassano et al., 1995; Pasquali et al., 1996; Romero et al., 1997).

In summary, the current methods for the measurement of radiation absorption lead to either simple approaches that tend to overestimate the radiation absorption based on broad assumptions or more complex approaches, that tend to underestimate the absorption of radiation while giving local information about the energy absorbed.

4.2. DETERMINATION OF ABSORPTION OF RADIATION IN PHOTO-CREC WATER-II REACTOR

The determination of the radiation absorption can be accomplished in a Photo-CREC Water-II Reactor. An experimental method for the determination of the rate of photon absorption is described in detail in this section. This experimental method corresponds to a semi-empirical technique of moderate complexity that combines spectroscopic measurements with modeling to obtain sufficient information for the determination of the radiation field distribution in photocatalytic reactors. The radiation absorbed is determined by the use of the Beer-Lambert equation with effective extinction coefficients obtained from spectroscopic measurements. A physical interpretation of these coefficients is also provided later in this chapter.

Radiation measurements are taken at several axial positions in Photo-CREC Water-II using UV-opaque collimators and UV-reflecting collimators. These collimators allow (Chapter III) the determination of average values of the radiation transmission in the

CuuDuongThanCong.com https://fb.com/tailieudientucntt

system. A radiation balance is performed subtracting the exiting scattering radiation from the incoming radiation. Using a radiation source model, the radiation field distribution is determined for both an empty reactor and a slurry-filled reactor. The above-described technique was found to be effective for several TiO_2 powders having different particle size and agglomerate size (Salaices et al, 2002).

Using this methodology, it was shown that the forward scattered radiation leaving the reactor can be represented by the addition of two exponential decay functions accounting for the total radiation transmission and the non-scattered radiation transmission. These two exponentials are functions of the particle concentration and the extinction coefficients, with the latter being strongly affected by the particle agglomerate size and the radiation wavelength.

4.2.1. Radiation Transmission Modeling

The rate of absorption of photons can be determined through a modeling process (Figure 4.1), which involves the application of a macroscopic radiation balance to a control reactor volume containing the slurried catalyst

$$P_a(t) = P_i(t) - P_t(t) - P_{bs}(t) \tag{4-1}$$

where $P_a(t)$ is the rate of absorption of photons, einstein s^{-1}; $P_i(t)$ is the rate of photons reaching the inner reactor surface, einstein s^{-1}; $P_{bs}(t)$ is the rate of back-scattered photons exiting the system, einstein s^{-1}; $P_t(t)$ is the rate of transmission of photons, einstein s^{-1}; and t is time, s.

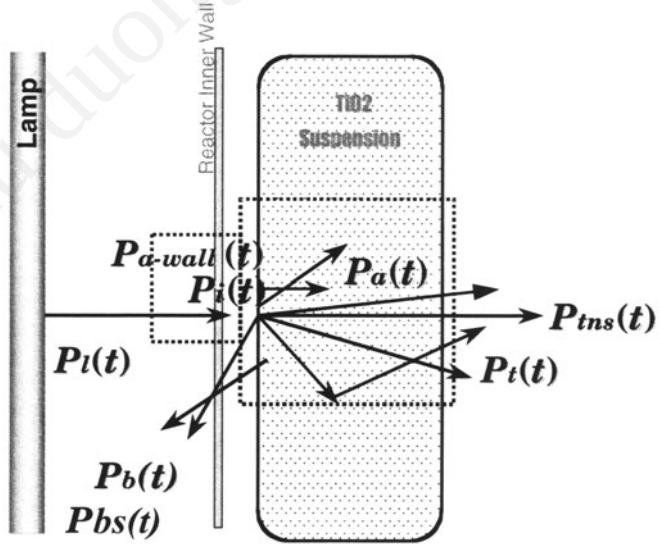

FIGURE 4.1. Macroscopic radiation balances around the catalyst suspension and the reactor inner wall. (Reprinted from *Chem. Eng. Sci.*, **59**, M. Salaices, B. Serrano and H.I. de Lasa, Photocatalytic conversion of phenolic compounds in slurry reactors, 3-15, Copyright 2004 with permission from Elsevier).

CuuDuongThanCong.com https://fb.com/tailieudientucntt

The various rates involved in the right side of equation (4-1) can be calculated as follows:

a) $P_i(t)$ can be estimated from the difference between the rate of emission of photons by the lamp, $P_l(t)$, and the rate of absorption of photons by the inner glass tube wall, $P_{a-wall}(t)$.

$$P_i(t) = P_l(t) - P_{a-wall}(t) \tag{4-2}$$

with $P_l(t)$ equal to:

$$P_l(t) = \frac{\bar{\lambda}}{hc} \int_{\lambda_1}^{\lambda_2} \int_0^{\infty} \int_0^{2\pi} q_{\theta,z,\lambda,t}\, r d\theta dz d\lambda \tag{4-3}$$

where $q_{\theta,z,\lambda,t}$ is the radiative flux, J s^{-1} m^{-3}; is the radiation wavelength, m; r is the radial coordinate, m; z is the axial coordinate, m; h is Planck's constant, J s; and c is the speed of light, m s^{-1}. The parameter $q_{\theta,z,\lambda,t}$ can be obtained from spectrometric measurements of the radiation emission by the lamp. Note that $P_{a-wall}(t)$ can be determined by spectroscopic measurements of inner glass tube transparency.

b) $P_t(t)$ or the rate of transmission of photons can be measured in the Photo-CREC Water-II reactor at each of the window positions using the UV-reflecting collimators.

c) $P_{bs}(t)$ can be approximated by the difference between $P_i(t)$ and $P_t(t)$ when the catalyst mass concentration approaches zero ($P_t(t)|_{C\to 0^+}$) (Augugliaro et al., 1991; Schiavello et al., 1991).

$$P_{bs}(t) = P_i(t) - P_t(t)|_{C\to 0^+} \tag{4-4}$$

d) The rate of photon emission by the lamp, which is a function of the lamp usage time, can be related to the rate of photons that the lamp would emit, W_N, based on its nominal power

$$W_l(t) = W_N \eta(t) \tag{4-5}$$

where $\eta(t)$ is the lamp efficiency which accounts for the initial lamp efficiency and its decay with time.

e) $P_t(t)$ can be represented as the addition of the non-scattered radiation transmission and the forward-scattered radiation transmission as

$$P_t(t) = P_{fs}(t) + P_{tns}(t) \tag{4-6}$$

where $P_{fs}(t)$ can be estimated from the difference between the measured radiation using the shortest UV-reflecting collimator (No. 1 in Table 3.3) and that obtained by using the longest UV-opaque collimator (No. 3 in Table 3.3). It has to be stressed that the UV-reflecting collimators account for the combined non-scattered radiation transmission and forward-scattered radiation transmission

CuuDuongThanCong.com https://fb.com/tailieudientucntt

while the UV-opaque tubes account only for the non-scattered radiation transmission.

Thus, from equation (4-6) it results

$$P_{fs}(t) = P_t(t) - P_{tns}(t) \tag{4-7}$$

4.2.1.1. Rate of Photons Reaching the Inner Reactor Surface Application of equation (4-1) requires the determination of the rate of photons reaching the inner reactor surface, $P_i(t)$. Consequently, the estimation of $P_i(t)$, according to equation (4-2), requires the estimation of the rate of emission of photons by the UV lamp, $P_l(t)$, and the rate of absorption of photons in the inner glass tube wall, $P_{a-wall}(t)$.

4.2.1.2. Rate of Emission of Photons by the UV Lamp The rate of emission of photons by the lamp, so-called lamp characterization can be developed in the LTU, as described in Chapter III. In the LTU, a radiometer is placed at a fixed distance form the lamp's axis. A radiomenter correction factor of 1.41 (equation 3-1) is used which relates the true absolute reading to the lamp emission spectrum and the radiometer normalized spectral response. Thus the radiometric measurement allowed for the determination of the spatial distribution of the lamp radiative flux, $q_{\theta,z,t}$.

The lamp radiative flux, $q_{\theta,z,t}$, can be calculated by using an extensive source superficial diffuse emission model (ESSDE) (Tsekov and Smirniotis, 1997). Figure 4.2 presents the $q_{\theta,z,t}$ distribution and the results of the ESSDE model at the radial positions, 3.1 and 4.5 cm from the lamp axis (or 1.9 and 3.2 cm from the lamp surface). As it can

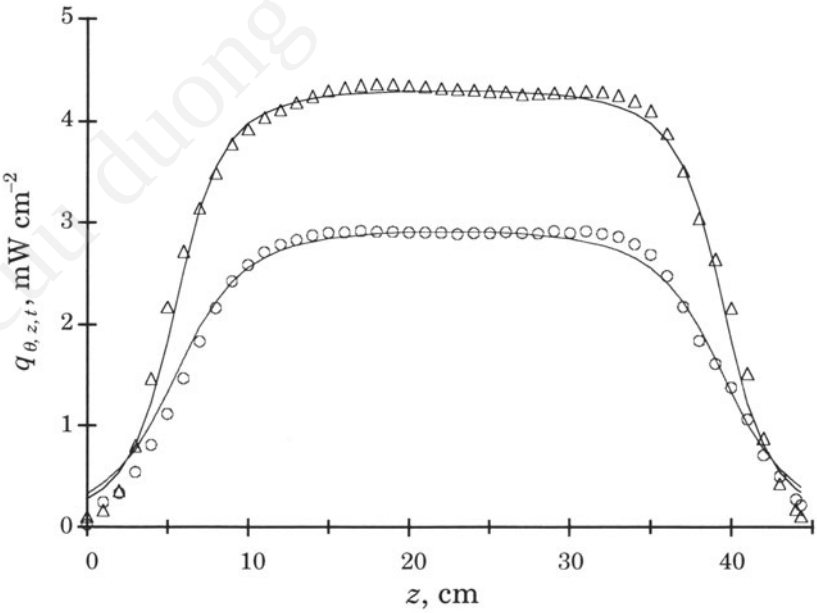

FIGURE 4.2. BL lamp axial radiative flux distribution measured at two radial positions: (Δ) 3.1-cm and (o) 4.5-cm. Solid lines represent the ESSDE model predictions evaluated at set radial positions (Reprinted from *Chem. Eng. Journ.*, **90**, M. Salaices, B. Serrano and H.I. de Lasa, Experimental evaluation of photon absorption in an aqueous TiO_2 slurry reactor, 219–229, Copyright 2002, with permission from Elsevier).

CuuDuongThanCong.com https://fb.com/tailieudientucntt

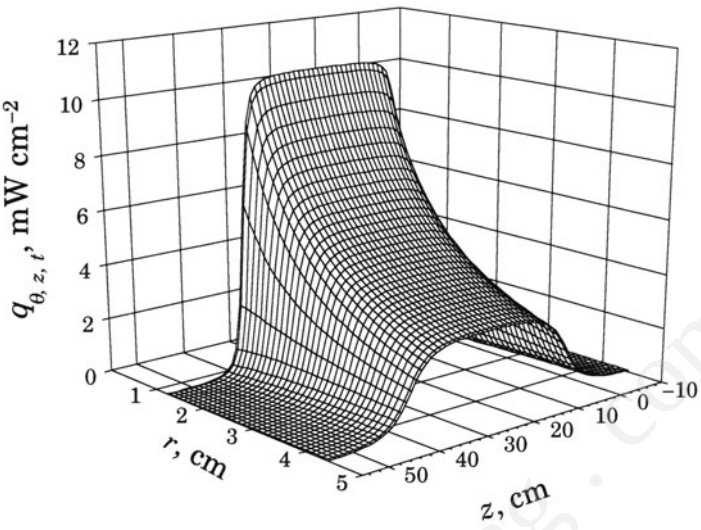

FIGURE 4.3. Radiative flux distribution in an empty annular reactor (Reprinted from *Chem. Eng. Journ.*, **90**, M. Salaices, B. Serrano and H.I. de Lasa, Experimental evaluation of photon absorption in an aqueous TiO_2 slurry reactor, 219-229, Copyright 2002, with permission from Elsevier).

be noticed, a good description of the $q_{\theta,z,t}$ radiometric measurements is obtained by the application of the ESSDE model.

Figure. 4.3 illustrates the net radiative flux distribution, $q_{\theta,z,t}$, in an empty annular reactor, as predicted by the validated ESSDE model. Several independent $q_{\theta,z,t}$ single measurements were taken at 1.47 cm from the lamp axis (0.2 cm from the lamp surface) and 22.2 cm axial position.

An average value of 9.17 mW cm^{-2} was determined for $q_{\theta,z,t}$ at this position. The predicted value by the ESSDE model at the same position was 9.29, 1.3% higher from the measured value. This error is well below the sensor accuracy of ±5%, which validates the applicability of the model for the simulation of the radiation field in an empty reactor. Besides the determination of the radiative flux spatial distribution, the energetic and spatial distributions of the radiative flux, $q_{\theta,z,\lambda,t}$, can be determined by spectroradiometric measurements in the LTU (Chapter III).

Typical spectroradiometric values of $q_{\theta,z,\lambda,t}$ are reported in Figure 4.4 at 6.64 cm from the lamp axis (5.37 cm from the lamp surface) and at about 22.2 cm axial position for both the MR and BL lamps. This figure illustrates that the MR lamps emit mainly in the 270-370-nm wavelength range with two peaks inside this range (312.5 and 364.5 nm) and two outside peaks (404 and 435.5 nm), whereas the BL lamps emit mainly in the 310-410-nm range with three main peaks (315, 364.5, and 404 nm).

Figure 4.5 reports the axial distribution of the radiative flux as predicted by the ESSDE model at the same radial distance than that of Figure 4.4 (6.6 cm from the lamp axis). Each point of Figure 4.5 represents the radiative flux integrated over the wavelength

$$q_{\theta,z,t} = \int_{\lambda_1}^{\lambda_2} q_{\theta,z,\lambda,t} d\lambda \tag{4-8}$$

CuuDuongThanCong.com https://fb.com/tailieudientucntt

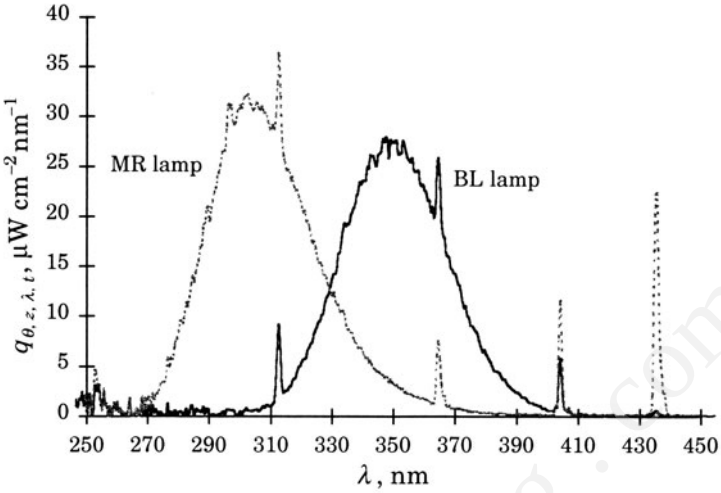

FIGURE 4.4. Typical radiative flux spectra of MR (- -) and BL (_) lamps (Reprinted with permission from *Ind. Eng. Chem. Res.*, **40**(23), M. Salaices, B. Serrano and H.I. de Lasa, Photocatalytic conversion of organic pollutants: Extinction coefficients and quantum efficiencies, 5455–5464. Copyright © 2001 American Chemical Society).

Thus, the rate of photon emission by the lamp $P_l(t)$ can be estimated by using equation (4-3), the lamp spectrum presented in Figure 4.4 at various axial positions or alternatively equation 4.3, and the radiative flux axial distribution presented in Figure 4.5. The estimated values using the second method are reported in Table 4-1. The lamp emission power at $t = 0$ or P_{l_0} is included in the second column of Table 4.1. In the last column of Table 4.1, the lamp efficiency, η_l, with respect to the nominal power (15 W) is reported. Thus, lamps exhibit efficiencies lower than 15%.

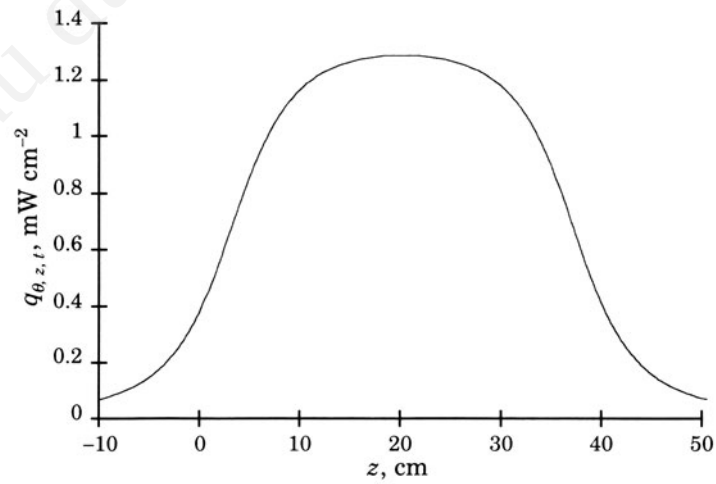

FIGURE 4.5. Axial distribution of the radiative flux as predicted by the ESSDE model at 6.6 cm from the lamp axis.

CuuDuongThanCong.com https://fb.com/tailieudientucntt

TABLE 4.1. Lamp emission rates

Lamp	P_{l0} (einstein s^{-1})	W_o (watts)	η_l
BL	$1.03\ 10^{-5}$	2.17	14.4
MR	$6.91\ 10^{-6}$	2.16	14.4

There is also lamp intensity decay that depends on the time of usage and that can be assessed using an exponential decay function,

$$P_l(t) = P_{l0} \exp(-\beta_l t) \tag{4-9}$$

where $P_l(t)$ is the lamp emission rate, einstein s^{-1}; P_{l0} is the initial lamp emission rate, $1.01.\ 10^{-5}$ einstein s^{-1}; β_l is the lamp decay coefficient, $7.85\ 10^{-4}\ h^{-1}$, and t is the lamp usage, h.

Figure 4.6 reports these findings and the best least squares curve fit. Lamps with a time of usage of 1000 h showed a decay of more than 50%. From the analysis of the emission spectra for the various lamps it can be concluded that the emission spectrum remains constant with lamp usage in spite of the decay in the emission power. This finding implies that the lamp power decay is equivalent to the decay in the rate of photon emission.

4.2.1.3. Rate of Absorption of Photons in the Inner Glass Tube Wall Figure 4.7 reports the transmission spectra, as obtained by using the spectrophotometer, for two sizes of glass inner tubes. This figure illustrates that the reactor with the smaller glass inner tube

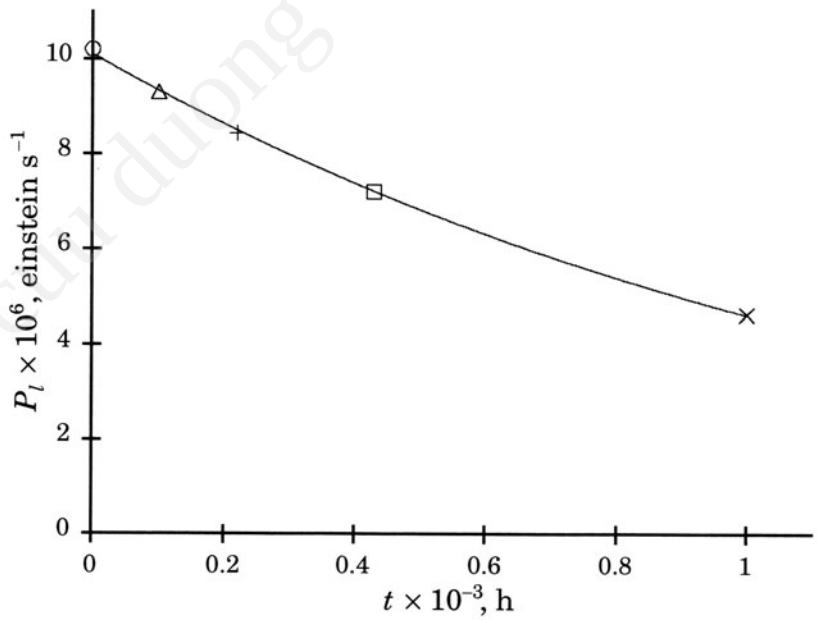

FIGURE 4.6. Lamp decay model. (o) BL lamp E, (Δ) BL lamp D, (+) BL lamp C, (□) BL lamp B and (×) BL lamp A (Reprinted with permission from *Ind. Eng. Chem. Res.*, **40**(23), M. Salaices, B. Serrano and H.I. de Lasa, Photocatalytic conversion of organic pollutants: Extinction coefficients and quantum efficiencies, 5455–5464. Copyright © 2001 American Chemical Society).

CuuDuongThanCong.com https://fb.com/tailieudientucntt

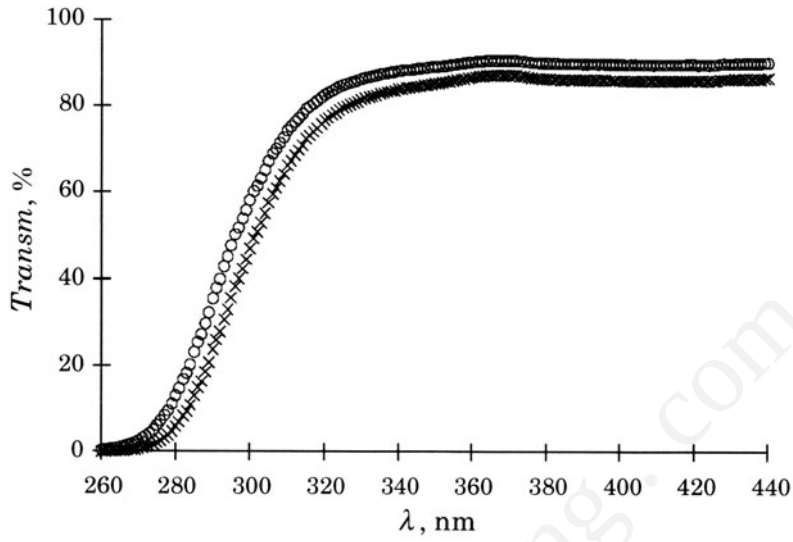

FIGURE 4.7. Inner glass tube transmittance. (o) 0.23-cm thickness, 3.2-cm diameter inner tube, (×) 0.32-cm thickness., 5.6-cm diameter inner tube.

(3.2-cm diameter, 0.23-cm thickness) has a transmittance above 90% for wavelengths larger than 340-nm. Nevertheless, the transmittance decreases to 60% at 300-nm. A close behavior is observed for a reactor with a 5.6-cm diameter, 0.32-cm thickness inner glass tube. In this case however, smaller transmittances are obtained. For instance, transmittances close to 85% and 45% are measured at 340-nm and at 300-nm, respectively.

Using the Beer's Law the extinction coefficient (β) of the Pyrex glass can be calculated. The change of the extinction coefficient with the wavelength is reported in Figure 4.8. The extinction coefficient decreases with the radiation wavelength reaching a

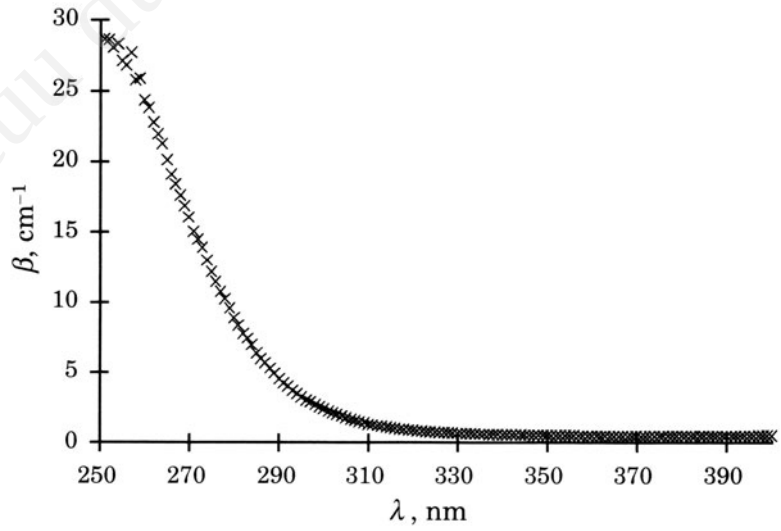

FIGURE 4.8. Pyrex glass extinction coefficient spectrum.

CuuDuongThanCong.com https://fb.com/tailieudientucntt

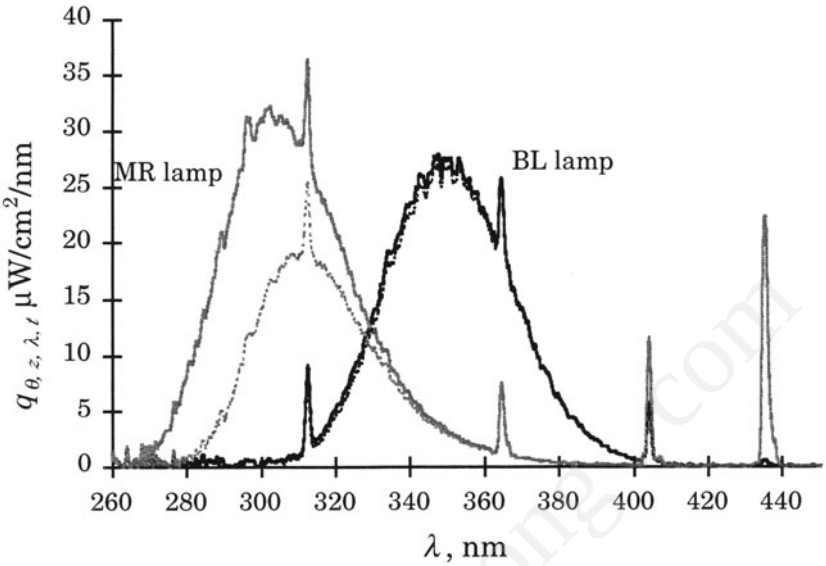

FIGURE 4.9. MR and BL lamp radiation spectra variation through the 0.23-cm-thickness × 3.2-cm-diameter inner tube (Reprinted with permission from *Ind. Eng. Chem. Res.*, **40**(23), M. Salaices, B. Serrano and H.I. de Lasa, Photocatalytic conversion of organic pollutants: Extinction coefficients and quantum efficiencies, 5455–5464. Copyright © 2001 American Chemical Society).

constant value of 0.52 cm^{-1} above 320 nm. Given the low β values obtained, it can be concluded that the glass material is essentially transparent for wavelengths over 320 nm.

Figure 4.9 reports the change of the spectrum emission as radiation evolves through the wall of the inner glass tube (dotted lines). In this respect, the spectrum from the BL lamp remains almost unchanged after crossing the inner tube wall. The spectrum of the MR lamp is however, significantly modified, with more than half of the radiation lower than 300 nm absorbed by the reactor inner wall.

The photon absorption rate in the inner glass tube wall can be estimated from the difference between the total radiative flux transmitted through the inner tube and the total incoming radiative flux.

For BL lamps, the transmission of photons through the smaller inner tube represents more than 95% of those emitted, whereas for MR lamps, only about 73% are transmitted. In addition, for the larger and thicker inner tube the transmission of photons represents about 94% of those emitted from the BL lamp and about 65% of those emitted by the MR lamp. Table 4.2 summarizes the above information.

The last column of Table 4.2 reports the fraction of the lamp power emission crossing the inner tube. This difference is particularly important when the MR lamp is used in conjunction with the inner thicker tube.

4.2.1.4. Rate of Transmission of Photons The third parameter of equation (4-1), $P_t(t)$, can be determined from radiometric measurements of the radiation transmission through a flowing catalyst suspension at each of the reactor window positions.

CuuDuongThanCong.com https://fb.com/tailieudientucntt

TABLE 4.2. Photon and energy distribution around the inner reactor wall

Lamp	inner tubes diam × thickness (cm)	$P_{a-wall,0}$ (% of P_{i0})	P_{i0} (einstein s^{-1})	P_{i0}/P_{l0} (%)	W_{i0} (W)	W_{i0}/W_{l0} (%)
BL	3.2 × 0.23	4.21	$9.87\ 10^{-6}$	95.8	2.07	95.7
MR	3.2 × 0.23	26.8	$5.06\ 10^{-6}$	73.2	1.24	57.6
BL	5.6 × 0.32	5.81	$9.70\ 10^{-6}$	94.2	2.04	94.1
MR	5.6 × 0.32	35.2	$4.48\ 10^{-6}$	64.8	1.10	51.0

Figure 4.10 displays typical values of transmitted radiative flux, $q_{ac\ \theta,z,t}$, at 7.6 cm from the reactor axis, as detected using the UVX radiometer and the UV-reflecting collimator No 1, placed at the various reactor windows. More details about the UV-reflecting collimators are provided in chapter III. Figure 4.10 reports results developed with several catalyst concentrations at a flow rate of 12 L min^{-1}.

It can be observed that in the central region of the reactor, from 10 to 36 cm axial length, the radiation profile develops with essentially no changes in the radiation levels. It is in this region where negligible end effects can be postulated and consequently, where radiation transmission measurements are more reliable. It can also be observed, that the uneven light distribution tends to moderate while the particle concentration increases. This is the result of a growing influence of particle light scattering smoothing of the reactor end effects.

Similar results can be obtained when using the other collimators. Figure 4.11 presents typical values of the radiative flux, $q_{bc_\theta,z,t}$, with the UV-opaque collimator 3, at 16.8 cm from the lamp axis.

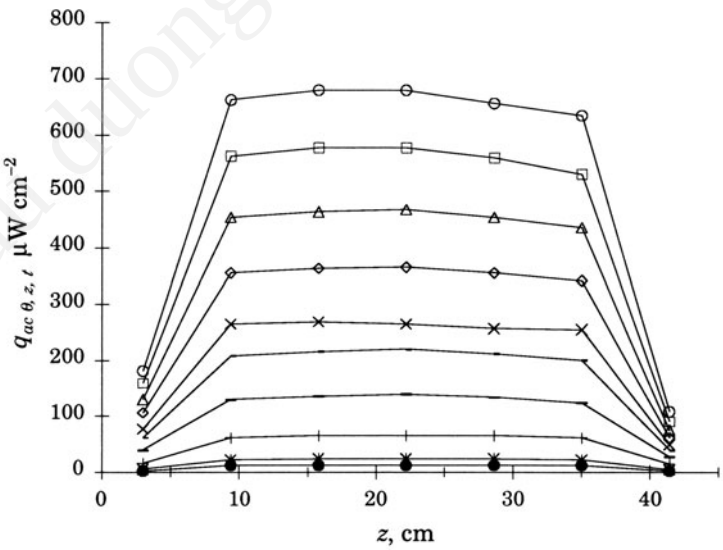

FIGURE 4.10. Axial radiation distribution for several Degussa P25 concentrations using the UV-reflecting collimator 1. Concentrations in mg L^{-1}. (o) 0, (□) 3; (Δ) 5; (◇) 10; (×) 15; (-) 20; (_) 30; (+) 50; (*) 80; (•) 100 (Reprinted from *Chem. Eng. J.*, **90**, M. Salaices, B. Serrano and H.I. de Lasa, Experimental evaluation of photon absorption in an aqueous TiO_2 slurry reactor, 219-229, Copyright 2002, with permission from Elsevier).

CuuDuongThanCong.com https://fb.com/tailieudientucntt

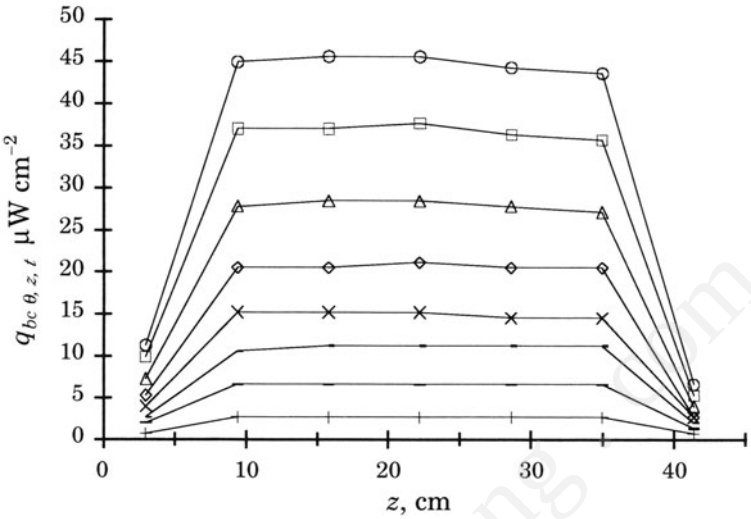

FIGURE 4.11. Axial distribution of the radiation transmission for several Degussa P25 catalyst concentrations using the UV-opaque collimator 3. Concentrations are in mg L^{-1}. (o) 0, (□) 3; (Δ) 5; (◇) 10; (×) 15; (-) 20; (_) 30; (+) 50.

Figure 4.12 reports the radiative flux evolving throughout the slurry versus the Degussa P25 catalyst concentration.

Figure 4.13 shows the natural logarithm of the radiative flux versus the catalyst concentration of Degussa P25. These results were obtained using the UV-collimator No. 1 and the radiometric cell placed at 7.6 cm from the lamp's axis.

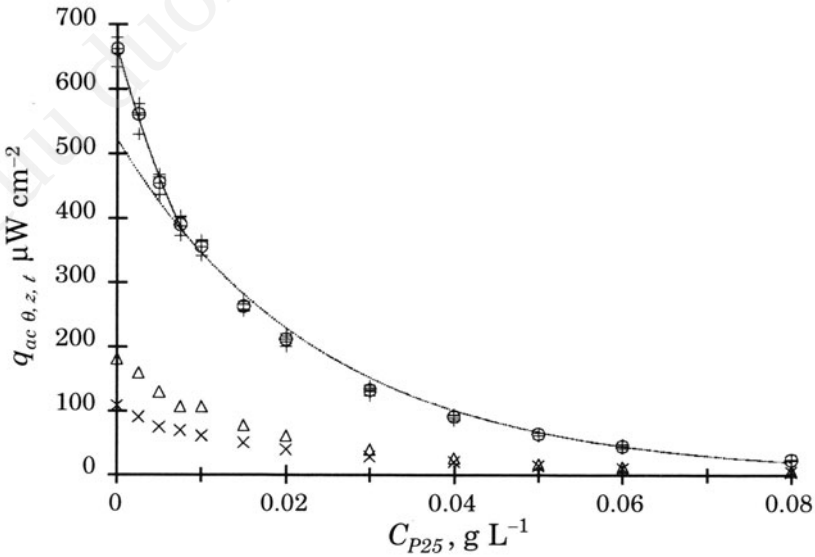

FIGURE 4.12. Radiation transmission at the reactor windows positions versus catalyst concentration using the UV-reflecting collimator No.1: (+) windows 2 to 6; (o) windows 2 to 6, average reading; (Δ) window 1; (×) window 7; (- -) exponential fit.

CuuDuongThanCong.com https://fb.com/tailieudientucntt

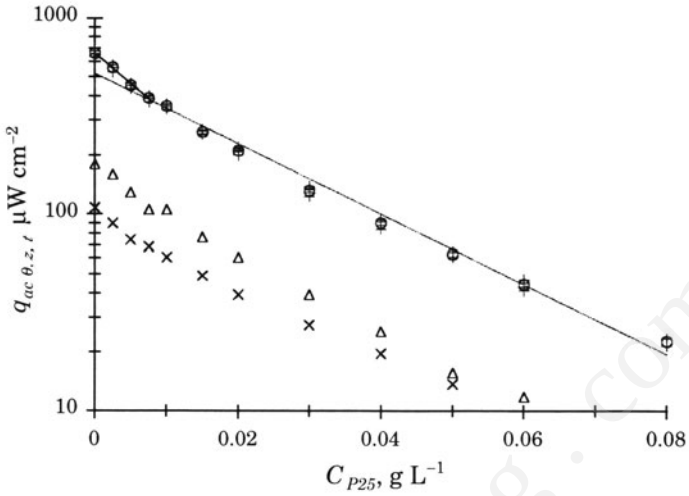

FIGURE 4.13. Logarithmic radiation transmission at the reactor window positions versus catalyst concentration using the collimator aluminum 1: (+) windows 2 to 6; (o) windows 2 to 6, average reading; (Δ) window 1; (×) window 7; (- -) exponential fit.

An exponential decay function (Beer-Lambert law) can be fitted to the averaged readings from windows 2 to 6. As can be observed, a good representation of the central data can be obtained for concentrations larger than 0.01 g L^{-1} ($R^2 = 0.990$). For smaller concentrations, however, a significant deviation is found. Figures 4.12 and 4.13 also display the readings from windows 1 and 7. Given that these readings incorporate the reactor end effects, they do not need to be considered further.

Thus, an exponential function applies to the central averaged readings

$$q_{ac\ \theta,z,t} = q_{ac\ \theta,z,t}|_{C_{cat}\to 0} \exp^{-\alpha_{cat} C_{cat}} \tag{4-10}$$

where $q_{ac\ \theta,z,t}$ in μW cm^{-2} is the measured transmitted radiative flux using the UV-reflective collimators; $q_{ac\ \theta,z,t}|_{C_{cat}\to 0}$ in μW cm^{-2} is the measured transmitted radiative flux using the UV-reflective collimator No.1 when the catalyst concentration approaches zero; α_{cat} in L g^{-1} is the effective extinction coefficient for the catalyst; and C_{cat} in g L^{-1} is the catalyst concentration.

In addition, an equivalent exponential fitting of the form

$$q_{bc\ \theta,z,t} = q_{bc\ \theta,z,t}|_{C_{cat}\to 0} \exp^{-\beta_{cat} C_{cat}} \tag{4-11}$$

can be applied to the averaged central readings obtained using the UV-opaque collimators.

The different variables and parameters of equation (4-11) are as follows:

a) $q_{bc\ \theta,z,t}$ is the transmitted radiative flux measured using the UV-opaque collimator No 3, in μW cm^{-2}

b) $q_{bc\ \theta,z,t}|_{C_{cat}\to 0}$ is the transmitted radiative flux measured using the UV-opaque collimator No. 3 when the catalyst concentration approaches zero, in μW cm^{-2}

c) β_{cat} is the true extinction coefficient for the catalyst, in L g^{-1}; and C_{cat} is the catalyst concentration, in g L^{-1}.

CuuDuongThanCong.com https://fb.com/tailieudientucntt

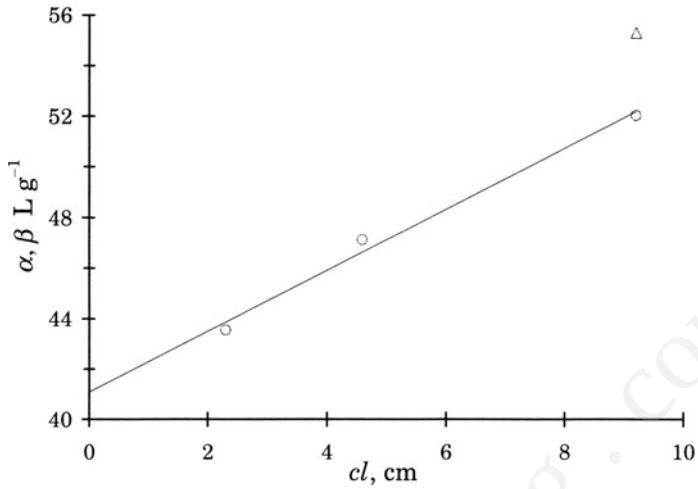

FIGURE 4.14. Exponential factors versus the collimator length for the determination of the effective extinction coefficient (o) α and (Δ)β.

Figure 4.14 reports the change of the exponential parameter with respect to the UV-reflecting collimator lengths (cl). The ordinate at the origin, in this figure, can be obtained via extrapolation of the best-fit line applied to the data and represents the effective extinction coefficient at the outer reactor wall.

This procedure corrects for any bias in the estimation of the effective extinction coefficients given the potential reflection losses in the UV-reflecting collimator during the radiation transport from the reactor wall to the sensor.

The catalyst concentration can be increased progressively until the condition of 0.2% of $q_{ac\ \theta,z,t}|_{C_{cat}\to 0}$ is obtained. This catalyst loading and the higher catalyst concentrations essentially ensure that all the radiation was absorbed in the slurry medium.

Moreover, in a set collimator-sensor-reactor geometry (same z, θ and t), the radiative flux detected is directly proportional to the radiative flux reaching the outer reactor wall, $q_{\theta,z,t\ |r=rw}$, or

$$q_{\theta,z,t\ |r=rw} = f_{ci}\ q_{ci\ \theta,z,t} \tag{4-12}$$

where f_{ci} is the proportionality factor for collimator i, dimensionless; and q_{ci} is the radiative flux detected using collimator i, einstein s^{-1}.

For the UV-reflective collimator, the radiative flux is defined by equation (4-10) and the transmitted radiative flux at the window position can be calculated as

$$q_{\theta,z,t\ |r=rw} = f_{ac}\, q_{ac\ \theta,z,t} = f_{ac} q_{ac\ \theta,z,t}|_{C_{cat}\to 0} \exp^{-\alpha_{cat} C_{cat}} \tag{4-13}$$

Furthermore, equation (4-13) can be rewritten with the use of equation (4-12) as,

$$q_{\theta,z,t|r=rw} = q_{\theta,z,t\,|[r=rw, C_{cat}\to 0]} \exp^{-\alpha_{cat} C_{cat}} \tag{4-14}$$

Thus, knowing the proportionally factor, the rate of transmission of photons reaching

CuuDuongThanCong.com https://fb.com/tailieudientucntt

the inner surface at r_w can be obtained from equation (4-14) as follows

$$P_t(t) = \frac{\bar{\lambda}}{hc} \int_0^{2\pi} \int_0^{\infty} q_{\theta,z,t|_{[r=rw,\ C_{cat}\to 0]}} r_w \exp^{-\alpha_{cat} C_{cat}} dz d\theta \tag{4-15}$$

Regarding $\bar{\lambda}$, it can be obtained iteratively from the lamp emission spectrum and the following relationship:

$$\int_{\lambda_1}^{\bar{\lambda}} q_{\theta,z,\lambda,t} d\lambda = \frac{1}{2} \int_{\lambda_1}^{\lambda_2} q_{\theta,z,\lambda,t} d\lambda \tag{4-16}$$

Typical estimated values for $\bar{\lambda}$ are 307.2 nm and 348 nm for the MR and BL lamps, respectively.

The exponential term of equation (4-15) can be taken out of the integral given that the slurry optical properties and the catalyst concentration are not a function of the position for a well-distributed catalyst suspension.

Consequently, equation (4-15) can be rewritten as,

$$P_t(t) = \exp^{-\alpha_{cat} C_{cat}} \frac{\bar{\lambda}}{hc} \int_0^{2\pi} \int_0^{\infty} q_{\theta,z,t|_{[r=rw,\ C_{cat}\to 0]}} r_w dz d\theta \tag{4-17}$$

The term $\frac{\bar{\lambda}}{hc} \int_0^{2\pi} \int_0^{\infty} q_{\theta,z,t|_{[r=rw,\ C_{cat}\to 0]}} r_w dz d\theta$ represents the transmission of photons when the catalyst concentration tends to zero, $P_t(t)|_{C_{cat}\to 0}$, and equation (4-17) can be simplified as

$$P_t(t) = P_t(t)|_{C_{cat}\to 0} \exp^{-\alpha_{cat} C_{cat}} \tag{4-18}$$

or using equation (4-4), it results

$$P_t(t) = [P_i(t) - P_{bs}(t)] \exp^{-\alpha_{cat} C_{cat}} \tag{4-19}$$

Thus, the rate of transmission of photons through a catalyst suspension can be determined by the rate of photons reaching the inner reactor wall $[P_i(t)]$, the back-scattered photons $[P_{bs}(t)]$, the effective extinction coefficient of the catalyst $[\alpha_{cat}]$, and the catalyst concentration $[C_{cat}]$.

4.2.1.5. Rate of Back-scattered Photons Exiting the System Two important assumptions are included in the development of equation (4-4) The first of these assumptions considers that the back-scattered photons exiting the system are those related to a number of back-scattering centers located in a boundary layer of particles very close to the inner

CuuDuongThanCong.com https://fb.com/tailieudientucntt

glass tube wall. A discontinuity of $d\,[\ln\ P_t(t)]\,/dC$ at very low catalyst concentration, supports this postulate (Salaices et al., 2001). The second assumption considers that once a maximum number of scattering centers in this boundary layer is reached, no additional back-scattering of photons leaving the system occurs.

Using the above postulates, the rate of back-scattered photons was estimated from equation (4-4). $P_{bs}(t)$ can be written in terms of radiative fluxes as follows,

$$P_{bs}(t) = \frac{\bar{\lambda}}{hc}\int_0^{2\pi}\int_0^{\infty} q_{0\ \theta,z,t} r_{wo} dz d\theta - \frac{\bar{\lambda}}{hc}\int_0^{2\pi}\int_0^{\infty} q_{\theta,z,t|_{C_{cat}\to 0}} r_{wo} dz d\theta \tag{4-20}$$

Dividing both sides of equation (4-20) by $P_i(t)$ gives

$$\frac{P_{bs}(t)}{P_i(t)} = \frac{\frac{\bar{\lambda}}{hc}\int_0^{2\pi}\int_0^{\infty} q_{0\ \theta,z,t}\, r_{wo} dz d\theta - \frac{\bar{\lambda}}{hc}\int_0^{2\pi}\int_0^{\infty} q_{\theta,z,t|_{C_{cat}\to 0}} r_{wo} dz d\theta}{\frac{\bar{\lambda}}{hc}\int_0^{2\pi}\int_0^{\infty} q_{0\ \theta,z,t}\ r_{wo} dz d\theta} \tag{4-21}$$

where $q_{0\ \theta,z,t}$ refers to the radiative flux reaching the outer wall of the inner reactor tube.

Given that the radiative fluxes are expected to display a similar functionality with respect to the space variables and that they are evaluated at the same position, equation (4-21) can be simplified as the ratio between radiative fluxes

$$\frac{P_{bs}(t)}{P_i(t)} = \frac{q_{0\ \theta,z,t} - q_{\theta,z,t|_{C_{cat}\to 0}}}{q_{0\ \theta,z,t}} \tag{4-22}$$

Furthermore, equation (4-22) can be rewritten in terms of the radiation flux detected by the UV-reflective collimator as

$$P_{bs}(t) = P_i(t)\frac{q_{ac0\ \theta,z,t} - q_{ac\ \theta,z,t|_{C_{cat}\to 0}}}{q_{ac0\ \theta,z,t}} \tag{4-23}$$

Regarding the application of equation (4-23), the least squares method was used to generate a best-fit curve and to correlate the measured transmitted radiative flux with the catalyst concentration. This curve was then extrapolated to the origin for an estimation of $q_{ac\ \theta,z,t}\big|_{Cc_{cat}\to 0}$ (refer to Figure 4.13).

Experimental observations in this study (Figures 4.12 and 4.13) reinforce this view showing that, at very low C_{cat} (lower than 0.01 g L^{-1} for Degussa P25), the transmitted power decays much faster than the typical exponential decay observed at higher catalyst concentrations.

It is worth noting, that although several experimental observations support the assumptions used for the estimation of back-scattered radiation, it is necessary to validate this approximation through direct measurements of this parameter.

CuuDuongThanCong.com https://fb.com/tailieudientucntt

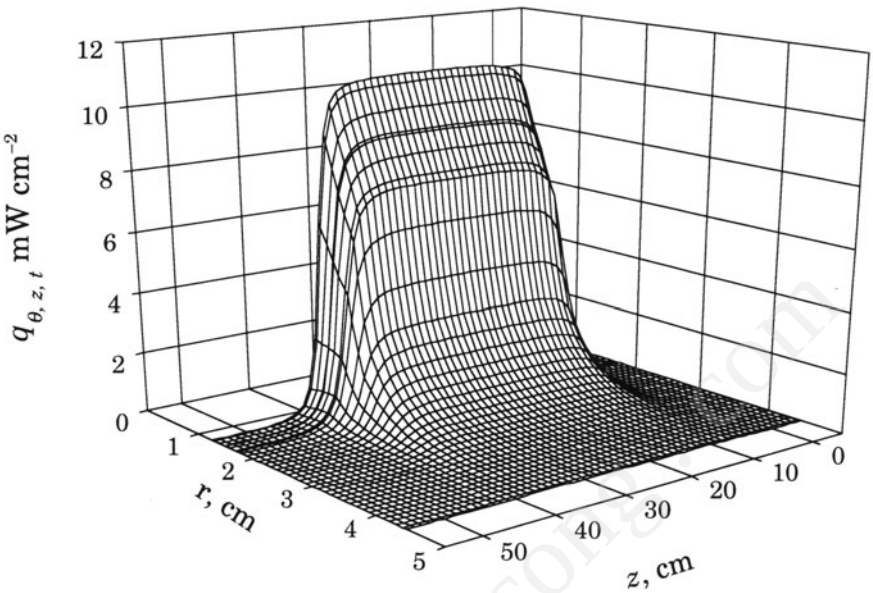

FIGURE 4.15. Radiative flux distribution in a Degussa P25 loaded annular reactor allowing for 0.2% light transmission (Reprinted from *Chem. Eng. J.*, **90**, M. Salaices, B. Serrano and H.I. de Lasa, Experimental evaluation of photon absorption in an aqueous TiO_2 slurry reactor, 219–229, Copyright 2002, with permission from Elsevier).

4.2.1.6. Rate of Absorption of Photons Finally, the rate of absorption of photons $P_a(t)$ can be calculated using equations (4-1), (4-18), and (4-23) as

$$P_a(t) = P_i(t)\left[1 - \frac{P_{t|_{C_{cat}\to 0}}(t)}{P_i(t)}\exp^{-a_{cat}C_{cat}} - \frac{q_{ac_{0\,\theta,z,t}} - q_{ac\,\theta,z,t|_{C_{cat}\to 0}}}{q_{ac_{0\,\theta,z,t}}}\right] \tag{4-24}$$

Figure 4.15 shows the radiative flux distribution in a Degussa P25 loaded reactor allowing for 0.2% light transmission and the estimated α coefficient. Good catalyst distribution is assumed ($\alpha_{cat}C_{cat} \approx \alpha_\ell \ell$, being ℓ the optical thickness of the suspension) in order to generate this figure. In this case, the radiation flux distribution for the lamps is established with an ESSDE model. Inner cylinder wall effects and the back-scattered radiation are also included in this simulation.

In order to have a quick visualization of the catalyst effect on the radiation distribution, Figure 4.15 can be compared to Figure 4.3. It can be noticed that there is a very sharp decline of the radiative flux in the near wall-central region of the annular channel under the transmission conditions of 0.2% of $P_i(t)$.

4.2.1.7. Rate of Forward-Scattered Photons Figure 4.16 reports for Degussa P25, the dimensionless radiative flux ratio in the central axial region of the reactor measured using both, polished-aluminum $q_{ac\,\theta,z,t}/q_{ac0\,\theta,z,t}$, and UV-opaque collimators $q_{bc\,\theta,z,t}/q_{bc0\,\theta,z,t}$ as a function of the catalyst concentration. In order to assist the

CuuDuongThanCong.com https://fb.com/tailieudientucntt

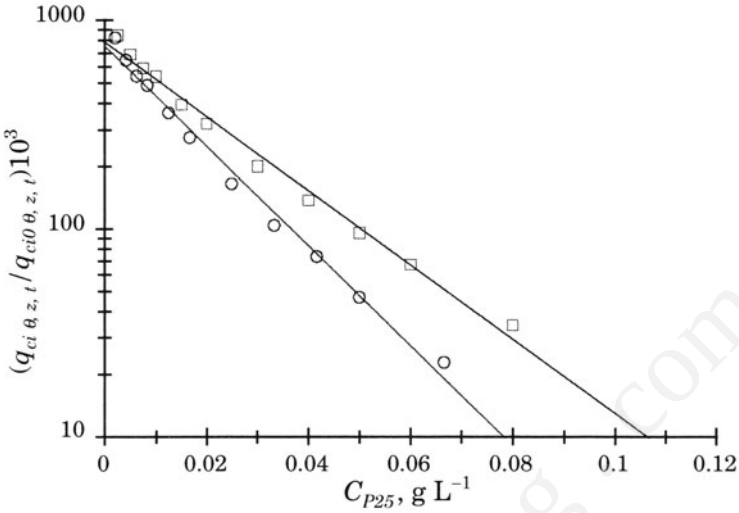

FIGURE 4.16. Dimensionless forward-transmitted radiative flux (□) and transmitted non-scattered radiative flux (o) versus Degussa P25 catalyst concentration at a flow rate of 12 L min^{-1} (Reprinted from *Chem. Eng. J.*, **90**, M. Salaices, B. Serrano and H.I. de Lasa, Experimental evaluation of photon absorption in an aqueous TiO_2 slurry reactor, 219-229, Copyright 2002, with permission from Elsevier).

comparison of coefficients, the readings are multiplied by a 10^3 factor. The significant difference between these coefficients (slopes) becomes apparent in this figure. This difference arises given that, for the case of the polished aluminum collimators, all the transmitted radiation contributes to the readings (scattered and non-scattered radiation), whereas for the case of the UV-opaque collimators, mainly the non-scattered radiation transmission contributes to the readings. Given these facts, the β_{P25} coefficients were found always larger than the α_{P25} coefficients.

Regarding the rate of forward-scattered photons, $P_{fs}(t)$, it can be calculated using equation (4-7),

$$P_{fs}(t) = P_t(t) - P_{tns}(t) \tag{4-7}$$

A similar treatment to that described in section 4.2.1.4 (equations (4-12) to (4-18)) is applied to the readings using a UVX radiometer with the UV-opaque collimator, $q_{bc\,\theta,z,t}$ in order to relate them to the rate of transmission non-scattered photons, $P_{tns}(t)$. The resultant equation becomes

$$P_{tns}(t) = P_{t(t)|_{C_{cat}\to 0}} \exp^{-\beta_{cat} C_{cat}} \tag{4-25}$$

Using equations (4-18) and (4-25), equation (4-7) can be rewritten as

$$P_{fs}(t) = P_t(t) - P_{tns}(t) = P_{t(t)|_{C_{cat}\to 0}} \left[\exp^{-\alpha_{cat} C_{cat}} - \exp^{-\beta_{cat} C_{cat}}\right] \tag{4-26}$$

In this respect, $P_{fs}(t)$ can be related to the transmission of photons by a difference between exponential functions involving the effective (α_{cat}), and the true (β_{cat}) extinction coefficients.

CuuDuongThanCong.com https://fb.com/tailieudientucntt

TABLE 4.3. Extinction coefficients corresponding to the different view angles of UV-opaque collimators

Collimator	view angle(deg)	β_{P25} (L g^{-1})
UV-opaque 3	12.2	55.3
UV-opaque 2	23.8	51.1
UV-opaque 1	44.4	49.1

Moreover, information about the forward-scattered radiation distribution can be obtained using UV-opaque collimators of different lengths and consequently different view angles. As explained in chapter III the virtual cones formed on the basis of radiation detection define the view angle.

Table 4.3 reports the various extinction coefficients for Degussa P25 and the view angles for the set of UV-opaque collimators used.

As can be noticed an increase in the view angle of 11.6°, between the collimators 3 and 2, decreases the extinction coefficient 7%, whereas an increase of 20.6° between the collimators 2 and 1 is responsible for a decrease of 4%. This indicates that most of the radiation is transmitted at close normal angles with respect to the reactor's axis and that radiation transmission decreases moderately as the angle gets far from the normal.

4.3. RADIATION TRANSMISSION THROUGH SEVERAL TiO_2 SAMPLES

Radiation transmission measurements can be preformed for different catalyst concentrations using both the UV-reflecting No.1 and UV-opaque No.3 collimators. Figure 4.17 reports the dimensionless transmitted radiative flux evolving through the slurry

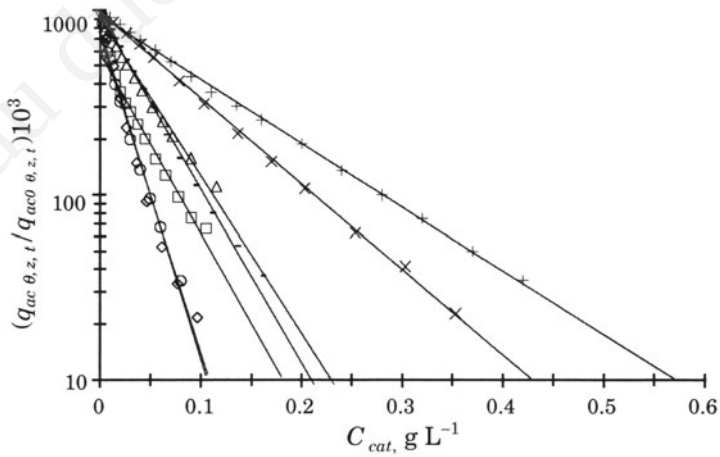

FIGURE 4.17. Transmitted radiative flux versus catalyst concentration. Polished aluminum collimator: (◇) Anatase 1, (□) Anatase 2, (Δ) Hombikat, (o) Degussa P25, (+) Rutile 1, (×) Rutile 2, and (-) Hombikat UV-100 (Reprinted from *Chem. Eng. J.*, **90**, M. Salaices, B. Serrano and H.I. de Lasa, Experimental evaluation of photon absorption in an aqueous TiO_2 slurry reactor, 219–229, Copyright 2002, with permission from Elsevier).

CuuDuongThanCong.com https://fb.com/tailieudientucntt

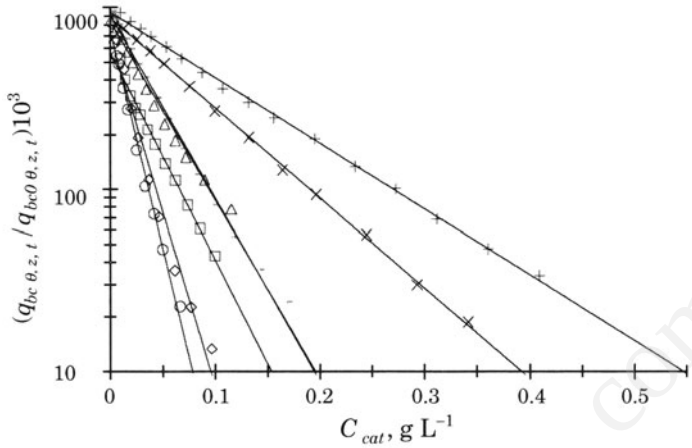

FIGURE 4.18. Transmitted non-scattered radiative flux versus catalyst concentration. UV-opaque collimator: (◊) Anatase 1, (□) Anatase 2, (Δ) Hombikat, (o) Degussa P25, (+) Rutile 1, (×) Rutile 2, and (-) Hombikat UV-100 (Reprinted from *Chem. Eng. J.*, **90**, M. Salaices, B. Serrano and H.I. de Lasa, Experimental evaluation of photon absorption in an aqueous TiO_2 slurry reactor, 219-229, Copyright 2002, with permission from Elsevier).

versus the catalyst concentration for a number of catalysts and water flow rates larger than 12 L min^{-1}.

As described by equation (4-10), the radiation transmission decreases with the catalyst concentration following, essentially for all cases, an exponential decreasing relationship.

Figure 4.18 reports the normalized non-scattered radiative flux versus the catalyst concentration for the various semiconductor materials. The non-scattered radiative flux is obtained using the UV-opaque collimator No 3.

In all cases, the exponential decrease of the non-scattered radiation transmission with the catalyst concentration is adequate ($R^2 > 0.990$ for Rutile 1, Rutile 2, Hombikat UV-100, and Degussa P25 samples; $R^2 > 0.982$ for Anatase 2 and Hombikat samples; and $R^2 = 0.976$ for Anatase 1 sample). It should be emphasized that in the case of UV-opaque collimators higher slopes were obtained, indicating larger extinction coefficients than those obtained using the UV-reflecting collimators.

Thus, given the suitability of the exponential decay model the effective and true extinction coefficients (α_{cat}, β_{cat}) can be estimated for various catalysts. The numerical values of the coefficients are reported in the 2nd and 3rd columns of Table 4.4. In this respect, there are significant differences in the β_{cat} values for various materials tested, with this coefficient ranging from 8.3 Lg^{-1} for Rutile 1 sample to 55.3 L g^{-1} for Degussa P25 catalyst.

Equations (4-10) and (4-11) can also be expressed in terms of specific extinction coefficients using the suspension optical thickness, ℓ, through the following relationship,

$$q_{ac\,\theta,z,t} = q_{ac\,\theta,z,t|_{C_{cat}\to 0}} \exp^{-(\alpha_{s\,cat}\,\ell\,C_{cat}\times 10^{-3})} \qquad (4\text{-}27)$$

CuuDuongThanCong.com https://fb.com/tailieudientucntt

TABLE 4.4. Extinction coefficients for several TiO_2 samples with catalyst loading C_{cat} allowing the transmission of 0.2% of $q_{ac\,\theta,z,t|C_{cat}\to 0}$

Catalyst	α_{cat} (L g^{-1})	β_{cat} (L g^{-1})	$\alpha_{s\,cat}10^{-4}$ (cm^2 g^{-1})	$\beta_{s\,cat}10^{-4}$ (cm^2 g^{-1})	$C_{cat\|0.002\,q_{ac\,\theta,z,t}}$ (g L^{-1})
Anatase 1	39.6	44.2	1.27	1.50	0.149
Anatase 2	22.4	26.3	0.72	0.85	0.254
Hombikat	19.6	22.9	0.63	0.74	0.312
Degussa P25	41.1	55.3	1.32	1.78	0.145
Rutile 1	7.9	8.3	0.26	0.27	0.774
Rutile 2	10.7	11.4	0.34	0.37	0.580
Hombikat UV-100	21.6	23.2	0.70	0.75	0.285

and

$$q_{bc\,\theta,z,t} = q_{bc\,\theta,z,t|_{C_{cat}\to 0}} \exp^{-(\beta_{s\,cat}\,\ell\,C_{cat}\times 10^{-3})} \tag{4-28}$$

with $\alpha_{s\,cat}$, $\beta_{s\,cat}$ being the specific extinction coefficients per unit catalyst mass defined respectively as: $\alpha_{s\,cat} = \left[\alpha_{cat}10^3/\ell\right](cm^2g^{-1})$ and $\beta_{s\,cat} = \left[\beta_{cat}10^3/\ell\right](cm^2g^{-1})$. In addition, $\ell = R_w - R_i$ represents the suspension optical thickness with R_w being the window's inner surface radial position and R_i the inner-cylinder outer-surface radial position. Values of the specific coefficients are reported in the 4th and 5th columns of Table 4.4.

The catalyst concentration required to allow 0.2% transmission of the incident radiative flux can be calculated using the effective specific extinction coefficients ($\alpha_{s\,cat}$), the reactor optical thickness (ℓ), and Equation (4-27) as follows,

$$C_{cat|0.002\,q_{ac\,\theta,z,t|C_{cat}\to 0}} = \frac{6215}{\ell\alpha_{s\,cat}} \tag{4-29}$$

Values of catalyst concentration for 0.2% transmittance are included in the last column of Table 4.4. It can be noticed that the effective specific extinction coefficients range from 2.6 10^3cm^2 g^{-1} for the Rutile 1 catalyst to 1.32 10^4 cm^2 g^{-1} for Degussa P25, with the photocatalysts with higher extinction coefficients requiring lower catalyst concentrations to reach the condition of 0.2% of $q_{ac\,\theta,z,t|_{C_{cat}\to 0}}$. Thus, it can be inferred that the type of catalyst used significantly affects the concentration needed to achieve the condition 0.2% of $q_{ac\,\theta,z,t|_{C_{cat}\to 0}}$.

Table 4.5 summarizes, for each of the TiO_2 samples, the rate of back-scattered, absorption, and forward-scattered photons using equations (4-23), (4-24), and (4-26), respectively. In this table, the values of absorption of photons and back-scattered photons are given as a percentage of $P_i(t)$, whereas the values of the forward-scattered photons are given as a percentage of $P_i(t)$.

As it can be observed, the rates of absorption of back-scattered and forward-scattered photons are a strong function of the type of catalyst used. $P_a(t)$ ranges from 57.8% to 96.5% of $P_i(t)$ and the rate of back-scattered photos ranges between 3.3 and 42% of $P_i(t)$. Under 0.2% of $P_i(t)$ transmittance conditions, a great portion of the radiation transmission through the system undergoes scattering such as in a Degussa P25

CuuDuongThanCong.com https://fb.com/tailieudientucntt

TABLE 4.5. Rate of absorption of photons and back-scattered photons for several TiO_2 samples as a percentage of $P_i(t)$, and the rate of forward-scattered photons as a percentage of $P_t(t).P_i(t) = 9.71\,10^{-6}$ einstein s^{-1}

Catalyst	P_a (%P_i)	P_{bs} (%P_i)	P_{fs} (%P_t)*
Anatase 1	72.7	27.1	66.2
Anatase 2	57.8	42.0	66.3
Hombikat	88.5	11.3	65.1
Degussa P25	78.5	21.3	88.3
Rutile 1	92.8	7.0	24.7
Rutile 2	96.5	3.3	35.4
Hombikat UV-100	93.1	6.7	36.9

* Estimated at conditions of $q_{ac\,\theta,z,t} \sim 0.002\, q_{ac\,\theta,z,t}|_{Ccat\to 0}$.

suspension with 88% of the transmitted radiation evolving in the system as forward-scattered radiation.

4.4. EXTINCTION COEFFICIENTS

The radiation transport equation in a direction along the ray trajectory, can be represented as follows, assuming a coherent dispersion, no-emission in the suspension, and no time dependence:

$$\frac{dI_\lambda(\vec{r},s)}{ds} + [k_\lambda(\vec{r},s) + \sigma_\lambda(\vec{r},s)]I_\lambda(\vec{r},s) = \frac{1}{4\pi}\sigma(\vec{r},s)\int_{\omega_{r'}=4\pi} p(\vec{r}'\to\vec{r})I_\lambda(\vec{r},s)d\omega_{r'} \tag{4-30}$$

where the first term of the left-hand side denotes the change of specific intensity $I_\lambda(\vec{r},s)$ in the direction $\vec{r}$, at the point determined by s; the second term represents the loss of specific intensity by radiation absorption $[k_\lambda(\vec{r},s)I_\lambda(\vec{r},s)]$ and out-scattering $[\sigma_\lambda(\vec{r},s)I_\lambda(\vec{r},s)]$ in the heterogeneous medium; the last term represents the gain of specific intensity by in-scattering which involves the scattering coefficient $\sigma_\lambda(\vec{r},s)$, the radiation absorption coefficient $k_\lambda(\vec{r},s)$, the phase function $p(\vec{r}'\to\vec{r})$, the specific intensity $I_\lambda(\vec{r},s)$ and the variables of integration over solid angle denoted by $d\omega_{r'}$. The phase function represents the photon-scattering distribution accounting for the incorporation of photons with direction $\vec{r}'$ into $\vec{r}$.

If we omit special cases, the material coefficients $\sigma_\lambda(\vec{r},s)$ and $k_\lambda(\vec{r},s)$ do not depend on direction $\vec{r}$. Therefore, $\vec{r}$ dependence can be cancelled.

Even more if σ_λ and k_λ dependence on physical conditions of the medium (temperature, density, chemical composition) can be neglected, so s dependence can be also omitted.

Under the previous considerations equation (4-30) can be written

$$\frac{dI_\lambda(\vec{r},s)}{ds} + (k_\lambda+\sigma_\lambda)I_\lambda(\vec{r},s) = \frac{1}{4\pi}\sigma_\lambda\int_{\omega_{r'}=4\pi} p(\vec{r}'\to\vec{r})I_\lambda(\vec{r},s)d\omega_{r'} \tag{4-31}$$

CuuDuongThanCong.com https://fb.com/tailieudientucntt

For isotropic scattering, $p(\Omega' \rightarrow \Omega) = 1$ and equation (4-30) can be simplified

$$\frac{dI_\lambda(\vec{r}, s)}{ds} + [k_\lambda + \sigma_\lambda] I_\lambda(\vec{r}, s) = \frac{\sigma_\lambda}{4\pi} G'_\lambda(s) \tag{4-32}$$

where the integral

$$G'_\lambda(s) = \int_0^{2\pi} \int_0^{\pi} I_\lambda(\vec{r}', s) \sin\theta d\theta d\varphi \tag{4-33}$$

is the spectral incident radiation in the direction $\vec{r}'$ to the point s.

Given the adopted geometrical characteristics of the reactor-collimator arrangement placed at the outer reactor wall, it is only possible to detect the incoming inner scattering with a semi-full solid angle that is

$$\int_0^{2\pi} \int_0^{\pi/2} I_\lambda(\vec{r}', s) \sin\theta d\theta d\varphi \equiv q_\lambda(\vec{r}', s) \tag{4-34}$$

defined as the radiative flux in the direction $\vec{r}'$.

Under the above considerations equation (4-32) becomes

$$\frac{dI_\lambda(\vec{r}, s)}{ds} + [k_\lambda + \sigma_\lambda] I_\lambda(\vec{r}, s) = \frac{\sigma_\lambda}{2\pi} q_\lambda(\vec{r}', s) \tag{4-35}$$

The integration of equation (4-35) over semi-full solid angle gives,

$$\frac{d}{ds} \int_0^{2\pi} \int_0^{\pi/2} I_\lambda(\vec{r}, s) \sin\theta d\theta d\varphi + [k_\lambda + \sigma_\lambda] \int_0^{2\pi} \int_0^{\pi/2} I_\lambda(\vec{r}, s) \sin\theta d\theta d\varphi =$$

$$= \frac{\sigma_\lambda}{2\pi} q_\lambda(\vec{r}', s) \int_0^{2\pi} \int_0^{\pi/2} \sin\theta d\theta d\varphi \tag{4-36}$$

Applying equation (4-34) to equation (4-36) and noting that $\int_0^{2\pi} \int_0^{\pi/2} \sin\theta d\theta d\varphi = 2\pi$, gives

$$\frac{dq_\lambda(\vec{r}, s)}{ds} + [k_\lambda + \sigma_\lambda] q_\lambda(\vec{r}, s) = \sigma_\lambda q_\lambda(\vec{r}', s) \tag{4-37}$$

CuuDuongThanCong.com https://fb.com/tailieudientucntt

Rearranging

$$\frac{dq_\lambda(\vec{r}, s)}{ds} + \alpha_\lambda \, q_\lambda(\vec{r}, s) = 0 \tag{4-38}$$

where

$$\alpha_\lambda = k_\lambda + \sigma_\lambda \left[1 - \frac{q_\lambda(\vec{r}', s)}{q_\lambda(\vec{r}, s)}\right] \tag{4-39}$$

is the effective extinction coefficient as a function of the wavelength and the radiative fluxes in the directions $\vec{r}'$and $\vec{r}$.

Averaging over wavelength we have

$$\alpha = k + \sigma \left[1 - \frac{q(\vec{r}', s)}{q(\vec{r}, s)}\right] \tag{4-40}$$

Equation (4-40) is equivalent to the effective extinction coefficient determined using equation (4-10) and represents a physical interpretation of the effective extinction coefficient determined through radiometric and spectroradiometric measurements of transmitted radiation and the UV-reflecting collimators.

Subtracting the actual extinction coefficient form the above equation results

$$(\beta - \alpha) = \sigma \frac{q(\vec{r}', s)}{q(\vec{r}, s)} \tag{4-41}$$

Equation (4-41) represents the fraction of in-scattering flux (forward scattering) that is incorporated to the incident radiative flux.

Radiation transmission throughout heterogeneous dilute TiO_2 suspensions can be modeled using the Beer-Lambert's Law as represented by equation (4-18),

$$P_t(t) = P_{t(t)|_{C_{cat}\to 0}} \exp^{-\alpha_{cat} C_{cat}} \tag{4-18}$$

The α_{cat}, effective extinction coefficient can be affected, among others, by several factors such as mixing conditions, average agglomerate size, incident radiation wavelength, and addition of other suspended particle materials.

4.4.1. Mixing Conditions

The particle terminal velocity (U_{tp}) can be estimated based on agglomerate particle size (d_a) and assuming a spherical shape. U_{tp} in the range 2.0 10^{-2} to 6.0 10^{-2}cm min^{-1} can calculated for d_a in the range 0.5 to 2.5 μm. These values of U_{tp}, represent about 1/300 of the average fluid velocity in the reactor for a flow rate of 1 L min^{-1}. In conclusion, the flow direction effect on the catalyst distribution is not an important factor under the operating conditions used.

Regarding the mixing regimes both inside the reactor and at the reactor entrance, Reynolds can be calculated both in the reactor and in the reactor distributor-injector.

CuuDuongThanCong.com https://fb.com/tailieudientucntt

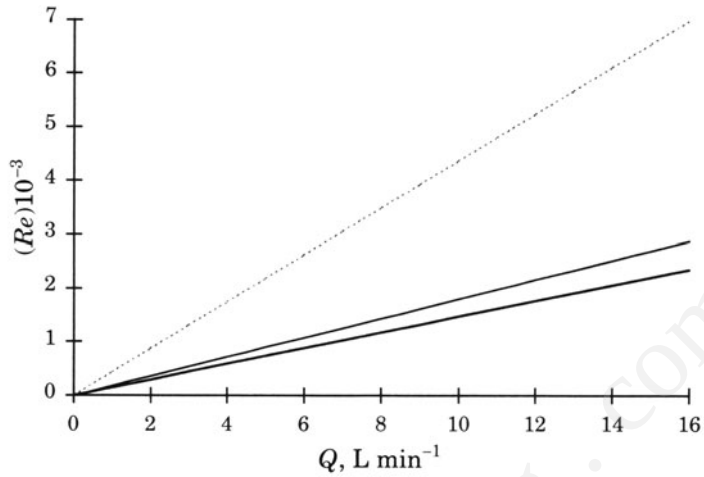

FIGURE 4.19. Reynolds numbers in the distributor-injector (- - -) and in the photocatalytic unit annular section for the 3.2 (—) and 5.6 (—) cm diameter inner tubes.

These values are reported in Figure 4.19 and can be calculated using the following equation:

$$Re = [\ d_o(1-k) < V_Z > \rho\ ]/\mu \tag{4-42}$$

with Re being the Reynolds number; d_o, in m, the outer tube diameter; k, dimensionless ratio between the diameters of the inner to the outer concentric tubes; $< V_Z >$, in m s^{-1}, the averaged flow axial velocity; μ in kg (m s)$^{-1}$ the suspension viscosity; and ρ, in kg m^{-3}, the suspension density.

As it can be observed, for the case of Photo-CREC Water II, this unit works slightly above the transition regime (Re > 2000) for flow rates larger than 15 L min^{-1}. However and given that at the injector section the turbulent regime is reached for flow rates above 5 L min^{-1}, flow rates larger than 15 L min^{-1} in the annular section of Photo-CREC-Water II are considered turbulent.

The effect of the flow rate, Q, on the extinction coefficients is reported, in Figure 4.20, for Degussa P25. It is observed that Q strongly influences the extinction coefficients with α and β increasing with the flow rate. An almost constant value of the extinction coefficients is reached, for the reactor geometry of Photo-CREC Water-II at a flow rate of 12 L min^{-1}. Further increases in Q seem to have little effect on the values of the extinction coefficients.

Two factors appear to be the cause of this behavior: catalyst distribution and particle agglomeration. At very low flow rates, there is some extent of uneven catalyst distribution. Catalyst is accumulated in some reactor sections being, as well, in lower concentrations in the flowing suspension promoting smaller extinction coefficients. At relative higher flow rates, however, catalyst particles are better distributed, and the particle agglomerates tend to be smaller due to an increase in the agitation yielding larger extinction coefficients. Further increases in the flow rate, above 12 L min^{-1}, had little effect on the values of the extinction coefficient.

CuuDuongThanCong.com https://fb.com/tailieudientucntt

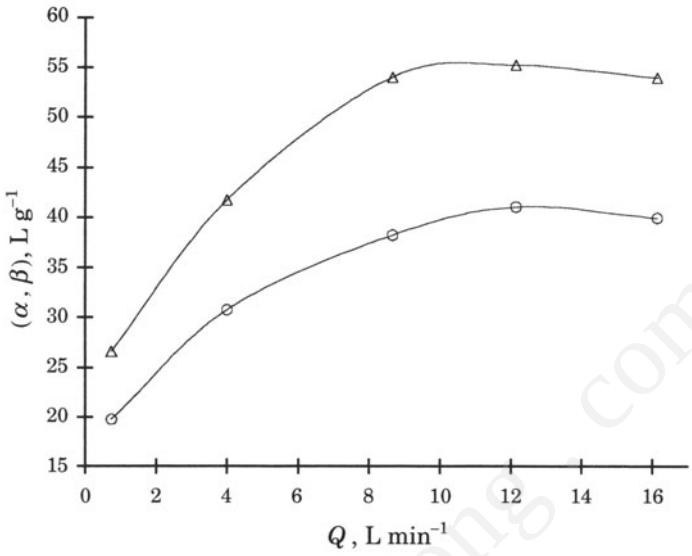

FIGURE 4.20. Effective extinction coefficients versus flow rate for Degussa P25. Keys: (Δ)β extinction coefficient, (o) α effective extinction coefficient, (Reprinted from *Chem. Eng. J.*, **90**, M. Salaices, B. Serrano and H.I. de Lasa, Experimental evaluation of photon absorption in an aqueous TiO_2 slurry reactor, 219–229, Copyright 2002, with permission from Elsevier).

4.4.2. Average Particle and Agglomerate Sizes

Figures 4.21 through 4.26 illustrate typical scanning electron micrographs of the various TiO_2 samples studied.

Based on the reported micrographs of Figures 4.21 to 4.26 and additional scanning electron micrographs (not include here), the particle size range (d_{pr}) and the volume equivalent particle size (d_p) was determined (Salaices, 2002). The only exception was Hombikat where particles agglomerates as irregular filaments 20-nm wide and 70-400 nm long. Under these conditions the volume equivalent particle size could not be calculated.

Regarding Hombikat UV-100 (micrograph not shown), this is a photocatalyst that tends to form large agglomerates of particles, but given its extremely small primary

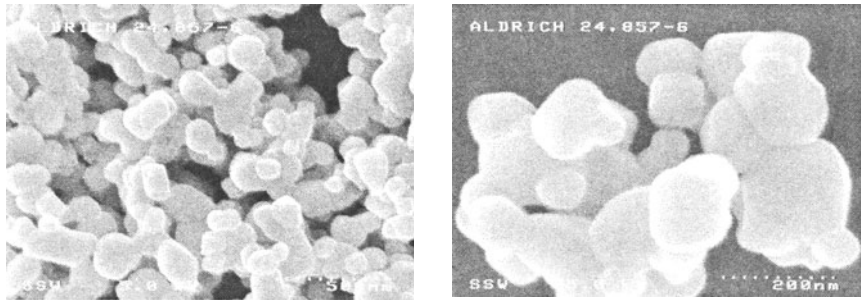

FIGURE 4.21. Scanning electron micrographs of Anatase 1. View of primary particles at two amplification levels.

CuuDuongThanCong.com https://fb.com/tailieudientucntt

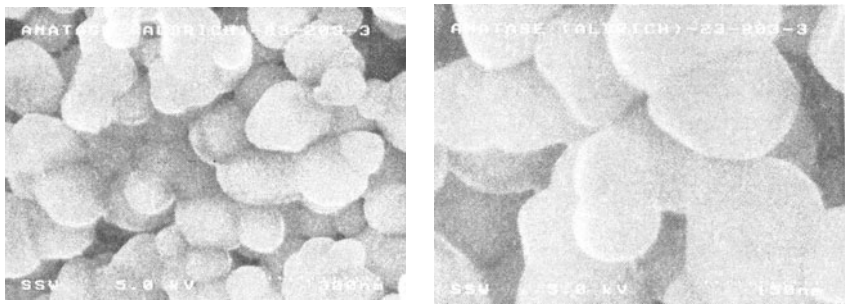

FIGURE 4.22. Scanning electron micrographs of Anatase 2. View of primary particles at two amplification levels.

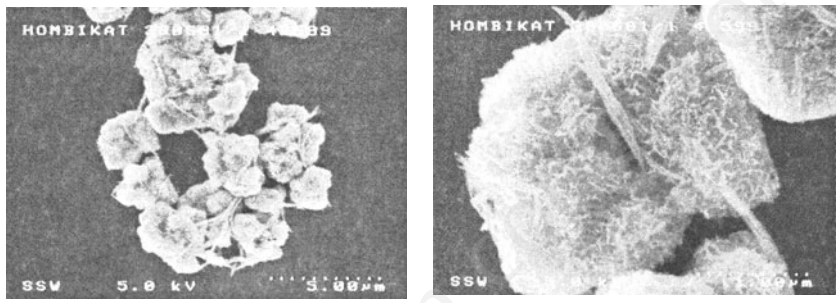

FIGURE 4.23. Scanning electron micrographs of Hombikat UV-100. View of primary particles at two amplification levels.

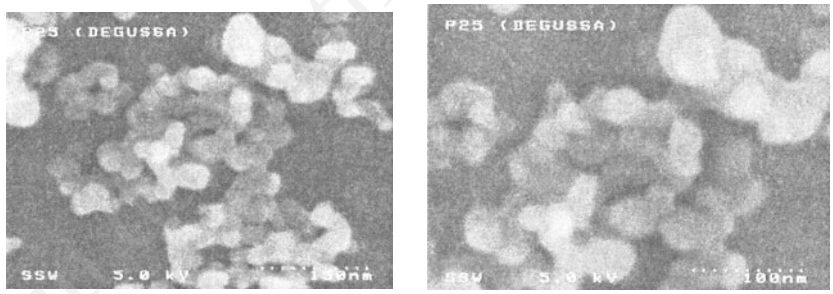

FIGURE 4.24. Scanning electron micrographs of Degussa P25. View of primary particles at two amplification levels.

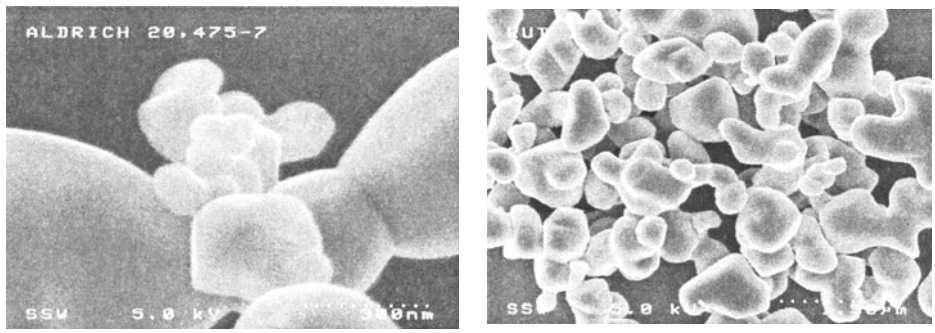

FIGURE 4.25. Scanning electron micrographs of Rutile 1. View of primary particles at two amplification levels.

CuuDuongThanCong.com https://fb.com/tailieudientucntt

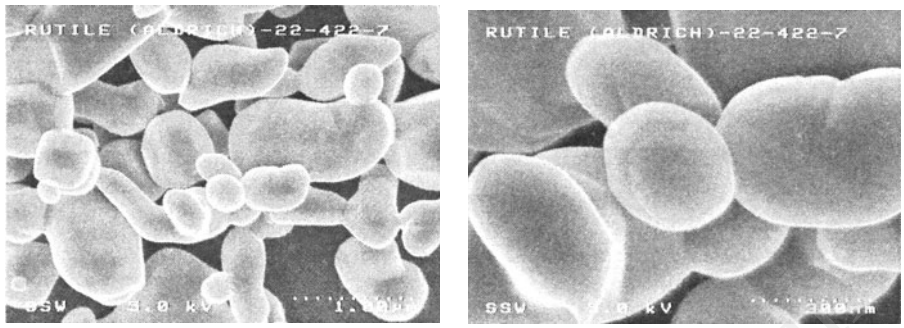

FIGURE 4.26. Scanning electron micrographs of Rutile 2. View of primary particles at two amplification levels.

particle size (d_p ~10 nm, Ibrahim, 2001) the primary particles (d_{pr}) could not be identified in the scanning electron micrographs.

The d_{pr} and d_p parameters for the TiO_2 samples are reported in the 2nd and 3rd columns of Table 4.6. Thus, the Hombikats are the catalysts with the smallest d_p, followed by Degussa P25, Anatase 1, Anatase 2, Rutile 1, and Rutile 2. The two Rutile catalysts, Rutile 1 and Rutile 2, provide as well, the largest spread of particle sizes.

Concerning the particle agglomeration based on the mean diameter of the solid powders dispersed in water, $d_{a[1,0]}$, most of the samples exhibit a significant degree of agglomeration.

$d_{a[1,0]}$ values are reported in the 4th column of Table 4.6 for each semiconductor material. The ratio between $d_{a[1,0]}$ and d_p, 5th column, is used to evaluate the extent of agglomeration. For instance, Degussa P25 shows a $d_{a[1,0]}/d_p$ ratio as large as 42, whereas the $d_{a[1,0]}/d_p$ ratios are restricted to the range 4 to 7 for other catalysts, excluding the Hombikat variety.

Thus, it can be observed that there is significant agglomeration in the case of the small particle catalyst such as Degussa P25. In addition, particle agglomeration in sizes of at least 2 times larger than the wavelengths of the incident radiation ($\bar{\lambda}_{300}^{400} \approx 348$ nm) allows the application of geometrical optics for the treatment of the radiation transfer through the slurry media (Siegel and Howell, 1992).

TABLE 4.6. Primary particle size ranges and mean diameters of various titanium dioxide samples

Sample	d_{pr}, nm	d_p, nm	$d_{a[1,0]}$, nm	$d_{a[1,0]}/d_p$
Anatase 1	80–180	134	750	6
Anatase 2	100–200	146	1050	7
Hombikat	10–70[m]	–	1540	–
Hombikat UV-100	10[m]	–	1275	–
Degussa P25	20–60	32	1340	42
Rutile 1	300–900	496	2300	5
Rutile 2	160–1060	576	2400	4

[m] Manufacturer's data.

CuuDuongThanCong.com https://fb.com/tailieudientucntt

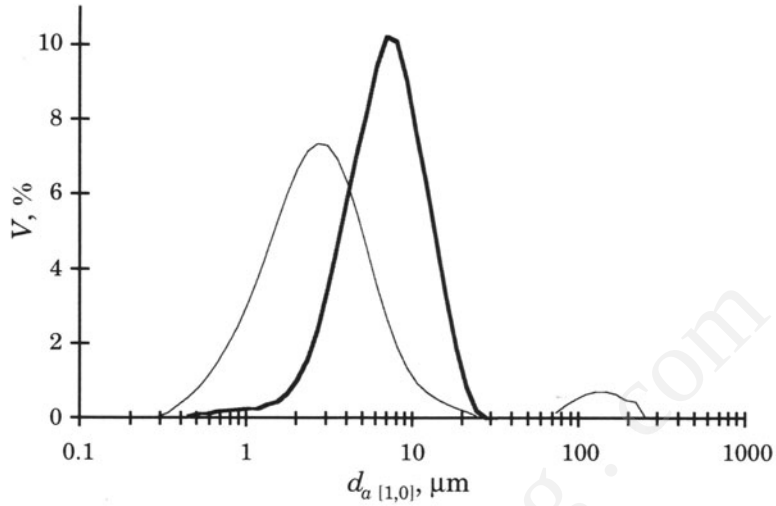

FIGURE 4.27. Particle size distribution variation for a Degussa P25 suspension: after sonication (—) and after one hour mixing in the reactor following sonication (—).

Figure 4.27 displays typical particle size distributions in volume percentage for Degussa P25, as obtained using the Malvern Mastersizer 2000 particle size analyzer. Particle size distributions correspond to one obtained immediately after sonication and another obtained after one-hour of mixing in the reactor at a flow rate of 16 L min^{-1}. As it can be observed, there is a shift in the maximum of the size distribution towards larger particle sizes due to particle agglomeration.

A similar change in the particle size distribution towards larger particle sizes can also be observed for Hombikat UV 100, as presented in Figure 4.28. Thus, the small primary particle size of Hombikat UV-100, provides a strong tendency to form agglomerates.

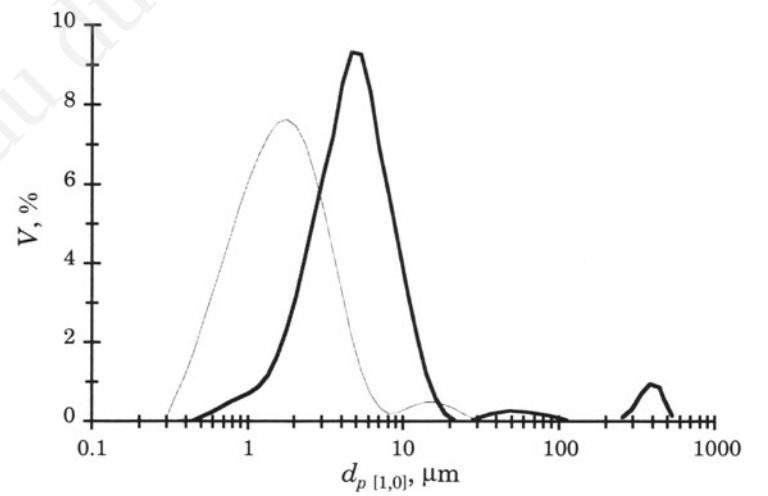

FIGURE 4.28. Particle size distribution variation for a Hombikat UV 100 suspension: after sonication (—) and after one hour mixing in the reactor following sonication (—).

CuuDuongThanCong.com https://fb.com/tailieudientucntt

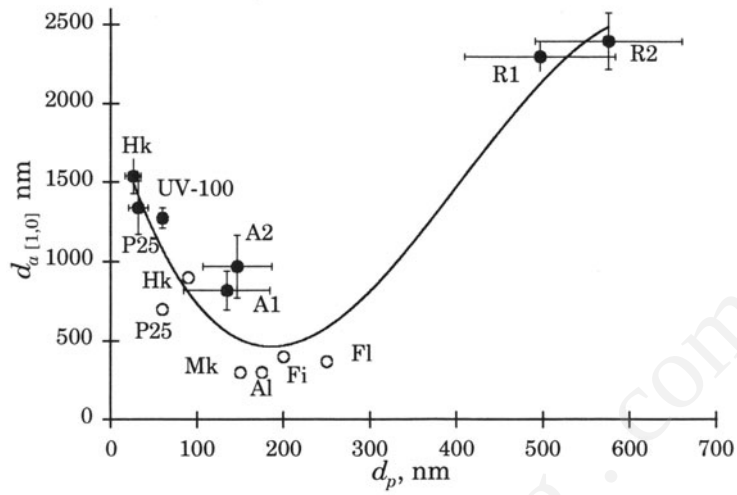

FIGURE 4.29. Average particle agglomerate diameter versus volume-equivalent particle diameter: Filled circles report data from Salaices et al (2002), open circles report data from Cabrera et al., (1996): A1 – Anatase 1, A2 – Anatase 2, Al – Aldrich, Fi – Fisher, Fl – Fluka, Hk – Hombikat, Mk – Merck, P25 – Degussa P25, R1 – Rutile 1, R2 – Rutile 2, and UV-100 – Hombikat UV-100. Horizontal bars represent standard deviations (Reprinted from *Chem. Eng. J.*, **90**, M. Salaices, B. Serrano and H.I. de Lasa, Experimental evaluation of photon absorption in an aqueous TiO_2 slurry reactor, 219–229, Copyright 2002, with permission from Elsevier).

Figure 4.29 compares $d_{a[1,0]}$ versus d_p for the various catalysts. Data from Salaices et al (2002) and from Cabrera et al. (1996) are reported with filled circles and open circles respectively.

As it can be observed, the $d_{a[1,0]}$ values decrease with the reduction of d_p until they reach a minimum value of around 300 nm for d_p in the range 150–300 nm.

From this region and on, as a result of an increasing influence of interparticle surface forces (presumably van der Waals' interactions), the agglomerate size starts to increase as particle diameter is further decreased.

Figure 4.30 reports the specific extinction coefficient, $\beta_{s\ cat}$ versus $d_{a_{[1,0]}}$ for the various catalysts studied by Salaices et al (2002) (filled circles) and for the values reported in the literature (Cabrera et al., 1996) (open circles). Standard deviations are included as error bars. It can be noticed that $\beta_{s\ cat}$ consistently increases as the agglomerate size decreases. In this respect, the Rutiles exhibit the lowest $\beta_{s\ cat}$ coefficients given that they form the largest agglomerates. Under these conditions, and consistently with the experimental data, larger $d_{a_{[1,0]}}$ values lead to smaller irradiated cross-sectional areas per unit volume, giving as a result, smaller extinction coefficients. This decrease of $\beta_{s_{cat}}$ with increasing particle agglomerate size explains the important role played by the size of the agglomerate on the extinction coefficient with the smaller agglomerates increasing absorption-scattering radiation and yielding larger extinction coefficients.

It can also be observed that the agglomerate sizes, found by Salaices et al (2002) (filled circles), are larger than those reported by Cabrera et al., (1996) and consequently the extinction coefficients observed are smaller. It is hypothesized that the differences observed in both parameters, $d_{a[1,0]}$ and $\beta_{s\ cat}$, are due to differences in the agglomeration state. Consistently, it is observed that there is a decrease in the extinction coefficient with

CuuDuongThanCong.com https://fb.com/tailieudientucntt

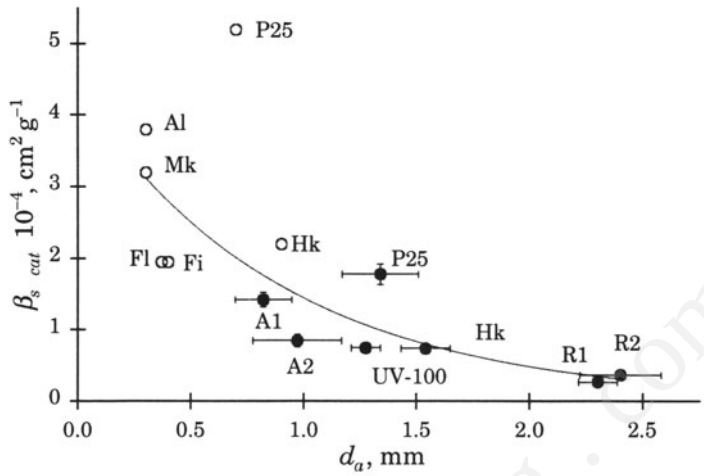

FIGURE 4.30. Extinction coefficient versus average agglomerate size: Filled circles represent data from Salaices et al (2002); open circles represent data from Cabrera et al., (1996); A1 – Anatase 1; A2 – Anatase 2; Al – Aldrich; Fi – Fisher; Fl – Fluka; Hk – Hombikat; Mk – Merck; P25 – Degussa P25; R1 – Rutile 1; Rutile 2- R2; and UV-100 – Hombikat UV-100 (Reprinted from *Chem. Eng. J.*, **90**, M. Salaices, B. Serrano and H.I. de Lasa, Experimental evaluation of photon absorption in an aqueous TiO_2 slurry reactor, 219–229, Copyright 2002, with permission from Elsevier).

the elapsed time once the suspension is sonicated. Thus, extinction coefficients estimated at different times with respect to the sonication time are different, with these coefficients being smaller for the longer times elapsed after sonication.

4.4.3. Radiation Wavelength

Spectroradiometric measurements permit the estimation of the wavelength specific (non-averaged) extinction coefficients, whereas radiometric transmission measurements allow for the determination of overall extinction coefficients.

Figure 4.31 displays the dependence of the effective extinction coefficients, $\alpha_{cat\ \lambda}$ on the radiation wavelength for both, Degussa P25, and Hombikat UV-100 catalysts.

For the radiation wavelength range analyzed, $\alpha_{cat\ \lambda}$ decreased with the increasing of λ. Regarding the differences between $\alpha_{cat\ \lambda}$ for Degussa P25 and Hombikat UV-100, the following can be noticed: a two-fold difference in the $\alpha_{cat\ \lambda}$ values for the 290 to 330 nm range; a decrease in the difference in the $\alpha_{cat\ \lambda}$ values until an approximate 20% difference with respect to $\alpha_{P25\ \lambda}$ is reached in the 330 to 350 nm wavelengths; and an almost constant difference in the $\alpha_{cat\ \lambda}$ values above 350 nm.

Thus, given the preferential radiation absorption in the lower wavelengths, a change in shape of the transmission spectra is observed for both catalysts. Typical transmission spectra for Hombikat UV-100 using the BL lamp are illustrated in Figure 4.32. These measurements were taken at window four, at 5.5 cm from the lamp surface. The catalyst concentration was varied from 0 to 0.258 g L^{-1}.

As it can be observed, the transmission spectra describing the intensity distribution change with the addition of catalyst both in strength and shape. With respect to the changes of light intensity spectra with catalyst loading, it can be stated that

CuuDuongThanCong.com https://fb.com/tailieudientucntt

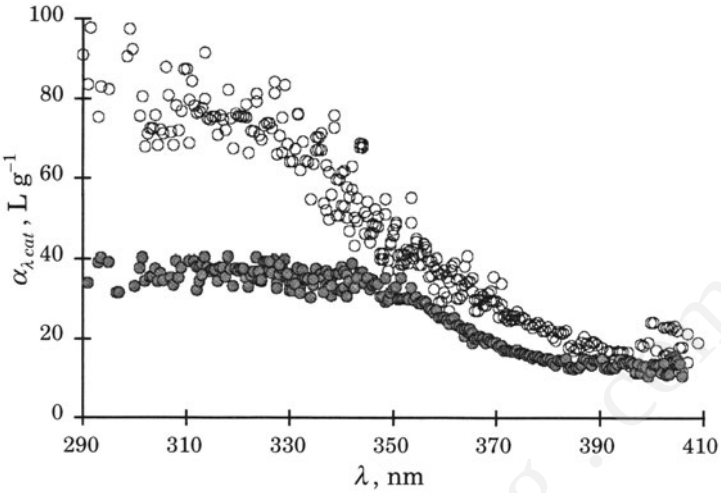

FIGURE 4.31. Effective extinction coefficient spectra for Degussa P25 (o) and Hombikat UV-100 (•) (Reprinted with permission from *Ind. Eng. Chem. Res.*, **40**(23), M. Salaices, B. Serrano and H.I. de Lasa, Photocatalytic conversion of organic pollutants: Extinction coefficients and quantum efficiencies, 5455–5464. Copyright 2001, Amrican Chemical Society).

absorption-scattering interactions of light increase with catalyst concentration add. A result is a decrease in the radiation transmission and absorption-scattering interactions much more significant at the lower wavelengths (290–350 nm) than at the higher wavelengths (350–400 nm). Therefore, consistently with the extinction coefficients changes with radiation wavelength, the TiO_2 suspension acts as a radiation filter, preferentially reducing the influence of the lower wavelength radiation.

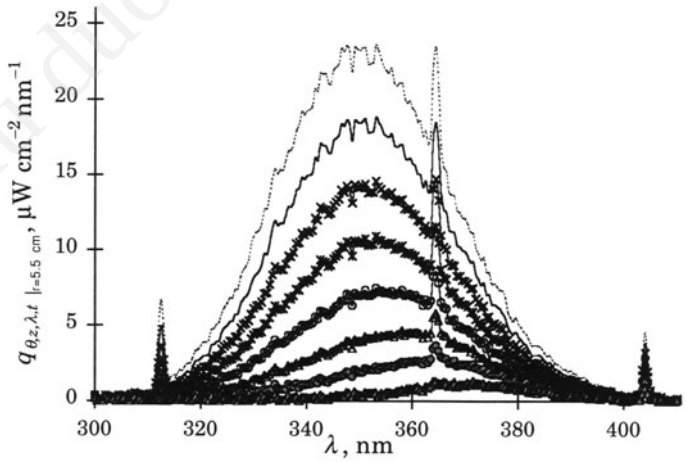

FIGURE 4.32. Transmission spectrum 5.5 cm from the lamp surface for several Hombikat UV-100 concentrations in g L^{-1}. (- - -) 0.0, (—) 0.017, (×) 0.033, (*) 0.05, (o) 0.075, (Δ) 0.108, (•) 0.150, and (*black* Δ) 0.258 (Reprinted with permission from *Ind. Eng. Chem. Res.*, **40**(23), M. Salaices, B. Serrano and H.I. de Lasa, Photocatalytic conversion of organic pollutants: Extinction coefficients and quantum efficiencies, 5455–5464, Copyright 2001 American Chemical Society).

CuuDuongThanCong.com https://fb.com/tailieudientucntt

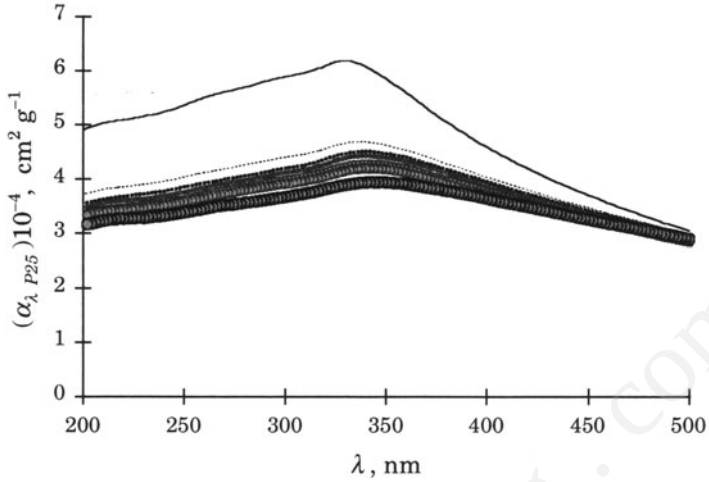

FIGURE 4.33. Degussa P25 specific effective extinction coefficient Evolution with λ and time after sonication: (—) 0, (- - -) 10, (·) 20, (•) 40, (•) 110, (●) 180, and (●) 443 min.

Figure 4.33 reports the spectrum evolution of the specific effective extinction coefficient for Degussa P25. The coefficients can be determined from the UV-Visible spectrophotometric measurements of a Degussa P25 suspension after sonication.

Thus the extinction coefficient spectrum changes both in strength and shape as time elapses after sonication. This dynamic behavior can be explained in terms of the state of the agglomerates. Starting from the initial agglomeration state, the suspension of particles tends to re-agglomerate again and this agglomeration process depends on the mixing conditions.

Figure 4.34 reports the evolution of the averaged specific extinction coefficients with elapsed time after sonication for several TiO_2 catalysts. As it can be noticed, $\alpha_{cat}(t)$

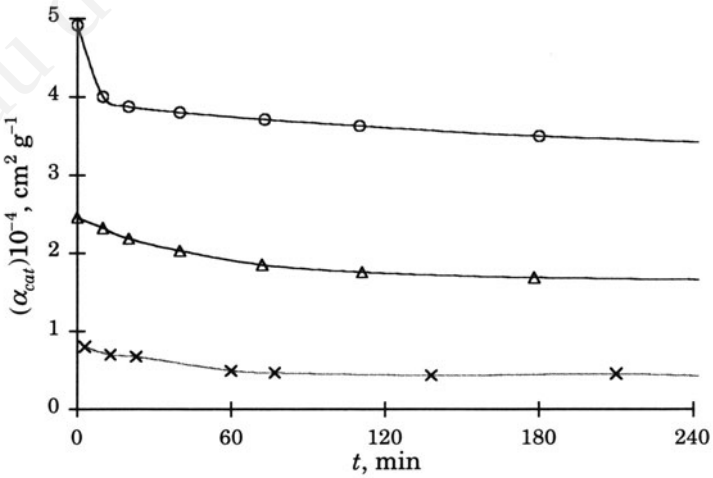

FIGURE 4.34. Evolution of the averaged effective specific extinction coefficients for several TiO_2 catalysts: (o) Degussa P25, (Δ) Hombikat UV-100, and (×) Rutile 1.

CuuDuongThanCong.com https://fb.com/tailieudientucntt

for Degussa P25 experiences a quick decrease to 20% of its original value in about a 10 minute period with the $\alpha_{cat}(t)$ coefficient continuously decreasing as time progresses. Regarding Hombikat UV-100 and Rutile 1 samples, an initial decrease in $\alpha_{cat}(t)$ can be noticed until an almost constant value is reached. For Degussa P25, this behavior can be explained in terms of a quick particle agglomeration followed by a much slower agglomeration process. For Hombikat and Rutile 1, however, only the slow period of agglomeration is observed. It can be stated that the variation of the optical properties of the suspension, linked essentially to the agglomeration processes, is an important parameter to be considered in the estimation of optimum radiation transmission conditions and of catalyst loading.

4.5. CONCLUSIONS

The following are the significant conclusions of the present chapter:

a) Lamps with long periods of usage may present uneven light emission that can influence the photoreactor performance.
b) Radiometric and spectroradiometric measurements in a concentric tubular TiO_2 slurry reactor allow the determination of the lamp radiation field, including axial, radial, and energetic distribution of the radiative flux. Inner polished and plastic UV-opaque collimators, connecting the fused silica windows to a radiometer, help in the determination of the rate of absorption of photons.
c) This method specifically developed for the evaluation of the rate of absorption of photons in an aqueous TiO_2 slurry reactor, allows the estimation of the total radiation transmission, of the non-scattered radiation transmission, and of the back-scattered photons exiting the system.
d) Total radiation transmission and non-scattered radiation transmission can be modeled using relatively simple exponential decay relationships. These decay functions incorporate extinction coefficients (α and β) and the influence of the TiO_2 concentration. It is proven that the extinction coefficient decrease with the agglomerate size, with this dimension being affected by the average agglomerate size.
e) Extinction coefficients in TiO_2 slurry suspension are a strong function of the radiation wavelength. The more energetic photons are absorbed-scattered preferentially with respect to the less energetic photons for both Degussa P25 and Hombikat UV-100.

NOMENCLATURE

Symbols

c	speed of light	$m\ s^{-1}$
cl	collimator length	cm
C	Concentration	$g\ L^{-1}$ or $M\ L^{-1}$

CuuDuongThanCong.com https://fb.com/tailieudientucntt

C_{cat}	Catalyst concentration	g L^{-1}
D	diameter, distance, or size	nm, cm
$d_{a_{[1,0]}}$	agglomerate mean diameter	$\sum_{n=1}^{\#\ part} d_i/n$
dp	primary particle diameter	nm
dp_r	primary particle diameter range	nm
f	proportionality factor	-
f_{ac}	proportionality factor for the UV-reflecting collimator	-
f_{ci}	proportionality factor for i collimator	-
h	Planck's constant	J s $photon^{-1}$
I_λ	specific intensity	Einstein m^{-2} s^{-2}
k_λ	radiation absorption coefficient	L g^{-1}
K	ratio between the diameters of the inner to the outer concentric tubes	-
ℓ	optical thickness	cm
$P(\vec{r}' \rightarrow \vec{r})$	phase function	-
P	rate of photons	Einstein s^{-1}
$P_a(t)$	rate of absorbed photons	Einstein s^{-1}
$P_{a-wall}(t)$	Rate of photons absorbed by the wall	Einstein s^{-1}
$P_{bs}(t)$	rate of back scattered photons	Einstein s^{-1}
$P_{fs}(t)$	rate of forward scattered photons	Einstein s^{-1}
$P_i(t)$	rate of incident photons reaching the external wall of the inner reactor tube	Einstein s^{-1}
P_{i0}	rate of incident photons reaching the inner wall of the out reactor tube at zero time of lamp of utilization (t = 0)	Einstein s^{-1}
$P_l(t)$	rate of photons emitted by the lamp	Einstein s^{-1}
P_{l0}	rate of photons emitted by the lamp at zero time of utilization (t = 0)	Einstein s^{-1}
$P_{nfs}(t)$	rate of normal forward scattered photons	Einstein s^{-1}
$P_t(t)\big\vert_{C_c \rightarrow 0}$	rate of transmitted of transmitted photons for a catalyst concentration approaching the zero level	Einstein s^{-1}
$P_{tns}(t)$	rate of transmitted non-scattered radiation (directly transmitted radiation)	Einstein s^{-1}
$q_{\theta,z,t}$	radiative flux over the lamp emission spectrum	J s^{-1} m^{-2}
$q_{\theta,z,t}\big\vert_{r=r_w}$	radiative flux over the lamp emission spectrum evaluated r = r_w (reactor inner wall)	J s^{-1} m^{-2}
$q_{\theta,z,\lambda,t}$	radiative flux for a given wavelength	J s^{-1} m^{-3}
q_l	radiative flux at the lamp surface based on the lamp nominal power	W cm^{-2}
$q_{ac,\theta,z,t}$	radiative flux over the lamp emission spectrum for the reflective UV-collimator	W cm^{-2}

CuuDuongThanCong.com https://fb.com/tailieudientucntt

$q_{ac,\theta,z,t\|C_{cat}\to 0}$	radiative flux over the lamp emission spectrum for the reflective UV-collimator for the condition of $C_{cat} \to 0$	W cm^{-2}
$q_{bc,\theta,z,t}$	radiative flux over the lamp emission spectrum for the opaque UV-collimator	W cm^{-2}
$q_{bc\ \theta,z,t\|C_{cat}\to 0}$	radiative flux over the lamp emission spectrum for the opaque UV-collimator for the condition of $C_{cat} \to 0$	W cm^{-2}
q_{ci}	radiative flux detected using collimator i	W cm^{-2}
$q_{0,\theta,z,t}$	Radiative flux reaching the external wall of the inner reactor tube	W cm^{-2}
$q_\lambda(\vec{r}, s)$	radiative flux	J s^{-1} m^{-3}
Q	volumetric flow rate	L s^{-1}
r_w	Radial coordinate for the inner surface of the outer reactor tube	m
r_{wo}	Radial coordinate for the external surface of the inner reactor tube	m
R	radial coordinate, radius	m
R^2	least-squares regression coefficient	-
Re	Reynolds number	-
t	Time	s, h
U	Velocity	m s^{-1}
$< V_Z >$	average flow axial velocity,	m s^{-1}
W	Lamp power	watts
z	axial coordinate	m

Greek letters

α		
α_v	effective extinction coefficient	L g^{-1}
β	true extinction coefficient or decay coefficient	L g^{-1}, s^{-1}
β_s	specific extinction coefficient	cm^2 g^{-1}
η	Efficiency	-
λ	radiation wavelength	nm, m
μ	suspension viscosity	kg (m s)$^{-1}$
ω	Solid angle	sr
σ_λ	Scattering coefficient	L g^{-1}
σ		
θ	angle in cylindrical coordinates	rad
ρ	Suspension density	kg m^{-3}

Subscripts

0	evaluated at initial or boundary conditions
a	absorbed, agglomerate
ac	detected using the UV-reflecting collimator
a-wall	absorbed by the inner glass wall

cuu duong than cong . com

CuuDuongThanCong.com https://fb.com/tailieudientucntt

bc	detected using the UV-opaque collimator
bs	backscattered
cat	catalyst
$C \rightarrow 0^+$	catalyst concentration approaching to zero from the right-hand side of the $dP_t(t)/dC$ discontinuity
ci	collimator i^{th}
fs	forward scattered
i	evaluated at inner reactor surface, incident
l	lamp
m	manufacturer
nfs	normal forward scattered
o	evaluated at outer surface of inner tube
p	particle
P25	Degussa P25
pr	particle size range
s	specific
tns	transmitted non-scattered
t	transmitted
tp	related to particle terminal velocity
w	corresponding to the window surface or reactor

Superscripts

$\bar{x}$	average value of the variable x

Acronyms

BL	black light
CF	correction factor
ESSDE	extensive source superficial diffuse emission
LTU	lamp testing unit
MR	midrange
P25	Degussa P25 catalyst
RTE	radiation transport equation
UV	ultraviolet

REFERENCES

Alfano, O. M., Cabrera, M. I., Cassano, A. E., 1994, Modelling of light scattering in photochemical reactors. *Chem. Eng. Sci.*, **49:**5327–5346.

Augugliaro, V., Palmisano, L., Schiavello, M., 1991, Photon absorption by aqueous TiO_2 dispersion contained in a stirred photoreactor. *AIChE J.*, **37:**1096–1100.

Augugliaro, V., Palmisano, L., Schiavello, M., Scalfani, A., 1995, Heterogeneous photocatalytic systems: Influence of some operational variables on actual photons absorbed by aqueous dispersions of TiO_2, *Solar Energy Materials and Solar Cells*, **38:**411–419.

CuuDuongThanCong.com https://fb.com/tailieudientucntt

Bahnemann, D., Bockelman, D., Goslich, R., 1991, Mechanistics studies on water detoxification in illuminated TiO_2 suspensions, *Solar Energy Materials*, **24:**564–583.

Brandi, R. J., Alfano, O. M., Cassano, A. E., 1996, Modeling of radiation absorption in a flat plate photocatalytic reactor. *Chem. Eng. Sci.,* **51:**3169–3174.

Brandi, R. J., Alfano, O. M., Cassano, A. E., 1999, Rigorous model and experimental verification of the radiation field in a flat-plate solar collector simulator employed for photocatalytic reactions. *Chem. Eng. Sci.*, **54**(13)**:**2817–2827.

Brandi, R. J., Alfano, O. M., Cassano, A. E., 2000, Evaluation of radiation absorption in slurry photocatalytic reactors. 1. Assessment of methods in use and new proposal. *Environ. Sci. Technol.*, **34**(12)**:**2623–2630.

Brucato, A., Rizzuti, L., 1997a, Simplified modeling of radiant fields in heterogeneous photoreactors. 1. Case zero reflectance. *Ind. Eng. Chem. Res.,* **36:**4740–4747.

Brucato, A., Rizzuti, L., 1997b, Simplified modeling of radiant fields in heterogeneous photoreactors. 2. Limiting "two-flux" model for the case of reflectance greater than zero. *Ind. Eng. Chem. Res.,* **36:**4748–4755.

Cabrera, M. I., Alfano, O. M., Cassano, A. E., 1994, Novel reactor for photocatalytic kinetic studies. *Ind. Eng. Chem. Res.,* **33:**3031–3042.

Cabrera, M. I., Alfano, O. M., Cassano, A. E., 1996 Absorption and scattering coefficients of titanium dioxide particulate suspensions in water. *J. Phys. Chem.,* **100:**20043–20050.

Cassano, A. E., Martin, C. A., Brandi, R. J., Alfano, O.M., 1995, Photoreactor analysis and design: fundamentals and applications. *Ind. Eng. Chem. Res.*, **34:**2155–2201.

Ibrahim, H., 2001, Photocatalytic reactor for the degradation of air borne pollutants. Photoconversion efficency and kinetic modeling, PhD Dissertation, University of Western Ontario, Canada.

Martin, C. A., Baltanas, M. A., Cassano, A. E., 1996a, Photocatalytic reactors 1. Quantum efficiencies allowing for scattering effects. An experimental approximation. *J. Photochem. Photobiol. A: Chem.*, **94:**173–189.

Martin, C. A., Baltanas, M. A., Cassano, A. E., 1996b, Photocatalytic reactors 3. Kinetics of the decomposition of chloroform including absorbed radiation effects. *Environ. Sci. Tech.,* **30**(7)**:**2355–2364.

Matthews, R. W., McEvoy, S. R., 1992, Destruction of phenol in water with sun, sand, photocatalysis. *Solar Energy*, **49**(6)**:**507–513.

Mills, G., Hoffmann, M. R., 1993, Photocatalytic degradation of pentachlorophenol on TiO_2 particles: Identification of intermediates and mechanism of reaction. *Environ. Sci. Tech.,* **27:**1681–1689.

Palmisano, L., Augugliaro, V. and Campostrini, R., 1993, A proposal for the quantitative assessment of heterogeneous photocatalytic processes. *J. Catal.,* **143:**149–154.

Pasqualli, M., Santarelli, F., Porter, J. F., Yue, P. L., 1996, Radiative transfer in photocatalytic systems. *AIChE J.,* **42:**532–537.

Pruden, A. L., Ollis, D. F., 1983, Photoassisted heterogeneous photocatalysis: The destruction of trichloroethylene in water. *J. Cat.*, **82:**404–417.

Romero, R. L., Alfano, O. M., Cassano, A. E., 1997, Cylindrical photocatalytic reactors. Radiation absorption and scattering effects produced by suspended fine particles in an annular space. *Ind. Eng. Chem. Res.*, **36:**3094–3109.

Salaices, M., Serrano, B., de Lasa, H., 2001, Photocatalytic conversion of organic pollutants. Extinction coefficients and quantum efficiencies, *Ind. Eng. Chem. Res.*, **40:**5455–5464.

Salaices, M., 2002, Photocatalyis in Slurry Reactors. Radiation Transmission and Kinetic Modelling, PhD Dissertation, University of Western Ontario, Canada.

Salaices, M., Serrano, B., de Lasa H., 2002, Experimental evaluation of photon absorption in an aqueous TiO_2 slurry reactor, *Chem. Eng. J.*, **90:**219–229.

Schiavello, M., Augugliaro, V., Palmisano, L., 1991, An Experimental method for the determination of the photon flow reflected and adsorbed by aqueous dispersions containing polycrystalline solids in heterogeneous photocatalysis. *J. Catal.* **127:**332–341.

Siegel, R., and Howell, J. R., 1992, *Thermal Radiation Heat Transfer*, 3rd ed.; Hemisphere Publishing Co.: Bristol, PA.

Tsekov, R., Smirniotis, P.G., 1997, Radiation filed in a continuous annular photocatalytic reactors role of the lamp of finite size, *Chem. Eng. Sci.* **52:**1667–1671.

Turchi, C. S., Ollis, D. F., 1989, Mixed reactant photocatalysis: Intermediates and mutual rate inhibition. *J. Catal.,* **119:**483–496.

CuuDuongThanCong.com https://fb.com/tailieudientucntt

5

Kinetic Modeling of the Photocatalytic Reaction Network: The Parallel-Series Approximation

5.1. KINETIC MODELING OF THE PHOTOCATALYTIC CONVERSION OF PHENOLIC COMPOUNDS: GENERAL OVERVIEW

Photocatalytic oxidation of phenol has been studied at a laboratory scale by several researchers (Al-Ekabi and Serpone, 1988; Matthews and McEvoy, 1992; Okamoto et al., 1985b; Tseng and Huang, 1990; Wei and Wan, 1992; Winterbottom et al., 1997). Phenol is a chemical species difficult to convert in conventional bio-treatment processes. Phenol is also a very useful model contaminant in photocatalytic research for ranking reactor performance.

Phenol is photooxidized via its hydroxylated compounds into CO_2 and H_2O. Para-dihydroxybenzene (*p-DHB*), ortho-dihydroxybenzene (*o-DHB*) and 1,2,3-trihydroxybenzene (1,2,3-*THB*) are identified as primary and secondary hydroxylation products (Al-Ekabi & Serpone, 1988). 1,2,4-trihydroxybenzene (1,2,4-*THB*) and 1,4-benzoquinone (1,4-*BQ*) are also documented as intermediate species. These species appear to be present prior to the total phenol mineralization (Trillas *et al.*, 1996; Winterbottom *et al.*, 1997). Tseng and Huang (1990) reported two intermediate species, *p-DHB* and 1,4-*BQ*, during the photodegradation of 5.10^{-2} mole/L^{-1} of phenol. Several other species are also suspected as possible intermediates with their formation following the aromatic ring break up: muconic acid, maleic acid, oxalic acid, formic acid, and acetic acid. Researchers have however, experienced difficulty until now to directly detect these species.

Photocatalytic conversion of phenol has been studied extensively, as stated above. Several issues remain, however, to be clarified such as the quantification of intermediate species and the kinetic rate modeling.

A parallel-series reaction model, based on the chemical species' concentrations in the liquid phase was proposed by Salaices et al. (2004) to describe the photodegradation of phenol under various operating conditions. These conditions include the variation of the initial pollutant concentration, the initial pH and the catalyst type.

CuuDuongThanCong.com https://fb.com/tailieudientucntt

The photocatalytic degradation of phenol over TiO_2 can be carried out in Photo-CREC-Water-II reactor. The experimental system and the experimental methods used are explained in Chapters II and III.

A 15-W black-light-blue lamp (BLB) with emission in the 300-410–nm wavelength range is used as radiation source. The initial emission of this lamp is assessed at 1.03. 10^{-5} einstein/s (3.5 W) using a 4D Controls Ltd spectroradiometer and a UVX digital radiometer (Salaices *et al.*, 2001). The initial total energy absorbed into the system is estimated at 2.66 W. This parameter can be corrected as needed, taking into account the lamp irradiation decay.

Degussa P25 (70–30% anatase-rutile CN 1610e) and Hombikat UV-100 (Sachtleben 100%-anatase, CAS–N 13463-67-7) samples are used at concentrations of 0.15 g/L^{-1} and 0.29 g/L^{-1} respectively. These catalyst concentrations do not allow radiation losses of more than 0.2% with respect to the radiation entering into the system. Losses of radiation can be established using several catalyst concentrations and can be estimated using radiometric and spectroradiometric measurements of the radiation transmitted through TiO_2 suspensions (Salaices *et al* 2002). Additional details are given in Chapter IV.

5.2. PHENOL PHOTOCONVERSION IN PHOTO CREC WATER-II REACTOR

Targeted experiments can be developed to investigate the phenol photocatalytic conversion mechanism (Salaices *et al.*, 2004). In this context, four main intermediates of phenol photo-degradation are identified: para-dihydroxybenzene ($p-DHB$), ortho-dihydroxybenzene ($o-DHB$), 1,2,4-trihydroxybenzene ($1,2,4-THB$), and 1,4-Benzoquinone ($1,4-BQ$).

The *p-DHB* is observed as the most abundant intermediate species in all the experiments. This species is, in many cases, followed in abundance by the *o-DHB*. When phenol is photoconverted over Degussa P25 at an initial pH of 7, maximum concentrations of *p-DHB* and *o-DHB* account for 15% and 7% of the initial concentration of phenol. The *o-DHB*, however, cannot be detected when the initial pH changes from 4 to 7 or when the catalyst changes from Degussa P25 to Hombikat *UV*-100. This indicates that both the pH and the catalyst type have important influence on the reaction path. Furthermore, the concentrations of 1,2,4-*THB* and 1,4-*BQ* remain below 3% of the initial phenol concentration for most of the operating conditions.

Figure 5.1 reports the changes of TOC (•) during the photo-conversion of 30.0 ppm-C of phenol on Degussa P25, at an initial pH of 4. This figure also shows the change in concentration of phenol (o) and of the main intermediate species (△, □, ◇, -) as well as the addition of the carbon masses of phenol and the various intermediate species (+).

At the beginning of the reaction, the curve representing the chemical species mass addition matches well the TOC curve. This indicates that most of the species remaining in the liquid phase are determined and quantified. At reaction times beyond 5 hours the species mass addition (+) curve consistently lays below the TOC curve. Greater separation between the two curves can be observed with increasing reaction times. In the worst case scenario, this difference is close to 10% of the initial phenol concentration and can be the result of two contributing factors: carbon-containing intermediate species

CuuDuongThanCong.com https://fb.com/tailieudientucntt

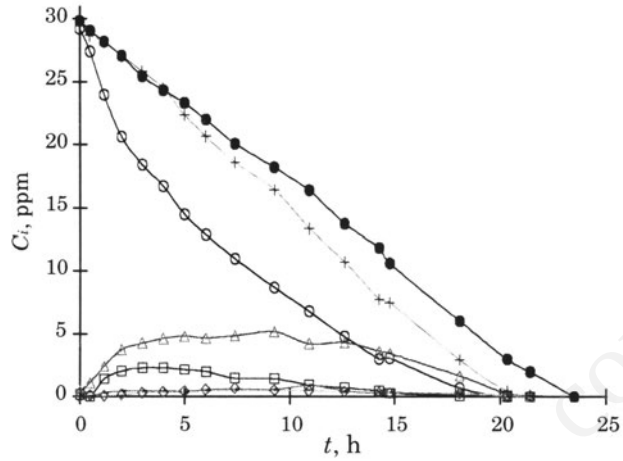

FIGURE 5.1. Concentration profiles of (o) phenol, (•) TOC,(△, □, ◇, -) intermediate species, and (+) species mass addition in the photodegradation of phenol over Degussa P25 at an initial pH of 4. (Reprinted from *Chem. Eng. Sci.*, **59**, M. Salaices, B. Serrano and H.I. de Lasa, Photocatalytic conversion of phenolic compounds in slurry reactors, 3–15, Copyright 2004, with permission from Elsevier).

that are neither detected nor quantified through HPLC and adsorption on the catalyst of detected and undetected intermediates.

5.3. THE PARALLEL-SERIES KINETIC MODEL APPROXIMATION

The proposed reaction mechanism uses the concentration curves corresponding to phenol and the observable intermediate species as a basis (Figure 5.1). This leads to the following observations: a) the phenol concentration decays consistently with a close to first order rate law, reaching an essentially zero concentration at the end of the experiment (complete phenol depletion); b) the detectable liquid phase concentrations of intermediate species initially rise and then diminish until they are virtually depleted; c) full depletion of the observable intermediate species occurs at times close to the complete depletion of phenol; d) the TOC drops monotonically, following essentially zero-order kinetics, indicating that there is already complete oxidation at very short reaction times.

These experimental observations call for a different mechanism than that proposed by Okamoto *et al.* (1985a). This parallel-in-series mechanism considers both *in-series* reaction steps where OH• groups are progressively incorporated in the phenol molecule and in the phenolic derived species, and *parallel* steps where the phenol molecule is being photo converted in oxidation steps of different strength. This *parallel-series* mechanism can be justified given the possible existence of a distribution of oxidation strengths of the photocatalytic sites.

The proposed *parallel-series* mechanism is summarized in Figure 5.2 and involves the following steps

a) Total oxidation of phenol to CO_2 ($r_{ph\rightarrow CO_2}$)
b) Partial oxidation of phenol to *p-DHB* ($r_{ph\rightarrow p-DHB}$)
c) Partial oxidation of phenol to *o-DHB* ($r_{ph\rightarrow o-DHB}$)
d) Partial oxidation of phenol to 1,4-*BQ* ($r_{ph\rightarrow 1,4-BQ}$)

CuuDuongThanCong.com https://fb.com/tailieudientucntt

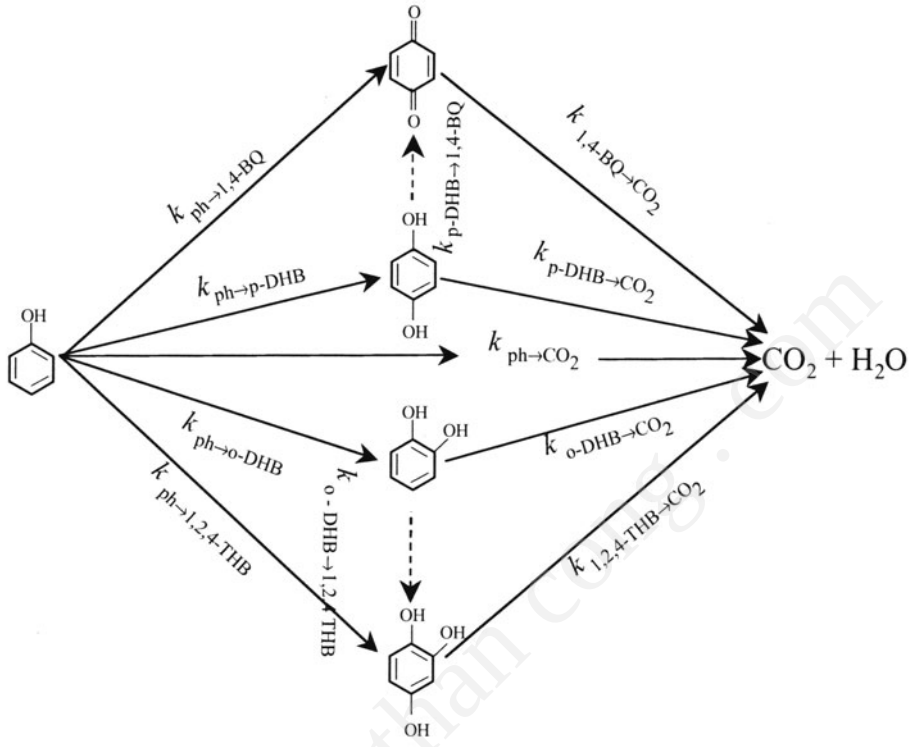

FIGURE 5.2. Proposed *parallel-series* reaction model based on the evolution of observable species on the liquid phase. Full arrows represent experimentally supported steps, whereas broken arrows represent possible steps, experimentally unconfirmed (Reprinted from *Chem. Eng. Sci.*, **59**, M. Salaices, B. Serrano and H.I. de Lasa, Photocatalytic conversion of phenolic compounds in slurry reactors, 3-15, Copyright 2004, with permission from Elsevier).

e) Partial oxidation of phenol to 1,2,4-*THB* ($r_{ph\rightarrow 1,2,4-THB}$)
f) Partial oxidation of *p-DHB* to 1,4-*BQ* ($r_{p-DHB\rightarrow 1,4-BQ}$)
g) Partial oxidation of *o-DHB* to 1,2,4-*THB* ($r_{o-DHB\rightarrow 1,2,4-THB}$)
h) Total oxidation of *p-DHB* to CO_2 ($r_{p-DHB\rightarrow CO_2}$)
i) Total oxidation of *o-DHB* to CO_2 ($r_{o-DHB\rightarrow CO_2}$)
j) Total oxidation of 1,4-*BQ* to CO_2 ($r_{1,4-BQ\rightarrow CO_2}$)
k) Total oxidation of 1,2,4-*THB* to CO_2 ($r_{1,2,4-THB\rightarrow CO_2}$).

The kinetic modeling of the photocatalytic conversion of phenol, involves important assumptions,

a) All identifiable species adsorb on the catalyst surface
b) There is no adsorption on the catalyst of the non-identifiable intermediate species
c) The CO_2 do not adsorb on the catalyst
d) All adsorption steps are considered at quasi-equilibrium with the steps involving surface adsorbed species controlling the overall reaction rate.

Concerning assumption c) and d) they can be justified on the basis of the studies and observations of Okamoto *et al.* (1985b).

CuuDuongThanCong.com https://fb.com/tailieudientucntt

Most of the described steps in the reaction mechanism can be supported via experimental observations (full lines in Figure 5.2), whereas others (broken lines in Figure 5.2) remain at this stage speculative. Some of these steps can be kept or dropped, as required, at the time of the estimation of kinetic parameters.

On the basis of these considerations, the following can be written (Ollis *et al.*, 1989):

$$r_i = \frac{v_i k_i^* K_i C_i}{1 + \sum_{j=1}^{n} K_j C_j} \tag{5-1}$$

where r_i is the reaction rate in mole $g_{cat}^{-1}\ s^{-1}$, k_i^* is the reaction kinetic constant for the species i in mole $g_{cat}^{-1}\ s^{-1}$, K_i and K_j are the specific adsorption constants for each of the i and j species participating in the reaction in L $mole^{-1}$, C_i is the species concentration in mole L^{-1}, n denotes the number of participant species, and i, j are the subscripts to denote the species involved in the photocatalytic reaction.

In a fluid-solid system (refer to Chapter I), the photocatalytic rate can be represented by

$$r_i = \frac{V}{W_{irr}} \frac{dC_i}{dt} \tag{5-2}$$

with W_{irr} being the mass of illuminated TiO_2 catalyst, g_{cat} and t the time, in s.

From equations (5-1) and (5-2), the change of concentration of the species i in the slurry can be expressed as

$$\frac{dC_i}{dt} = \frac{v_i k_i''' C_i}{1 + \sum_{j=1}^{n} K_j C_j} \tag{5-3}$$

$$k_i''' = \frac{W_{irr} k_i^* K_i}{V} = \frac{W_{irr} k_i}{V} \tag{5-4}$$

Consequently, the balance of various species including reactants and products (Figure 5.2) can be described by the following set of differential equations:

$$\frac{dC_{ph}}{dt} = (r_{ph\to o\text{-}DHB} + r_{ph\to p\text{-}DHB} + r_{ph\to 1,2,4\text{-}THB} + r_{ph\to 1,4\text{-}BQ} + r_{ph\to CO_2}) \frac{W_{irr}}{V}$$

$$= \frac{-(k'''_{ph\to o\text{-}DHB} + k'''_{ph\to p\text{-}DHB} + k'''_{ph\to 1,2,4\text{-}THB} + k'''_{ph\to 1,4\text{-}BQ} + k'''_{ph\to CO2}) C_{ph}}{1 + \sum_{j=1}^{5} K_j C_j} \tag{5-5}$$

$$\frac{dC_{p\text{-}DHB}}{dt} = (r_{ph\to p\text{-}DHB} + r_{p\text{-}DHB\to 1,4\text{-}BQ} + r_{p\text{-}DHB\to CO_2}) \frac{W_{irr}}{V}$$

CuuDuongThanCong.com https://fb.com/tailieudientucntt

$$= \frac{k'''_{ph\to p-DHB}C_{ph} - \left(k'''_{p-DHB\to 1,4-BQ} + k'''_{p-DHB\to CO_2}\right)C_{p-DHB}}{1 + \sum_{j=1}^{5} K_j C_j} \tag{5-6}$$

$$\frac{dC_{o-DHB}}{dt} = \left(r_{ph\to o-DHB} + r_{o-DHB\to 1,2,4-THB} + r_{o-DHB\to CO_2}\right)\frac{W_{irr}}{V}$$
$$= \frac{k'''_{ph\to o-DHB}C_{ph} - \left(k'''_{o-DHB\to 1,2,4-THB} + k'''_{o-DHB\to CO_2}\right)C_{o-DHB}}{1 + \sum_{j=1}^{5} K_j C_j} \tag{5-7}$$

$$\frac{dC_{1,2,4-THB}}{dt} = \left(r_{ph\to 1,2,4-THB} + r_{o-DHB\to 1,2,4-THB} + r_{1,2,4-THB\to CO_2}\right)\frac{W_{irr}}{V}$$
$$= \frac{k'''_{ph\to 1,2,4-THB}C_{ph} + k'''_{o-DHB\to 1,2.4-THB}C_{o-DHB} - k'''_{1,2,4-THB\to CO_2}C_{1,2,4-THB}}{1 + \sum_{j=1}^{5} K_j C_j} \tag{5-8}$$

$$\frac{dC_{1,4-BQ}}{dt} = \left(r_{ph\to 1,4-BQ} + r_{p-DHB\to 1,4-BQ} + r_{1,4-BQ\to CO_2}\right)\frac{W_{irr}}{V}$$
$$= \frac{k'''_{ph\to 1,4-BQ}C_{ph} + k'''_{p-DHB\to 1,4-BQ}C_{p-DHB} - k'''_{1,4-BQ\to CO_2}C_{1,4-BQ}}{1 + \sum_{j=1}^{5} K_j C_j} \tag{5-9}$$

5.4. PARAMETER EVALUATION

Equations (5-5) to (5-9) represent the contribution of various steps of the parallel-series model and contain 16 unknown parameters that are to be estimated through fitting the model to the experimental data. To achieve this, multiple non-linear regressions are applied to simultaneously fit all the equations to the experimental data. These equations can also be represented in a compressed form by

$$\boldsymbol{C}' = \boldsymbol{f}(t, \boldsymbol{C}, \boldsymbol{p}) \tag{5-10}$$

where $\boldsymbol{C}'$ is the vector of derivatives of $\boldsymbol{C}$, $\boldsymbol{f}$ is the vector of functions, t is the independent variable, $\boldsymbol{C}$ is the vector of dependent variables and $\boldsymbol{p}$ is the vector of parameters.

In addition, the boundary condition vector can be expressed as follows:

$$\boldsymbol{C}(t_0) = \boldsymbol{C}_0 \tag{5-11}$$

CuuDuongThanCong.com https://fb.com/tailieudientucntt

The integration of the various differential equations as given by equation (5-10) then becomes

$$\boldsymbol{C} = \boldsymbol{f}(t, \boldsymbol{p}) \tag{5-12}$$

When more than one equation is fitted to multi-response data, the sum of the square of the residuals is given as

$$\Psi = \sum_{n=1}^{N} (\boldsymbol{C}_{\text{exp},n} - \boldsymbol{C}_{\text{mod,n}})^T (\boldsymbol{C}_{\text{exp},n} - \boldsymbol{C}_{\text{mod,n}}) \tag{5-13}$$

with the vector $\boldsymbol{p}$ that minimizes Ψ representing the *best-fit* solution.

Individual confidence intervals for the various parameters can be calculated using the following equation, as recommended by Draper and Smith (1981) and Constantinides (1987),

$$\mathrm{p_i} \pm \mathrm{t}(\nu, 1 - 0.5\alpha)\sigma_{\mathrm{p_i}} \tag{5-14}$$

where t is the argument of the cumulative *Student* $\boldsymbol{t}$ distribution function, ν is the degree of freedom of the system (# of data points sets minus the number of parameters), σ_{p_i} is the estimated standard deviation of the parameter p_i, and $\alpha = 100 - C.L.\%$ with $C.L.$ being the confidence limits interval (95%).

Tables of the cumulative *Student t* can be found in Himmelblau (1970). Parameter significance tests can be performed for each of the parameters by applying the null hypothesis. This hypothesis can be accepted when the following is valid:

$$\frac{\mathrm{p_i}}{\sigma_{\mathrm{p_i}}} < \mathrm{t}(\nu - 0.5\alpha) \tag{5-15}$$

5.5. ANALYSIS AND DISCUSSION OF RESULTS

5.5.1. Initial Phenol Concentration

Figure 5.3 displays the concentration profiles for the photodegradation of 416 μM/L (30.0 ppm-C) over Degussa P25 at an initial pH of 4. As it can be observed, the concentrations of the 1,2,4-*THB* and 1,4-*BQ* species are quite small and consequently the values of the related parameters to these species ($k'''_{ph\rightarrow 1,2,4-THB}$, $k'''_{ph\rightarrow 1,4-BQ}$, $k'''_{1,2,4-THB\rightarrow 1,4-BQ}$, $k'''_{1,2,4-THB\rightarrow CO_2}$, $k'''_{1,4-BQ\rightarrow CO_2}$, $k'''_{p-DHB\rightarrow 1,2,4-THB}$ and $k'''_{o-DHB\rightarrow 1,4-BQ}$) are not statistically significant and can thus be neglected. Consistently, the related adsorption constants for these species can also be disregarded.

CuuDuongThanCong.com https://fb.com/tailieudientucntt

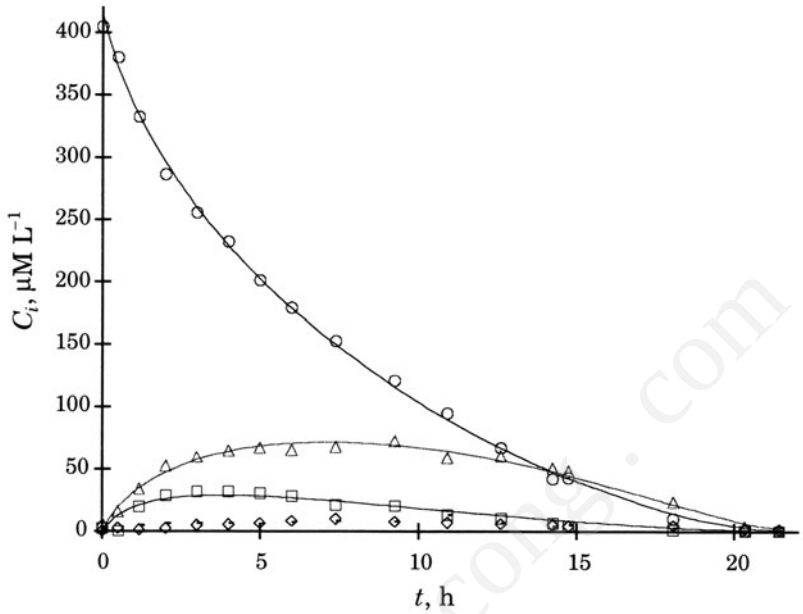

FIGURE 5.3. Concentration profiles of the photodegradation of 416 μ mole L^{-1} (30.0 ppm-C) of phenol over Degussa P25 at an initial pH of 4: (o) phenol, (Δ) *p-DHB*, (□) *o-DHB*, (◇) 1,2,4-*THB*, (-) 1,4-*BQ*. Full lines represent best-fit model curves. (Reprinted from *Chem. Eng. Sci.*, **59**, M. Salaices, B. Serrano and H.I. de Lasa, Photocatalytic conversion of phenolic compounds in slurry reactors, 3-15, Copyright 2004, with permission from Elsevier).

Applying the above simplification, the set of differential equations described by equations (5-5) to (5-9) reduces to

$$\frac{dC_{ph}}{dt} = -\frac{k'''_{ph}C_{ph}}{1 + K_{ph}C_{ph} + K_{p-DHB}C_{p-DHB} + K_{o-DHB}C_{o-DHB}} \tag{5-16}$$

$$\frac{dC_{p-DHB}}{dt} = \frac{k'''_{ph\rightarrow p-DHB}C_{ph} - k'''_{p-DHB\rightarrow CO_2}C_{p-DHB}}{1 + K_{ph}C_{ph} + K_{p-DHB}C_{p-DHB} + K_{o-DHB}C_{o-DHB}} \tag{5-17}$$

$$\frac{dC_{o-DHB}}{dt} = \frac{k'''_{ph\rightarrow o-DHB}C_{ph} - k'''_{o-DHB\rightarrow CO_2}C_{o-DHB}}{1 + K_{ph}C_{ph} + K_{p-DHB}C_{p-DHB} + K_{o-DHB8DHB}C_{o-DHB}} \tag{5-18}$$

This set of equations leads to the determination of k'''_{ph}, $k'''_{ph\rightarrow p-DHB}$, $k'''_{ph\rightarrow o-DHB}$, $k'''_{p-DHB\rightarrow CO_2}$ and $k'''_{o-DHB\rightarrow CO_2}$ parameters with k'''_{ph} defined as the addition of $k'''_{ph\rightarrow o-DHB}$, $k'''_{ph\rightarrow p-DHB}$, $k'''_{ph\rightarrow CO_2}$ and the calculation of K_{ph}, K_{p-DHB} and K_{o-DHB} with K_{p-DHB} and K_{p-DHB} considered as equal.

CuuDuongThanCong.com https://fb.com/tailieudientucntt

TABLE 5.1. Estimated regression parameters for the kinetic model described by equations (5-16) to (5-18). Photodegradation of 416 μmole L^{-1} of phenol over degussa P25 at an initial pH of 4

Parameter	k_i''', K_i	$\pm\sigma_i$	$\pm$95% C. L.	k_i''
k_{ph} (s^{-1})	$5.74.10^{-4}$	$1.10.10^{-4}$	$2.46.10^{-4}$	$1.38.10^{-3}$
$k_{ph\rightarrow p-DHB}$ (s^{-1})	$2.70.10^{-4}$	$4.91.10^{-5}$	$1.09.10^{-4}$	$6.49.10^{-4}$
$k_{ph\rightarrow o-DHB}$ (s^{-1})	$1.95.10^{-4}$	$3.68.10^{-5}$	$8.22.10^{-5}$	$4.68.10^{-4}$
$k_{p-DHB\rightarrow CO_2}$ (s^{-1})	$5.84.10^{-4}$	$1.03.10^{-4}$	$2.30.10^{-4}$	$1.40.10^{-3}$
$k_{o-DHB\rightarrow CO_2}$ (s^{-1})	$1.59.10^{-3}$	$3.05.10^{-4}$	$6.80.10^{-4}$	$3.82.10^{-3}$
$K_{ph}(L\,\mu mole^{-1})$	$1.62.10^{-2}$	$3.44.10^{-3}$	$7.66.10^{-3}$	-
$K_{p-DHB} = K_{o-DHB}(L\,\mu mole^{-1})$	$1.28.10^{-1}$	$2.60.10^{-2}$	$5.79.10^{-2}$	-

Table 5.1 reports the values of the apparent kinetic constants as obtained from fitting equations (5-16) to (5-18) to the experimental data. The standard deviations of the apparent kinetic constants and the individual 95% confidence are also included.

Given that the photocatalytic reactions only proceed in the annulus of the photoreactor, the experimental data measured with samples taken from a well non-irradiated mixed tank, provides apparent kinetic constants (k_i'''). These constants can be related to the intrinsic ones as follows (Wolfrum and Turchi, 1992),

$$k_i''' = \frac{V_{irr}}{V_{irr} + V_d} k_i'' \tag{5-19}$$

where V_{irr} is the irradiated reactor, L; V_d is the volume of the stirred tank, L; and k_i'' is the intrinsic kinetic constant, s^{-1}. The numerical values of these intrinsic constants are reported in the last column of Table 5.1.

The accuracy of the model is illustrated through the best-fit model curves in Figure 5.3. It can be observed that the postulated *parallel-series* model is adequate to simulate the photo-conversion of the phenol with the regressed model parameters as reported in Table 5.1 ($R^2 = 0.992$) with a fairly normal distribution of residuals.

Figures 5.4 and 5.5 display the concentration profiles and the best-fit curves obtained during the photodegradation of phenol over Degussa P25 at an initial pH of 4 at initial concentrations of 300 μmole/L (21.7 ppm-C) and 155 μmole/L (11.2 ppm-C) respectively. The concentrations for 1,2,4-*THB* and 1,4-*BQ* are quite small, allowing the kinetic model to be represented by equations (5-16) to (5-18). The postulated model was found to be suitable to represent the experimental results in both cases ($R^2 = 0.993$ and $R^2 = 0.992$, respectively).

Tables 5.2 and 5.3 report the values of the regressed parameters, the standard deviations and the individual 95% confidence intervals for the 300 μmole L^{-1} and 155 μmole L^{-1} initial concentrations of phenol. The values of the intrinsic kinetic constants are reported in the last column of these tables.

Figure 5.6 shows the concentration profiles obtained regressing parameters for the combined set of runs developed with different initial phenol concentrations (Table 5.4).

CuuDuongThanCong.com https://fb.com/tailieudientucntt

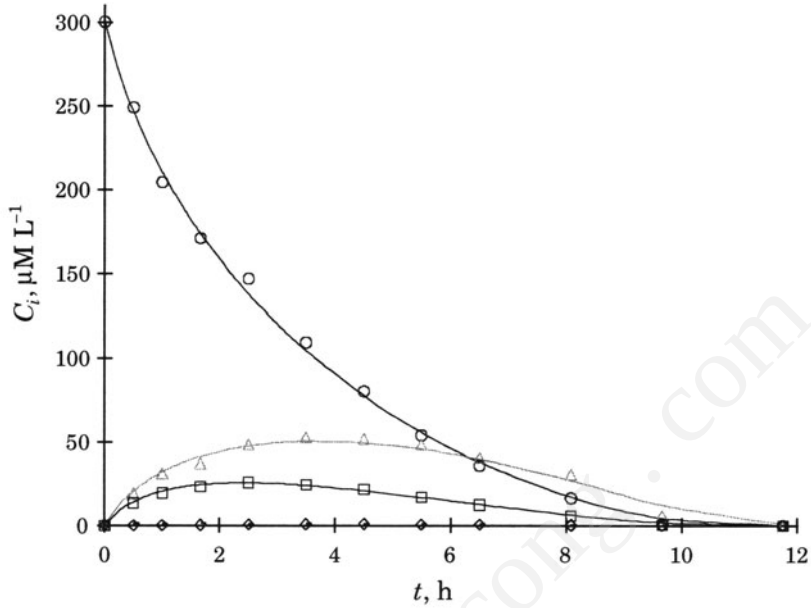

FIGURE 5.4. Concentration profiles of the photodegradation of 300 μmole L^{-1} of phenol over Degussa P25 at pH 4: (o) phenol, (△) *p-DHB*, (□) *o-DHB*, (◇) 1,2,4-*THB*, (-) 1,4-*BQ*. Full lines represent best-fit model curves. (Reprinted from *Chem. Eng. Sci.*, **59**, M. Salaices, B. Serrano and H.I. de Lasa, Photocatalytic conversion of phenolic compounds in slurry reactors, 3-15, Copyright 2004, with permission from Elsevier).

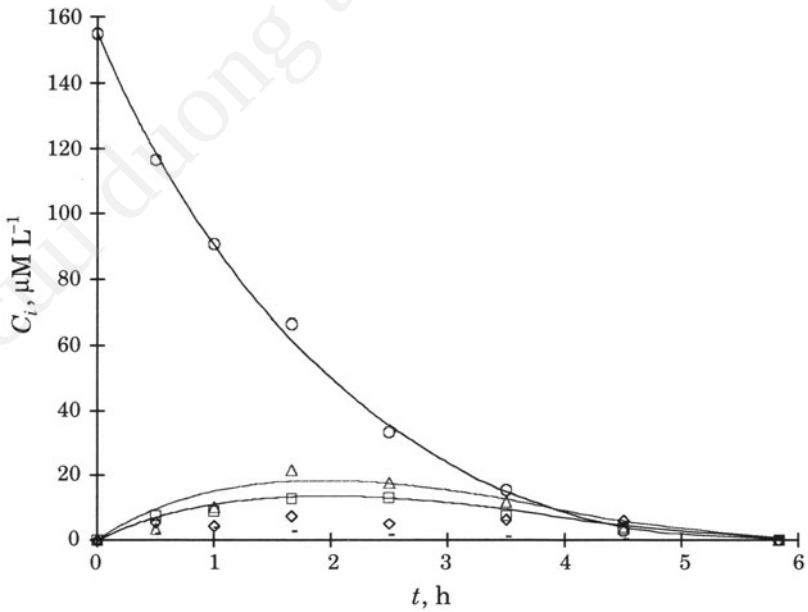

FIGURE 5.5. Concentration profiles of the photodegradation of 155 μmole L^{-1} of phenol over Degussa P25 at an initial pH of 4: (o) phenol, (△) p-*DHB*, (□) o-*DHB*, (◇) 1,2,4-*THB*, (-) 1,4-*BQ*. Full lines represent best-fit model curves. (Reprinted from *Chem. Eng. Sci.*, **59**, M. Salaices, B. Serrano and H.I. de Lasa, Photocatalytic conversion of phenolic compounds in slurry reactors, 3-15, Copyright 2004, with permission from Elsevier).

CuuDuongThanCong.com https://fb.com/tailieudientucntt

TABLE 5.2. Estimated regression parameters for the kinetic model described by equations (5-16) to (5-18). Photodegradation of 300 μ mole L^{-1} of phenol over Degussa P25 at an initial pH of 4

Parameter	k_i''', K_i	$\pm\sigma_i$	$\pm$95% C. L.	k_i''
k_{ph} (s^{-1})	$7.10.10^{-4}$	$1.21.10^{-4}$	$2.80.10^{-4}$	$1.70.10^{-3}$
$k_{ph\rightarrow p-DHB}$ (s^{-1})	$2.93.10^{-4}$	$4.81.10^{-5}$	$1.11.10^{-4}$	$7.03.10^{-4}$
$k_{ph\rightarrow o-DHB}$ (s^{-1})	$2.21.10^{-4}$	$3.68.10^{-5}$	$8.50.10^{-5}$	$5.31.10^{-4}$
$k_{p-DHB\rightarrow CO_2}$ (s^{-1})	$5.74.10^{-4}$	$8.99.10^{-5}$	$2.08.10^{-4}$	$1.38.10^{-3}$
$k_{o-DHB\rightarrow CO_2}$ (s^{-1})	$1.22.10^{-3}$	$2.03.10^{-4}$	$4.70.10^{-4}$	$2.93.10^{-3}$
$K_{ph}(L\,\mu mole^{-1})$	$1.41.10^{-2}$	$2.87.10^{-3}$	$6.62.10^{-3}$	-
$K_{p-DHB} = K_{o-DHB}(L\,\mu mole^{-1})$	$8.68.10^{-2}$	$1.66.10^{-2}$	$3.83.10^{-2}$	-

TABLE 5.3. Estimated regression parameters for the kinetic model described by equations (5-16) to (5-18). Photodegradation of 155 μ mole L^{-1} of phenol over Degussa P25 at an initial pH of 4

Parameter	k_i''', K_i	$\pm\sigma_i$	$\pm$95% C. L.	k_i''
k_{ph} (s^{-1})	$9.25.10^{-4}$	$2.16.10^{-4}$	$5.56.10^{-4}$	$2.22.10^{-3}$
$k_{ph\rightarrow p-DHB}$ (s^{-1})	$2.75.10^{-4}$	$6.15.10^{-5}$	$1.58.10^{-4}$	$6.59.10^{-4}$
$k_{ph\rightarrow o-DHB}$ (s^{-1})	$1.98.10^{-4}$	$4.44.10^{-5}$	$1.14.10^{-4}$	$4.76.10^{-4}$
$k_{p-DHB\rightarrow CO_2}$ (s^{-1})	$7.74.10^{-4}$	$1.66.10^{-4}$	$4.28.10^{-4}$	$1.86.10^{-3}$
$k_{o-DHB\rightarrow CO_2}$ (s^{-1})	$7.43.10^{-4}$	$1.59.10^{-4}$	$4.10.10^{-4}$	$1.78.10^{-3}$
$K_{ph}(L\,\mu mole^{-1})$	$3.31.10^{-2}$	$8.96.10^{-3}$	$2.30.10^{-2}$	-
$K_{p-DHB} = K_{o-DHB}(L\,\mu mole^{-1})$	$7.80.10^{-2}$	$2.40.10^{-2}$	$6.16.10^{-2}$	-

It can be noticed that both the kinetic constants and the adsorption parameters are closer in range when compared to the ones determined for the individual runs (refer to Tables 5.1 to 5.3). This proves the applicability of the simplified Hinselwood Langmuir *parallel-series* model in the range of the initial phenol concentration considered.

5.5.2. *The Influence of pH*

To study the effect of pH on the reaction path, the photo-degradation of 156 μmole/L^{-1} (11.3 ppm-C) can be performed on Degussa P25 at an initial pH of 7 (Figure 5.7). Experimental observation shows the absence of the *o-DHB* species and this result suggests a change in the relative importance of the various steps described in the general reaction mechanism (Figure 5.2).

Under these conditions, a set of differential equations based on a *parallel-series* reaction mechanism can still be applicable. It should be emphasized that the main assumptions of this model (Figure 5.2) are still be applicable. On this basis, the following set of equations can be considered:

$$\frac{dC_{ph}}{dt} = -\frac{k_{pH7}''' C_{ph}}{1 + K_{ph}C_{ph} + K_{p-DHB}C_{p-DHB} + K_{1,2,4-THB}C_{1,2,4-THB}} \qquad (5\text{-}20)$$

CuuDuongThanCong.com https://fb.com/tailieudientucntt

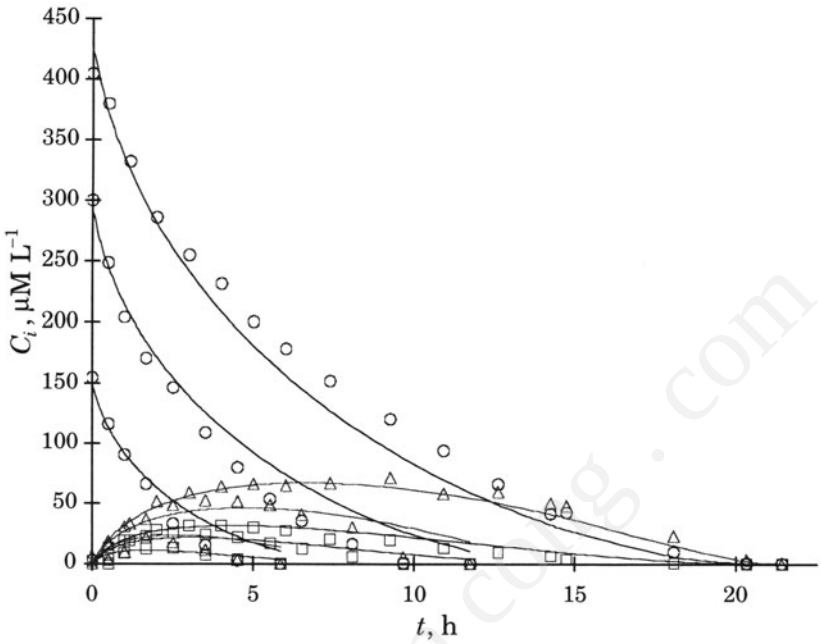

FIGURE 5.6. Concentration profiles of the photodegradation of 3 different initial concentrations of phenol over Degussa P25 at an initial pH of 4: (o) phenol, (Δ) *p-DHB*, (□) *o-DHB*. Full lines represent best-fit curves of the joint model. (Reprinted from *Chem. Eng. Sci.*, **59**, M. Salaices, B. Serrano and H.I. de Lasa, Photocatalytic conversion of phenolic compounds in slurry reactors, 3-15, Copyright 2004, with permission from Elsevier).

$$\frac{dC_{p-DHB}}{dt} = \frac{k'''_{ph\rightarrow p-DHB}C_{ph} - k'''_{p-DHB\rightarrow CO_2}C_{p-DHB}}{1 + K_{ph}C_{ph} + K_{p-DHB}C_{p-DHB} + K_{1,2,4-THB}C_{1,2,4-THB}} \tag{5-21}$$

$$\frac{dC_{1,2,4-THB}}{dt} = \frac{k'''_{ph\rightarrow 1,2,4-THB}C_{ph} - k'''_{1,2,4-THB\rightarrow CO_2}C_{1,2,4-THB}}{1 + K_{ph}C_{ph} + K_{p-DHB}C_{p-DHB} + K_{1,2,4-THB}C_{1,2,4-THB}} \tag{5-22}$$

TABLE 5.4. Estimated regression parameters for the kinetic model described by equations (5-16) to (5-18). Photodegradation of phenol over Degussa P25 at an initial pH of 4. Ranges of initial concentrations 155 μmoleL^{-1} to 416 μmoleL^{-1}

Parameter	k'''_i, K_i	$\pm\sigma_i$	±95% C. L.	k''_i
k_{ph} (s^{-1})	$7.13.10^{-4}$	$2.23.10^{-4}$	$4.97.10^{-4}$	$1.71.10^{-3}$
$k_{ph\rightarrow p-DHB}$ (s^{-1})	$2.81.10^{-4}$	$8.41.10^{-5}$	$1.87.10^{-4}$	$6.75.10^{-4}$
$k_{ph\rightarrow o-DHB}$ (s^{-1})	$1.93.10^{-4}$	$6.11.10^{-5}$	$1.36.10^{-4}$	$4.64.10^{-4}$
$k_{p-DHB\rightarrow CO_2}$ (s^{-1})	$5.93.10^{-4}$	$1.76.10^{-4}$	$3.93.10^{-4}$	$1.42.10^{-3}$
$k_{o-DHB\rightarrow CO_2}$ (s^{-1})	$1.21.10^{-3}$	$4.02.10^{-4}$	$8.96.10^{-4}$	$2.92.10^{-3}$
K_{ph}($L\,\mu mole^{-1}$)	$1.46.10^{-2}$	$5.48.10^{-3}$	$1.22.10^{-2}$	-
$K_{p-DHB} = K_{o-DHB}$($L\,\mu mole^{-1}$)	$1.47.10^{-1}$	$4.73.10^{-2}$	$1.06.10^{-1}$	-

CuuDuongThanCong.com https://fb.com/tailieudientucntt

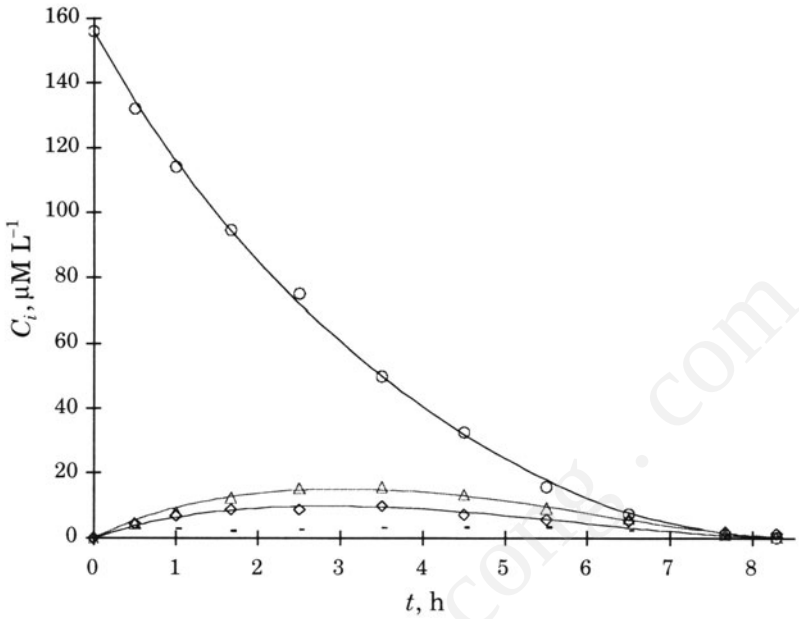

FIGURE 5.7. Concentration profiles of the photodegradation of 156 μmole L^{-1} of phenol over Degussa P25 at an initial pH of 7; (o) phenol, (Δ) p-*DHB*, (◊) 1,2,4-*THB*, (-) 1,4-*BQ*. Full lines represent best-fit model curves. (Reprinted from *Chem. Eng. Sci.*, **59**, M. Salaices, B. Serrano and H.I. de Lasa, Photocatalytic conversion of phenolic compounds in slurry reactors, 3-15, Copyright 2004, with permission from Elsevier).

The following parameters can be adjusted through numerical regression: k'''_{ph7}, $k'''_{ph\rightarrow p-DHB}$, $k'''_{ph\rightarrow 1,2,4-THB}$, $k'''_{1,2,4-THB\rightarrow CO_2}$ and $k'''_{p-DHB\rightarrow CO_2}$, K_{ph}, K_{p-DHB}, $K_{1,2,4-THB}$. Note that the parameter k'''_{ph7} is defined as the sum of the $k'''_{ph\rightarrow 1,2,4-THB}$, $k'''_{ph\rightarrow p-DHB}$, and $k'''_{ph\rightarrow CO_2}$ parameters.

Table 5.5 reports the values of the regressed parameters, their standard deviations and the individual 95% confidence intervals. The values of the intrinsic kinetic constants are reported in the last column of this table.

Figure 5.7 illustrates the concentration profiles of various species with full lines representing the best-fit model curves. The postulated model, represented by equations (5-20) to (5-22), adequately simulates the photo-conversion of phenol under these conditions ($R^2 = 0.992$). For essentially all parameters, the relative narrow 95% confidence intervals obtained are good indicators of the model adequacy.

When comparing the values of the parameters of Tables 5.4 and 5.5, it can also be observed that an increase in pH consistently reduces the kinetic parameters. This result agrees with the findings of Okamoto *et al.*, (1985a). In addition, it can be noted that changes in pH modified the relative importance of some specific steps of the parallel-series reaction model (*i.e.* o-*DHB* was not detectable at an initial pH of 7).

5.5.3. Influence of the Catalyst Type

Hombikat *UV*-100 can be tested in the photodegradation of 158 μmole L^{-1} (11.4 ppm-C) of phenol at pH of 7 (Salaices et al, 2004). Considering the optical properties of

CuuDuongThanCong.com https://fb.com/tailieudientucntt

TABLE 5.5. Estimated regression parameters for the model described by equations (5-20) to (5-22) in the photodegradation of 156 μmole L^{-1} of phenol over Degussa P25 at an initial pH of 7

Parameter	k_i''', K_i	$\pm\sigma_i$	$\pm$95% C. L.	k_i''
k_{ph} (s^{-1})	$6.82.10^{-4}$	$9.88.10^{-5}$	$2.75.10^{-4}$	$1.64.10^{-3}$
$k_{ph\rightarrow p-DHB}$ (s^{-1})	$1.89.10^{-4}$	$2.54.10^{-5}$	$7.05.10^{-5}$	$4.53.10^{-4}$
$k_{ph\rightarrow 1,2,4-THB}$ (s^{-1})	$1.32.10^{-4}$	$1.81.10^{-5}$	$5.03.10^{-5}$	$3.17.10^{-4}$
$k_{p-DHB\rightarrow CO_2}$ (s^{-1})	$7.46.10^{-4}$	$9.68.10^{-5}$	$2.69.10^{-4}$	$1.79.10^{-3}$
$k_{1,2,4-THB\rightarrow CO_2}$ (s^{-1})	$8.51.10^{-3}$	$1.16.10^{-4}$	$3.23.10^{-4}$	$2.04.10^{-3}$
$K_{ph}(L\,\mu M^{-1})$	$4.61.10^{-2}$	$7.22.10^{-3}$	$2.01.10^{-2}$	-
$K_{p-DHB} = K_{1,2,4-THB}(L\,\mu M^{-1})$	$1.16.10^{-1}$	$2.21.10^{-2}$	$6.13.10^{-2}$	-

a sonicated suspension of Hombikat *UV*-100, a 1.71 g sample of catalyst is adequate for this experiment (Salaices, 2002). Results under the above conditions, given in Figure 5.8, denote the detection of only two intermediate species, *p-DHB* and *1,4-BQ*. The absence of the *o-DHB* and 1,2,4-*THB* intermediates shows that phenol photodegradation occurs via a similar photodegradation mechanism but displays a different balance of the various photoconversion steps (Figure 5.2).

Given the absence of the *o-DHB* and 1,2,4-*THB*, as a detectable species in the *parallel-series* reaction mechanism, the set of equations described by equations (5-5) to (5-9) can be reduced as follows

$$\frac{dC_{ph}}{dt} = -\frac{k'''_{phH}C_{ph}}{1 + K_{ph}C_{ph} + K_{p-DHB}C_{p-DHB} + K_{1,4-BQ}C_{1,4-BQ}} \tag{5-23}$$

$$\frac{dC_{p-DHB}}{dt} = \frac{k'''_{ph\rightarrow p-DHB}C_{ph} - k'''_{p-BHD\rightarrow CO_2}C_{p-DHB}}{1 + K_{ph}C_{ph} + K_{p-DHB}C_{p-DHB} + K_{1,4-BQ}C_{1,4-BQ}} \tag{5-24}$$

$$\frac{dC_{1,4-BQ}}{dt} = \frac{k'''_{ph\rightarrow 1,4BQ}C_{ph} - k'''_{1,4-BQ\rightarrow CO_2}C_{1,4-BQ}}{1 + K_{ph}C_{ph} + K_{p-DHB}C_{p-DHB} + K_{1,4-BQ}C_{1-4,BQ}} \tag{5-25}$$

with k'''_{phH} defined now as the sum of $k'''_{ph\rightarrow 1,4-BQ}$, $k'''_{ph\rightarrow p-DHB}$, and $k'''_{ph\rightarrow CO_2}$.

Table 5.6 reports the values of the regression parameters, their standard deviations and the individual 95% confidence intervals. The values of the kinetic and adsorption constants can be obtained from the fitting of equations (5-23) to (5-25) to the experimental data, with the intrinsic kinetic constants being reported in the last column of this table.

Figure 5.8 displays the concentration profiles and the best-fit curves determined. The postulated model appears to be adequate to simulate the photoconversion of 158 μM L^{-1} of phenol over Hombikat *UV*-100 at initial pH of 7 ($R^2 = 0.993$).

CuuDuongThanCong.com https://fb.com/tailieudientucntt

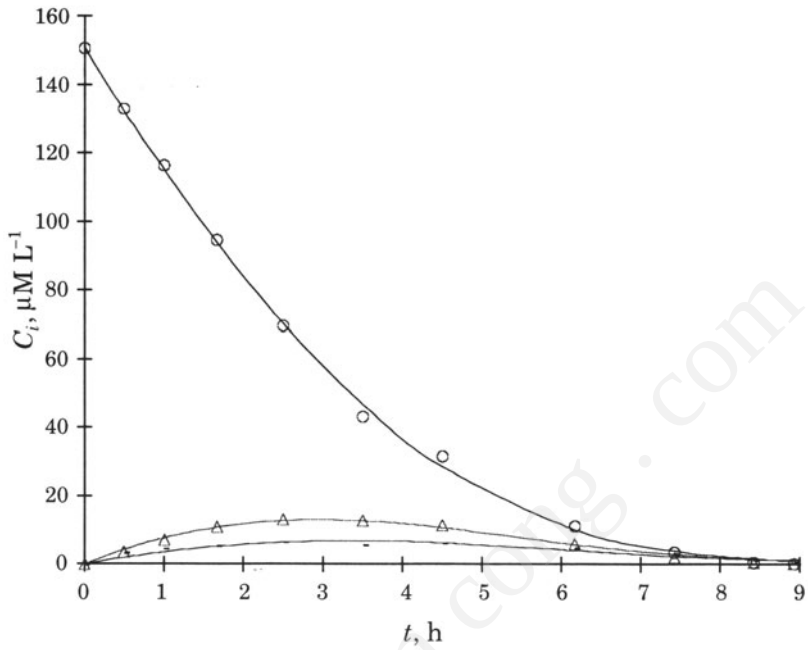

FIGURE 5.8. Concentration profiles of the photodegradation of 158 μ mole L^{-1} of phenol over Hombikat UV-100 at an initial pH of 7: (o) phenol, (Δ) *p-DHB*, (-) 1,4-*BQ*. Full lines represent best-fit model curves. (Reprinted from *Chem. Eng. Sci.*, **59**, M. Salaices, B. Serrano and H.I. de Lasa, Photocatalytic conversion of phenolic compounds in slurry reactors, 3-15, Copyright 2004, with permission from Elsevier).

Comparing the results obtained using Degussa P25 with those obtained using Hombikat *UV*-100 at an initial pH of 7, it can be observed that Hombikat *UV*-100 essentially eliminates the 1,2,4-*THB* species. However, when these initial rates are related to the catalyst weight, 0.87 g and 1.71 g for Degussa P25 and Hombikat *UV*-100 respectively, Degussa P25 catalyst appears to be approximately twice as active. As reported by Salaices *et al.*, 2002, this difference is due mainly to the different agglomeration characteristics of the catalysts with different associated extinction coefficients.

TABLE 5.6. Estimated regression parameters for the model described by equations (5-23) to (5-25) in the photodegradation of 158 μmole L^{-1} of phenol over hombikat *UV*-100 at an initial pH of 7

Parameter	k_i''', K_i	$\pm\sigma_i$	±95% C. L.	k_i''
k_{ph} (s^{-1})	$2.52.10^{-4}$	$2.03.10^{-5}$	$5.63.10^{-5}$	$6.04.10^{-4}$
$k_{ph\rightarrow p-DHB}$ (s^{-1})	$6.26.10^{-5}$	$4.62.10^{-6}$	$1.28.10^{-5}$	$1.50.10^{-4}$
$k_{ph\rightarrow 1,4-BQ}$ (s^{-1})	$2.79.10^{-5}$	$2.35.10^{-6}$	$6.54.10^{-6}$	$6.71.10^{-5}$
$k_{p-DHB\rightarrow CO_2}$ (s^{-1})	$2.82.10^{-4}$	$2.15.10^{-5}$	$5.97.10^{-5}$	$6.78.10^{-4}$
$k_{1,4-BQ\rightarrow CO_2}$ (s^{-1})	$2.01.10^{-4}$	$1.94.10^{-5}$	$5.39.10^{-5}$	$4.81.10^{-4}$
$K_{ph}(L\,\mu M^{-1})$	$1.75.10^{-2}$	$1.65.10^{-3}$	$4.59.10^{-3}$	-
$K_{p-DHB} = K_{1,4-BQ}(L\,\mu M^{-1})$	$1.06.10^{-2}$	$4.53.10^{-3}$	$1.26.10^{-2}$	-

CuuDuongThanCong.com https://fb.com/tailieudientucntt

5.6. CONCLUSIONS

On the basis of the information reported in this chapter, the following conclusion can be drawn:

a) During the photocatalytic degradation, a total mineralization of phenol and the various intermediate species can be achieved.
b) The TOC photoconversion rate shows a zero-order kinetics, whereas the phenol photoconversion rate follows a first-order functionality.
c) A parallel-series model, based on the experimentally observed liquid phase species, can be adopted. This parallel-series model closely simulates the photocatalytic conversion of phenol under various operating conditions. This adequate simulation is applicable to a broad range of initial pollutant concentration.
d) The kinetic parameters of the proposed series-parallel model are calculated within narrow value spans and consistently provide a good representation of the experimental data.
e) The kinetic parameters are defined establishing the distinction between the apparent values defined on the basis of the system reactor volume and the intrinsic ones defined on the basis of the irradiated reactor volume.
f) The *parallel-series* model remains applicable when the catalyst type and pH are changed, with the various mechanistic steps displaying a different balance.

NOMENCLATURE

Symbols

C_i	concentration of i species	g L^{-1} mole L^{-1}
C_j	concentration of $j$species	g L^{-1} mole L^{-1}
$\boldsymbol{C}$	vector of dependent variables	
$\boldsymbol{C}'$	vector of derivatives of C	
f	vectorial function	
k_i	heterogeneous reaction kinetic constant	L g_{cat}^{-1} s^{-1}
k_i''	homogeneous reaction kinetic constant based on the irradiated volume	(L^{-1} L_{irr}) s^{-1}
k_i'''	homogeneous reaction kinetic constant	(mole L^{-1})$^{1-n}$ s^{-1}
k_{ph7}'''	homogeneous reaction kinetic constant for phenol at the initial pH of 7 and Degussa P25	(mole L^{-1})$^{1-n}$ s^{-1}
k_{phH}'''	homogeneous reaction kinetic constant for phenol at the initial pH of 7 and Hombikat UV-100	(mole L^{-1})$^{1-n}$ s^{-1}
k^*	k_i / K_i	mole g_{cat}^{-1} s^{-1}

CuuDuongThanCong.com https://fb.com/tailieudientucntt

K_i	adsorption parameter for the i chemical species	L mole^{-1}
$\boldsymbol{p}$	vector of parameters	
Q	volumetric flow rate, L min^{-1}, rate of energy absorption	J s^{-1}
r_i	heterogeneous reaction rate for the i species	mole g_{cat}^{-1} s^{-1}
R^2	least-squares regression coefficient	
t	time; cumulative *Student t* distribution argument	s, h
V	total reactor volume	L
V_d	non-irradiated reactor volume	L
V_{irr}	Irradiated reactor volume	L
W_{irr}	mass of irradiated catalyst	g_{cat}

Greek letters

α	$100 - C.L.\ \%$
ν	degree of freedom for the system
ν_i	stoichiometric coefficient for "i" species (positive for products, negative reactants)
σ_{pi}	estimated standard deviation of the parameter k_i
Ψ	sum of squared residuals

Subscripts

1,4-BQ	1,4-benzoquinone
1,2,4-THB	1,2,4 – trihydroxybenzene
exp	experimental
i, j	reactant evaluated at the inner reactor surface
mod	modeled
o-DHB	ortho-dihydroxybenzene
p-DHB	para-dihydroxybenzene
ph	phenol
pH7	phenol at pH of 7

Superscripts

n	number of reaction species, order of reaction
T	transpose matrix
$\bar{x}$	denotes the mean value of the variable x

Acronyms

C.L.	interval of confidence limits
HPLC	high performance liquid chromatography
TOC	total organic carbon

CuuDuongThanCong.com https://fb.com/tailieudientucntt

REFERENCES

Al-Ekabi, H., and Serpone, N., 1988, Kinetic studies in heterogeneous photocatalysis. 1. Photocatalytic degradation of chlorinated phenols in aerated aqueous solutions over TiO_2 supported on a glass matrix, *Jour. Phys. Chem.* **92:**5726–5731.

Constantinides, A., 1987, *Applied Numerical Methods with Personal Computers,* McGraw-Hill Inc., Chapter 7.

Draper, N. R., and Smith, H., 1981, *Applied Regression Analysis*, John Willey & Sons Inc., New York, Chap. 2.

Himmelblau, D. M., 1970, *Process Analysis by Statistical Methods*, John Willey & Sons Inc., New York, p. 427.

Matthews, R. W., and McEvoy, S. R., 1992, Destruction of phenol in water with sun, sand and photocatalysis, *Solar Energy*. **49:**507–513.

Okamoto, K., Yamamoto, Y., Tanaka, H., and Itaya, A., 1985a, Kinetics of heterogeneous photocatalytic decomposition of phenol over anatase TiO_2 powder, *Bulletin Chem. Soc. Jpn.* **58:**2015–2021.

Okamoto, K., Yamamoto, Y., Tanaka, H., and Itaya, A., 1985b, Kinetics of heterogeneous photocatalytic decomposition of phenol over anatase TiO_2 powder, *Bulletin Chem. Soc. Jpn.*, **58:**2023–2028.

Ollis, D. F., Pelizzetti, E., and Serpone, N., 1989, Heterogeneous photocatalysis in the environment: application to water purification, in: *Photocatalysis fundamentals and applications*. N. Serpone, E. Pelizzetti, ed., Wiley Interscience, New York, pp. 603–637.

Salaices, M., Serrano, B., and de Lasa, H., 2001, Photo-catalytic conversion of organic pollutants. Extinction coefficients and quantum efficiencies, *Ind. Eng. Chem. Res.* **40:**5455–5464.

Salaices, M., Serrano, B., and de Lasa, H., 2002, Experimental evaluation of photon absorption in an aqueous TiO_2 slurry reactor, *Chem. Eng. J.*, **90:**219–229.

Salaices, M., 2002, Photocatalysis in Slurry Reactors - Radiation Transmission and Kinetic Modeling, *Ph.D. Dissertation*, University of Western Ontario, pp. 109–115, 212–215.

Salaices, M., Serrano, B., and de Lasa, H., 2004, Photocatalytic conversion of phenolic compound in slurry reactors. *Chem. Eng. Sci.* **59:** 3–15.

Trillas, M., Pujol, M., and Domenech, X., 1992, Phenol photodegradation over titanium dioxide, *J. Chem. Tech. Biotech.* **55:**85–90.

Trillas, M., Pujol, M., and Domenech, X., 1996, Photocatalyzed degradation of phenol, 2,4-dichlorophenol, phenoxyacetic acid and 2,4-dichlorophenoxyacetic acid over supported TiO2 in a flow system, *J. Chem. Tech. Biotech.* **67:**237–242.

Tseng, J., and Huang; C. P., 1990, Mechanistic aspects of the photocatalytic oxidation of phenol in aqueous solutions, in: *Emerging Technologies in Hazardous Waste Management*, D. W. Tedder, F. G. Pohland, eds. American Chemical Society: Washington, DC, **2:**12–39.

Wei, T., and Wan, C., 1992, Kinetics of photocatalytic oxidation of phenol on TiO_2 surface, *J. Photochem. Photobiol. A: Chem.* **69:**241–249.

Winterbottom, J. M., Khan, Z., Boyes, A. P., and Raymahasay, S., 1997, Photocatalyzed oxidation of phenol in water using a Cocurrent Downflow Contactor Reactor (CDCR), *Environ. Prog.* **62:**125–131.

Wolfrum, E. J., and Turchi, G. S., 1992, Comments on reactor dynamics in the evaluation of photocatalytic oxidation kinetics, *J. Cat.* **136:**626–628.

CuuDuongThanCong.com https://fb.com/tailieudientucntt

6

The Energy Efficiency Factors in Photocatalytic Processes

6.1. INTRODUCTION

Heterogeneous photocatalysis on metal oxide semi-conductors has been shown to be effective in degrading organic pollutants in gaseous and aqueous streams (Fox and Dulay, 1993; Hoffmann, et al., 1995). In photocatalysis, the definition of energy yield parameters describing the light utilization efficiency is very critical (Fox, 1988).

Energy efficiencies have been evaluated using factors such as the Electrical Energy per Order (EE/O) (Bolton and Cater, 1994; Notarfonzo and McPhee, 1994), the quantum yield and the apparent quantum yield (Fox and Dulay, 1993; Nimlos *et al.*, 1993; Sczechowski *et al.*, 1995; Valladares and Bolton, 1993; Zhang *et al.*, 1994a). More recently, Serrano and de Lasa (1997) proposed a photo-catalytic thermodynamic efficiency factor (*PTEF*) based on thermodynamic considerations.

This chapter reviews these available efficiency parameters and provides examples that highlight their application.

6.2. EE/O-ELECTRICAL ENERGY PER ORDER

The EE/O is a semi-empirical parameter useful in various water treatment processes. The EE/O is defined as the kilowatt-hours of electricity required to reduce the concentration of a compound in 1000 gallons of water by one order of magnitude (Bolton and Cater, 1994; Notarfonzo and McPhee, 1994).

$$EE/O = \frac{P\frac{t}{60}3785}{V log(C_{in}/C)} \tag{6-1}$$

with P representing the lamp-emitted power in kW, t the irradiation time in min., V the total reactor volume, C_{in} the initial model pollutant concentration and C the model pollutant concentration at time t.

CuuDuongThanCong.com https://fb.com/tailieudientucntt

Smaller values of the EE/O indicate a more efficient process since less energy is required to achieve a fixed drop in concentration of model pollutants in the photocatalytic system.

The EE/O parameter is based on electrical lamp power requirements and, as such, does not account separately for the lamp efficiency and the glass tube absorption. As a result, it is an overall parameter with limited phenomenological value.

Furthermore, the following limitations of the EE/O efficiency parameter described above can be identified:

a) The EE/O is not a dimensionless group as required by consistent thermodynamic definitions
b) The EE/O contains the implicit assumption of first order reaction kinetics
c) The EE/O neglects the light energy used to photoconvert intermediate chemical species, given that its assessment is based on a C/C_{in} ratio expressing the change of the model pollutants only, and as a result underestimates photo-catalytic efficiency.

6.3. QUANTUM YIELDS

Quantum parameters are important and useful efficiency estimators in photocatalysis (Cabrera *et al.*, 1994). These parameters are based on a *"number ratio"*, either of photoconverted molecules over absorbed photons or photoconverted molecules over photons entering the reactor, as described in Table 6.1 Using this idea as the basis there are several possible quantum yield definitions:

a) Primary quantum yield;
b) Overall quantum yield and,
c) Apparent quantum yield or global quantum yield.

TABLE 6.1. Quantum parameter definitions (Ibrahim, 2001)

Parameter	Definition and Reference
Primary Quantum Yield (*Primary QY*)	$\frac{number\ of\ pollutant\ molecules\ degraded\ from\ a\ primary\ process}{number\ of\ photons\ absorbed}$ Cassano et al. (1995), Davydov et al (1999)
Overall Quantum Yield (*Overall QY*)	$\frac{number\ of\ pollutant\ molecules\ degraded\ from\ a\ primary\ and\ secondary\ process}{number\ of\ photons\ absorbed}$ Cassano et al (1995)
Quantum Yield *(Apparent QY)*	$\varphi = \frac{number\ of\ pollutant\ molecules\ degraded}{number\ of\ photons\ absorbed}$ Peil and Hoffmann(1995); Valladares and Bolton (1993),Yamazaki-Nishida et al (1994)
Apparent Quantum Yield (*) or Global Quantum Yield (*QE*)	$\varphi_{app} = \frac{number\ of\ pollutant\ molecules\ degraded\ from\ a\ primary\ process}{number\ of\ photons\ entering\ the\ reactor}$ Fox and Dulay (1993), Nimlos *et al.* (1993); Sczechowski *et al*, (1995); Zhang *et al.*, (1994a), (1994b) (*) the term "apparent or *app*" is also introduced to highlight the difficulty of measuring absorbed photons

CuuDuongThanCong.com https://fb.com/tailieudientucntt

The *primary quantum yield (Primary Q.Y.)* establishes the number of molecules degraded from a primary process or event that involves direct absorption of radiation over the number of photons absorbed (Cassano *et al.*, 1995 and Davydov *et al.*, 1999). Cassano *et al.*, (1995) argue that according to the second law of photochemistry, the absorption of light by a molecule is a one-quantum process. Therefore a quantum yield factor involving the sum of all primary processes must be less than or equal to unity and this as a result that the energy absorbed by the molecule is partially lost by re-emission, collision or other processes (Alfano and Cassano, 1988).

The *overall quantum yield* (Overall Q.Y.) is defined as the ratio of the total number of pollutant molecules degraded via primary and secondary processes over the total number of photons absorbed (Cassano *et al.*, 1995). This overall quantum yield can, in principle, be greater than 100% (Cassano *et al.*, 1995). This fact puts forward interesting prospects for photocatalytic processes.

To simplify the evaluation, the quantum yield is often based on the rate of photo-converted molecules at initial conditions.

$$\varphi_{in} = \frac{\left[\frac{dN_i}{dt}\right]_{in}}{P_a} \tag{6-2}$$

with P_a representing the rate of absorbed photons and $\left[dN_i/dt\right]_{in}$ the rate of photoconversion of i species molecules at initial conditions.

Determining quantum yields requires the assessment of P_a the rate of absorbed photons in the heterogeneous reactor (Cabrera *et al.*, 1996). Semiconductor surfaces are highly reflective (Fox and Dulay, 1993) and therefore errors can arise from light back-scattering or forward-scattering from the catalyst particles (Valladares and Bolton, 1993).

For this reason, and given that the rate of photons entering the reactor is a parameter much simpler to measure, researchers frequently consider an "*apparent quantum yield*", $\varphi_{app,in}$ defined as the ratio of converted reactant molecules over the photons entering the reactor (Fox and Dulay, 1993; Nimlos *et al.*, 1993; Sczechowski *et al.*, 1995; Zhang *et al.*, 1994a, 1994b):

$$\varphi_{app,in} = \frac{\{\frac{dN_i}{dt}\}_{in}}{\int_{\lambda_1}^{\lambda_2} \frac{R.A_{irr}\,\lambda\,d\lambda}{hc}} \tag{6-3}$$

with R being the radiation intensity in W $(m^2.nm)^{-1}$; A_{irr} the irradiated catalyst area in m^2; h the Plank's constant ($6.62.10^{-34}$ J.s); c the speed of light in vacuum ($2.997.10^8$ m/s); λ_1 the lower wavelength of the spectrum in the range of interest (300 nm) and λ_2 the higher wavelength of the spectrum in the range of interest (390 nm) (Ibrahim, 2001).

Given that the rate of photons entering the reactor is always smaller than the rate of photons absorbed, the "apparent quantum yield" provides a non-conservative estimation of the "quantum yield": $\varphi_{in} \geq \varphi_{app,in}$.

CuuDuongThanCong.com https://fb.com/tailieudientucntt

Peill and Hoffmann, (1995) also define an *average apparent quantum efficiency* for photooxidation based on the time required to achieve a 90% conversion of pollutant molecules.

$$\varphi_{app,av} = \frac{\left(\frac{N_{90\%}}{t_{90\%}}\right)}{\int_{\lambda_1}^{\lambda_2} \frac{R.A_{irr}\,\lambda\,d\lambda}{hc}} \qquad \varphi_{in} \geq \varphi_{app,av} \tag{6-4}$$

with $N_{90\%}$ being the number of pollutant molecules degraded at the 90% conversion level; $t_{90\%}$ the time required to achieve 90% conversion in seconds. All other parameters have been previously defined in Eq. (6-3).

Proper definition of quantum yields (φ) requires the careful assessment of photons absorbed by the photocatalyst. Methods based on chemical actinometry are limited as they provide only the total rate of photons entering the reactor and do not account for various light scattering losses. The use of physical methods involving spectrophotoradiometers and collimators (Salaices et al., 2001), as described in chapter IV, enables macroscopic energy balances, the proper assessment of irradiation energy absorbed by the photocatalyst and, consequently, an adequate definition of quantum efficiencies.

6.4. PTEF-PHOTOCHEMICAL THERMODYNAMIC EFFICIENCY FACTOR

The Photochemical Thermodynamic Efficiency Factor (*PTEF*) is an energy ratio equating the energy used to achieve the photocatalytic conversion of organic molecules over the energy absorbed by the photocatalyst. This parameter was first introduced by Serrano and de Lasa (1997) and evaluates the performance of photocatalytic reactors on a thermodynamic basis.

If Q_a represents the irradiation energy absorbed and Q_{used} the irradiation energy used for the desired formation of $OH^{\bullet}$ radicals which then interact with adsorbed species, the reactor's efficiency can be defined as:

$$PTEF = \eta = Q_{used}/Q_a \tag{6-5}$$

The *PTEF* is a generally applicable parameter as it is not restricted to either a homogenous or an heterogeneous photoconversion chemical process.

More specifically, the Q_{used} in the photoconversion process can be represented via the $r_{OH^{\bullet}}\,\Delta H_{OH^{\bullet}}\,W_{irr}$ group with the *PTEF* being represented by

$$PTEF = \eta = \frac{r_{OH^{\bullet}}\,\Delta H_{OH^{\bullet}}\,W_{irr}}{Q_a} \tag{6-6}$$

with $r_{OH^{\bullet}}$ representing the rate of formation of $OH^{\bullet}$ radical groups per unit weight of irradiated catalyst; $\Delta H_{OH^{\bullet}}$ being the enthalpy of formation of an $OH^{\bullet}$ group and W_{irr} the total amount of irradiated catalyst.

CuuDuongThanCong.com https://fb.com/tailieudientucntt

Alternatively, a *PTEF* definition can be introduced based on A_{irr} the area of irradiated catalyst,

$$PTEF = \eta = \frac{r'_{OH^\bullet} \Delta H_{OH^\bullet} A_{irr}}{Q_a} \tag{6-7}$$

While photocatalytic reactions are frequently considered to be pseudo-homogeneous reactions with a rate based on either the unit volume of irradiated catalyst or the total reactor volume (Chapter I), definitions of the *PTEF* can be given as follows:

$$PTEF = \eta = \frac{r''_{OH^\bullet} \Delta H_{OH^\bullet} V_{irr}}{Q_a}$$
$$PTEF = \eta = \frac{r'''_{OH^\bullet} \Delta H_{OH^\bullet} V}{Q_a} \tag{6-8}$$

where $r_{OH^\bullet} W_{irr} = r'_{OH^\bullet} A_{irr} = r''_{OH^\bullet} V_{irr} = r'''_{OH^\bullet} V$

It can be observed from equations (6-6), (6-7) and (6-8) that the *PTEF*s are efficiency factors that involve both the rate of formation of $OH^\bullet$ radicals and the enthalpies of $OH^\bullet$ radical formation.

Regarding the rate of $OH^\bullet$ radical formation, it can be considered to be the sum of two terms, the rate of $OH^\bullet$ consumption and the rate of $OH^\bullet$ accumulation:

$$r_{OH^\bullet} = -r_{OH^\bullet,c} + r_{OH^\bullet,acc} \tag{6-9}$$

with $r_{OH^\bullet,c}$ having a negative sign (consumption of OH radicals).

Evaluation of $OH^\bullet$ radicals ($r_{OH^\bullet}$) formation presents inherent problems. The $OH^\bullet$ radicals react with both the adsorbed model pollutant and the adsorbed intermediates (Pelizzetti et al., 1992; Turchi and Ollis, 1990). Furthermore, the evaluation of the rate of $OH^\bullet$ radicals involves stochiometric coefficients such as:

$$r_{OH^\bullet,c} = \nu \sum_P \frac{r_P}{\nu_P} \tag{6-10}$$

with ν being the stochiometric coefficient for the consumption of $OH^\bullet$ groups, and r_P and ν_P the rate and the stochiometric number for the consumption of organic chemical species (including model pollutant and intermediate species) respectively.

As a result, $r_{OH^\bullet}$ of equation (6-9) can be expressed as follows:

$$r_{OH^\bullet} = -\nu \sum_P \frac{r_P}{\nu_P} + r_{OH^\bullet,acc} \tag{6-11}$$

At the beginning of the photoconversion, when the surface concentration of all chemical species is equal to the surface concentration of the model compound, the model compound is the only $OH^\bullet$ group scavenger. Therefore

$$\nu \sum_P \frac{r_P}{\nu_P} = \frac{\nu r_{1,in}}{\nu_1} \tag{6-12}$$

CuuDuongThanCong.com https://fb.com/tailieudientucntt

with $r_{1,in}$ representing the rate of consumption of the model pollutant and ν_1 the stoichiometric coefficient for the consumption of the model pollutant.

Alternatively,

$$r_{OH^\bullet} = -\frac{\nu\, r_{1,in}}{\nu_1} + r_{OH^\bullet,acc} \tag{6-13}$$

At initial conditions, the model pollutant concentration is very high, in large excess with respect to the other species and it is very likely that the model pollutant is going to consume all the $OH^\bullet$ radicals with no accumulation of the $OH^\bullet$ groups ($r_{OH^\bullet,acc} = 0$). As a result, the following is achieved:

$$r_{OH^\bullet} = -\frac{\nu\, r_{1,in}}{\nu_1} \tag{6-14}$$

Under the situation described, the *PTEF* given by equation (6-6) can be evaluated as,

$$PTEF = \eta = \frac{-\nu/\nu_1 r_{1,in} \Delta H_{OH^\bullet} W_{irr}}{Q_a} \tag{6-15}$$

Or alternatively

$$\begin{aligned} PTEF = \eta &= \frac{-\nu/\nu_1 r'_{1,in} \Delta H_{OH^\bullet} A_{irr}}{Q_a} \\ PTEF = \eta &= \frac{-\nu/\nu_1 r''_{1,in} \Delta H_{OH^\bullet} V_{irr}}{Q_a} \\ PTEF = \eta &= \frac{-\nu/\nu_1 r'''_{1,in} \Delta H_{OH^\bullet} V}{Q_a} \end{aligned} \tag{6-16}$$

Frequently, it is observed that photocatalytic reactions follow the Langmuir-Hinselwood model (refer to the discussion regarding the kinetic modeling of photocatalytic reactions described in chapter V, equation (5-16)),

$$r_{1,in} = \frac{-k_1 C_1}{1 + K_1 C_1} \tag{6-17}$$

with k_1 representing the apparent intrinsic constant for phenol photoconversion, C_1 the model pollutant volumetric concentration and K_1 the model pollutant adsorption constant.

At large pollutant concentrations, $1 << K_1 C_1$ can be expected and consequently the rate of photoconversion of a model pollutant shows a maximum value. Under these conditions, the *PTEF* reaches as well an upper limit.

$$PTEF_{max} = \eta_{max} = \frac{-\nu/\nu_1 (r_{1,in})_{max} \Delta H_{OH^\bullet} W_{irr}}{Q_a} \geq \eta \tag{6-18}$$

CuuDuongThanCong.com https://fb.com/tailieudientucntt

or

$$PTEF_{max} = \eta_{max} = \frac{-\nu/\nu_1 [r'_{1,in}]_{max} \Delta H_{OH^\bullet} A_{irr}}{Q_a} \geq \eta$$
$$PTEF_{max} = \eta_{max} = \frac{-\nu/\nu_1 [r''_{1,in}]_{max} \Delta H_{OH^\bullet} V_{irr}}{Q_a} \geq \eta \quad (6\text{-}19)$$
$$PTEF_{max} = \eta_{max} = \frac{-\nu/\nu_{1,in} [r'''_{1,in}]_{max} \Delta H_{OH^\bullet} V}{Q_a} \geq \eta$$

To calculate the $PTEF_{max}$ value for a specific photocatalytic system, the initial concentration of the model pollutant has to be increased progressively until the *PTEF* approaches a constant value, the $PTEF_{max}$, as proposed by Serrano and de Lasa (1997):

$$PTEF_{max} = \eta_{max} \geq PTEF = \eta \quad (6\text{-}20)$$

This upper value for the *PTEF* is an intrinsic characteristic of a photocatalytic reactor as well as of the pollutant being photoconverted. This efficiency factor includes various reactor characteristics such as the absorbed irradiation, the rate of photoconversion and the enthalpy of $OH^\bullet$ group formation.

A relationship can also be established between the quantum yield and the *PTEF* given that the $PTEF_{max}$ can be expressed as,

$$PTEF_{max} = \eta_{max} = \frac{-\nu/\nu_1 (r_{1,in})_{max} W_{irr} \alpha \left[\frac{N_A hc}{\lambda}\right]}{Q_a} \frac{\Delta H_{OH^\bullet}}{\alpha \left[\frac{N_A hc}{\lambda}\right]} \quad (6\text{-}21)$$

with α being the number of photon needed for the formation of a $OH^\bullet$ group, N_A the Avogadro's number ($6.023.\ 10^{23}$) molecules $mole^{-1}$, h the Planck's constant ($6.62.10^{34}$J s $photon^{-1}$), c the speed of light in vacuum ($2.997.10^{10}$cm s^{-1}), and λ the average wave length (nm).

Then,

$$PTEF_{max} = \eta_{max} = \varphi_{in,max} \eta_{OH} \quad (6\text{-}22)$$

with $\varphi_{in,\ max}$ representing the maximum quantum yield (defined at initial conditions), or the maximum fraction of photons absorbed in the photocatalyst that results in the formation of $OH^\bullet$ radicals, and η_{OH} being the fraction of the photon energy used in the formation of $OH^\bullet$ radicals.

Equation (6-22) shows that energy efficiency evaluations using *PTEF* require not only a maximum quantum yield definition at initial conditions, based on the energy absorbed by the catalyst, but also η_{OH}, the fraction of the photon energy used in forming $OH^\bullet$ groups. The product of these two parameters provides an assessment of the energy efficiency of a photocatalytic reactor system.

CuuDuongThanCong.com https://fb.com/tailieudientucntt

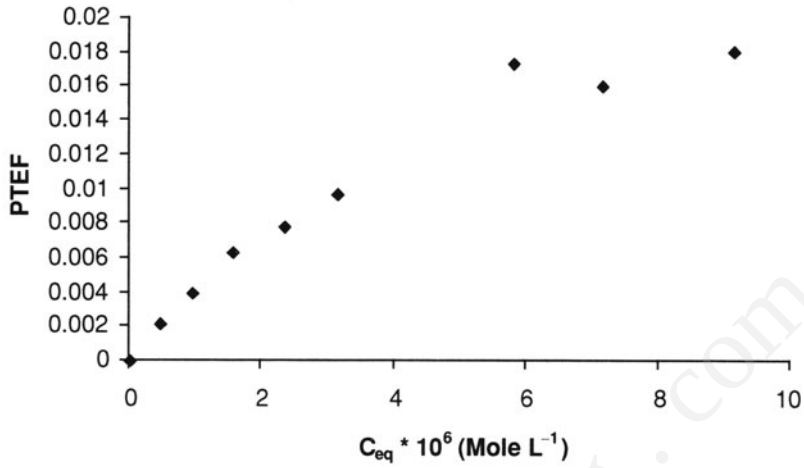

FIGURE 6.1. Variation of *PTEF* with equilibrium methylene blue liquid concentration (Reprinted with permission from *Ind. Eng. Chem. Res*, **36**(11), B. Serrano and H.I. de Lasa, Photocatalytic degradation of water organic pollutants: Kinetic modeling and energy efficiency, 4705-4711. Copyright 1997 American Chemical Society).

The *PTEF* is a dimensionless quantity, as required by thermodynamic consistency. The *PTEF* definition can be broadly applied, covering various kinetic models and being appropriate for various photochemical reactors, either homogenous or heterogeneous.

In practice, the calculation of $PTEF_{max}$ can be done using equations (6-18) or (6-19) for conditions where the initial photoconversion rates reach maximum values and with $\nu/\nu_1 = 1$.

Figure 6.1 reports an example of *PTEF* for the photocatalytic conversion of methylene blue under the conditions of the experiments described in Chapter VII. It can be noticed that the maximum $PTEF_{max}$ and $\varphi_{max} = \frac{PTEF_{max}}{0.289}$,the maximum quantum yields, are smaller than 0.018 and 0.062 respectively. For evaluations of $r_{1,in}$ and PTEF for methylene blue refer to Chapter VII ($PTEF_{neq}$ in page 143).

Considering that the allowed maximum $PTEF_{max}$ is 0.289 with $\varphi = 1$ (only primary process involved) and $\eta_{OH} = 0.289$ (section 6.5), this sets a possible target for improvement of the Photo-CREC-Water II reactors of 16 times the values currently observed.

6.5. EVALUATION OF THE ΔH_{OH}

Given a particular photocatalytic reactor configuration, (e.g. suspended TiO_2 reactor or immobilized TiO_2 reactor for photoconversion of water pollutants) calculation of the $PTEF_{max}$ requires the estimation of the enthalpy of $OH^{\bullet}$ radical formation ($\Delta H_{OH^{\bullet}}$), in addition to the initial photoconversion reaction rates.

As advanced in chapter I, the basic mechanism of heterogeneous photocatalysis is related to the exciting of the TiO_2 or other metal oxides. It is generally accepted that this photon-induced state of excitation promotes an electron from the valence band level to

CuuDuongThanCong.com https://fb.com/tailieudientucntt

a highly delocalized level in the conduction band. It is believed that this process creates an oxidizing site (a "hole") and a reduction site (an "electron").

$$TiO_2 \xrightarrow{h\nu} h^+ + e^- \tag{6-23}$$

Species adsorbed on the photocatalyst surface can then capture this photogenerated electron-hole pair. Electron transfer from either an adsorbed pollutant molecule or an adsorbed water molecule can fill the hole. In the later case, a hydroxyl occupies the electron hole, forming an $OH^\bullet$ species.

$$H_2O \rightarrow OH^- + H^+ \tag{6-24}$$

$$h^+ + OH^- \rightarrow OH^\bullet \tag{6-25}$$

Following these steps, there is a number of possible other steps for ensuing reactions in the photocatalytic reaction network.

$$e^- + O_2 \rightarrow O_2^- \tag{6-26}$$

$$O_2^- + H^+ \rightarrow O_2H^\bullet \tag{6-27}$$

$$H^+ + O_2^- + O_2H^\bullet \rightarrow H_2O_2 + O_2 \tag{6-28}$$

$$H_2O_2 \xrightarrow{h\nu} 2OH^\bullet \tag{6-29}$$

Considering that the enthalpy of formation of the $OH^\bullet$ groups is a path independent state function, $\Delta H_{OH^\bullet}$ can be calculated without the certainty that the proposed reaction network be fully satisfactory. A possible reaction mechanism is thus presented with the purpose of illustrating the enthalpy calculation.

A linear combination of equations (6-23) to (6-29), with equations (6-27), (6-28) and (6-29) multiplied by a factor of $1/2$, demonstrates that the overall stochiometry for the formation of $OH^\bullet$ radicals can be represented as follows,

$$H_2O(l) + \frac{1}{2}O_2(aq) \rightarrow 2OH^\bullet(l) \tag{6-30}$$

Accordingly, the enthalpy of formation of $OH^\bullet$ radicals from H_2O and O_2 is given by:

$$\Delta H_{OH^\bullet} = \Delta H_f(OH^\bullet) - \frac{1}{2}\Delta H_f(H_2O) - \frac{1}{4}\Delta H_f(O_2) \tag{6-31}$$

The enthalpies of formation involved in equation (6-31) can be estimated as proposed by Serrano and de Lasa (1997), considering the heat of formation of $OH^\bullet$ radicals, by using the data reported by Kerr (1966) and Wagman et al (1982). On these bases, the enthalpy of formation of the $OH^\bullet$ groups in aqueous media, starting from H_2O and dissolved oxygen, was estimated at 94600 J mole^{-1}.

CuuDuongThanCong.com https://fb.com/tailieudientucntt

Since η_{OH} involves the energy of a photon at a wavelength of 365 nm (evaluated as 327000 J mole^{-1}), and considering $\alpha = 1$, this yields η_{OH}, the fraction of photon energy used in forming $OH^{\bullet}$ radicals, equal to 0.289 (equation (6-20)).

In the ideal case of a photocatalytic reactor for the conversion of water pollutants with a quantum yield $\varphi = 1$ (primary process involved), and for a $\lambda = 365$ nm, an η_{ideal} of 0.289 is obtained using equation (6-22) and this value (28.9%) represents the upper efficiency limit for a photocatalytic reactor irradiated with a 365 nm wavelength.

6.6. CONCLUSIONS

The following are the major conclusions of the present chapter

a) The evaluation of a photocatalytic reactor's performance requires the calculation of quantum yields, φ, and Photochemical Thermodynamic Efficiency Factors (*PTEF* or η)
b) A careful review of the various terms involved in the definition of φ and η show that these two parameters are related through the η_{OH} factor, which represents the fraction of the photons used in the formation of the $OH^{\bullet}$ groups
c) The estimation of quantum efficiency requires careful evaluation of key parameters such as rates of photons absorbed and photoconversion rates at initial conditions
d) The evaluation of $PTEF_{max}$ or η_{max} requires planned experimentation or modeling with increased concentrations of model pollutants.

NOTATION

Symbols

A_{irr}	catalyst irradiated area	m^2
c	speed of light in vacuum	2.997 10^{10} cm s^{-1}
C	pollutant concentration	mole L^{-1}
C_{in}	initial pollutant concentration	mole L^{-1}
h	Plank's constant	6.62 10^{34} (J.s)
k_1	kinetic reaction constant, equation (6-17)	
K_1	model pollutant adsorption equilibrium constant	L mole^{-1}
n_a	number of absorbed photons	photons s^{-1}
N_A	Avogadro's number	6.023 10^{23}(photons mole^{-1})
N_i	moles of chemical species	mole
P	lamp emitted power	W
P_a	rate of absorbed photons	Einstein s^{-1}
Q_a	rate of irradiated energy absorbed in photocatalytic reactor	J s^{-1}

CuuDuongThanCong.com https://fb.com/tailieudientucntt

Q_{used}	rate of irradiated energy used for the formation of OH radicals	J s^{-1}
r_{OH}	rate of $OH^{\bullet}$ radical formation	mole $gcat^{-1}$ s^{-1}
r'_{OH}	rate of $OH^{\bullet}$ radical formation	mole m^{-2} s^{-1}
r''_{OH}	rate of $OH^{\bullet}$ radical formation	mole L^{-1} s^{-1}
r'''_{OH}	rate of $OH^{\bullet}$ radical formation	mole L^{-1} s^{-1}
r_p	rate of pollutant photodegradation of the chemical species "p"	mole L^{-1} s^{-1}
r_1	rate of disappearance of model pollutant	mole L^{-1} s^{-1}
$r_{1.in}$	rate of disappearance of model pollutant at initial conditions	mole L^{-1} s^{-1}
R	radiation intensity	watts m^{-2} nm^{-1}
t	time	min
V_{irr}	irradiated reactor volume	L
V	reactor volume	L
W_{irr}	irradiated weight of catalyst	Kg

Greek Symbols

α	number of photons required for the formation of an $OH^{\bullet}$ radical	
η	Photochemical thermodynamic efficiency factor, $= Q_{used}/Q_a$	
η_{OH}	fraction of photon energy used in the formation of $OH^{\bullet}$ radicals	
$\Delta H_{OH^{\bullet}}$	enthalpy of $OH^{\bullet}$ radical formation in a photochemical reaction	J mole-^{1}
λ	wavelength	nm
φ	quantum yield or fraction of photons absorbed by the photocatalyst resulting in the formation of $OH^{\bullet}$ radicals	
φ_{app}	apparent quantum yield or fraction of photons entering the reactor resulting in the formation of $OH^{\bullet}$ radicals	
φ_{in}	quantum yield or fraction of photons absorbed by the photocatalyst resulting in the formation of $OH^{\bullet}$ radicals defined at the initial conditions of irradiation	
$\varphi_{app.in}$	apparent quantum yield or fraction of photons entering the reactor resulting in the formation of $OH^{\bullet}$ radicals defined at the initial conditions of irradiation	
ν	stochiometric number for the $OH^{\bullet}$ reacting with the model compound	negative number

CuuDuongThanCong.com https://fb.com/tailieudientucntt

ν_1	stochiometric number for the model pollutant reacting with $OH^\bullet$ group radicals	negative number
ν_p	stochiometric number for the pollutant chemical species (model pollutant and intermediates) reacting with the $OH^\bullet$ group	negative number

Subscripts

acc	accumulation
app	apparent
c	consumption
in	initial condition
ma	maximum
p	pollutant
0	initial condition

Acronyms

PTEF	Photochemical Thermodynamic Efficiency Factor
QY	quantum yield

REFERENCES

Alfano, O., and Cassano, A., 1998, Modeling of a gas–liquid tank photoreactor irradiated from the bottom 1, Theory, *Ind. & Eng. Chem. Res.*, **27**:1087–1095.

Alfano, O., and Cassano, A., 1988, Modeling of a gas – liquid tank photoreactor irradiated from the bottom 2. Experiments, Industrial and Engineering Chemistry Researchy, *Ind. & Eng. Chem. Res.*, **27**:1095–1103.

Bolton, J., and Cater, S., 1994, Homogeneous photodegradation of pollutants on contaminated water: An introduction, in: *Aquatic and Surface Photochemistry*, Hels, G., Zepp, R., and Crosby, D., eds., Lewis Publications, pp.467.

Cabrera, M., Alfano, O., and Cassano, A., 1994, Novel reactor for photocatalytic kinetic studies, *Ind. & Eng. Chem. Res.*, **33**:3031–3042.

Cabrera, M., Alfano, O., and Cassano, A., 1996, Absorption and scattering coefficients of titanium dioxide particulate suspensions in water, *J. Phys. Chem.*, **100**(51):20043–20050.

Cassano, A., Martin, C., Brandi, R., and Alfano, O., 1995, Photoreactor analysis and design: Fundamentals and applications, *Ind. & Eng. Chem. Res.*, **34**:2155–2201.

Davydov, L., Smirniotis, G., and Pratsinis, E., 1999, Novel differential reactor for the measurement of overall quantum yields, *Ind. & Eng. Chem. Res.*, **38**(4):1375–1383.

Fox, M., 1988, Photocatalytic oxidation of organic substances, in: *Photocatalysis and environment: Trends and applications*, Schiavello, M., ed, Kluwer Academic Publishers, pp.445–467.

Fox, M. and Dulay, M., 1993, Heterogeneous photocatalysis, *Chem. Rev.*, **93**:341–357.

Hoffman, M., Martin, S., Choi, W., and Bahnemann, D., 1995, Environmental applications of semiconductor photocatalysis, *Chem. Rev.*, **95**(1):69–96.

Ibrahim, H., 2001, Photocatalytic Reactor for the degradation of airborne pollutants. Photoconversion efficiency and kinetic modelling, PhD Dissertation, the University of Western Ontario, Canada.

Kerr, J.A., 1966, Bond dissociation energies by kinetic methods, *Chem. Rev.*, **66**(5):465–500.

Nimlos, M., Jacoby, W., Blake, D., and Mllne T., 1993, Direct mass spectrometric studies of the destruction of hazardous wastes. 2. Gas phase photocatalytic oxidation of trichloroethylene over TiO_2: Products and mechanisms, *Environ. Sci. & Tech.*, **27**(4):732–740.

CuuDuongThanCong.com https://fb.com/tailieudientucntt

Notarfonzo, R., and McPhee W., 1994, How to evaluate a UV/oxidation system, *Pollution Engineering*, **26**(10):74–76.

Peill, N., and Hoffmann, M., 1995, Development and optimization of a TiO_2 coated fiber optic cable reactor: Photocatalytic degradation of 4-chlorophenol, *Environ. Sci. & Tech.* **29**:2974–2981.

Pelizzetti, E., Minero, C., and Pramauro, E., 1992, Photocatalytic process for destruction of organic chemicals, in *Chemical reactor technology for environmentally safe reactors and products,* de Lasa, H., Dogu, G., and Ravella, A., eds., Kluwer Academic Publishers, The Netherlands, pp. 557–608.

Salaices, M., Serrano, B., and de Lasa, H., 2001, Photocatalytic conversion of organic pollutants. Extinction coefficients and quantum efficiencies, *Ind. & Eng. Chem. Res.*, **40**:5455–5464.

Sczechowski, J., Koval, C., and Noble, R., 1995, A Taylor vortex reactor for heterogeneous photocatalysis, *Chem. Eng. Sci.*, **50**(20):3163–3173.

Serrano, B., and de Lasa, H., 1997, Photocatalytic degradation of water organic pollutants. Kinetic modeling and energy efficiency. *Ind. & Eng. Chem. Res.,* **36**:4705–4711.

Turchi, C.S., and Ollis, D., 1990, Photocatalytic degradation of organic water contaminants: Mechanisms involving hydroxyl radical attack, *J. Cat.*, **122**:178–192.

Valladares, J., and Bolton, J., 1993, A method for the determination of quantum yields in heterogeneous systems: The titanium dioxide photocatalyzed bleaching of methylene blue. *Trace Metals in the Environment,* **3**:111–120.

Wagman, D., Evans, W., Parker, V., Schum, R., Halow, I., Bailey, S., Churney, K., and Nutall, R., 1982, The NBS tables of chemical thermodynamics properties. Selected values for inorganic and C1 and C2 organic substances in SI Units, *J. Phys. Chem. Ref. Data*. 11 Supl. 2.

Yamazaki–Nishida, S., Read, H., Nagano, J., Jarosch, T., Eddy, C., Cervera–March, S., and Anderson, M., 1994, Gas phase photocatalytic degradation on TiO_2 pellets of volatile chlorinated compounds from a soil vapor extraction well. *J. Soil Contam.*, **3**(4): 363–378.

Zhang, Y., Crittenden, J., and Hand, D., 1994a, The solar photocatalytic decontamination of water, *Chem. & Ind.*, **18**:714–717.

Zang, Y., Crittenden, J., Hand, D., and Perram, D., 1994b, Fixed bed photocatalysts for solar decontamination of water. *Environ. Sci. & Tech.*, **28**(3):435–442.

cuu duong than cong . com

CuuDuongThanCong.com https://fb.com/tailieudientucntt

7

Water Decontamination of Organic Species: Modeling Reaction and Adsorption Processes

7.1. INTRODUCTION

Modeling photocatalytic reaction processes requires careful consideration of reaction and adsorption phenomena. In order to establish the importance of these matters, experiments can be developed using model pollutants such as methylene blue, phenol, 2-chlorophenol, 2,4-dichlorophenol, catechol (or 1,2 benzenediol), and pyrogallol (or 1,2,3 benzenetriol), each having quite different behaviours of adsorption and reaction.

These model pollutants are also of special interest as they can be representative of typical water contaminants (Al-Ekabi and Serpone, 1988; Al-Sayyed, et al., 1991; Ku et al., 1996; Okamoto et al., 1985; Sehili, et al., 1989). In the case of MeB, for example, the model compound can provide a quick visualization of the photoconversion efficiency.

7.2. EXPERIMENTAL CONDITIONS FOR APPROPRIATE KINETIC MODELING

The modeling and evaluation of adsorption-reaction processes in Photo-CREC-Water reactors require the compliance of a number of conditions and model assumptions. These conditions and assumptions are important in order to ensure that the adopted mathematical models and related simplifications are applicable. The following are the conditions and assumptions adopted

a) Every experiment is initiated with the addition of a model pollutant to water contained in a reservoir-reactor system. A pump provides high water recirculation in a unit operating in the batch mode.
b) During the preparatory phases of the experiment, water flows upwards purging the air inside the unit. Later, the flow direction is reversed ensuring a liquid-solid two-phase flow (slurry reactor), or a liquid phase flow (immobilized catalyst on

CuuDuongThanCong.com https://fb.com/tailieudientucntt

a mesh) with no air bubbles, high mixing and quasi-constant pollutant concentration throughout the entire unit.

c) Air is continuously bubbled in an auxiliary reservoir, keeping the water solution saturated with oxygen (Barbeni et. al, 1985; Gerisher and Heller, 1991). Air is delivered using a perforated pipe air distributor (Salaices et al., 2001; Serrano and de Lasa, 1997). Air bubbling also helps with the solution mixing and, in the case of slurry reactors, with the re-suspension of TiO_2.

d) The preliminary phase of each experiment belongs to the "dark" reaction period as the lamp is kept "off" (Matthews, 1989). During this preparatory period, pollutant adsorption is the only physico-chemical phenomenon taking place.

e) Following the "dark" period, and once adsorption equilibrium is reached; the lamp is turned "on". The TiO_2 is activated and the photoconversion reaction is initiated. This process continues until very low levels of model pollutants are reached and complete pollutant mineralization is achieved.

f) Water samples (e.g. 10 mL) are withdrawn from the tank at regular intervals. These samples are analyzed using several analytical techniques to determine the model pollutant and the intermediate species concentrations.

7.3. MODELING THE ADSORPTION AND REACTION PROCESSES

Mathematical modeling of the photocatalytic processes is an important task. This allows to establish the reactor performance from a conversion of model pollutants perspective as well as on the basis of the calculation of energy efficiencies.

We have already described in Chapter V phenol photoconversion in slurry photocatalytic systems with adsorption assumed at quasi-equilibrium. In many cases, however, photocatalytic reactors are operated under non-equilibrium conditions: the pollutant concentrations in the solid phase and in the fluid phase are significantly far away from the adsorption equilibrium values. As demanded by careful modeling, accounting for adsorption at non-equilibrium conditions is needed.

To achieve this, separate species balances for both the liquid phase (water solution) and the solid phase (TiO_2 particles) have to be considered.

Liquid phase

$$\frac{dC_i}{dt} = \frac{W}{V}\left[-k_{i,ads}C_i\left(q_{i,m} - \sum q_i\right) + k_{i,des}q_i\right] \tag{7-1}$$

Catalyst phase

$$\frac{dq_i}{dt} = \frac{V}{W}\left[-\frac{dC_i}{dt} + \frac{W_{irr}}{V}\sum_k \nu_{i,k}k_{i,r}q_i\right] \tag{7-2}$$

Initial conditions:

$$At\ t = t_{eq}, \quad C_1 = C_{1,eq}, \quad q_1 = q_{1,eq}, \quad q_i = 0, \quad C_i = 0 \tag{7-3}$$

CuuDuongThanCong.com https://fb.com/tailieudientucntt

with i representing chemical species other than the model pollutant and 1 the model pollutant, W the total weight of adsorbent phase (irradiated TiO_2, non-irradiated TiO_2, TiO_2-support) and W_{irr} the weight of irradiated TiO_2 photocatalyst.

Equation (7-2) states that the observed pollutant solid phase concentration is the result of the competition processes: adsorption, desorption and reaction. Furthermore, equation (7-1) establishes that the observed bulk fluid phase species concentration is the result of the difference between the adsorption and desorption rates.

Thus, one has to consider the combined set of equations (7-1), (7-2) and (7-3), in addition to the various adsorption and reaction parameters involved in these equations, to provide an adequate phenomenological description of pollutant concentration changes in photocatalytic reaction systems with respect to the reaction time.

7.4. ADSORPTION AND REACTION OF MODEL POLLUTANTS

Methylene blue (MeB) is a pollutant present in water stream effluents from dye factories.

Experiments performed using MeB have intrinsic advantages as MeB blue's colour disappears as photoconversion progresses and provides a quick assessment of the reactor performance. This colour change is easy to follow via spectrophotometery ($\lambda = 664$ nm).

Runs were developed in the Photo-CREC-Water I (Chapter II) with a water recirculation of 1720 mL min^{-1}. Initial MeB concentrations were varied in the 5-50-μmole range during the experiments. Samples were analyzed at 664 nm using a PU8625 UV/VIS spectrophotometer and Shimadzu 5050 TOC model. This allows to follow the disappearance of the model compound, the intermediate species and the total organic carbon.

Figure 7.1 illustrates the MeB concentration changes using the UV/Vis spectrometry. Particularly relevant is the concentration change during the "dark" period when only adsorption occurs. During this initial "dark" phase, about 80% of the MeB pollutant is adsorbed on the TiO_2 once the adsorption equilibrium is reached.

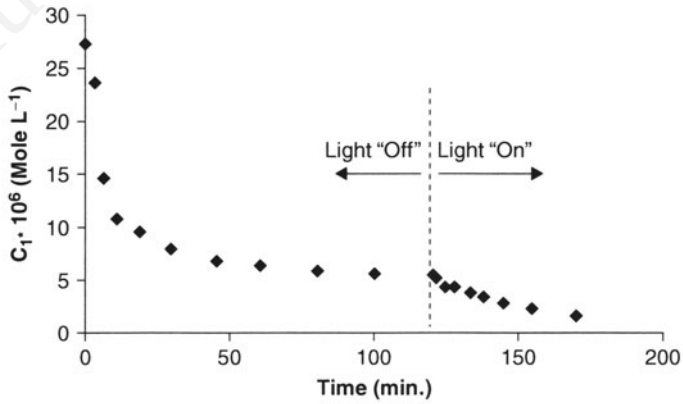

FIGURE 7.1. Change of MeB liquid phase concentration with time. Initial concentrations: (♦) 27 10^{-6} mole L^{-1}. (a) Period with light "off"; (b) Period with light "on". Water recirculation: 1.72 L min^{-1}.

CuuDuongThanCong.com https://fb.com/tailieudientucntt

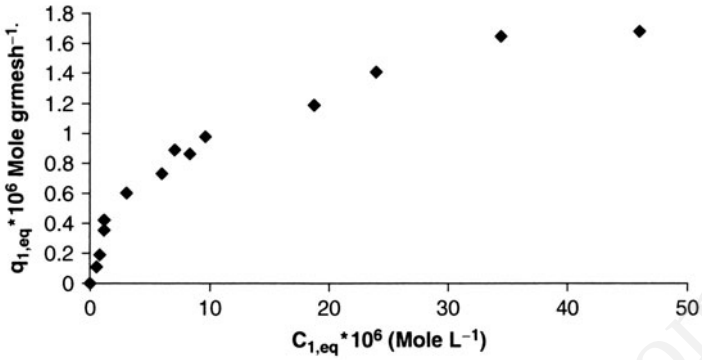

FIGURE 7.2. Equilibrium isotherm for methylene blue and TiO_2-mesh at 20°C. Water recirculation: 1.72 L min^{-1}. (Reprinted with permission from *Ind. Eng. Chem. Res*, **36**(11), B. Serrano and H.I. de Lasa, Photocatalytic degradation of water organic pollutants: Kinetic modeling and energy efficiency, 4705–4711. Copyright 1997 American Chemical Society).

Using mass balances and liquid phase concentrations (C_{eq}), the adsorbed concentration at equilibrium can be calculated (q_{eq}). With these data (C_{eq}, q_{eq}), adsorption isotherms, as the one reported in Figure 7.2 for methylene blue, are obtained.

Alternatively, during the "reaction", when the lamp is turned "on" (Figure 7.1), the modeling requires the consideration of both adsorption and reaction phenomena, as described by equations (7-1) and (7-2).

Numerical solution of the set of equations (7-1) and (7-2) enables the evaluation of intrinsic kinetic constants and subsequently, the calculation of *PTEF* and quantum yield factors.

Phenol photoconversion in the Photo-CREC-Water I is reported in Figure 7.3. This shows weak phenol adsorption (8%) during the initial "dark" period. This weak

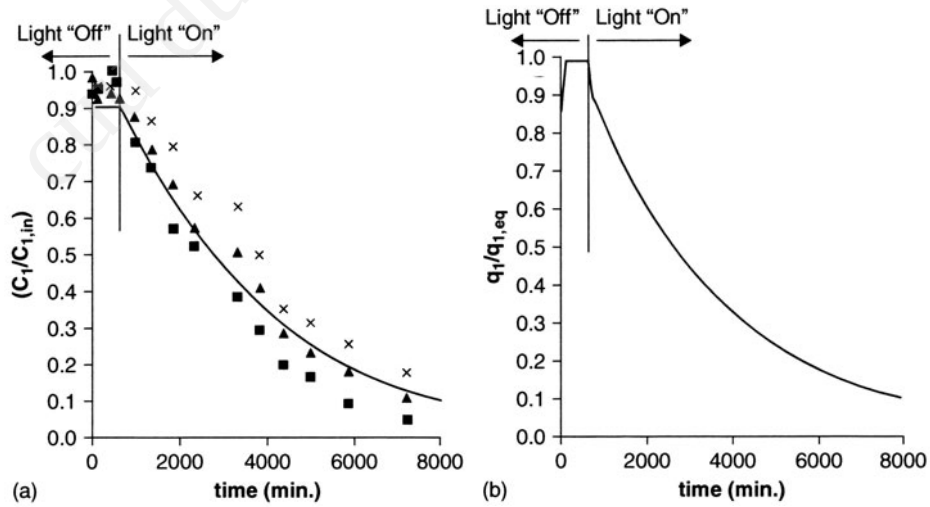

FIGURE 7.3. Phenol dimensionless concentration changes in (a) liquid and (b) solid phase (x) TOC, (▲) Spectrophotometer, 270 nm, (■) HPLC with detector at 270 nm. Full line: Model results with equations (7-6) and (7-7) and parameters from Table 7.2 and 7.3.

CuuDuongThanCong.com https://fb.com/tailieudientucntt

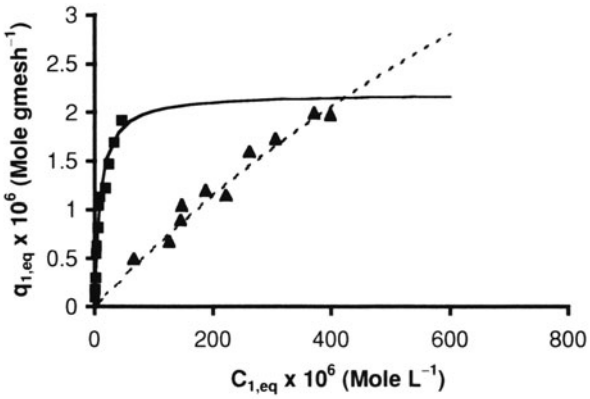

FIGURE 7.4. Equilibrium adsorption isotherms: (■) for MeB, (▲) for phenol.

adsorption is in sharp contrast with 80% MeB concentration drop observed during the "dark" period (Figure 7.1). This different magnitude of adsorption at equilibrium is further shown in Figure 7.4, where MeB displays a strong, non-linear Langmuir isotherm while phenol shows a close-to-linear isotherm.

There are also important differences in reaction times between phenol and MBe, with phenol requiring much more reaction time for complete mineralization than does MeB. It can therefore be concluded that different model pollutants display different adsorption-reaction behaviors under the same operating conditions.

7.5. MODELING ADSORPTION AND REACTION PARAMETERS OF A MODEL POLLUTANT

The general adsorption-reaction model given by the set of equations (7-1) and (7-2) can be simplified and extended to describe two possible sub-cases:

- "Dark" operation: lamp remains turned "off"
- Initial phase of irradiated TiO_2 operation with the lamp turned "on".

Under "dark" conditions, equations (7-1) and (7-2) become a set of two equations including competing adsorption and desorption terms only:

$$\frac{dC_i}{dt} = \frac{W}{V}[-k_{ads}C_i(q_{i,m} - q_i) + k_{i.des}q_i] \tag{7-3a}$$

and

$$\frac{dq_i}{dt} = \frac{V}{W}\left[-\frac{dC_i}{dt}\right] \tag{7-3b}$$

Initial conditions can be adopted to solve equation (7-3a) and (7-3b) at t = 0.

$$at\ t = 0, \quad C_i = C_{i,in}, \quad q_i = 0, \quad C_j = 0, \quad q_j = 0 \tag{7-4}$$

CuuDuongThanCong.com https://fb.com/tailieudientucntt

with j representing other intermediate chemical species formed during the photoconversion process.

The main requirement for the adoption of these initial conditions is that the photocatalytic reactor be completely pollutant free from previous experiments, at the time of initiation of the dark reaction.

Given that a single chemical species is used (e.g. MeB) in experiments with model pollutants, the "i" subscript becomes "1".

$$\frac{dC_1}{dt} = \frac{W}{V}[-k_{1,ads}C_1(q_{1,m} - q_1) + k_{1.des}q_1] \tag{7-5a}$$

and

$$\frac{dq_1}{dt} = \frac{V}{W}\left[-\frac{dC_1}{dt}\right] \tag{7-5b}$$

Initial conditions can be adopted to solve equation (7-5a) and (7-5b) at t = 0.

$$at\ t = 0, \quad C_1 = C_{1,in}, \quad q_1 = 0, \quad C_i = 0, \quad q_i = 0,\ i > 1 \tag{7-5c}$$

7.6. INITIAL PHASE OF IRRADIATED TiO_2 OPERATION

During this initial phase of TiO_2 irradiation, the original set of equations (7-1) and (7-2) can be retained. The model pollutant, however, must be the only relevant species considered: the generic "i" subscript is now exchanged by the subscript "1".

Liquid Phase

$$\frac{dC_1}{dt} = \frac{W}{V}[-k_{1,ads}C_1(q_{1,m} - q_1) + k_{1.des}q_1] \tag{7-6}$$

Catalyst Phase

$$\frac{dq_1}{dt} = \frac{V}{W}\left[-\frac{dC_1}{dt} + \frac{W_{irr}}{V}k_{1,r}q_1\right] \tag{7-7}$$

Regarding the initial condition chosen for the solution of equations (7-6) and (7-7), it is assumed that the lamp is turned "on" once the model pollutant in both the liquid and the solid phases reaches adsorption equilibrium.

$$at\ t = t_{eq},\ C_1 = C_{1,eq}, \quad q_1 = q_{1,eq} \tag{7-8}$$

Moreover, under some conditions, a "special case" of equations (7-6) and (7-7) can be considered for low/moderate concentrations ($q_{1,eq} = q_{1,m}K_1C_{1,eq}$), as

$$\frac{dC_1}{dt} = \frac{W}{V}k_{1,des}\left[-K_1q_{1,m}C_1 + q_1\right] \tag{7-9}$$

CuuDuongThanCong.com https://fb.com/tailieudientucntt

$$\frac{dq_1}{dt} = -\frac{V}{W}\left[\frac{dC_1}{dt} + \frac{W_{irr}}{V}k_{1,r}q_1\right] \tag{7-10}$$

with $K_1 = \frac{k_{1,ads}}{k_{1,des}}$ and $K_1 q_{1,m}$ obtained from the slope of the linear section of the isotherm and $k_{1,ads}q_{1,m}$ determined using the slope of the pollutant concentration profile as $t \to 0$,

$$\frac{dC_1}{dt} = -\frac{W}{V}k_{1,ads}q_{1,m}C_1 \tag{7-11}$$

Equations (7-9), (7-10) and (7-11) allow modeling the photo–catalytic conversion of 2-chlorophenol and 2,4 dichlorophenol, under this "special case" and, as a result, without the requirement of having to define $q_{1,m}$. Only the groups $k_{1,ads}q_{1,m}$ and $K_1 q_{1,m}$ are assessed with experimental data.

7.7. EVALUATION OF ADSORPTION PARAMETERS

Evaluating the adsorption parameters involves the consideration of equation (7-5) at the following conditions,

a) $t = t_{eq}$,or adsorption at equilibrium: This condition allows calculation of both K_1 and $q_{1,m}$, Langmuir parameters, from the adsorption isotherm $q_{1,eq} = \frac{q_{1,m}K_1C_{1,eq}}{1+K_1C_{1,eq}}$. This equation is fitted to the experimental adsorption isotherm via non-linear regression, as shown in Figure 7.4. For methylene blue, the calculated K_1 and $q_{1,m}$ are 0.11 10^6 L mole^{-1} and 2.02 10^{-6} mole (g of mesh)$^{-1}$ respectively (Serrano and de Lasa, 1999).

b) $t < t_{eq}$ or adsorption rate before reaching equilibrium. This allows the evaluation of $k_{1,ads}$ parameter, fitting equation 7-5 to the experimental data, and using also the values of K_1 and $q_{1,m}$. For methylene blue, the $k_{1,ads}$ obtained is 1750 (L mole^{-1} min^{-1}) and for phenol is 14.5 (L mole^{-1} min^{-1}) (Serrano and de Lasa. 1999).

For some model pollutants such as 2-chlorophenol and 2-4-dichlorophenol, there are important challenges in achieving the adsorption equilibrium, and consequently, in obtaining equilibrium adsorption parameters. For 2-chlorophenol and 2-4-dichlorophenol, for instance, it is impractical to reach $q_{1,m}$ with increasing pollutant concentrations (Figure 7.5). For 2-chlorophenol, a minimum of 1000 min is required to reach equilibrium starting with an initial concentration of 200.10^{-6} mole L^{-1}.

In addition to the equilibrium adsorption constants for methylene blue and phenol, Table 7.1 reports those for pyrogallol (1,2,3 benzenetriol) and catechol (1,2 benzenediol), chemical species involved as intermediate in the phenol photoconversion (Chapter V). These equilibrium constants are almost 10 times greater than those for phenol (Table 7.1). It is therefore concluded that these intermediates are more strongly adsorbed on the TiO_2-mesh of the Photo-CREC-Water I. A possible explanation for the higher pyrogallol and catechol adsorption with respect to phenol is the higher dissociation constants associated with these species.

CuuDuongThanCong.com https://fb.com/tailieudientucntt

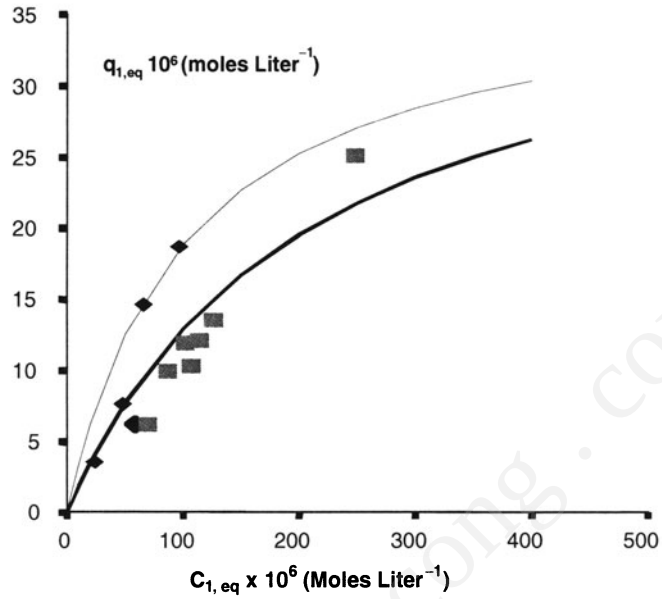

FIGURE 7.5. Equilibrium adsorption isotherms: (♦) 2-4 dichlorophenol, (■) chlorophenol (Reprinted from *Chem. Eng. Sci.*, **54**, B. Serrano and H.I. de Lasa, Photocatalytic degradation of water organic pollutant reactivity and kinetic modeling, 3063–3069, Copyright 1999, with permission from Elsevier).

TABLE 7.1. K_1 and $q_{1,m}$ for Different Chemical Species. Parameters Evaluated with Langmuir Adsorption Isotherm and "Special Case" Method. (*) Estimated Value of $q_{1,m}$ Using the "Special Case"

Compound	K_1(L mole^{-1})	$q_{1,m}$ x 10^6 (mole gmesh^{-1})
Methylene blue	110000 ± 15530	2.2 ± 0.323
Phenol	631.5 ± 766	10.23 ± 10.09
Catechol	6213	27.69
Pyrogallol	6213	38.14
2-Chlorophenol	4829 ± 1613*	39.87 ± 23.8*
2,4-Dichlorophenol	9822 ± 2403*	38.14 ± 27.3*

As reported by Serrano and de Lasa (1999) 2-chlorophenol, 2-4-dichlorophenol, phenol and MeB display different degrees of adsorption during the "dark" reaction (light turned off). For 2-4-dichlorophenol, the dimensionless concentration drop during the dark period was close to 0.75, contrasting with the 0.6 decrease for 2-chlorophenol and the 0.08 reduction for phenol. The addition of chlorine atoms to the phenol molecules further enhances pollutant adsorption on the TiO_2 –mesh of Photo-CREC-Water I.

7.8. EVALUATION OF INTRINSIC REACTION PARAMETERS

Once the adsorption equilibrium is reached, the operation conditions are satisfactory for the lamp to be turned on. The model pollutant concentration changes are

CuuDuongThanCong.com https://fb.com/tailieudientucntt

TABLE 7.2a. $k'''_{1,r}$ Parameters for Methylene Blue Determined Using the Set of Equations (7-6) and (7-7) (adapted from Serrano (1998))

Initial Equilibrium Concentration Mole $L^{-1}.10^6$	$k'''_{1,r}$ g_{ads} L^{-1} min^{-1}
0.48	2.71 ± 0.55
3.10	2.49 ± 0.29
9.18	2.55 ± 0.48

described using equations (7-6) and (7-7). As stated, these equations apply at conditions where intermediate products are of little influence on chemical pollutant photoconversion changes.

Assuming that all adsorption parameters ($q_{1,m}$, $k_{1,ads}$, K_1) derived during the "dark" operation can be adopted for the reaction period, the $k'''_{1,r}$ parameters can be calculated, according to Serrano (1998). The fitting of the model predictions to the experimental data is illustrated for phenol in Figure 7.3. As reported in Tables 7.2a and 7.2b, the $k'''_{1,r}$ values remain in a relatively narrow range, and this supports the heterogeneous model proposed by Serrano and de Lasa (1999).

Compounds 2-chlorophenol and 2,4-dichlorophenol offer special challenges for determining $q_{1,m}$. One can consider that experiments developed for these species fall within the linear section of the adsorption isotherm ($q_1 = q_{1,m} K_1 C_1$). Using this condition, the $k_{1,ads} q_{1,m}$ and $K_1 q_{1,m}$, $k'''_{1,r}$ groups can be calculated through equations (7-9), (7-10) and (7-11), as reported in Table 7.3. Therefore $k'''_{1,r}$ can be calculated while circumventing the need for a prior definition of $q_{1,m}$.

To verify the validity of the proposed simplified method, values of $k_{1,ads} q_{1,m}$, and $K_1 q_{1,m}$ obtained for phenol can be used to recalculate the $k'''_{1,r}$ values reported in Table 7.2b. Serrano and de Lasa (1999) noted that deviations between the more rigorous approach and the simplified method were less than 6.5% when calculating $k'''_{1,r}$.

The observed photoconversion rate for 2,4-dichlorophenol is higher than those measured for 2-chlorophenol and phenol. To convert 90% of dichlorophenol, 1000 minutes were required, while 1300 minutes were needed for 2-chlorophenol and 1400 minutes for phenol (including in all three cases the adsorption and reaction period).

Reviewing the parameters reported in Table 7.3, it is observed that the addition of chlorine to the phenol molecule increases $K_1 q_{1,m}$ significantly: 0.0056 l L

TABLE 7.2b. $k'''_{1,r}$ Parameters for phenol Determined Using the Set of Equations (7-6) and (7-7) (adapted from Serrano (1998))

Initial Equilibrium Concentration Mole $L^{-1}.10^6$	$k'''_{1,r}$ g_{ads} L^{-1} min^{-1}
66.1	0.085 ± 0.004
221.8	0.087 ± 0.01
398.2	0.078 ± 0.004

CuuDuongThanCong.com https://fb.com/tailieudientucntt

TABLE 7.3. $K_1 q_{1,m}$, $k_{1,ads} q_{1,m}$ and $k'''_{1,r}$ Parameters Determined Using the "Special Case"

Model Pollutant	$K_1 q_{1,m}$ (L g_{ads}^{-1})	$[k_{1,ads} q_{1,m}]_{ave}$ ($Lmin^{-1}$ g_{ads}^{-1})	$[k'''_{1,r}]_{ave}$ (g_{ads} L^{-1} min^{-1})
Phenol	0.00561	$10 . 10^{-5}$	0.084
2-Chlorophenol	0.1185	$16.77 . 10^{-5}$	0.23
2,4-Dichlorophenol	0.236	$30.46 . 10^{-5}$	0.128

g_{ads}^{-1} for phenol, 0.1185 L g_{ads}^{-1} for 2-chlorophenol and 0.236 L g_{ads}^{-1} for 2-4-dichlorophenol.

It was also noted that $k_{1,r}$ increased considerably: 0.0840 g_{ads} L^{-1} min^{-1} for phenol, 0.23 g_{ads} L^{-1} min^{-1} for 2-chlorophenol and 0.128 g_{ads} L^{-1} min^{-1} for 2-4-dichlorophenol. A possible explanation for the increased reaction with chlorine is a higher molecular dissociation. Dissociation constants are $1.28\ 10^{-10}$ for phenol (Lide, 1997); $30\ 10^{-10}$ for 2-chlorophenol (Lide, 1997) and $140\ 10^{-10}$ for 2-4-dichlorophenol (Dean, 1985). This progressive increase of dissociation constants with chlorine content parallels the increasing adsorption constants. The Photo-CREC-Water-I unit tends thus, to adsorb chlorophenol pollutants strongly, photoconverting them at higher rates than phenol.

Serrano (1998) also reports useful data in establishing relative reactivities. Intrinsic reaction constants were calculated assuming that adsorption constants for phenol, and for parent phenol molecules (e.g. catechol, pyrogallol) were identical. These calculations show that chemical species display reaction constants as follows: 0.084 g_{ads} L^{-1} min^{-1} for phenol, 0.18 L g_{ads}^{-1} min^{-1} for catechol and 0.27 L g_{ads}^{-1} min^{-1} for pyrogallol; an important finding for a formulation of a photocatalytic network for phenol conversion.

7.9. *PTEF* AND QUANTUM YIELD CALCULATIONS

The evaluation of the performance of a photocatalytic reactor through quantum efficiencies and *PTEF* involves the evaluation of total photoconversion rates (Serrano and de Lasa, 1999).

One possible approximation, for pollutant photoconversion processes taking place at quasi-equilibrium conditions (e.g. phenol photo- conversion), is to express the total photoconversion rate using the method outlined in Chapter I:

$$PTEF = \eta = \frac{-\nu/\nu_{mp} r_{1T} \Delta H_{OH} W_{irr}}{Q_a} \tag{7-12}$$

and

$$PTEF = \eta = \frac{-\nu/\nu_{mp} r_{1,in} (1 + K') \Delta H_{OH} W_{irr}}{Q_a} \tag{7-13}$$

CuuDuongThanCong.com https://fb.com/tailieudientucntt

TABLE 7.4. $PTEF_{eq}$ and $PTEF_{neq}$ for Phenol and MeB

Model Pollutant	Initial Equilibrium Concentration.10^6 Mole L^{-1}	$PTEF_{eq}$	$PTEF_{neq}$
Phenol	100	0.0006	0.0006
	200	0.0011	0.0011
	400	0.0014	0.0014
Methylene Blue	1.5	0.001	0.0085
	4.0	0.005	0.0125
	8.5	0.009	0.023

Assuming that the ν and ν_{mp} stochiometric coefficients are both equal to -1, and following the considerations reported in Chapter VI, $r_{1.in}W_{irr} = r'''_{1.in}V$ equation (7-13) is reduced to:

$$PTEF_{eq} = \eta_{eq} = \frac{r'''_{1.in}(1 + K')\Delta H_{OH}V}{Q_a} \tag{7-14}$$

For processes where the photoconversion does not take place under quasi-equilibrium conditions, however, the *PTEF* factor has to be expressed by

$$PTEF_{neq} = \eta_{neq} = \frac{k_{1,r}q_{1.m}W_{irr}\Delta H_{OH}}{Q_a} = \frac{k'''_{1r}q_{1.m}V\Delta H_{OH}}{Q_a} \tag{7-15}$$

Thus, the *PTEF* factor both at quasi-equilibrium and non-equilibrium conditions, equations (7-14) and (7-15), can be computed for phenol and MeB considering that,

a) the $k'''_{1,r}$ and $q_{1.m}$ parameters are known, as reported in Tables 7-1, 7-2a and 7-2b.
b) the ΔH_{OH} is 94600 Joule $mole^{-1}$.
c) the estimated absorbed irradiation in the Photo - CREC - Water-I, is assessed at $Q_a = 0.531$ W.
d) the volume of the Photo-CREC-Water-I is 3 Liters.

Using this method, $PTEF_{eq}$ and $PTEF_{neq}$ can be calculated (Table 7.4).

It can be observed in Table 7.4 that for phenol photodegradation the $PTEF_{eq}$ and $PTEF_{neq}$ leads to essentially the same results and this is consistent with the frequently adopted assumption of chemical special species at equilibrium. As it can also be observed in Table 7.4, the MeB display however, for $PTEF_{eq}$ and $PTEF_{neq}$ quite different values. This emphasizes the critical importance of properly modeling photocatalytic degradation processes taking place under non-equilibrium conditions. Thus, adequate modeling of these processes as well as calculation of the related kinetic parameters leads to proper calculation of *PTEF* reactor energy efficiencies.

PTEF for MeB, phenol, 2-chlorophenol and 2,4-dichlorophenol are reported in Figure 7.6. A maximum *PTEF* can also be evaluated at high enough model pollutant concentrations. *PTEF* maximum obtained via observed experimental rates ($PTEF_{max}$,

CuuDuongThanCong.com https://fb.com/tailieudientucntt

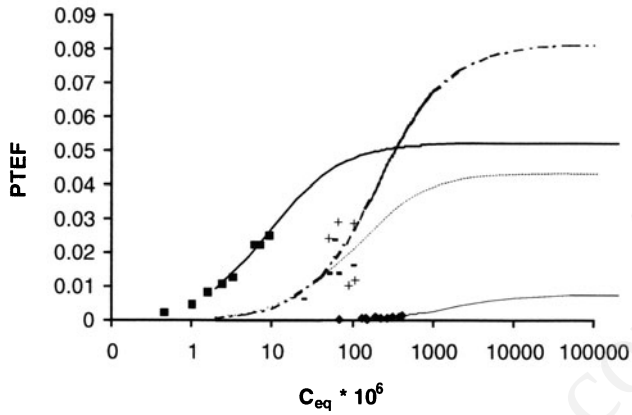

FIGURE 7.6. *PTEF* changes with initial equilibrium pollutant concentration. (■) Methylene Blue, (+) chlorophenol, (-) dichlorophenol, (♦) Phenol. (Reprinted from *Chem. Eng. Sci.*, **54**, B. Serrano and H.I. de Lasa, Photocatalytic degradation of water organic pollutant reactivity and kinetic modeling, 3063-3069, Copyright 1999, with permission from Elsevier).

TABLE 7.5. Maximum *PTEF* and QY values

Model Pollutant	$PTEF_{max,exp}$	$QY_{max,exp}$ (%)	$PTEF_{max,model}$	$QY_{max,model}$ (%).
MeB	0.025	8.65	0.0552	19.10
Phenol	0.00147	0.498	0.0076	2.65
2-Chlorophenol	0.0293	10.13	0.0818	28.31
2,4-Dichlorophenol	0.0168	5.82	0.0434	15.04

experimental) are reported in Figure 7.6 and Table 7.5. Considering that $\varphi = \eta/\eta_{OH}$ and $\eta_{OH} = 0.289$ (refer to Chapter VI) the highest calculated *PTEF* gives QY values of 0.0014 and 0.49% for phenol and 0.0293 and 10.13% for 2-chlorophenol.

Furthermore, considering $q_{1,m}$ of 2.30 10^{-6} mole g_{ads}^{-1} for MeB, 10.20 10^{-6} mole g_{ads}^{-1} for phenol, 39.80 10^{-6} mole g_{ads}^{-1} for 2-chlorophenol and 38.10 10^{-6} mole g_{ads}^{-1} for 2-4-dichlorophenol, the *PTEF* and QY calculations can be extended to high pollutant concentrations. Asymptotic maximum values predicted for *PTEF* and QY ($PTEF_{max,model}$ and $QY_{max,model}$) are 0.0076 and 2.65% for phenol and 0.0818 and 28.31% for 2-chlorophenol.

7.10. CONCLUSIONS

The main conclusions in this chapter can be summarized as,

a) Even if in many cases physical adsorption can be considered at quasi-equilibrium, a more general approach should consider adsorption at "non-equilibrium" conditions.
b) Adsorption and reaction phenomena can be mathematically modeled through a combined set of equations: one for the liquid phase and the other for the solid phase.

CuuDuongThanCong.com https://fb.com/tailieudientucntt

c) Application of this model is contingent to the soundness of the mixing and re-oxygenation assumptions. The model applicability requires as well that initial conditions be met: equilibrium adsorption (end of the "dark" period) and complete removal of pollutants from previous experiments.
d) Using this approach, the adsorption isotherms and the adsorption parameters are evaluated during "dark" conditions. Intrinsic kinetic constants are calculated during the initial phases of catalyst irradiation.
e) Evaluated parameters allow the calculation of efficiency factors such as the *PTEF* and quantum yields.
f) There is close agreement between the *PTEF* for phenol calculated using an adsorption equilibrium model and employing a non-adsorption equilibrium model.
g) There is significant discrepancy between the PTEF calculated using an adsorption equilibrium and an adsorption non-equilibrium model for certain chemical species and this stresses the significance of efficiency calculations using adsorption non-equilibrium models.

NOTATION

Symbols

C_i	liquid phase concentration of the i chemical species	g L^{-1} μmole L^{-1}
C_1	liquid phase concentration of model pollutant	g L^{-1} μmole L^{-1}
$C_{1,eq}$	liquid phase concentration of model pollutant at equilibrium	g L^{-1} μmole L^{-1}
C_{1T}	total concentration of model pollutant	g L^{-1} μmole L^{-1}
$C_{1,in}$	initial liquid phase concentration of model pollutant	g L^{-1} μmole L^{-1}
$k_{i,r}$	intrinsic kinetic reaction constant for "i" species based on W_{irr}	g_{ads} $g_{cat,irr}^{-1}$ s^{-1}
$k'''_{i,r}$	intrinsic kinetic reaction constant for "i" species based on V, $\frac{W_{irr}}{V} k_{i,r}$	g_{ads} L^{-1} s^{-1}
$k_{i,ads}$	adsorption rate constant for "i" species	L $mole^{-1}$ s^{-1}
$k_{i,des}$	desorption rate constant for "i" species	s^{-1}
$k_{1,r}$	intrinsic kinetic reaction constant	g_{ads} $g_{cat,irr}^{-1}$ s^{-1}
$k_{1,ads}$	adsorption rate constant	L $mole^{-1}$ s^{-1}
$k_{1,des}$	desorption rate constant	s^{-1}
$k'''_{1,r}$	kinetic reaction constant	g_{ads} L^{-1} s^{-1}
K_i	Adsoption constants for I species	L $mole^{-1}$
K_j	adsorption constants for j species	L mol^{-1}
K'	dimensionless adsorption constant, refer to equation (1-31) in Chapter I	
Q_a	rate of irradiated energy absorbed in the photocatalytic reactor	J s^{-1}

CuuDuongThanCong.com https://fb.com/tailieudientucntt

q_i	solid phase adsorbed concentration for the "i" species	mole g_{ads}^{-1} μmole g_{ads}^{-1}
$q_{i,m}$	maximum solid phase adsorbed concentration for the "species"	mole g_{ads}^{-1} μmole g_{ads}^{-1}
q_1	solid phase model pollutant adsorbed concentration	mole g_{ads}^{-1} μmole g_{ads}^{-1}
$q_{1,eq}$	solid phase model pollutant adsorbed concentration at equilibrium	mole g_{ads}^{-1} μmole g_{ads}^{-1}
$q_{1,m}$	maximum solid phase model pollutant adsorbed concentration	mole g_{ads}^{-1} μmole g_{ads}^{-1}
r_i	reaction rate for chemical species i with units consistent with R_k	$i = 1$ for model pollutant
r_i'''	reaction rate for chemical species i with units consistent with R_k'''	$i = 1$ for model pollutant
r_1	reaction rate for model pollutants 1 with units consistent with R_k	μmoles $(g_{cat,irr}s)^{-1}$
$r_{1,in}$	initial reaction rate for model pollutants 1 with units consistent with $R_{k,in}$	μmoles $(g_{cat,irr}s)^{-1}$
r_{1T}	total reaction rate for model pollutants 1 with units consistent with $R_{k,in}$	μmoles $(g_{cat,irr}s)^{-1}$
$r_{1,in}'''$	initial reaction rate for model pollutants 1 with units consistent with $R_{k,in}'''$	μmole $(L\ s)^{-1}$
r_{1T}'''	total reaction rate for model pollutants 1 with units consistent with $R_{k,in}'''$	μmole $(L\ s)^{-1}$
R_k	reaction rate for reaction step k based on irradiated weight of catalyst	μmoles $(g_{cat,irr}s)^{-1}$
R_k'	reaction rate for reaction step k based on irradiated reactor area	μmole $(m_{irr}^2\ s)^{-1}$
$R_{k,in}'''$	initial reaction rate for reaction step k based on total reactor volume	μmole $(L\ s)^{-1}$
t	time	s
V	system reactor volume	L
W	weight of catalyst/mesh/adsorbent	g_{ads}
W_{irr}	weight of irradiated catalyst/mesh/adsorbent	$g_{cat,irr}$

Greek Symbols

α	number of photons required for the formation of an $OH^\bullet$ radical	
η	Photochemical Thermodynamic Efficiency Factor, *PTEF*	Q_{used}/Q_a
$\eta_{OH^\bullet}$	fraction of photon energy used in the formation of $OH^\bullet$ radicals	
$\Delta H_{OH^\bullet}$	enthalpy of $OH^\bullet$ radical formation in a photochemical reaction	J $mole^{-1}$
λ	wavelength	nm

CuuDuongThanCong.com https://fb.com/tailieudientucntt

φ	quantum yield or fraction of photons absorbed by the photocatalyst resulting in the formation of $OH^{\bullet}$ radicals	
ν	stochiometric number for the $OH^{\bullet}$ reacting with the model compound	negative number
ν_1	stochiometric number for the model pollutant reacting with $OH^{\bullet}$ group radicals	negative number
ν_{mp}	stochiometric number for the model pollutant reacting with the $OH^{\bullet}$ group	"−1" negative number
$\nu_{i.k}$	stoichiometric number for the conversion of i chemical species via the k reaction step	

Acronyms

MeB	methylene blue
$PTEF_{eq}$	Photochemical Thermodynamic Efficiency Factor calculated at equilibrium adsorption conditions
$PTEF_{max}$	Photochemical Thermodynamic Efficiency Factor calculated at equilibrium conditions and conditions of maximum reaction rate
$PTEF_{neq}$	Photochemical Thermodynamic Efficiency Factor calculated at non-equilibrium adsorption conditions
QY	Quantum yield

REFERENCES

Al-Ekabi, H. and Serpone, N., 1988, Kinetic studies in heterogeneous photocatalysis. 1. Photocatalytic degradation of chlorinated phenols in aerated aqueous solutions over TiO_2 supported on a glass matrix, *J. Phys. Chem.*, **92**: 5726–5731.

Al-Sayyed, G., D'Oliveira, J. C. and Pichat, P., 1991, Semiconductor – sensitized phot-degradation of 4-chlorophenol in water, *J. Photochem. Photobiol. A: Chem.*, **58**: 99–114.

Barbeni, M., Pramauro, E., Pelizzetti, E., Borgarello, E., Serpone, N., 1985, Photodegradation of pentachlorophenol catalyzed by semiconductor particles. *Chemosphere,* **14**(2):195–208.

Dean, A.J., 1985, Lange's handbook of chemistry. *McGraw Hill Company*, 13th Edition, p.18.

Gerischer, H. and Heller, A., 1991, The role of oxygen in photooxidation of organic molecules on semiconductor particles. *J. Phys. Chem.,* Vol. **95**(13): 5261–5267.

Ku, Y., Leu, R. M. L., and Kuen C., 1996, Decomposition of 2-chlorophenol in aqueous solution irradiation with the presence of titanium dioxide. *Wat. Res.,* **30**:2569–2578.

Lide, D.R., 1997, CRC handbook of chemistry and physics, *CRC Press*, 78th Edition, p.43.

Matthews, R. W., 1989, Photocatalytic oxidation and adsorption of methylene blue on thin films of near-ultraviolet-illuminated TiO_2. *J. Chem. Soc., Faraday Trans. 1*, **85**(6): 1291–1302.

Okamoto, K., Yamamoto, Y., Tanaka, H., Itaya, A., 1985, Kinetics of heterogeneous photocatalytic decomposition of phenol over anatase TiO_2 powder. *Bull. Chem. Soc. Japan*, Vol. **58**:2023–2028.

Salaices, M., Serrano, B. and de Lasa, H., 2001, Photocatalytic conversion of organic pollutants: extinction coefficients and quantum efficiencies. *Ind. & Eng. Chem. Res.*, **40**: 5455–5464.

Sehili, T., Boule, P. and Lemaire, J., 1989, Photocatalyzed transformation of chloroaromatic derivatives on zinc oxide III: chlorophenols. *J. Photochem. Photobiol. A: Chem.,* **50**: 117–127.

Serrano, B., 1998, Photocatalytic degradation of organic water pollutants: energy efficiency and kinetic modelling, PhD Dissertation, The University of Western Ontario.

Serrano, B. and de Lasa, H., 1997, Photocatalytic degradation of water organic pollutants. kinetic modeling and energy efficiency. *Ind. & Eng. Chem. Res.*, **36**: 4705–4711.

Serrano, B. and de Lasa, H., 1999, Photocatalytic degradation of water organic pollutants: pollutant reactivity and kinetic modeling. *Chem. Eng. Sci.*, **54**: 3063–3069.

CuuDuongThanCong.com https://fb.com/tailieudientucntt

8

Photocatalytic Degradation of Air Borne Pollutants

8.1. INTRODUCTION

Heterogeneous photocatalytic oxidation of organic air contaminants is a promising technology that offers distinct advantages. These advantages include potential lower operating costs, the elimination of treatment reagents or electron acceptors, the possible recovery, regeneration and reuse of the photocatalyst and finally its widespread applicability for the complete mineralization of organic compounds (Miller and Fox, 1993; Suri *et al.*, 1993). Cabrera *et al.*, (1994) indicated that almost any organic pollutant, and many inorganic ones, could be completely mineralized or separated by means of heterogeneous photocatalysis. Additionally, photocatalytic technology can be used in conjunction with solar radiation (Suri *et al.*, 1993) at close to ambient temperature (Cassano *et al.*, 1995; Falconer and Magrini-Bair, 1998; Miller and Fox, 1993). Photocatalysis also shows important prospects for certain air treatment applications, given that the observed apparent quantum efficiencies can be in excess of 100% (Ibrahim and de Lasa, 2003).

Heterogeneous photocatalysis steps were reviewed by Cunningham and Hodnett, (1981), Jacoby *et al.*, (1996) and Yue (1993) among others. These steps include the mass transfer of substrate from the bulk of the fluid to the catalyst surface, the transport of the reactants within the catalyst particle and the adsorption of substrates on the active catalytic surface. Once the TiO_2 is irradiated, photon energy is absorbed, followed by the generation of electron-hole pairs, the formation of radicals, the surface reaction, radical recombination and finally the desorption and mass transfer of products from the particle surface into the bulk of the fluid.

Under certain conditions, some of these steps may not need to be considered. For instance, if the photocatalyst particle is not porous, the mass transfer process within the catalyst particle can be ignored. In reactors where a high fluid velocity is contacting the catalyst, mass transport limitations on the surface of the TiO_2 particles may be neglected with the intrinsic photocatalytic reaction becoming the controlling step (Jacoby *et al.*, 1996).

Mathematical models have been developed to describe the behavior of the oxidation of organic compounds over titanium dioxide. Postulated models include: a)

CuuDuongThanCong.com https://fb.com/tailieudientucntt

Langmuir-Hinshelwood models involving the reaction between adsorbed oxygen and adsorbed reactant molecules (Luo and Ollis, 1996; Nimlos *et al.*, 1996; Peral and Ollis, 1992) and b) Eley–Rideal models, which consider the reaction between adsorbed oxygen and gas phase reactant molecules (Fox, 1988). Cunningham and Hodnett (1981) suggested a combination of the Langmuir-Hinshelwood and Eley-Rideal kinetics.

The novel Photo-CREC-Air reactor described in Chapter II optimizes the mesh irradiation as well as the contact of air with the supported TiO_2. This configuration highlights TiO_2supported on a fiberglass mesh and a Venturi section that displays high catalytic performance with high apparent quantum efficiencies (in excess of 100%) (Ibrahim and de Lasa, 2003). Under these performance conditions, kinetic modeling of the photodegradation of organic compounds becomes particularly relevant.

8.2. PHOTOCATALYTIC REACTION KINETIC MODELING: MODEL AND ASSUMPTIONS

In order to establish a kinetic model, a number of assumptions regarding the operation of the photocatalytic reactor should apply (Ibrahim, 2001). Consideration of the applicability of model assumptions is relevant for any type of photocatalytic reactor model. In the specific case of Photo-CREC-Air, and given the special design of this unit, the following model simplifications can be adopted:

a) There is uniform gas flow across the mesh providing both intimate contact of the airflow with the supported TiO_2 and essentially constant gas phase species concentrations throughout the unit at any given reaction time. An adequate pressure drop across the mesh and high gas recirculation in the reactor, operating under batch conditions, allows for these conditions to be met.
b) There is uniform and constant irradiation of the mesh supporting the TiO_2. This is accomplished because of a specially selected design that has parabolic light reflectors as well as the frequent replacement of the near UV lamps.
c) The windows in the reacting section are free of deposited particles. This is achieved through a gas flow pattern that promotes high shear near the window. This prevents the attachment of TiO_2 particles to the window surface and eliminates irradiation absorption and back reflection due to particles attached to the windows.
d) There is negligible adsorption of reactants on the material of the reactor wall.
e) There is an insignificant contribution from the thermal decomposition reactions.

Thus consistant with equations reported in Chapters I and VII, the following can be postulated:

$$V\frac{dC_i}{dt} = r'_{i,g}\,A_{irr} \tag{8-1a}$$

and

$$r'_{i,T} = r'_{i,g}\,(1 + K'_i) \tag{8-1b}$$

CuuDuongThanCong.com https://fb.com/tailieudientucntt

where V represents the total gas hold up in Photo-CREC-Air in m^3, C_i the $i$model pollutant concentration in μmole m^{-3}, $r'_{i,g}$ the rate of photoconversion calculated with gas phase concentration changes in μmole $min^{-1}.m^2$, $r'_{i,T}$ the total rate of photoconversion in μmolemin^{-1}m^{-2}, A_i is the uniformly irradiated mesh area holding an optimum loading of TiO_2 particles in $cm^2$and $K'_i = \frac{K_i W q_{i,m}}{V}$ a dimensionless adsorption group.

In addition to equations (8-1a) and (8-1b), one must establish a specific mathematical form for the rate of photoconversion. For instance, the initial photoconversion rate, which is valuable in the calculation of quantum efficiencies (Ibrahim and de Lasa, 2003), can be represented using a Langmuir-Hinshelwood expression:

$$r'_{i,g} = \frac{V}{A_{irr}} \frac{dC_i}{dt} = \frac{V}{A_{irr}} \frac{-k_i^* K_i C_i}{1 + K_i C_i} \tag{8.2}$$

with C_i representing the concentration of the i chemical species and K_i and k_i^* the equilibrium adsorption and kinetic constants, respectively.

Once the photoreaction is initiated, the rate equation may involve the formation of one or more kinetically important intermediate species that can be adsorbed onto the photocatalyst surface and detected in the gas phase. In order to reflect this, equation (8-2) has to be modified, incorporating the intermediate species concentration in the gas phase.

$$r'_{i,g} = \frac{V}{A_{irr}} \frac{-k_i^* K_i C_i}{1 + K_i C_i + \sum K_j C_j} \tag{8.3}$$

The $\sum K_j C_j$ term represents the combined effect of all adsorbed intermediate species, other than the model pollutant. This term involves the summation of the products of the respective adsorption constant and the gas phase concentration.

Providing a fairly adequate and consistent description of the chemical species concentrations in the gas phase, this simple model can be used to analyze the photodegradation kinetics of various model pollutants (sections 8.3, 8.4 and 8.5).

Once the selection of a possible kinetic model and suitable reactor model are complete (equation (8-1)), a non-linear, least square method can be adopted to determine the kinetic and adsorption parameters. This can be achieved by minimizing an objective function representing the sum of the differences between the model concentration estimates and the measured experimental concentrations. This non-linear, least square fit can be performed using the curve fit functions available in Matlab, as recommended by Ibrahim (2001).

8.3. ACETONE PHOTODEGRADATION KINETIC MODELING

Experimental results for the photoconversion of acetone using Degussa P25 and Hombikat UV-100 show that acetone and carbon dioxide are the only observable gas phase species (Figure 8.1).

CuuDuongThanCong.com https://fb.com/tailieudientucntt

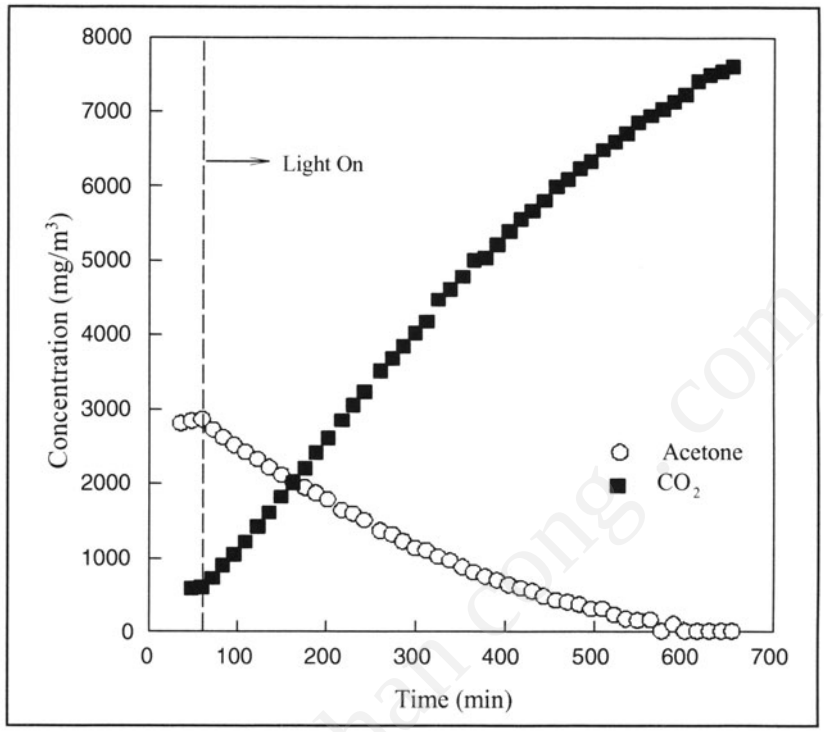

FIGURE 8.1. Photo conversion of acetone using Hombikat UV-100 showing gas-phase chemical species concentration changes with reaction time (AIChE Journal Copyright 2004, Vol. 50, Issue. 5,Wiley InterScience, p. 1017–1027).

On this basis and given the expected negligible carbon dioxide adsorption, the following relationships are proposed:

$$r'_{AC,g} = \frac{dC_{AC,g}}{dt}\frac{V}{A_{irr}} = -\frac{k^*_{AC}K_{AC}C_{AC,g}}{1+K_{AC}C_{AC,g}}\frac{V}{A_{irr}} = -\frac{C_{AC,g}}{\theta_{1,AC}+\theta_{2,AC}C_{AC,g}}\frac{V}{A_{irr}} \tag{8.4}$$

$$r'_{AC,T} = (1+K'_{AC})r'_{AC,g} \tag{8.5}$$

The K'_{AC} or $\frac{K_{AC}Wq_{AC,m}}{V}$ parameter of equation (8-5) represents the ratio of the number of μmoles of acetone adsorbed to the number of μmoles of acetone in the gas phase, with $q_{AC,m}$ being the maximum number of μmoles of acetone adsorbed per gram of catalyst in $\mu\text{mole}_{\text{cat}}^{-1}$. K'_{AC} can be evaluated for Degussa P25 and Hombikat UV-100 as 0.06 and 0.08, respectively (Ibrahim, 2001).

In addition, equation (8-4) can be alternately expressed in terms of $\theta_{1,AC}$ and $\theta_{2,AC}$ parameters: $\theta_{1,AC} = 1/(k^*_{AC}K_{AC})$ (min) and $\theta_{2,AC} = 1/k^*_{AC}$ (min.m^3/μmole). This

CuuDuongThanCong.com https://fb.com/tailieudientucntt

TABLE 8.1. Optimized Parameters for Acetone Data Modeling

Catalyst	D.O.F	R^2	S.S.R	$\theta_{1,AC}10^{-1}$ (min)	$\theta_{2,AC}10^{3}$ (min.m^3/μmole)
Degussa P25	115	0.99	1.06 10^8	10.77±0.47	4.88±0.19
Hombikat UV-100	121	0.98	3.74 10^8	4.06±0.62	7.79±0.29

yields a model reaction rate equation having a mathematical form with reduced parameter cross-correlation.

Table 8.1 reports the parameters obtained for three acetone concentrations, using both Degussa P25 and Hombikat UV-100, with the associated statistical indicators such as the correlation coefficient (R^2) and the sum of squared residuals (S.S.R).

The proposed model appears to be adequate to monitor the changes in acetone concentration in the gas phase during the photoconversion experiments.

The agreement between the model and the collected data, with only slight mismatch with respect to carbon dioxide (Figures 8.2b and 8.3b), supports the assumption that acetone photodegradation in Photo-CREC-Air has acetone conversion as the rate-controlling step, with little adsorption competition from the other chemical species.

The evaluated parameters of $r_{AC,g}$ at the initial reaction conditions (t = 0), are 115 μmole m^{-3}min^{-1} for Hombikat UV-100 and 130 μmole m^{-3} min^{-1} for Degussa P25. Considering the relation between $r'_{AC,g}$ and $r'_{AC,T}$ (equation 8-5), this yields a total acetone initial reaction rate of 125 μmole m^{-3}min^{-1} and 137 μmole m^{-3}min^{-1} for Hombikat UV-100 and Degussa P25 respectively.

It can thus be concluded that under the conditions of reaction testing in Photo-CREC-Air, both Hombikat UV-100 and Degussa P25 display a close photoactivity.

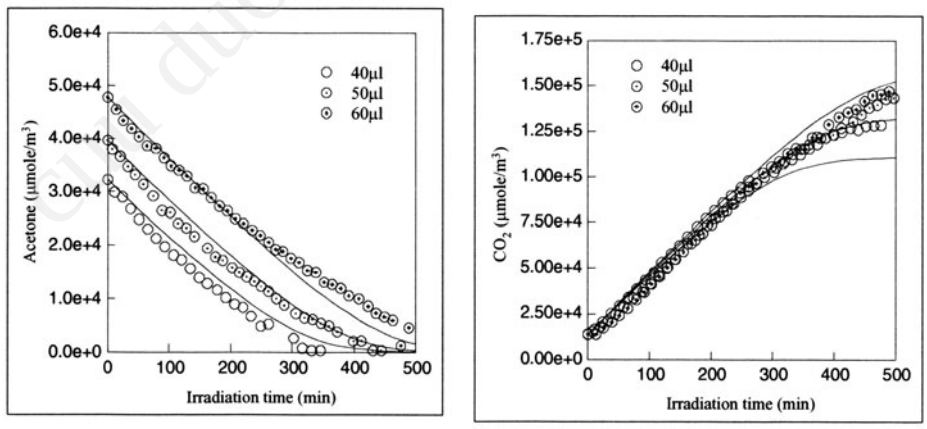

(a) (b)

FIGURE 8.2. Changes of acetone concentrations (a) and CO_2 (b) with reaction time using Hombikat UV-100. Full line: model predictions, circles: experimental data. (AIChE Journal Copyright 2004, Vol. 50, Issue. 5,Wiley InterScience, p. 1017–1027).

CuuDuongThanCong.com https://fb.com/tailieudientucntt

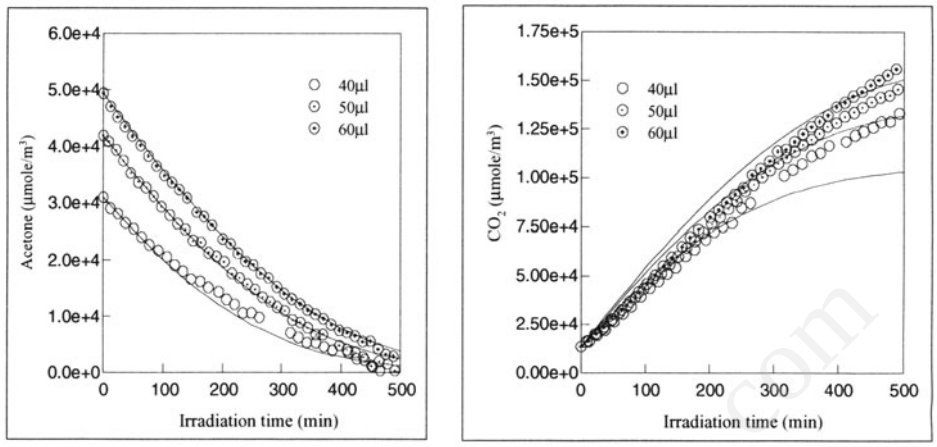

(a) (b)

FIGURE 8.3. Changes of acetone concentrations (a) and CO_2 (b) with reaction time using Degussa P25. Full line: model predictions. Circles: experimental data (AIChE Journal Copyright 2004, Vol. 50, Issue. 5,Wiley InterScience, p. 1017–1027).

8.4. ACETALDEHYDE PHOTODEGRADATION KINETIC MODELING

Using a kinetic modeling methodology similar to that described in section 8.3, acetaldehyde photodegradation can be modeled assuming that carbon dioxide and acetaldehyde are the only gas phase chemical species (Figure 8.4).

It is hypothesized that the acetaldehyde photoconversion rates in both Degussa P25 and Hombikat UV-100 can be described using a Langmuir-Hinshelwood rate form.

$$r'_{AA,g} = \frac{dC_{AA,g}}{dt}\frac{V}{A_{irr}} = -\frac{k^*_{AA}K_{AA}C_{AA,g}}{1+K_{AA}C_{AA,g}}\frac{V}{A_{irr}} = -\frac{C_{AA,g}}{\theta_{1,AA}+\theta_{2,AA}C_{AA,g}}\frac{V}{A_{irr}} \tag{8.6}$$

$$r'_{AA,T} = (1+K'_{AA})r'_{AA,g} \tag{8.7}$$

The K'_{AA} parameter of equation (8-7) is evaluated as 0.07 and 0.13 for Degussa P25 and Hombikat UV-100 respectively (Ibrahim, 2001).

Again, an alternate rate equation (8-6) can be considered in terms of $\theta_{1,AA}$ and $\theta_{2,AA}$parameters: $\theta_{1,AA} = 1/(k^*_{AA}K_{AA})$(min) and $\theta_{2,AA} = 1/k^*_{AA}$ (min.m^3/μmole^{-1}). Regressed parameters can be obtained by minimizing the $\sum_{i=1}^{i=n}(C_{AA,exp,i} - C_{AA,\ mod\ el,i})^2$ objective function using a least square method. The resulting parameters are reported in Table 8.2; constants $\theta_{1,AA}$ and $\theta_{2,AA}$ are obtained with low standard deviation and high correlation coefficients.

It can be observed that equation (8-6), with the parameters reported in Table 8.2, provides good estimates of the experimental data with Hombikat UV-100 data giving a somewhat better fit than that of the Degussa P25 data (Figure 8.5a). On this basis,

CuuDuongThanCong.com https://fb.com/tailieudientucntt

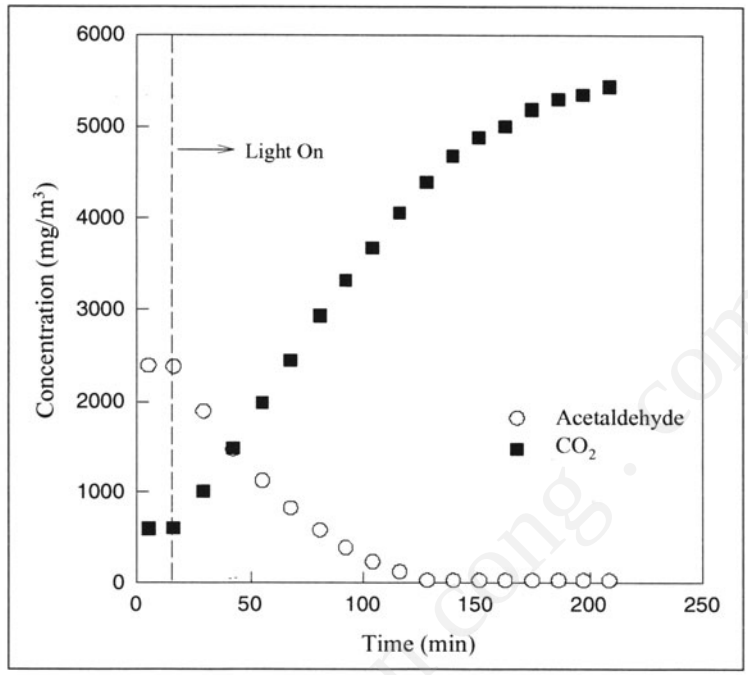

FIGURE 8.4. Photo-conversion of acetaldehyde using Hombikat UV-100 Gas phase chemical species concentration changes with reaction time (AIChE Journal Copyright 2004, Vol. 50, Issue. 5,Wiley InterScience, p. 1017–1027).

intrinsic rate constants of 2762 μmole $m^{-3}min^{-1}$ and 1455 μmole $m^{-3}min^{-1}$ can be assessed for Degussa P25 and Hombikat UV-100, respectively.

The evaluated parameters also allow the total initial reaction rate conditions to be quantified using equation (8-7). This gives a total acetaldehyde initial reaction rate of 1073 μmole m^{-3} min^{-1} and 833 μmole $m^{-3}min^{-1}$ for Hombikat UV-100 and Degussa P25 respectively. Under the conditions of testing in the Photo-CREC-Air, Hombikat UV-100 displays better photocatalytic activity towards acetaldehyde than Degussa P25.

When the fitted parameters are used to calculate carbon dioxide formation, it can be observed that the proposed model consistently predicts a faster carbon dioxide formation rate than the one observed experimentally (Figure 8.5b). Only towards the end of the experiments does the cumulative measured CO_2 become higher than the model predictions. This phenomenon, not noticed in the case of acetone photodegradation, suggests some failure of the kinetic model assumptions. One possible explanation is the

TABLE 8.2. Optimized parameters for acetaldehyde data modeling

Catalyst	D.O.F	R^2	S.S.R	$\theta_{1,AA}10^{-1}$ (min)	$\theta_{2,AA}10^{4}$ (min.m^3/μmole)
Degussa P25	74	0.97	4.70 10^8	5.10±0.45	3.62±1.55
Hombikat UV-100	48	0.99	1.46 10^8	1.99±0.218	6.87±0.89

CuuDuongThanCong.com https://fb.com/tailieudientucntt

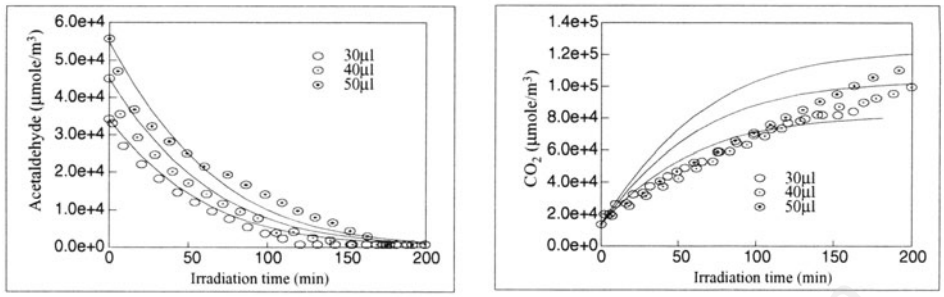

(a) (b)

FIGURE 8.5. Changes of acetaldehyde (a) and CO_2 (b) concentrations with reaction time using Degussa P25. Full line: model predictions. Circles: experimental data (AIChE Journal Copyright 2004, Vol. 50, Issue. 5, Wiley InterScience, p. 1017–1027).

existence of an unaccounted, strongly adsorbed intermediate species, presumably acetic acid, that photodegrades at a lower rate than acetaldehyde. In this respect, acetic acid should eventually be incorporated in the photoconversion network, as adsorbed species, without being present in the gas phase at detectable levels. These observations are in agreement with the results of Ohko *et al.*, (1998) who reported that the amount of measured carbon dioxide was less than the expected from acetaldehyde photoconversion. In the case of Ohko *et al.*, (1998) catalyst extracts revealed the presence of acetic acid in non-negligible amounts, helping to close their carbon balance.

Nimlos *et al.* (1996) provided additional support to a mechanism involving acetic acid and even formaldehyde. In this case, the acetic acid appeared as a detectable gas phase species with acetic acid having an assigned adsorption constant fourteen times larger than those of acetaldehyde.

Consequently, results strongly suggest that while equations (8-6) and (8-7) are satisfactory for modeling the conversion of acetaldehyde, a more sophisticated model is needed for accurate carbon dioxide predictions, a matter that should motivate further research.

8.5. ISO-PROPANOL PHOTODEGRADATION KINETIC MODELING

Iso-propanol is a model compound that can be mineralized following a path that involves acetone as an observable gas phase intermediate species (Figure 8.6).

With respect to $r'_{IP,g}$ the rate of iso-propanol photoconversion, it can also be postulated that iso-propanol photodegradation follows a Langmuir-Hinshelwood competitive model with both iso-propanol and acetone competing for the same catalyst sites.

$$r'_{IP,g} = \frac{dC_{IP,g}}{dt}\frac{V}{A_{irr}} = -\frac{k^*_{1,IP}K_{IP}C_{IP,g}}{1 + K_{IP}C_{IP,g} + K_{AC}C_{AC,g}}\frac{V}{A_{irr}} \tag{8.8}$$

Equation (8-8) can also be expressed in terms of an alternate equation as follows:

$$r'_{IP,g} = -\frac{C_{IP,g}}{\theta_{1,IP} + \theta_{2,IP}C_{IP,g} + \theta_{3,IP}C_{AC,g}}\frac{V}{A_{irr}} \tag{8.9}$$

CuuDuongThanCong.com https://fb.com/tailieudientucntt

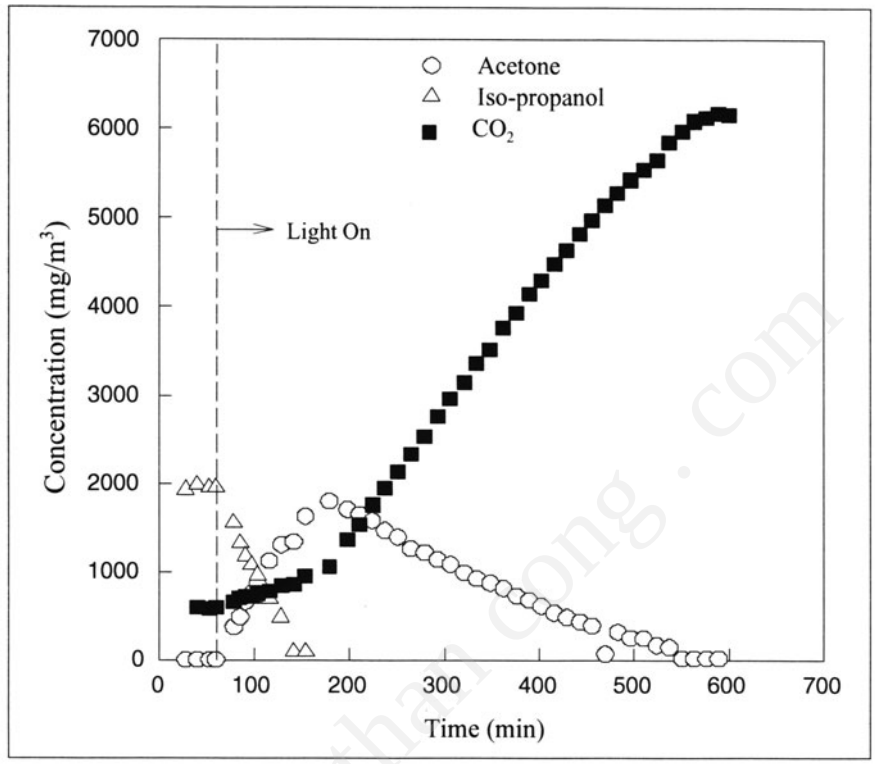

FIGURE 8.6. Photo-conversion of iso-propanol using Hombikat UV-100. Gas-phase chemical species concentration changes with reaction time (AIChE Journal Copyright 2004, Vol. 50, Issue. 5,Wiley InterScience, p. 1017–1027).

In addition, the rate of acetone photoconversion in the context of the iso-propanol degradation can be approximated using the following relationship:

$$r'_{AC,g} = \frac{dC_{AC,g}}{dt}\frac{V}{A_{irr}} = -\frac{k^*_{2,IP}K_{AC}C_{AC,g}}{1 + K_{IP}C_{IP,g} + K_{AC}C_{AC,g}}\frac{V}{A_{irr}} \tag{8.10}$$

where $k^*_{2,IP}$ is the reaction rate constant of the second reaction (acetone $\rightarrow$ CO_2+H_2O) in μmole/m^3.min. Similarly equation (8-10) can also be expressed by

$$r'_{AC,g} = -\frac{C_{AC,g}}{\theta_{4,IP} + \theta_{5,IP}C_{IP,g} + \theta_{6,IP}C_{AC,g}}\frac{V}{A_{irr}} \tag{8.11}$$

Thus, the modeling of the Photo-CREC-Air unit for the photoconversion of iso-propanol involves the simultaneous solution of the following set of differential equations with $\theta_{1,IP}$, $\theta_{2,IP}$, $\theta_{3,IP}$, $\theta_{4,IP}$, $\theta_{5,IP}$ and $\theta_{6,IP}$ parameters.

$$\frac{dC_{IP,g}}{dt} = -\frac{C_{IP,g}}{\theta_{1,IP} + \theta_{2,IP}C_{IP,g} + \theta_{3,IP}C_{AC,g}} \tag{8.12}$$

CuuDuongThanCong.com https://fb.com/tailieudientucntt

$$\frac{dC_{AC,g}}{dt} = \frac{C_{IP,g}}{\theta_{1,IP} + \theta_{2,IP}C_{IP,g} + \theta_{3,IP}C_{AC,g}}\zeta - \frac{C_{AC,g}}{\theta_{4,IP} + \theta_{5,IP}C_{IP,g} + \theta_{6,IP}C_{AC,g}} \tag{8.13}$$

$$\frac{dC_{CO_2}}{dt} = 3\frac{C_{AC,g}}{\theta_{4,IP} + \theta_{5,IP}C_{IP,g} + \theta_{6,IP}C_{AC,g}} \tag{8.14}$$

and

$$\frac{dC_{IP,T}}{dt} = (1 + K'_{IP})\frac{dC_{IP,g}}{dt} \quad \text{and} \quad \frac{dC_{AC,T}}{dt} = (1 + K'_{AC})\frac{dC_{AC,T}}{dt} \tag{8.15}$$

with $\zeta = (1 + K'_{IP})/(1 + K'_{AC})$ as proposed by Ibrahim (2001).

These equations with $\zeta = 1.3$ for Degussa P25 and $\zeta = 1.15$ for Hombikat UV-100 (Ibrahim, 2001) can be solved simultaneously using Matlab. The regression of parameters can be obtained by minimizing the following objective function:

$$\sum (C_{IP,\,exp\,,i} - C_{IP,\,mod\,el,i})^2 + (C_{AC,exp\,,i} - C_{AC,mod\,el,i})^2 \tag{8.16}$$

Regarding the proposed kinetic model described above, it can be noted that iso-propanol displayed an almost zero order reaction and probably first order at very low concentrations. In order to be consistent with the experimental data, parameters $\theta_{1,IP}$ and $\theta_{3,IP}$ are not numerically significant and can be deleted from the analysis, as reported in Table 8.3.

According to Table 8.3, the iso-propanol photodegradation on Degussa P25, can be reexamined using a reduced four-parameter model involving $\theta_{2,IP}$, $\theta_{4,IP}$, $\theta_{5,IP}$ and $\theta_{6,IP}$. Fitting of a model of this type can be performed for each concentration individually as well as for all the concentrations together. Ibrahim and de Lasa (2002) noticed that under these conditions, the optimized parameter ($\theta_{5,IP}$) is negative for most cases, which raised suspicions about the adequacy of including the $\theta_{5,IP}$ parameter. This suggests that the four-parameter model represents an over-parameterization and that a reduced three-parameter model, with $\theta_{2,IP}$, $\theta_{4,IP}$ and $\theta_{6,IP}$, should be adequate.

The above-described three-parameter model can be tested yielding positive parameters for all the runs (Table 8.4). Once the parameter fitting is completed, the resulting

TABLE 8.3. Summary of the Parameters Involved in the Iso-propanol Modeling

Parameter	Selected
$\theta_{1,IP}$	No
$\theta_{2,IP}$	Yes
$\theta_{3,IP}$	No
$\theta_{4,IP}$	Yes
$\theta_{5,IP}$	Yes
$\theta_{6,IP}$	Yes

CuuDuongThanCong.com https://fb.com/tailieudientucntt

TABLE 8.4. Optimized parameters for the iso-propanol photo degradation data using degussa P25 and a three-parameter model

Amount (μl)	DOF	R^2	S.S.R	$(I/\theta_{2,IP})10^{-2}$ (μmole/min.m3)	$\theta_{4,IP}\ 10^{-1}$ (min)	$\theta_{6,IP}10^{3}$ (min.m3/μmole)
40	79	0.974	2.03E+08	8.54±0.60	5.48±0.0003	14.3±0.00
50	99	0.993	2.58E+08	7.93±0.29	0.61±0.07	15.7±0.02
60	117	0.972	6.96E+08	5.69±0.26	1.08±0.08	15.1±0.02
All	297	0.987	7.35E+08	7.44±0.13	7.20±0.14	12.2±0.01

parameters can be used to generate the iso-propanol, acetone and carbon dioxide concentration curves to test the model's adequacy. Close fitting are obtained for iso-propanol and acetone in the case of Degussa P25 (Figure 8.7 and Table 8.4) with a less reliable fittings for Hombikat UV-100 (Ibrahim, 2001).

It can be also observed that the proposed model has the intrinsic difficulty of being unable to predict further increases in carbon dioxide, especially once the acetone disappears from the gas phase. As a result, the model tends to under-predict CO_2 concentrations towards the end of the run. This fact also points towards the existence of unaccounted intermediates, other than acetone, which are adsorbed either onto the catalyst surface or at levels below the detectable limits in the gas phase.

Another interesting observation relates to the comparison of $\theta_{4,IP}$ and $\theta_{6,IP}$ parameters (Tables 8.4) with the $\theta_{1,AC}$ and $\theta_{2,AC}$ values (Table 8.1). The reported constants

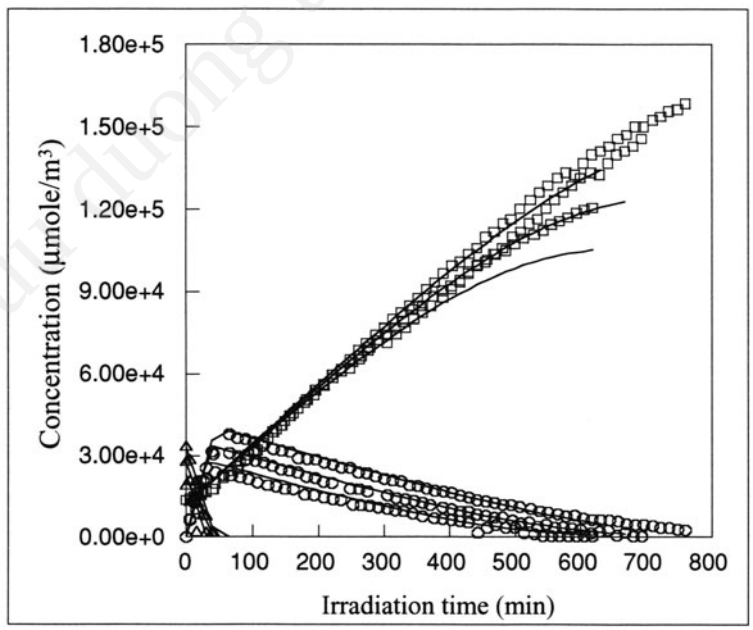

FIGURE 8.7. Changes of concentrations with reaction time for iso-propanol photo degradation using Degussa P25 Data collected for the 40μl, 50μl, and 60μl injection concentrations (△) Isopropanol, (O) Acetone, (□) CO_2 (AIChE Journal Copyright 2004, Vol. 50, Issue. 5,Wiley InterScience, p. 1017–1027).

CuuDuongThanCong.com https://fb.com/tailieudientucntt

are very close for Hombikat 100 and in the same order of magnitude for Degussa P25. This is encouraging given that all the parameters associated with acetone photoconversion are determined under quite different reaction conditions. Acetone was in one case the reactant while an intermediate species of iso-propanol photoconversion in the other.

8.6. CONCLUSIONS ABOUT KINETIC MODELING

On the basis of the kinetic modeling reported, under the conditions of Photo-CREC-Air operation, it can be concluded :

a) A Langmuir-Hinshelwood rate of reaction, involving a one-site one-model pollutant mechanism, is adequate to describe the photodegradation of acetone on both Degussa P25 and Hombikat UV-100. This rate equation appears however, to be less appropriate for predicting carbon dioxide formation from acetaldehyde and iso-propanol.
b) These kinetic models and the related parameters can be established using a least square non–linear regression analysis with the related statistical indicators.

8.7. PHOTOCATALYTIC CONVERSION OF AIR POLLUTANTS: ENERGY EFFICIENCIES OVERVIEW

Heterogeneous photocatalysis on metal oxide semiconductors has been shown to provide an effective method for the degradation of organic pollutants from gaseous and aqueous streams (Fox and Dulay, 1993; Hoffmann *et al.*, 1995; Ollis and Al-Ekabi, 1993). Research in this area has been mainly concerned with reaction rates, mechanistic paths, kinetic models, catalysts and reactor development (Cassano *et al.*, 1995; Hoffmann *et al.*, 1995; Ollis and Al Ekabi, 1993; Yue, 1993). In addition to the rate of photoconversion, one should define an energy yield describing the light utilization efficiency in photocatalysis (Fox, 1988).

Reactor efficiencies can be evaluated for the photocatalytic conversion of water pollutants (Chapter VI) using a number of efficiency factors such as the Electrical Energy per Order (EE/O) (Notarfonzo and McPhee, 1994), the quantum yield, the quantum efficiency (Bockelmann *et al.*, 1993; Valladares and Bolton, 1993) and the photocatalytic thermodynamic efficiency factor (PTEF) (Serrano and de Lasa, 1997).

Extension of these parameters to the photocatalytic conversion of air pollutants is still in the preliminary phases with the "quantum yield", a reactor dependant parameter, being the one currently adopted. The "quantum yield" can be defined as the number of pollutant molecules degraded in a reaction, from either a primary or secondary reaction, over the number of photons absorbed.

The "quantum yield" can be in excess to 100% (Cassano *et al.*, 1995). To explain this behavior Ohko *et al*, (1998) invoke a chain reaction mechanism involving the following steps for the photocatalytic conversion of acetaldehyde:

CuuDuongThanCong.com https://fb.com/tailieudientucntt

a) Preliminary illumination steps leading to the formation of OH· radicals
$TiO_2 + h\nu \rightarrow h^+ + e^-$
$h^+ + OH^- \rightarrow OH^\bullet$ or $h^+ + H_2O \rightarrow OH^\bullet + H^+$
$e^- + O_2 \rightarrow O_2^{\bullet -}$
$O_2^{\bullet -} + H^+ \rightarrow HO_2^{\bullet -}$

b) Formation of the aldehyde radical and *peroxo* radical
$CH_3CHO + OH^\bullet \rightarrow CH_3CO^\bullet$ *(aldehyde radical)* $+ H_2O$
$CH_3CO^\bullet + O_2 \rightarrow CH_3(CO)OO^\bullet$ *(peroxo radical)*

c) Conversion and regeneration with oxygen of the peroxo radicals,
$CH_3(CO)OO^\bullet + CH_3CHO \rightarrow CH_3COOH + CH_3CO^\bullet$
$CH_3CO^\bullet + O_2 \rightarrow CH_3(CO)OO^\bullet$

Once an aldehyde radical is formed through the intervention of an OH· group, the subsequent step proceeds via a peroxo radical, producing acetic acid. This peroxo radical is consumed and can be regenerated via the direct interaction of aldehyde radicals with oxygen. This chain reaction mechanism explains the findings than one photon can contribute to the photoconversion of several pollutant molecules and can give as a result, quantum yields in excess of 100%.

One additional problem with the quantum yield is in the evaluation of the absorbed radiation inside the photocatalytic reactor (Cabrera *et al.*, 1996). This is due to the fact that semiconductor particles are highly reflective (Fox and Dulay, 1993), favoring photon scattering and reflection (Valladares and Bolton, 1993) reducing, as a result, the photons absorbed. An "apparent quantum yield" can be considered when the absorbed photon rate is not available, providing a minimum value that bounds the actual quantum yields (refer to Chapter VI). While, the quantum yield was meant for monochromatic radiation, both "quantum efficiencies" and "apparent quantum efficiencies" should be considered for polychromatic radiation (Cabrera et al., 1994). As well quantum yields and quantum efficiencies are affected by the light intensity reaching the photocatalyst as reported by Pelizzetti *et al* (1993).

The debate still remains regarding which configurations are the most adequate for the photocatalytic reactors to photoconvert air borne pollutants (Ollis and Al-Ekabi, 1993). Several options have been described (Chapter II): fluidized bed (Brucato *et al.*, 1992; Dibble and Raupp, 1992; Yue *et al.*, 1983;), annular packed bed (Raupp *et al.*, 1997), coated honeycomb (Sauer and Ollis, 1994; Suzuki *et al.*, 1991; Suzuki, 1993), fixed powder layer (Formenti *et al.*, 1971; Peral and Ollis, 1992) and fiber optic reactor (Peill and Hoffmann, 1995). The Photo-CREC-Air reactor (Ibrahim and de Lasa, 2002) optimizes TiO_2-mesh irradiation and air contacting the supported TiO_2. As reported in the upcoming section, this configuration yields model pollutant conversions with high apparent quantum efficiencies.

8.8. APPARENT QUANTUM EFFICIENCY IN PHOTO-CREC-AIR REACTORS

Quantum yield and quantum efficiency (φ) are two parameters of significant value in photocatalysis (Chapter VI). In principle, these parameters should be defined with the

CuuDuongThanCong.com https://fb.com/tailieudientucntt

photons absorbed by the mesh-TiO_2 system. In cases where there is no available data of back-reflected and forward-scattered photons, an "apparent quantum efficiency" based on the total number of polychromatic photons reaching the mesh may be considered as a conservative estimation.

$$\varphi_{app} = \frac{Rate\ of\ Converted\ Molecules}{Rate\ of\ Photons\ Reaching\ the\ Mesh\ -\ TiO_2\ System} \tag{8.17}$$

The polychromatic photons supplied to the system and reaching the mesh supporting the TiO_2 can be estimated using the spectral intensity distribution with intensity in watts m^{-2} nm^{-1}. The intensity spectrum can be measured using the Sola Scope 2000 spectro-radiometer for the 300–390 nm range for every 0.5 nm (Ibrahim and de Lasa, 2002). In addition, similar measurements with the Sola Scope 2000 probe at different locations of the mesh of the Photo-CREC-Air unit can be used to confirm the uniform intensity distribution of photons reaching the mesh (Ibrahim, 2001).

Regarding the number of pollutant molecules converted per unit time involved in the apparent quantum efficiency, φ_{app} can be evaluated using the initial reaction rate ($\varphi_{app,in}$) (Chapter VI):

$$\varphi_{app,in} = \frac{\left(\frac{dN_i}{dt}\right)_{in}}{\int_{\lambda_1}^{\lambda_2} \frac{R.A_{irr}\,\lambda\,d\lambda}{hc}} \tag{8.18}$$

Alternatively an average apparent quantum efficiency ($\varphi_{app,av}$), can be calculated on the basis of the mineralized pollutant molecules for a given conversion level (e.g. 90% conversion). On this basis, $\varphi_{app,av}$ can be calculated.

$$\varphi_{app,av} = \frac{\left(\frac{N_{90\%}}{t_{90\%}}\right)}{\int_{\lambda_1}^{\lambda_2} \frac{R.A_{irr}\,\lambda\,d\lambda}{hc}} \tag{8.19}$$

with $N_{90\%}$ as the number of pollutant molecules degraded at the 90% conversion level, $t_{90\%}$ the time required to achieve 90% conversion in seconds, R the radiation intensity in watts $m^{-2}nm^{-1}$, A_{irr} the total area of irradiated impregnated mesh in 0.0510 m^2 and h the Plank's constant in $6.62.10^{-34}$J.s photon^{-1}. The other parameters are described as c, the speed of light in vacuum $2.997.10^8$ m s^{-1}, λ the lower wavelength of the spectrum in the range of interest (300 nm) and λ_2 the higher wavelength of the spectrum in the range of interest (390 nm). A detailed example of $\varphi_{app,av}$ calculation is reported in Ibrahim (2001).

The $\varphi_{app,av}$ and $\varphi_{app,in}$ apparent efficiencies can be used to estimate φ , keeping in mind that the resulting parameters provide a lower bound to the actual quantum efficiency of the system.

$$\varphi \geq \varphi_{app,in} \geq \varphi_{app,av} \tag{8.20}$$

Using the data reported in Figure 8.2b and equation (8-19) the average apparent quantum efficiencies for acetone, $\varphi_{app,av}$ are evaluated in the 28-36% range (Table 8.5).

CuuDuongThanCong.com https://fb.com/tailieudientucntt

TABLE 8.5. Apparent Quantum Efficiencies of Acetone Photo Degradation on Degussa P25 and Hombikat UV-100 Using the 90% Conversion ($\varphi_{app,av}$) and the Initial Photoconversion Rates ($\varphi_{app,in}$)

	$\varphi_{app,av}$(%)			
Catalyst	40μl	50μl	60μl	$\varphi_{app,in}$(%)
Degussa P25	28	32	33	55
Hombikat UV-100	36	36	33	50

The calculated $\varphi_{app,av}$ are slightly affected by the initial concentration as well as by the type of catalyst, with Hombikat UV-100 displaying slightly higher average apparent quantum efficiencies. These oscillations are in the range of the experimental error.

In addition, considering the initial photoconversion rates, apparent quantum efficiencies, $\varphi_{app,in}$ were assessed to be in the 50-55% range. These apparent quantum efficiencies are approximately 1.5 times higher than the $\varphi_{app,av}$ obtained using equation (8-19).

These results can be compared with the technical literature using data from Sauer and Ollis (1994). These authors studied the photoconversion of acetone using Degussa P25 catalyst and two 100-watt lamps. The initial acetone photoconversion rates obtained under these conditions were 3.0 10^{-8} kg/(m^3.s). The initial rates of acetone photoconversion, obtained in Photo-CREC-Air are 19.6 10^{-8} kg/($m^{-3}s^{-1}$) with a total supplied power of only 8 watts favorably compare with the previously reported data.

On the basis of the acetaldehyde conversion data reported in Figures 8.4 and 8.5b, the average apparent quantum efficiencies can be calculated and they surpass the 100% level for both Degussa P25 and Hombikat UV-100 (Table 8.6).

This $\varphi_{app,av}$ in excess to 100% is consistent with apparent quantum efficiencies reported in the literature with the high apparent quantum yields being justified on the basis of the potential role assigned in the oxygenate photoconversion to a free radical chain mechanism (Cassano *et al.*, 1995; Jacoby *et al.*, 1995; Luo and Ollis, 1996; Nimlos *et al.*, 1996; Raupp and Junio, 1993; Sauer and Ollis, 1994). Furthermore, the $\varphi_{app,in}$ apparent quantum efficiencies for acetaldehyde were in the 345-450% range as reported in Table 8.6. These $\varphi_{app,in}$ values are about 3-3.5 times larger than the $\varphi_{app,av}$ obtained using equation (8-19).

Using the typical example for iso-propanol photoconversion reported in Figure 8.6, both $\varphi_{app,av}$ and $\varphi_{app,in}$ can be defined using the carbon dioxide formed at 90% pollutant

TABLE 8.6. Apparent Quantum Efficiencies of Acetaldehyde Photodegradation on Degussa P25 and Hombikat UV-100 Using the 90% Conversion ($\varphi_{app,av}$) and the Initial Photoconversion Rates ($\varphi_{app,in}$)

	$\varphi_{app,av}$(%)			
Catalyst	30μl	40μl	50μl	$\varphi_{app,in}$(%)
Degussa P25	88	94	99	345
Hombikat UV-100	157	134	123	450

CuuDuongThanCong.com https://fb.com/tailieudientucntt

TABLE 8.7. Apparent Quantum Efficiencies of Iso-propanol Photodegradation on Degussa P25 and Hombikat UV-100 Using the 90% Conversion ($\varphi_{app,av}$) and the Initial PhotoConversion Rates ($\varphi_{app,in}$)

	$\varphi_{app,av}$ (%)			
	Catalyst 40μl	50μl	60μl	$\varphi_{app,in}$ (%)
Degussa P25	21	23	24	423
Hombikat UV-100	31	30	27	166

photoconversion level and the initial photoconversion rate. Results are reported in Table 8.7 where it is shown that the $\varphi_{app,av}$ values for both Degussa P25 and Hombikat UV-100 remain below 100%, while the apparent quantum efficiencies defined with the initial reaction rate surpassed the 100% level, with $\varphi_{app,av}$ and $\varphi_{app,in}$ differing by a factor of 10.

This important and consistent difference between $\varphi_{app,av}$ and $\varphi_{app,in}$, noted for the two catalysts, can be assigned to the much lower intermediate species conversion rates, as in the case of acetone, versus the photoconversion observed for iso-propanol.

It also appears that the Degussa P25 catalyst displays a higher iso-propanol photoconversion rate and this can be linked to the high adsorption affinity of iso-propanol with Degussa P25, yielding as a result a higher $\varphi_{app,in}$. Moreover given that the rate-controlling step for the iso-propanol mineralization is the photoconversion of acetone as shown in Figure 8.1, differences in $\varphi_{app,in}$ do not translate in major variations in $\varphi_{app,av}$. This low acetone photoconversion rate is consistent with the results obtained using acetone as model pollutant (Ibrahim, 2001).

In summary, the quantum efficiencies in Photo-CREC-Air design are high. These are promising results given that the apparent quantum efficiencies (equation (8-19)) represent conservative estimates. Not all polychromatic photons reaching the mesh-TiO_2 are absorbed, since a fraction of them are back reflected or forward scattered and actual quantum efficiencies can only be higher than the already high and encouraging φ values observed in Photo-CREC-Air unit.

8.9. CONCLUSIONS ABOUT QUANTUM EFFICIENCIES IN PHOTO-CREC-AIR REACTORS

The following conclusions can be drawn:

a) The Photo-CREC-Air, an innovative design for the photoconversion of air pollutants, displays advantageous features in terms of photoconversion performance and apparent quantum efficiencies.
b) In many experimental conditions, the apparent quantum efficiencies in Photo-CREC-Air are in excess of 100%. This is a significant fact and a positive indicator showing the extensive applications of photocatalytic processes for air purification.
c) Apparent quantum efficiencies larger than 100% confirm the possible radical chain reaction pathway of the photocatalytic conversion of air pollutants.

CuuDuongThanCong.com https://fb.com/tailieudientucntt

NOTATION

Symbols

A_{irr}	Uniformly irradiated mesh area holding an optimum amount of TiO_2	m^2
A_{mesh}	Total area of impregnated mesh	0.0510 m^2
c	Speed of light in vacuum	$2.997.10^8$ m s^{-1}
C_i	Model pollutant concentration in the gas phase	g m^{-3}, μmole m^{-3}
C_j	Chemical species other than the I species	g m^{-3}, μmole m^{-3}
h	Plank's constant	6.6210^{-34} J.s photon^{-1}
k_i^*	reaction rate constant for i chemical species	μmole m^{-3}.min^{-1}
$k_{1,IP}^*$	reaction rate constant of the first reaction (IP $\rightarrow$ acetone)	μmole m^{-3}.min^{-1}
$k_{2,IP}^*$	reaction rate constant of the second reaction (acetone$\rightarrow$ CO_2+H_2O)	μmole m^{-3}.min^{-1}
K_i	"i" chemical species adsorption constant	$m^3\mu$mole^{-1}
K_i'	$\frac{K_i W q_{i,m}}{V}$ or ratio of the number of moles of the "i" species adsorbed over the number of moles of "i" species in the gas phase	- -
N_i	Number of i chemical species molecules	mole
$N_{90\%}$	Number of model pollutant molecules degraded at the 90% mineralization level	mole
$q_{i,m}$	Maximum number of μmoles of "i" species adsorbed per gram of catalyst	μmoleg_{cat}^{-1}
R	Radiation intensity	Watts $m^{-2}$$nm^{-1}$
$r_{i,g}'$	"i" species photodegradation rate calculated with gas phase concentration changes (based on the unit irradiated mesh area)	μmole $m^{-2}$$min^{-1}$
$r_{i,T}'$	Total rate of "i" species photodegradation (based on the unit irradiated mesh area)	μmole m^{-2}.min^{-1}
t	Time	s
$t_{90\%}$	Time of the experiment required to achieved 90% mineralization of pollutant molecules	s
V	Total hold up of gas in Photo-CREC-Air	m^{-3}
W	weight of mesh-catalyst	g

Subscripts

AA	Acetaldehyde
AC	Acetone
exp	Experimental
IP	Iso-propanol
model	Model

CuuDuongThanCong.com https://fb.com/tailieudientucntt

Greek Symbols

φ	Rate of molecules converted over rate of polychromatic photons absorbed in the mesh	
$\varphi_{app,in}$	rate of molecules converted at $t \rightarrow 0$ over rate of polychromatic photons reaching the mesh	
$\varphi_{app,av}$	Rate of mineralized molecules at 90% conversion over rate of polychromatic photons reaching the mesh	
θ_j	The $K_j/(K_i k^*)$ group	$s.m^3 mole^{-1}$
θ_1	The $1/(k^* K_j)$ group	s^{-1}
$\theta_{1,AA}$	$1/(k^*_{AA} K_{AA})$	min
$\theta_{2,AA}$	$1/k^*_{AA}$	$min.m^3 \mu mole^{-1}$
$\theta_{1,AC}$	$1/(k^*_{AC} K_{AC})$	min
$\theta_{2,AC}$	$1/k^*_{AC}$	$min.m^3 \mu mole^{-1}$
$\theta_{1,IP}$	$1/(k^*_{1,IP} K_{IP})$	min
$\theta_{2,IP}$	$1/k^*_{1,IP}$	$min.m^3 \mu mole^{-1}$
$\theta_{3,IP}$	$K_{AC}/(k^*_{1,IP} K_{IP})$	$min.m^3 \mu mole^{-1}$
$\theta_{4,IP}$	$1/(k^*_{2,IP} K_{AC})$	min
$\theta_{5,IP}$	$K_{IP}/(k^*_{2,IP} K_{AC})$	$min.m^3 \mu mole^{-1}$
$\theta_{6,IP}$	$1/k^*_{2,IP}$	$min.m^3 \mu mole^{-1}$
ζ	$1 + K'_{IP}/(1 + K'_{AC})$	
λ_l	Lower wavelength of the spectrum in the range of interest	300 nm
λ_2	Higher wavelength of the spectrum in the range of interest	390 nm

REFERENCES

Bockelmann, D., Goslich, R., Weichgrebe, D., and Bahnemann, D., 1993, Solar detoxification of polluted water: comparing the efficiencies of a parabolic reactor and a novel film fixed bed reactor, in: Photocatalytic Purification and Treatment of Water and Air: Proc.1st International Conference on TiO_2, D. Ollis and H. Al-Ekabi, ed., Elsevier, pp. 771–776.

Brucato, A., Iatridis D., Rizzuti L., and Yue, P., 1992, Modeling of light transmittance and reflectance in a flat fluidized bed, *Canadian J. of Chem. Eng.* **70:**1063–1070.

Cabrera, M., Alfano, O., and Cassano, A., 1994, Novel reactor for photocatalytic kinetic studies, *Ind. Eng. Chem. Res.* **33:**3031–3042.

Cabrera, M., Alfano, O., and Cassano, A., 1996, Absorption and scattering coefficients of titanium dioxide particulate suspensions in water, *J. of Phys. Chem.* **100:**20043–20050.

Cassano, A., Martin, C., Brandi R., and Alfano, O., 1995, Photoreactor analysis and design: fundamentals and applications, *Ind. Eng. Chem. Res.* **34:**2155–2201.

Cunningham, J., and Hodnett, B., 1981, Kinetic studies of secondary alcohol photooxidation on ZnO and TiO_2 at 348K studied by gas chromatograph analysis, *J. Chem. Soc. Faraday Transactions 1.* **77:**2777–2801.

de Lasa, H., and Ibrahim, H., 1998, Photocatalytic reactor and method for the destruction of organic air pollutants, Filed U.S. Patent Office.

Dibble, L., and Raupp, G., 1992, Fluidized bed photocatalytic oxidation of trichloroethylene in contaminated air streams, *Env. Sci. Tech.* **26**(3)**:**492–495.

CuuDuongThanCong.com https://fb.com/tailieudientucntt

Falconer, J., and Magrini-Bair, K., 1998, Photocatalytic and thermal oxidation of acetaldehydeon Pt/TiO_2, *J. of Catalysis.* **179:**171–178.

Formenti, M., Juillet, F., Meriaudeau, P., and Teichner, S., 1971, Heterogeneous photocatalysis for partial oxidation of paraffin, *Chem. Tech.* **1:**680–681.

Fox, M., 1988, Photocatalytic oxidation of organic substances, in: *Photocatalysis and Environment: Trends and Applications*, M. Schiavello, ed., Kluwer Academic Publishers, New York, pp. 445–467.

Fox, M., and Dulay, M., 1993, Heterogeneous photocatalysis, *Chem. Rev.* **93:**341–357.

Hoffmann, M., Martin, S., Choi, W., and Bahnemann, D., 1995, Environmental applications of semiconductor photocatalysis, *Chem. Rev.* **95**(1)**:**69–96.

Ibrahim, H., 2001, *Photocatalytic Reactor for the Degradation of Airborne Pollutants. Photoconversion Efficiency and Kinetic Modeling, PhD Dissertation*, The University of Western Ontario, London Ontario, Canada.

Ibrahim, H., and de Lasa, H., 2002, Photocatalytic conversion of air borne pollutants. Effect of catalyst type and loading in novel Photo-CREC-Air Unit, *Appl. Cat.* **38:**201–213.

Ibrahim, H., and de Lasa, H., 2003, Photocatalytic degradation of air borne pollutants. Apparent quantum efficiencies in a novel Photo-CREC-Air reactor, *Chem. Eng. Sci.* **58:**943–949.

Ibrahim, H., and de Lasa, H., 2004, Kinetic Modeling of the Photocatalytic Degradation of Air Borne Pollutants. *AIChE.J.* **50:**1017–1027.

Jacoby, W., Blake, D., Noble, R., and Koval, C., 1995, Kinetics of oxidation of TCE in air via heterogeneous photocatalysis, *J. of Catalysis.* **157:**87–96.

Jacoby, W., Black, D., Fennel, D., Boutlet, J., Vargo, L., George, M., and Dolberg, S., 1996, Heterogeneous photocatalysis for control of volatile organic compounds in indoor air, *J. Air and Waste Man. Ass.* **46:**691–898.

Luo, Y., and Ollis, D., 1996, Heterogeneous photocatalytic oxidation of trichloroethylene and toluene mixtures in air: kinetic promotion and inhibition, time-dependent catalyst activity, *J of Catalysis.***163:**1–11.

Miller, R., and Fox, R., 1993, Treatment of organic contaminants in air by photocatalytic oxidation: a commercialization perspective, in: *Photocatalytic Purification and Treatment of Water and Air: Proceedings of the 1st International Conference on* TiO_2., D. Ollis, H. Al-Ekabi, ed., Elsevier, 573–578.

Nimlos, M., Wolfrum, E., Brewer, M., Fennell, J., and Bintner, G., 1996, Gas phase heterogeneous photocatalytic oxidation of ethanol: pathways and kinetic modeling, *Env. Sci. Tech.* **30**(10)**:**3102–3110.

Notarfonzo, R., and McPhee, W., 1994, How to evaluate a UV/Oxidation system, *Poll. Eng.* **26**(10)**:**74–76.

Ohko, Y., and Fujishima, A., 1998, Kinetics analysis of the photocatalytic degradation of gas-phase 2-propanol under mass transport-limited conditions with a TiO_2 film photocatalyst, *J. Phys. Chem. B* **102:**1724–1729.

Ohko, Y., Tryk, D., Hashimoto, K., and Fujishima, A., 1998, Autoxidation of acetaldehyde by TiO_2 photocatalysis under weak UV illumination, *J. Phys. Chem. B*, **102**(15)**:**2699–2704.

Ollis, D., and Al-Ekabi, H., 1993, *Photocatalytic Purification and Treatment of Water and Air: Proceedings of the 1st International Conference on* TiO_2, Elsevier.

Peill, N., and Hoffmann, M., 1995, Development and optimization of a TiO_2 coated fiber optic cable reactor: photocatalytic degradation of 4-chlorophenol, *Env. Sci. Tech.***29:**2974–2981.

Pelizzetti, E., Minero, C., and Pramauro, E., 1993, Photocatalytic processes for destruction of organic water contaminants, in: *Chemical Reactor Technology for Environmentally Safe Reactors and Products,* H. de Lasa, G. Dogu, and A. Ravella, ed., Kluwer Academic Publishers, 577–608.

Peral, J., and Ollis, D., 1992, Heterogeneous photocatalytic oxidation of gas-phase organics for air purification: acetone, 1-butanol, butyraldehyde, formaldehyde, and m-xylene oxidation". *J. of Catalysis* **136:**554–565.

Raupp, G., and Junio, C., 1993, Photocatalytic oxidation of oxygenated air toxics, *Appl. Sur. Sci.***72:**321–327.

Raupp, G., Nico, J., Annangi, S., Changrani, R., and Annapragada, R., 1997, Two flux radiation-field model for an annular packed-bed photocatalytic oxidation reactor, *AIChE J* **43**(3)**:**792–801.

Sauer, M., and Ollis, D., 1994, Acetone oxidation in a photocatalytic monolith reactor, *J of Catalysis.* **149:**81–91.

Serrano, B., and de Lasa, H., 1997, Photocatalytic degradation of water organic pollutants. Kinetic modeling and energy efficiency, *Ind. Eng. Chem. Res.* **36:**4705–4711.

Shifu, C., Xueli, C., Yaowu, T., and Mengyue, Z., 1998, Photocatalytic degradation of trace gaseous acetone and acetaldehyde using TiO_2 supported on fiberglass cloth", *J. Chem. Tech. and Biotech.* **73:**264–268.

CuuDuongThanCong.com https://fb.com/tailieudientucntt

Suri R., Liu, J., Hand, D., Crittenden, J., Perram, D., and Mullims, M., 1993, Heterogeneous photocatalytic oxidation of hazardous organic contaminants in water, *Water Env. Res.* **65**(5)**:**665–673.

Suzuki, K., 1993, Photocatalytic air purification on TiO_2 coated honeycomb support, in: *Photocatalytic Purification and Treatment of Water and Air: Proceedings of the 1st International Conference on* TiO_2, D. Ollis, H. Al-Ekabi, ed., Elsevier, 412–434.

Suzuki, K., Satoh, S., and Yoshida, T., 1991, Photocatalytic deodorization on TiO_2 coated honeycomb ceramics, *Denki Kagaku* **59**(6)**:**521–523.

Valladares, J., and Bolton, J., 1993, A method for the determination of quantum yields in heterogeneous systems: the titanium dioxide photocatalyzed bleaching of methylene blue, *Trace Metals in the Env.* **3:**111–120.

Yue, P., 1993, Modeling, scale up and design of multiphasic photoreactors, in: *Photocatalytic Purification and Treatment of Water and Air: Proceedings of the 1st International Conference on* TiO_2, D. Ollis, H. Al-Ekabi, ed., Elsevier, 495–510.

Yue, P., Khan, F., and Rizzuti, L., 1983, Photocatalytic ammonia synthesis in a fluidized bed reactor, *Chem. Eng. Sci.* **38:**1893–1900.

cuu duong than cong . com

CuuDuongThanCong.com https://fb.com/tailieudientucntt

9

Advances and Perspectives for Photocatalysis

9.1. INTRODUCTION

Photocatalysis is a new advanced oxidation process based on the irradiation of semiconductor materials, normally TiO_2, with UV light having a wavelength smaller than 390 nm. Heterogeneous photocatalysis has emerged as a promising technology that could be instrumental in eliminating pollutants from air and water streams.

In order for this technology to be successful and to reach widespread application, significant advances are still required. This is particularly true in the area of the removal of organic and inorganic species from air and water streams and for the inactivation of water-contaminating microorganisms.

Potential advances and technological improvements achieved in these areas based on recent results obtained in Photo-CREC-Water reactors are discussed in this chapter.

9.2. OXIDATION-REDUCTION ENHANCED PHOTOCATALYSIS

When a photon reaches the surface of a semiconductor (e.g. TiO_2), the formation of an electron-hole and a mobile electron are promoted through an electron shift from the valence band to the conduction band (Fox and Dulay, 1993). Electrons and electron holes can migrate to the semiconductor surface, reacting with the adsorbed species. The hole is a site for $OH^{\bullet}$ radical formation, which in turn oxidizes the adsorbed hydrocarbon species. Oxygen dissolved in water can scavenge the formed electron, though not very effectively.

One main drawback of photocatalysis is the potential recombination of the hole and the electron, leading to process inefficiencies and the accomplishment of no useful work.

Studies in photocatalysis have focused on either the oxidation of organic compounds; case of phenol, aromatics, herbicides, pesticides, solvents and aliphatics in the absence of inorganic cations (Barbeni *et al.*, 1984; Lu and Chen, 1997; Mills *et al.*, 1996; Ollis *et al.*, 1984) or the photoreduction of inorganic ionic species in water free of

CuuDuongThanCong.com https://fb.com/tailieudientucntt

organic species (such as Ag, Pt, Au, Cr, Hg) (Aguado *et al.*, 1991; Burns *et al.*, 1999; Chenthamarakshan *et al.*, 2000; Herrman *et al.*, 1998; Navio *et al.*, 1998). In particular and for the case of photoreduction, it has been shown that only cations with standard reduction potentials greater than 0.3 V can be treated via TiO_2 photocatalysis.

To overcome the intrinsic process limitations of electron/electron-hole recombination which lead to low quantum yields and *PTEF* values, photocatalysis can be developed under enhanced electron and hole-scavenging processes. This can be achieved in processes where the simultaneous conversion of organic and inorganic species takes place.

In the technical literature, this approach was considered, in only a few studies. For instance, Ag, Au, Cd, Cr, Hg, Ni and Pt dissolved as metal cations in water media were successfully photoreduced in the presence of methanol, formic acid, salicylic acid, EDTA, phenol and nitrobenzenes (Burns *et al.*, 1999; Prairie *et al.*, 1993). Furthermore, the reduction of these inorganic species can be enhanced in the presence of the described organic molecules (hole scavengers) (Buttler and Davis, 1993; Chen and Ray, 2001; Prairie *et al.*, 1993). Thus, there is evidence of the importance of the combined organic and inorganic pollutant photoconversion and this topic deserves continued attention in order to take full advantage of enhancement effects.

With the goal of having a more in-depth understanding of oxidation-reduction effects and of engineering efficient photocatalytic reactors operating with limited recombination of electron-holes and electrons, the photoconversion of phenol and silver is currently considered in a Photo-CREC-Water II slurry unit.

9.2.1. *Photocatalytic Thermodynamic Efficiency Factor (*PTEF*) for oxidation-reduction processes*

Serrano and de Lasa (1997, 1999) evaluated the efficiency of the photocatalytic conversion of organic pollutants using a *PTEF* (Photocatalytic Thermodynamic Efficiency Factor). This factor is based on both photochemical and thermodynamic principles.

The *PTEF* factor ($PTEF=\eta= Q_{used}/ Q_a$), equates the used energy in the photochemical transformation and the photon energy absorbed by the photocatalyst. The *PTEF* is of general applicability with its application not being restricted to a specific chemical species, reaction order, reactor geometry or reactor type (i.e. homogenous or heterogeneous).

The *PTEF* can also describe the energy efficiency in a process where there is simultaneous oxidation and reduction of water contaminants. In such a process, the Q_{used} of the *PTEF*, represents the additive contribution of the enthalpy requirements to sustain both the reduction and oxidation processes. Consistently with this view, the numerator of the *PTEF* shall include the addition of energy used for the oxidation and reduction processes:

$$\eta = PTEF = \frac{[r_{OH^\bullet}(\Delta H_{OH^\bullet}) - r_{M^+}(\Delta H_{M^+})]W_{irr}}{Q_a} \tag{9-1}$$

or

$$\eta = PTEF = \frac{[r'_{OH^\bullet}(\Delta H_{OH^\bullet}) - r'_{M^+}(\Delta H_{M^+})]A_{irr}}{Q_a} \tag{9-2}$$

CuuDuongThanCong.com https://fb.com/tailieudientucntt

where $r_{OH^\bullet}$ and $r'_{OH^\bullet}$ represent the rates of formation of $OH^\bullet$ radicals, r_{M^+} and r'_{M^+} the rates of consumption of the metal cation M^+, $\Delta H_{OH^\bullet}$ the enthalpy of formation of $OH^\bullet$ radicals (J mole^{-1}), ΔH_{M^+} the enthalpy of reduction of metal cations (J mole^{-1}), Q_a the energy absorbed by the photocatalyst (J s^{-1}), W_{irr} the weight of irradiated catalyst and A_{irr} (m^2) the area of irradiated TiO_2.

Alternatively and as described in Chapter VI, other less meaningful yet useful definitions of *PTEF* in simultaneous oxidation-reduction photocatalysis leads to the following:

$$\eta = PTEF = \frac{[r''_{OH^\bullet}(\Delta H_{OH^\bullet}) - r''_{M^+}(\Delta H_{M^+})]V_{irr}}{Q_a} \tag{9-3}$$

or

$$\eta = PTEF = \frac{[r'''_{OH^\bullet}(\Delta H_{OH^\bullet}) - r'''_{M^+}(\Delta H_{M^+})]V}{Q_a} \tag{9-4}$$

where $r''_{OH^\bullet}$ and $r'''_{OH^\bullet}$ represent the rates of formation of $OH^\bullet$ radicals, r''_{M^+} and r'''_{M^+} the rates of consumption of the metal cation M^+, V the reactor volume and V_{irr} the irradiated volume section.

Considering that $\eta_{OH^\bullet} = \frac{\Delta H_{OH^\bullet}}{\alpha\left[\frac{N_A hc}{\lambda}\right]}$ represents the fraction of the photon energy used to form $OH^\bullet$ groups, and $\eta_{M^+} = \frac{\Delta H_{M^+}}{\alpha\left[\frac{N_A hc}{\lambda}\right]}$ the fraction of the photon energy employed to reduce a metal cation, one can express the *PTEF* parameter as follows.

$$\eta = PTEF = (\varphi_1 \eta_{OH} + \varphi_2 \eta_{M^+}) \tag{9-5}$$

with φ_1 and φ_2 representing the quantum efficiencies for the oxidation and reduction processes respectively.

Furthermore, in the ideal case of a photocatalytic reactor with a quantum yield of $\varphi_1 = 1$ and $\varphi_2 = 1$ (only primary processes involved), one can expect a $PTEF_{max}$ for combined oxidation-reduction processes equal to the following.

$$\eta_{max} = PTEF_{max} = (\eta_{OH} + \eta_{M^+})_{max} \geq \eta = PTEF \tag{9-6}$$

9.2.2. Evaluation of the $PTEF_{max}$ *for Oxidation-Reduction Processes*

Regarding the $PTEF_{max}$ parameter, an evaluation can be performed using phenol as the organic model pollutant and silver (Ag^+) as the inorganic model cation pollutant. The α parameter is set to unity and the following enthalpies for silver reduction and for the formation of the $OH^\bullet$ group are considered:

a) Enthalpy of the $OH^\bullet$ free radical is assessed at 94600 Joule mole^{-1} (Serrano and de Lasa, 1997),
b) Enthalpy for the reduction of the silver ion is estimated at 77200 Joule mole^{-1}, using the information regarding reduction potential, as reported in (Weast and Astle, 1982).

$$Ag^+(aq) + e^- \rightarrow Ag(s), \quad E^o = 0.8 \text{ Volt}, \quad \Delta H_{Ag^+} = 77200 \; Joule/mole Ag^+$$

CuuDuongThanCong.com https://fb.com/tailieudientucntt

As a result, $\eta_{OH^\bullet} = \frac{\Delta H^{\bullet}_{OH}}{\alpha\left[\frac{N_A hc}{\lambda}\right]} = 0.289$ and $\eta_{M^+} = \frac{\Delta H_{M^+}}{\alpha\left[\frac{N_A hc}{\lambda}\right]} = 0.236$ leading to $\eta_{max} = PTEF_{max} = (\eta_{OH} + \eta_{M^+}) = 0.527$.

Thus, the highest possible *PTEF* ($PTEF_{max}$) for the ideal condition of both quantum yields equal to unity is 0.527. This means that 52.7% of the energy absorbed by the photocatalyst is used in combined oxidation-reduction processes.

9.2.3. Assessing the PTEF *for Oxidation-Reduction Processes*

Calculation of the *PTEF* involves the evaluation of equation (9-1) or (9-2). However even if equations (9-1) and (9-2) are phenomenologically sound, it may be difficult to establish W_{irr}, the amount of irradiated catalyst in a slurry medium. This is particularly the case when silver cations are photo reduced forming Ag^o with Ag^o being deposited on the TiO_2 surface

Thus, when proceeding with energy efficiency calculations, *PTEF* definitions using pseudo homogenous reaction rates; r'''_{OH} or r'''_{M^+} are preferred. For this reason data analysis is developed on the basis of equation (9-4).

$$\eta = PTEF = \frac{[r'''_{OH^\bullet}(\Delta H_{OH^\bullet}) - r'''_{M^+}(\Delta H_{M^+})]V}{Q_a} \tag{9-7}$$

Considering that the rate of consumption of $OH^\bullet$ can be related to the initial rate of consumption of the model pollutant, as explained in Chapter VI, equation (9-5) becomes:

$$\eta = PTEF = \frac{[-\frac{\nu}{\nu_1} r'''_{1,in}(\Delta H_{OH^\bullet}) - r'''_{M^+}(\Delta H_{M^+})]V}{Q_a} \tag{9-8}$$

Regarding the evaluation of Q_a and given that the Photo-CREC-Water II unit is operated with 0.12 g L^{-1} of TiO_2 providing complete light absorption for Ag^+ free conditions, addition of silver cations can only lead to the same $Q_a$with the light absorption taking place in a close-to-light source thinner wall region. Thus, in the case of oxidation-reduction, there is no change to the value to be assigned to the Q_a parameter.

9.2.4. Modeling Reaction and Adsorption Processes for Phenol and Silver

As shown in chapter I, both the organic compound and the metal cation consumption rates can be related to the rate of species photoconversion through the observed changes of concentration in the fluid phase. This approach requires, as described in Chapter VII that the adsorption-desorption process for both silver and phenol be at quasi-equilibrium. Under these conditions the following can be postulated

CuuDuongThanCong.com https://fb.com/tailieudientucntt

a) For phenol

$$r'''_{1T,in} = r'''_{1,in}(1 + K'_1) \text{ and } r'''_{1,in} = \left.\frac{dC_1}{dt}\right|_{in} \tag{9-9}$$

with $K'_1 = \frac{K^*_1 W q_{1,m}}{V}$ and:

b) For silver

$$r'''_{Ag^+T,in} = r'''_{Ag^+,in}(1 + K'_{Ag^+}) \text{ and } r'''_{Ag^+,in} = \left.\frac{dC_{Ag}}{dt}\right|_{in} \tag{9-10}$$

with $K'_{Ag^+} = \frac{K^*_{Ag^+} W q_{Ag,m}}{V}$

Thus, one should carefully consider equations (9-9) and (9-10) in order to assess the total rate of converted species in the photocatalytic reactor system. Defining these parameters is critical for the proper evaluation of energy efficiencies.

9.2.5. Experimental Results

In order to demonstrate the significance of combined oxidation-reduction, three series of experiments are developed.

a) Photoreduction of silver cations in aqueous TiO_2 slurry
b) Photooxidation of phenol in aqueous TiO_2 slurry
c) The combined photoreduction and photooxidation of silver cations and phenol in aqueous TiO_2 slurries.

Figure 9.1 reports the photoreduction of silver cations at different initial Ag^+ concentrations. A continuous decrease of silver cations is consistently observed. These rates of photoreduction are much faster than the rates of phenol photooxidation, as it will be described later.

Regarding the macroscopic changes in the TiO_2-water slurry, it is noticed that a number of color changes occur in the slurry, first becoming light gray and, then after few minutes of irradiation, turning to dark gray. These changes in the solution's appearance are attributed to the higher concentration of silver metal particles. These conditions affect light transmission with increased absorption in the near wall region. These conditions, they do not lead however, to changes in the Q_a parameter.

As shown in Figure 9.1, 40 minutes of irradiation, after the dark reaction period, are required to photoreduce the silver cation from a solution with an initial Ag^+ ion concentration of 45 ppm. In the same figure, it can also be observed that it takes 130 minutes to completely deplete the silver cations from a 100-ppm solution. It is therefore apparent that the initial silver cation concentration has an important effect on the time required for achieving the complete removal of silver cations. The inspection of the silver cation decay curves shows silver cation concentration experiments with a close to zero order kinetics and this is more apparent at the higher silver concentration.

With the data shown in Figure 9.1; $V = 6L$; $W = 0.72g$; $\Delta H_{OH^\bullet} = 77200\, J\, mole^{-1}$; $Q_a = 89.382\, J\, min^{-1}$; and $q_{Ag^+} = \frac{0.696 C_{Ag^+}}{1+0.00157 C_{Ag^+}}$, for the silver cation

CuuDuongThanCong.com https://fb.com/tailieudientucntt

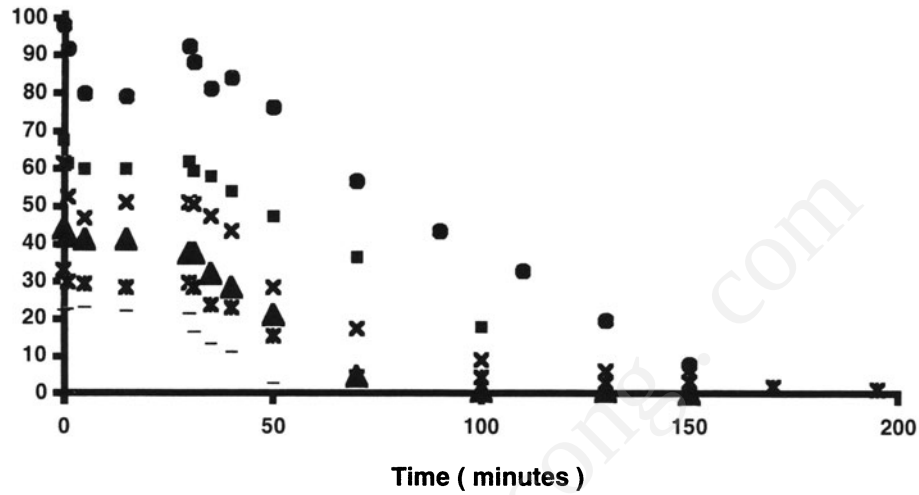

FIGURE 9.1. Photo reduction of silver at different initial concentrations (●) 100 ppm, t_{util} = 101.37 h,(■) 68 ppm C, t_{util} = 93.3 h, (×) 63 ppm, t_{util} = 91.3 h, (▲) 45 ppm, t_{util} = 97.7 h), (∗) 35 ppm, t_{util} = 96.05) and (□) 25 ppm, t_{util} = 99.37 h.

isotherm, the *PTEF* can be calculated as,

$$\eta = PTEF = \frac{[-r'''_{Ag^+T}(\Delta H_{M^+})]V}{Q_a} \tag{9-11}$$

with $r'''_{Ag^+T,in} = r'''_{Ag,in}(1 + K'_{Ag})$ and $r'''_{Ag^+,in} = \frac{dC_{Ag}}{dt}|_{in}$

Calculated *PTEF*s are reported in Table 9.1. It is shown that the *PTEF*s for silver cations are in the 3.0 – 5.7 % range. It should be noticed that the *PTEF* is maintained in a narrow range despite of the broad interval of silver cation concentrations studied.

Figure (9-2) reports the changes of phenol concentration using phenol as the sole model pollutant. The initial concentration of phenol is changed in the 10-30 ppm-C range.

TABLE 9.1. *PTEF* Values for Silver Cations in Water Solution

Initial Ag^+ Concentration (mg/L)	$PTEF^\circ$ for silver alone
100	0.0388
72	0.0344
63	0.0368
44	0.0458
35	0.0305
32	0.0411
23	0.0572

CuuDuongThanCong.com https://fb.com/tailieudientucntt

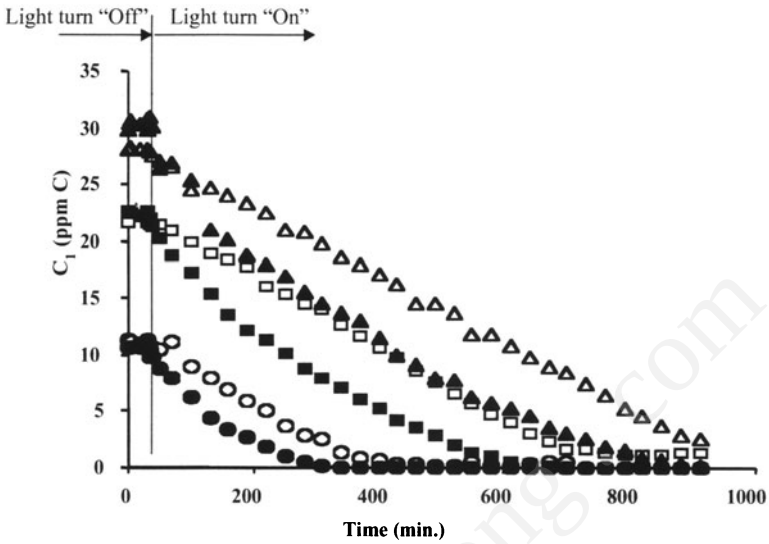

FIGURE 9.2. Phenol and TOC degradation in Photo-CREC-Water II at 12, 22 and 30 ppm-C. Open symbols: TOC. Filled symbols: phenol.

Thus, considering the definition of the *PTEF* for the photoconversion of an organic pollutant, case of phenol, it results

$$\eta = PTEF = \frac{\left[-\frac{\nu}{\nu_1} r'''_{1,in}(\Delta H_{OH})\right] V}{Q_a} \tag{9-12}$$

with $r'''_{1T,in} = r'''_{1,in}(1 + K'_1)$, $r'''_{1,in} = \left.\frac{dC_1}{dt}\right|_{in}$

Given that $\Delta H_2 = 94600\, J mole^{-1}$ and $Q_a = 89.38 J min^{-1}$, the *PTEF* values reported in Table 9.2 are obtained. This table shows that the *PTEF*s for phenol are smaller than those for silver and this is consistent with the following statements:

a) The rates for silver photoreduction are higher than those for phenol photoconversion
b) The heat of formation of $OH^{\bullet}$ radicals is 20% more endothermic than that of the reduction of Ag^{+} cations.

TABLE 9.2. PTEF for phenol photooxidation

Concentration of Phenol (ppm C)	*PTEF*
10	0.005434
20	0.005903
30	0.0063
46	0.0053
55	0.00571

CuuDuongThanCong.com https://fb.com/tailieudientucntt

TABLE 9.3. Calculated *PTEF*s using equation (9-8). *PTEF* evaluated with data from experiments using silver (alone) and phenol (alone)

Initial Phenol Concentration (ppm)	*PTEF* calculated with equation (9-12) (phenol alone)	Initial silver concentration (ppm)	*PTEF* calculated with equation (9-11) (silver alone)	*PTEF* Total
10.33	0.00543	23	0.0572	0.0627
10.33	0.00543	44	0.0459	0.0512
10.33	0.00544	98	0.0388	0.0443
19.22	0.00590	98	0.0388	0.0447

As a result, if *PTEF*s are calculated for water solutions containing phenol or silver and if one considers that oxidation-reduction processes proceed as the direct addition of individual processes, one should expect, following equation (9-8), the results reported in the last column of Table 9.3.

9.2.6. PTEF Evaluation for Oxidation-Reduction

Experiments can also be developed to have both phenol and silver cations simultaneously present in a water solution that requires treatment. Photocatalytic conversion under these conditions shows that the concurrent conversion of organic compounds and inorganic species enhances the overall process efficiency.

Figure 9.3 reports silver cation photoreduction in the presence of phenol. Phenol is added to the water solution with a 20-ppm-C initial concentration. It can be observed that in all cases there is a consistent improvement of the rate of silver photoreduction versus the photoreduction rates of silver alone. For instance, if one compares (Figure 9.4) the time for silver cation depletion (initial Ag^+ concentration of 100 ppm) a reduction of the photoconversion time from 140 min. to 80 min. is observed.

Thus, as a result of the simultaneous reduction-oxidation process, there is an increase in Ag^+ photoreduction with mobile electrons having a much lower probability of recombining with electron holes. This leads to an enhanced silver reduction with the

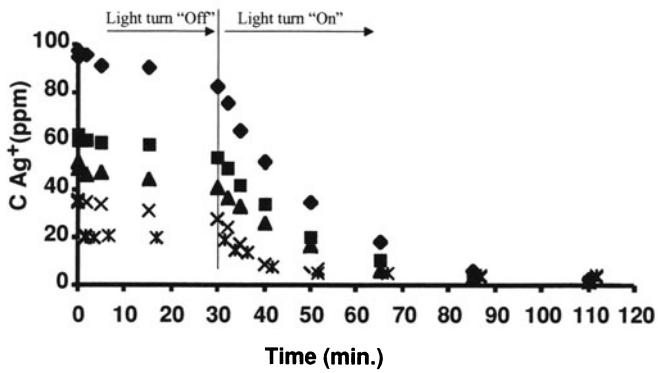

FIGURE 9.3. Effect of Phenol 20 ppm C on Silver photoreduction. (♦) 100 ppm, t_{util} = 173.67, (■) 68 ppm C, t_{util} = 141.84), (▲) 50 ppm, t_{util} = 209.31 h, (×) 35 ppm, t_{util} = 196.32 h and (*) 22 ppm, t_{util} = 137.1 h.

CuuDuongThanCong.com https://fb.com/tailieudientucntt

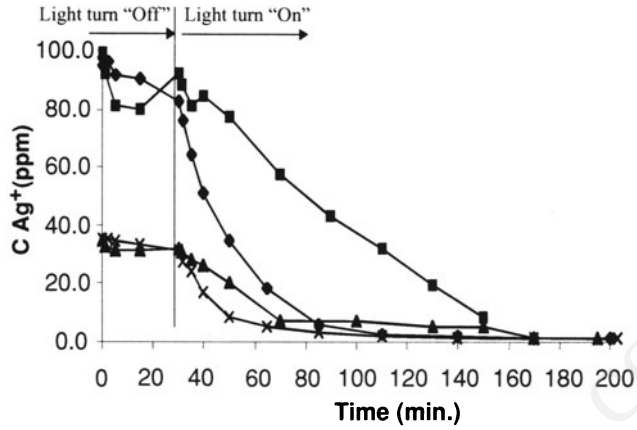

FIGURE 9.4. Effect of 20 ppm-C of phenol on silver reduction. (■) 100 ppm of silver, 0 ppm-C of phenol, $t_{util} = 101$ h, (♦) 100 ppm of silver, 20 ppm-C of phenol, $t_{util} = 173$ h, (▲) 35 ppm of silver, 0 ppm-C of phenol, $t_{util} = 96$ h, (×) 35 ppm of silver and 20 ppm-C of phenol, $t_{util} = 196$ h.

PTEF for silver (Table 9.3) being much higher than the values of Table 9.1 for silver alone.

Figure 9.5 reports the changes in phenol concentration when silver cations are present in the water solution. In this case, there is also faster phenol decay during the initial phase of photoconversion leading to *PTEF* values in the 0.014 to 0.022 range, as reported in Table 9.4. These values are at least 3-4 times larger than those observed in cases where phenol is the only water contaminant.

It can also be observed in Figure 9.5 that at 150 min of irradiation time and for the initial concentrations of 50 ppm of silver and 10 ppm-C of phenol the photoconversion

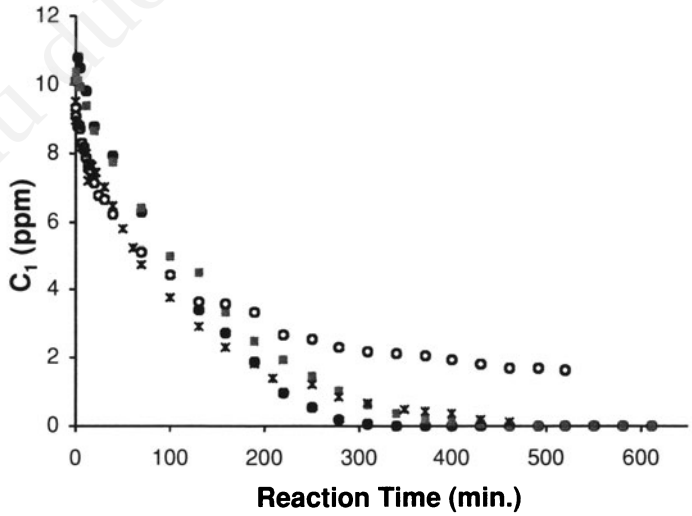

FIGURE 9.5. Changes of phenol concentration with irradiation time. (○) 50 ppm Ag^+, $t_{util} = 100$ h; (▩) 0 ppm Ag^+, $t_{util} = 30$ h; (•) 100 ppm Ag^+, $t_{util} = 80$ h and (*) 100 ppm Ag^+, $t_{util} = 90$ h.

CuuDuongThanCong.com https://fb.com/tailieudientucntt

TABLE 9.4. *PTEF* factor calculated using equations (9-5) or (9-8): direct addition of *PTEF* simultaneous photo reaction of phenol and silver

Initial concentration	η for silver	η for phenol	η calculated with equation (9-5)
phenol = 10 ppm-C, silver = 25 ppm	0.257	0.0147	0.272
phenol = 10 ppm-C, silver = 50 ppm	0.103	0.0188	0.122
phenol = 10 ppm-C, silver = 100 ppm	0.132	0.0219	0.154
phenol = 20 ppm-C, silver = 100 ppm	0.086	0.0144	0.100

rates become smaller than the ones with no silver addition. These slower rates are attributed to the influence of silver deposited on the TiO_2 particles.

While silver is a good model cation for fundamental studies leading to better understanding of the phenomena affecting combined oxidation-reduction photocatalytic processes, the use of silver is not recommended for full exploitation of the oxidation-reduction principle. Silver can also be very toxic and difficult to remove.

The difficulties experienced with silver metal deposition can be circumvented if a photocatalytic oxidation-reduction process is developed in which the reduced cation is kept in solution and it can be easily brought back to the oxidized state.

In brief, it is shown that combined photooxidation and photoreduction of organic and inorganic species can considerably enhance the efficiency of photocatalytic reactors. It is also expected that a proper selection of the cation will optimize simultaneous oxidation-reduction processes.

9.3. APPLICATION OF PHOTOCATALYSIS TO THE INACTIVATION OF MICROORGANISMS

Titanium dioxide-based photocatalysis for water purification has been the focus of a large volume of research over the past twenty years. In spite of that fact, only a few studies have explored its possibilities for biocidal applications (Stuart *et al.*, 2003, Kabir et al., 2003).

9.3.1. Inactivation Apparent Quantum Yield

Chapter VI indicates that photocatalysis can benefit from the definition and use of efficiency parameters, which are based on fundamentals thermodynamic and kinetic properties. Such parameters permit the direct comparison of results obtained from different experimental systems and conditions.

Considering the work of Stuart et al. (2003), an inactivation quantum yield (*IQY*) parameter can be defined as the ratio of the number of carbon atoms inactivated over the number of photons absorbed:

$$IQY = \varphi_{inact,in} = \frac{\left[\frac{dN_c}{dt}\right]_{in}}{P_a} \tag{9-13}$$

CuuDuongThanCong.com https://fb.com/tailieudientucntt

with P_a representing the rate of absorbed photons and $\left[\frac{dN_c}{dt}\right]_{in}$ the rate of photoinactivation of carbon atoms at initial conditions (atoms of carbon inactivated s^{-1}).

9.3.2. Microorganisms Inactivation Results

To evaluate the efficiency of photocatalytic processes for the inactivation of microorganisms, experiments can be developed using a 6-liter Photo-CREC-Water-II slurry reactor with 0.24g of Degussa P25 TiO_2/L^{-1} and powered with a 15 W near-UV lamp (Stuart et al. (2003)). The inactivation of both MS2 bacteriophage (ATCC-15597-B1) and *E. coli* can be considered. Monitoring the MS2 ability to infect E. coli allows to assess the progress of MS2 inactivation. Phage particles from bacterial lysates can be purified, concentrated and titrated to determine the number of PFU (particle forming units) per milliliter.

In both cases, TiO_2-based photocatalysis shows much better inactivation than straight near-UV light or catalyst without irradiation. Typical inactivation times range from 5–10 minutes with results confirmed via triplicate-plate counts averages.

E. coli displays during the above described experiments a distinctive pattern with a three-minute lag phase in the inactivation kinetics. This lag was assigned to the ROS (reactive oxygen species)-neutralizing enzymes that are inherent to *E. coli*.

9.3.3. Evaluation of the Inactivation Quantum Yields

For biocidal applications, the quantum yield efficiency can be modified by introducing an inactivation quantum yield (IQY), as described in equation (9-13). For *E. coli*, the *IQY* values were calculated with initial rates of inactivation, assessed after the 3-minutes lag phase period.

Table 9.5 reports *IQE*s for both MS2 and *E. coli* using an initial concentration of 10^4 particles (or cells) per milliliter. In both cases *IQE*s were much larger than 1. *IQE* values for both MS2 and *E. coli* are encouraging, particularly since quantum efficiencies for the photoconversion of organic molecules in water consistently remains below 1.

The much larger *IQE*s for *E. coli* versus MS2 can be attributed to the more abundant oxidative-inactivation of *E. coli* bacteria. This is due to the greater dependence of *E. coli* on numerous interrelated physiological systems for survival.

TABLE 9.5. IQY for *E. coli* and MS2 bacteriophage TiO_2-black light mediated inactivation

Organism	First Order inactivation constant (min^{-1})	*IQY* (Carbons inactivated/ photon)
MS2 Bacteriophage	0.817	22
E. coli	0.237	$5.19\ 10^5$

Note: Average carbon contents of MS2 phage and *E. coli* assessed at $1.16\ 10^5$ and $7.27\ 10^9$ respectively.

CuuDuongThanCong.com https://fb.com/tailieudientucntt

9.4. CONCLUSIONS

From this chapter, we can conclude that

(a) The combined photooxidation and photoreduction of organic and inorganic species can considerably enhance the efficiency of photocatalytic reactors.
(b) The assessment of energy efficiencies in photocatalytic reactors with a combined oxidation-reduction requires the introduction of a modified *PTEF*.
(c) Photocatalytic reactors show important enhancement effects when simultaneous reaction of phenol and silver occur. At the beginning of the reaction, the phenol photoreaction in the presence of silver is faster than that of the phenol alone.
(d) The application of photocatalysis to the inactivation of microorganisms requires the consideration of a *IQY*, inactivation quantum yield efficiency factor.
(e) The *IQY*s for both MS2 and *E. coli* well in excess of unity shows the ability of a photon to inactivate a large number of carbon atoms, an important characteristic of photocatalysis when applied to physiological systems.

NOMENCLATURE

Symbols

A_{irr}	catalyst irradiated area	m^2
c	speed of light in vacuum	$2.99\ 10^7$ cm s^{-1}
C_1	model pollutant concentration	mole L^{-1}
C_{Ag^+}	Silver cation concentration	mole L^{-1}
C_{in}	initial pollutant concentration	mole L^{-1}
h	Plank's constant	6.62618×10^{-34} J s
K'_{Ag^+}	Adsorption group involved in equation (9 –10)	-
K^*_{Ag}	Slope of the adsorption isotherm $q_1/q_{1,m}$ at pollutant concentration C_{Ag^+}	L $mole^{-1}$
K'_1	Adsorption group involved in equation (9–9)	-
K^*_1	Slope of the adsorption isotherm $q_1/q_{1,m}$ at pollutant concentration C_1	L $mole^{-1}$
N_A	Avogadro's number	6.023×10^{23} molecules $mole^{-1}$
N_c	number of carbon atoms in microorganisms to be inactivated	mole
P_a	rate of irradiated energy adsorbed in the photocatalytic reactor	J s^{-1}
P_{used}	rate of irradiated energy used for the formation of $OH^\bullet$ radicals	J s^{-1}
$q_{Ag^+,m}$	Maximum adsorbed concentration of model pollutant	mole $gcat^{-1}$
$q_{1,m}$	Maximum adsorbed concentration of model pollutant	mole $gcat^{-1}$

CuuDuongThanCong.com https://fb.com/tailieudientucntt

Q_a	Rate of irradiated energy absorbed in the mesh	J s^{-1}
Q_{used}	Rate of irradiated energy used in the oxidation-reduction process	J s^{-1}
$r'''_{Ag^+,in}$	Initial reaction rate of silver, based on the unit system reactor volume	mole L^{-1} s^{-1}
r'''_{Ag^+T}	total reaction rate of silver, based on the unit system reactor volume	mole L^{-1} s^{-1}
$r'''_{Ag^+T,in}$	total initial rate of silver reduction based on the unit system reactor volume.	mole L^{-1} s^{-1}
r_{M^+}	rate of reduction of M^+ cations based on the unit weight of irradiated catalyst	mole $gcat^{-1}$ s^{-1}
r'_{M^+}	rate of reduction of M^+ cations based on the unit area of irradiated catalyst	mole m^{-2} s^{-1}
r''_{M^+}	rate of reduction of M^+cations (mole L^{-1} s^{-1})	mole L^{-1} s^{-1}
r'''_{M^+}	rate of reduction of M^+ cations rate of OH radical formation	mole L^{-1} s^{-1}
$r_{OH^\bullet}$	rate of $OH^\bullet$ radical formation based on the unit weight of irradiated catalyst	mole $gcat^{-1}$ s^{-1}
$r'_{OH^\bullet}$	rate of $OH^\bullet$ radical formation based on the unit area of irradiated catalyst	mole m^{-2} s^{-1}
$r''_{OH^\bullet}$	rate of $OH^\bullet$ radical formation based on the unit of irradiated reactor volume	mole L^{-1} s^{-1}
$r'''_{OH^\bullet}$	rate of $OH^\bullet$ radical formation based on the unit reactor volume	mole L^{-1} s^{-1}
$r'''_{1,in}$	rate of disappearance of model pollutant at initial conditions	mole L^{-1} s^{-1}
$r'''_{IT,in}$	total initial rate of organic model pollutant photoconversion based on the unit system reactor volume	mole L^{-1} s^{-1}
t	irradiation time	min.
t_{util}	time of utilization of the lamp	min.
V_{irr}	irradiated reactor volume	L
V	$V = V_D + V_{irr}$, reactor volume system	L
W	Weight of adsorbent material	g_{ads}
W_{irr}	irradiated weight of catalyst	g_{cat}

Greek Symbols

α	Number of photons required for the formation of an $OH^\bullet$ radical	-
η	photochemical thermodynamic efficiency factor	-
η_{max}	maximum photochemical thermodynamic efficiency factor	-
η_{M^+}	fraction of photon energy used in the formation of the metallic silver	-

CuuDuongThanCong.com https://fb.com/tailieudientucntt

$\eta_{OH^\bullet}$	fraction of photon energy used in the formation of $OH^\bullet$ radicals	-
ΔH_{M^+}	enthalpy of formation of metallic silver.	J mole^{-1}
$\Delta H_{OH^\bullet}$	enthalpy of $OH^\bullet$ radical formation in a photochemical reaction	J mole^{-1}
λ	wavelength.	nm
φ_1	quantum yield or fraction of photons absorbed by the photocatalyst resulting in the formation of $OH^\bullet$ radicals	-
φ_2	quantum yield or fraction of photons absorbed by the photocatalyst resulting in the reduction of silver cations	-
$\varphi_{inact.in}$	inactivation quantum yield.	-
ν	stochiometric number for the $OH^\bullet$ radical reacting with the model compound (negative number)	-
ν_1	stochiometric number for the model pollutant reacting with $OH^\bullet$ group radicals (negative number)	-
ν_p	stochiometric number for the pollutant chemical species (model pollutant and intermediates) reacting with the $OH^\bullet$ group (negative number)	-

Subscripts

in	initial condition
max	maximum
p	pollutant

Acronyms

PTEF	Photochemical Thermodynamic Efficiency Factor
IQY	Inactivation Quantum Yield.

REFERENCES

Aguado, M. A., Gimenez, J. and Cervera–March, S., 1991, Continuous photocatalytic treatment of Cr(VI) effluents with semiconductor powders, *Chem. Eng. Comm.* **104**:71–75.

Barbeni, M., Pramauro, E. and Pelizzetti, E., 1984, Photodegradation of 4-chlorophenol catalyzed by titanium dioxide particles", *Nouveau Journal de Chimie*, **8**(8–9):547–550.

Burns, R. A., Crittenden, J. C., Hand, D. W., Seizer, V.H., Sutter, L. L., and Slman R. Salman, S. R., 1999, Effect of inorganic ions in heterogeneous photocatalysis of TCE, *J. of Envir. Eng*, January , **125** ,77–85

Buttler, E. C. and Davis, A. P., 1993, Photocatalytic oxidation in aqueous titanium dioxide suspensions: The influence of dissolved transition metals, *J. Photochem. Photobiol. A: Chem.*, **70**:273–283.

Chen, D. and. Ray, A.K., 2001, Removal of toxic metal ions from wastewaters by semiconductor photocatalysis, *Chem.Eng. Sci.*, **56**:1561–1570.

Chenthamarakshan, C. R., Yang, H., Ming, Y. and Rajeshwar, K., 2000, Photocatalytic reactivity of zinc and cadmium ions in UV-irradiated titania suspensions., *J. of Electrochemical Chemistry*, **494**:79–86.

Fox, M. A. and Dulay, T. M., 1993, Heterogeneous photocatalysis. *Chem. Rev.* **93**:341–357 .

Herrman, J. M., Disidier, H. and Pichat, P. 1998, Photocatalytic deposition of silver on powder titania: Consequences for the recovery of silver. *J. of Catalysis* **113**:72–81.

CuuDuongThanCong.com https://fb.com/tailieudientucntt

Kabir, M. F., Haque, F., Vaisman, E., Langford, C. H. and Kantzas, A., 2003, Desinfecting E. coli in drinking water using a novel fluidized bed reactor., *Int. J. Chem. Reactor Engineering*, **1:** A 39,1–12

Lu, M. C., and Chen, J. N., 1997,. Pretreatment of pesticide wastewater by photocatalytic oxidation., *Wat. Sci. Tech*, **36**(2–3):117–122.

Mills, A., Belghazi, A., and Rodman, D.,1996, Bromate removal from drinking water by semiconductor photocatalysis, *Wat. Res*. 30(9):1973–1978.

Navio, J. A., Colon, G., Trillas, M., Peral, J., Domenech, X, Testa, J. J., Padron, J., Rodriguez, D. and Litter, M. I., 1998, Heterogeneous photocatalytic reactions of nitrite oxidation and Cr(VI) reduction on iron-doped titania prepared by the wet impregnation method., *Applied Catalysis B*: **16**:187–196.

Ollis, D. F., Hsiao, C. Y., Budiman, L. and Lee, C. L., 1984, Heterogeneous photoassisted catalysis: conversions of perchloroethylene, dichloroethane, chloriacetic acids and chlorobenzenes.", *J. of Catalysis*, **88**:89–96

Prairie, M. R., Evans, L. R., Stange, B. M., and Martinez, S. L., 1993, An investigation of TiO2 photocatalysis for the treatment of water contaminated with metals and organic chemicals, *Env. Sci. Technol*. **27**:1776–1782.

Salaices, M., Serrano, B. and de Lasa, H. I., 2002, Experimental evaluation of photon absorption in an aqueous TiO_2 slurry reactor, *Chem. Eng. Journal*, **90**:219–229.

Salaices, M., Serrano, B. and de Lasa, H., 2001, Photocatalytic conversion of organic pollutants extintion coefficients and quantum efficiencies, *Ind. Eng Chem Res*, **40**:5455–5464.

Serrano, B. and de Lasa, H, 1997, Photocatalytic degradation of water organic pollutants: Kinetic and energy modeling, *Ind. Chem. Eng. Res*., **36**(11):4705–4711.

Serrano, B. 1998, Photocatalytic Degradation of organic water pollutants: Energy efficiency and kinetic modeling. PhD Dissertation, The University of Western Ontario, Canada.

Serrano, B. and de Lasa, H. 1999, Photocatalytic degradation of water organic pollutants: Pollutant reactivity and kinetic modeling, *Chem. Eng. Sci.,* **54**: 3063–3069.

Stuart, J., Salaices, M., Valvano M. and de Lasa H., 2003 Photocatalytic inactivation of MS2 bacteriophage and E.coli. Kinetics modeling and quantum efficiency. *Proc. 18th North American Catalysis Symp*. pp247

Weast, R. C. and Astle, M. J.,1982–1983, Handbook of chemistry and physics, *63 Edition, CRC Press.* pp D–162.

cuu duong than cong . com

CuuDuongThanCong.com https://fb.com/tailieudientucntt

Subject Index

CuuDuongThanCong.com https://fb.com/tailieudientucntt

CuuDuongThanCong.com https://fb.com/tailieudientucntt

cuu duong than cong . com

CuuDuongThanCong.com https://fb.com/tailieudientucntt